Fast Terahertz Metamaterial/Graphene-Based Optoelectronic Devices for Wireless Communication

Abdullah (Mohammed) Zaman, BSc, MSc
School of Engineering
Lancaster University

A thesis submitted for the degree of
Doctor of Philosophy

July, 2023

I dedicate this thesis to my parents, brothers, daughters, and daughters' mother who were extremely patient and supportive during all these years.

Declaration

I declare that the work presented in this thesis is, to the best of my knowledge and belief, original and my own work. The material has not been submitted, either in whole or in part, for a degree at this, or any other university. This thesis does not exceed the maximum permitted word length of 80,000 words including appendices and footnotes, but excluding the bibliography. A rough estimate of the word count is: 30417

Abdullah (Mohammed) Zaman

Fast Terahertz Metamaterial/Graphene-Based Optoelectronic Devices for Wireless Communication

Abdullah (Mohammed) Zaman, BSc, MSc.
School of Engineering, Lancaster University

A thesis submitted for the degree of *Doctor of Philosophy*. July, 2023

Abstract

Research in the terahertz (THz) band, which is broadly defined as 0.1-10 THz, is an active area of research driven by applications in sixth generation (6G) and beyond for communications, spectroscopy, imaging, and sensing. In order to exploit the full potential of all these applications, fast integrated circuitry is required. This work revolves around removing this bottleneck. Achievement of efficient dynamic modulation requires the implementation of active material. Amongst many different approaches to achieve active modulation, metamaterials/graphene-based technology is establishing itself as a benchmark for THz operation due to its versatility, power efficiency, small footprint, and integration capabilities. Our devices have been modulated all-electronically, as described in Chapters 4 and 6, and all-optically as reported in Chapter 5.

The fabrication of the novel design based on metamaterial (MM) and graphene for amplitude, phase, and polarization modulations is reported in Chapter 3. The optoelectronic behaviour of this modulator is tested in a THz time-domain spectroscopy (THz-TDS) setup as demonstrated in Chapter 4. By choosing the appropriate THz-TDS setup configuration, a spectral amplitude extinction ratio of >10 dB (>93%) at the resonant frequency of 0.8 THz is demonstrated. The spectral phase of THz radiations is actively tuned by >27° at 0.62 THz frequency. Linear to circular polarization conversion with nearly 100% of conversion efficiency is reported demonstrating almost an independent control of circular dichroism (CD) and optical activity (OA) as mentioned explicitly in Chapter 6. Dynamic changes of ellipticity are reported to exceed 0.3 in ratio at resonance. The OA of transmitted THz radiations is continuously rotated by >21.5° at 0.71 THz by varying the gate. These values are in line with acquainted literature with graphene-based or 2-dimensional electron gas modulators but with higher reconfiguration speed. The helicity, either right or left circular polarization states, of elliptical waves can be controlled. These results are of great importance for fundamental research of polarization spectroscopy, polarization imaging, or THz applications in the pharmaceutical and biomedical fields.

An all-electronic controlled metamaterial-based THz modulator is demonstrated to achieve a recorded operating speed >3 GHz which is limited by the available instrumentation as illustrated in Section 7.1. The achievements in the modulation speed (in GHz range), amplitude extinction ratio (>10 dB), phase shift tuning (27°),

and nearly decoupled control of OA and CD of THz waves are the key values of this device, which is undoubtedly meaningful for communication applications and has a certain impact on the THz modulator technology.

The achieved GHz modulation speed of this hybrid MMs/graphene device is within very good agreement with previous literature reported on pristine graphene. This result provides an upper intrinsic limit of the maximum reconfiguration speed of these devices to 100s of GHz and, at the same time, reinforces the use of metamaterial/graphene optoelectronic devices for ultrafast modulation of terahertz waves. This overall remarkable performance of an optoelectronic modulator based on metamaterial/graphene resonators is capable of efficiently modulating THz radiation all-electronically with GHz-reconfiguration speed. It is worth highlighting that this exceptionally high reconfiguration speed, the highest reported so far to the best of our knowledge for a graphene-based integrated device, was not achieved at the expense of the other performances, e.g. amplitude and polarization modulation depths. These results represent great progress for several terahertz research and ultrafast photonic applications, such as the realization of fast deep, and efficient THz circuitry for the investigation of exotic quantum phenomena, wireless communications, and laser diodes stabilization in quantum electronics.

Publications

Abdullah M. Zaman et al. (2023). "Versatile and active THz wave polarization modulators using metamaterial/graphene resonators". In: *Front. in Nanotechnol.* 5. ISSN: 2673-3013. DOI: 10.3389/fnano.2023.1057422. URL: https://www.frontiersin.org/articles/10.3389/fnano.2023.1057422

Abdullah M. Zaman et al. (2022d). "Ultrafast modulation of a THz metamaterial/graphene array integrated device". In: *Appl. Phys. Lett.* 121.9, p. 091102. DOI: https://doi.org/10.1063/5.0104780

Abdullah M. Zaman et al. (2022b). "Terahertz Metamaterial Optoelectronic Modulators with GHz Reconfiguration Speed". In: *IEEE Transactions on Terahertz Science and Technology* 12.5, pp. 520–526. DOI: 10.1109/TTHZ.2022.3178875

Yuezhen Lu, Lucy L Hale, **Abdullah M Zaman**, Sadhvikas Addamane, Igal Brener, Oleg Mitrofanov, Riccardo Degl'Innocenti (2023). "Near-field spectroscopy of high Q modes in individual asymmetric split-ring Terahertz resonators". In: Submitted

Yuezhen Lu, Haitao Zhu, **Abdullah M Zaman** et al. (2023). "Non-contact 3D Surface Roughness and Height Levelling Characterisation of Electrochemically Polished Additive Manufactured Steel Components using Reflection Terahertz Time-domain Spectroscopy and Laser Scanning Microscopy". In: Submitted

Peer-Reviewed Conference Proceeding and Participation

Lucy Hale , Yuezhen Lu, **Abdullah Zaman**, Sadhvikas Addamane, Igal Brener, Oleg Mitrofanov, Riccardo Degl'Innocenti (2023). "Near Field Analysis Of Individual High Quality Factor THz Resonators". Submitted to the *2023 48th International Conference on Infrared, Millimeter, and Terahertz Waves (IRMMW-THz).*

Abdullah M. Zaman et al. (2022a). "Active Polarization Modulation of Terahertz Radiation Using Metamaterial/Graphene-Based Optoelectronic Devices". In: *2022 47th International Conference on Infrared, Millimeter and Terahertz Waves (IRMMW-THz)*, pp. 1–3. DOI: 10.1109/IRMMW-THz50927.2022.9895720

Yuezhen Lu, Haitao Zhu, **Abdullah M. Zaman** et al. (2022). "Surface Roughness Measurement of 3D-Printed 316L Stainless Steel Surface using Terahertz

Time-Domain Spectroscopy". In: *2022 47th International Conference on Infrared, Millimeter and Terahertz Waves (IRMMW-THz)*, pp. 1–2. DOI: 10.1109/IRMMWTHz50927.2022.9920607

Abdullah M. Zaman et al. (2022c). "Towards Ultrahigh Modulation Speed of Terahertz Optoelectronic Devices Based on Metamaterial/Graphene Split-Ring Resonators". In: *2022 9th International Conference on Optical Terahertz Science and Technology (OTST2022), held at Mercure Budapest Castle Hill Hotel, Budapest, Hungary, June 19-24, 2022.* URL: https://www.otst2022.hu/

Abdullah M. Zaman et al. (2021). "Graphene-based External Optoelectronic Terahertz Modulators for High Speed Wireless Communications". In: *2021 14th UK-Europe-China Workshop on Millimetre-Waves and Terahertz Technologies (UCMMT)*, pp. 1–3. DOI: 10.1109/UCMMT53364.2021.9569931

Awards and Distinctions

Selected as a **keynote presenter and acted as a chair** of the metasurfaces and plasmonic session at the 47^{th} International Conference on Infrared, Millimeter and Terahertz Waves (IRMMW-THz) in August-September 2022

Invited peer-reviewer to the Manchester Elite Research Conference (MERC2022) held at Roscoe Building, University of Manchester on 18 September 2022, organized by Saudi researchers in the UK, and sponsored by the Royal Embassy of Saudi Arabia Cultural Bureau (SACB)

Awarded the $\mathbf{3}^{rd}$ **prize** in the year 3 or equivalent category for their presentation at the Engineering Postgraduate Research Conference at Lancaster University on 6-7 July 2022

Awarded the **best poster** for the track of Computer and Engineering Sciences at the Britain Saudi Research Forum (UKSRF) on 6 March 2022, organized by Saudi researchers in the UK, and sponsored by the Royal Embassy of Saudi Arabia Cultural Bureau (SACB)

Awarded the $\mathbf{3}^{rd}$ **prize** in the year 1 or equivalent category for their presentation at the Engineering Postgraduate Research Conference at Lancaster University in July 2020

Acknowledgements

I am very grateful to my advisor, Dr Riccardo Degl'Innocenti, for original ideas, his positive support, and thoughtful guidance during my PhD program. I owe him many thanks for believing in me and keeping me motivated all the time.

I would like to thank my PhD viva committee, Dr George Adamopoulos and Dr Darren Graham (University of Manchester) for their insightful comments and questions.

I would like to thank my appraisal committee, Dr Hungyen Lin and Prof Claudio Paoloni, and my mentor, Dr Rosa Letizia, for their great advice and thoughtful discussion during my thesis work. My sincere appreciation to my scholarship sponsor, Taibah University, Madina, Saudi Arabia.

I want to specifically thank Dr Xavier Romain for his great advice and thoughtful discussions during my thesis work. I also want to thank Dr Nikita W. Almond (Cavendish Laboratory at University of Cambridge) who contributed a great deal on devices' fabrication. Without her help and effort in the cleanroom facility none of this work would have been possible. I want to specifically thank Mr. Yuezhen Lu for his continues help and tremendous support throughout this journey.

I would like to thank Mr. Garry Vernon and Dr Kunal Lulla for keeping the Quantum Technology Centre (QTC-cleanroom) at the Physics department up and running. I am thankful to all the School of Engineer staff members and technicians who have helped in one way or another. Also my appreciation to all my collaborators over the years, including School of Engineering at Lancaster University: Dr Decio Alves de Lima and Mrs. Rupa Basu; Department of Engineering at University of Cambridge: Dr Oliver J. Burton, Dr Jack Alexander-Webber, and Prof Stephan Hofmann; Cavendish Laboratory at University of Cambridge: Prof Thomas Mitchell, Prof Jonathan D. P. Griffiths, Prof Harvey E. Beere, and Prof David A. Ritchie; Physics Department at Lancaster University: Dr Rostislav V. Mikhaylovskiy, Mr. Yuichi Saito, and Dr Farhan Nur Kholid; University of Birmingham: Dr Stephen Hanham for their help, support, and permission to use their facilities.

To my father and my mother, Mohammed and Manal, who supported and encouraged me from the time I opened my eyes, I am forever thankful. Without their endless love and sacrifices none of this would have been possible.

This work is dedicated to my sweetheart daughters, Hala (10-year) and Farah (4-year) who always inspire, motivate, and make me smile everyday. Lastly, I would like to thank my daughters' mother (Shahad) who was with me through thick and thin, providing constant support, and for all the late nights. Thank you for being my best friend. I owe you a lot.

Contents

List of Figures

List of Tables

Chapter 1

The terahertz range

1.1 Introduction

The terahertz (THz) electromagnetic waves are defined broadly between 0.1-10 THz, which corresponds to 3 mm to 30 μm vacuum wavelengths. This spectral range is allocated between microwave and infrared frequencies as illustrated in fig. 1.1. Advances in the THz generation and detection techniques have accelerated the field of THz science and technology including sensing and manipulations (Carpintero et al., 2015; Rieh, 2020; Y.-S. Lee and Y.-S. Lee, 2008; Dexheimer, 2008). The rapid growth of research and developments in the THz band have broadened the applications and fundamental sciences into the fields of communications, spectroscopy, and imaging sensing (Song and Tadao Nagatsuma, 2015; Peiponen, J. Axel Zeitler, and Kuwata-Gonokami, 2013; Y.-S. Lee and Y.-S. Lee, 2008; Saeedkia, 2013). Developments in the THz regime have been experiencing rapid growth as well as their related number of publications as presented by IEEE and Web of Science (Elayan et al., 2020). Wireless communications beyond fifth generation (5G) are being deployed for near-field applications for ground communications, due to atmospheric absorption, on the promise of wide unallocated bandwidth and ultrafast communication (100 Gb-1 TB/s). The theoretical bottleneck of communication systems with a limited capacity is determined by the Shannon-Hertlet formalism (Venkatesh et al., 2020). Its shorter wavelength and its higher frequency offer an advantage over the microwave range in terms of antenna gain and directionality. However, the lack of fast and efficient circuitry to manipulate and detect the THz wave properties is among the bottlenecks limiting the exploration of the THz regime. The non-ionization properties of the THz frequencies make them not harmful to the human body, similar to the RF/microwave, which means they are safe for indoor/outdoor applications. An ultrafast communication platform is also needed for high-resolution imaging and sensing for most of the applications which depict the future of digital society including

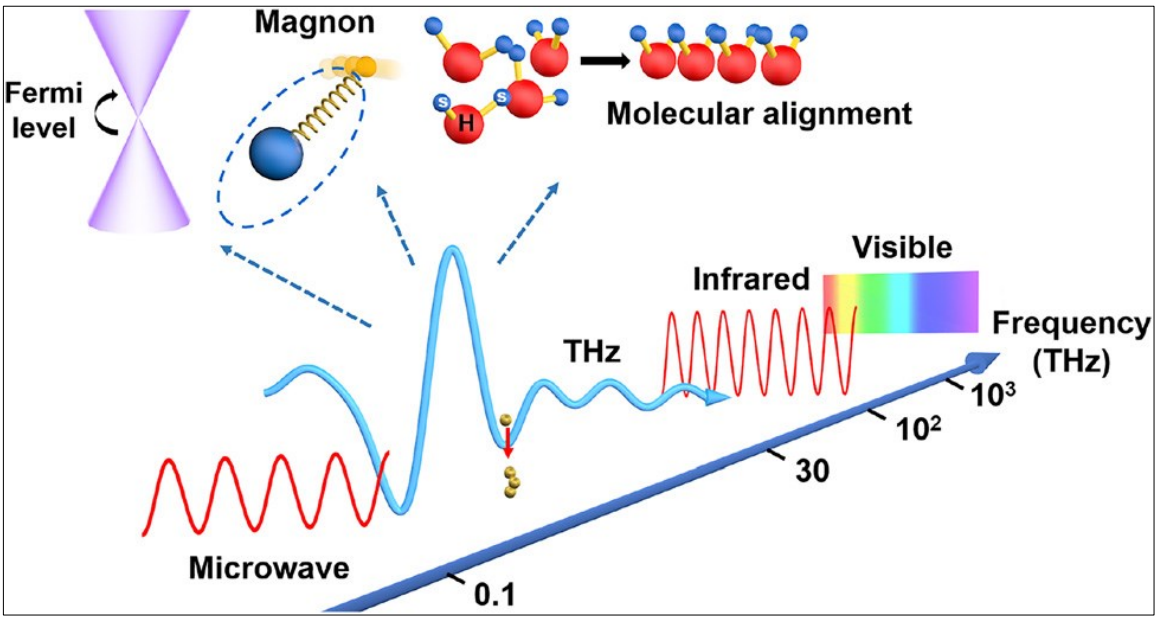

Figure 1.1: Terahertz waves applications in the spectra from (Zhenzhe Ma et al., 2022).

the digital twin world, digital fabrications, augmented reality, or holograms. All of these hungry data-rate applications have motivated research into compact and integrated THz optoelectronic devices. This thesis focuses on solving these issues by providing a novel integrated graphene versatile device, which can be implemented as a fast external amplitude/phase/polarization modulator. Interestingly, the high speed of this device makes this approach the fastest THz modulator/detector so far to the best of our knowledge for the area of integrated graphene with metamaterials platform. The novelty and key performances of the class of devices are greatly beneficial in various applications in the THz band in general and wireless communication community.

1.2 Applications

1.2.1 Imaging

Advances in THz science and technology have contributed to the developments in the field of THz imaging over the past decade. THz imaging can be realized using either optoelectronics or all-electronic techniques. Spatial and axial resolutions of THz waves are relatively low compared to the IR or Raman spectroscopy technologies. These limitations make it even harder to use THz frequencies in molecular or cellular

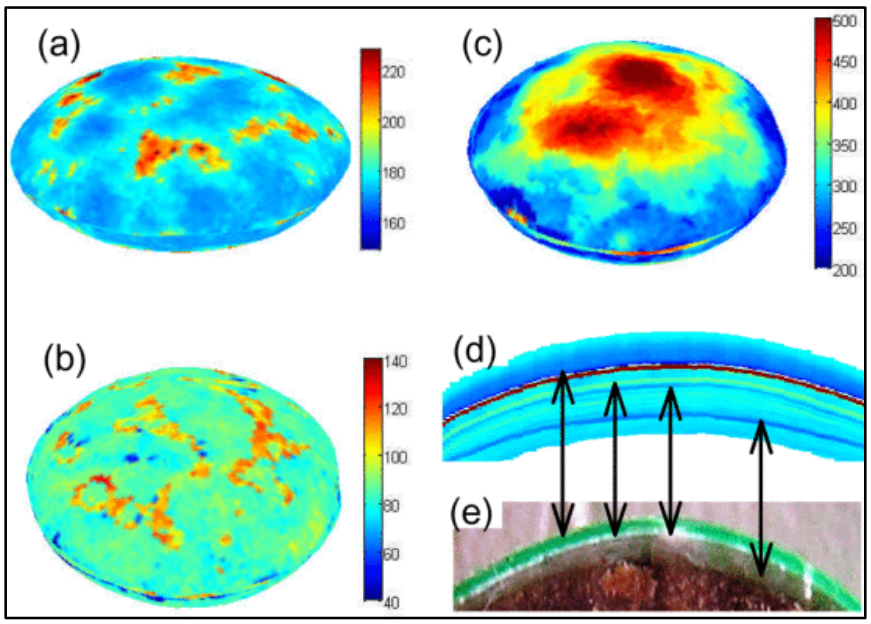

Figure 1.2: Reconstructed 3D image using THz imaging techniques (Y.-C. Shen and Taday, 2008).

imaging required by the medical imaging community. More difficulties arise in vivo imaging when using THz frequencies due to their low range of penetration depth. This issue is mainly because of severe water and fat absorption in the THz regime in tissues. These bottleneck factors require more fundamental research investigations and developments to further broaden the THz imaging applications.

The coherent detection properties in THz measurements allow for image contrast techniques to have a wide range (Huang, Y. Shen, and J. Wang, 2022). This is of great benefit for a variety of novel applications ranging from digital twins, and real-time imaging, to holograms. Physical properties of objects can be extracted in THz imaging measurements using only the time-domain traces of the detected THz waves. Under-testing materials usually can be scanned in pixel-by-pixel arrangements by moving them spatially via a motorized holder stage. In (Y.-C. Shen and Taday, 2008), a three-dimensional (3D) image of the scanned object can be recovered using THz imaging techniques by plotting the spatial location of each pixel in both vertical and horizontal axes while time delay is the third axis as plotted in fig. 1.2. The non-destructive and quantitative properties can also be examined using coherent detection methods for testing paints in the automobile industry (Yasui et al., 2005; Su, Y.-C. Shen, and J. Axel Zeitler, 2014). and protective coatings (Tu et al., 2016).

Severe water absorption experienced by some of the THz frequencies can be used as an advantage in THz spectroscopy and imaging for the medical and biological

communities (C. Yu et al., 2012). A distinguished observation was reported between diseased and healthy tissues by carefully considering changes in the THz spectra in absorption coefficient and refractive index (Wallace et al., 2006). The lack of sharp spikes in the THz spectra hardens the differentiation of THz wave propagation in normal tissue, cancerous tissue, and water for THz frequencies at <2 THz. This latter challenge makes untrustable and unreliable simultaneous detection of cancerous tissues. However, problems of measurement-specificity could be overcome by advances and developments of polarization-sensitive THz imaging devices integrated with dielectric probing (Huang, Y. Shen, and J. Wang, 2022). Progress toward the characterization of tissue properties could experience exponential growth in the near future. An ultrafast communication platform is needed for high-resolution imaging and sensing for most of the applications which depict the future of digital society including the digital twin world, digital fabrications, augmented reality, or holograms.

Like in the communication field, THz imaging systems require high processing speed (Huang, Y. Shen, and J. Wang, 2022). For example, faster sampling speed is a key factor that determines the imaging collection data rate (Beck et al., 2019). Moreover, high image acquisition speed can be improved by using more powerful THz transmitters (Berry et al., 2013). The power conversion efficiency from optical to terahertz of 7.5% was demonstrated by (S.-H. Yang et al., 2014). This value was achieved by using 3D plasmonic contacts on a low temperature (LT) GaAs platform where most of the generated photocarriers are only nano-meters away from the center of the THz emitter. This mechanism allows more photoinduced electrons to drift toward the THz transmitter in a sub-picosecond time-scale enhancing the THz generation efficiency. The method of using two separate detectors for the THz probe and the femtosecond (fs) optical pump can extensively influence the imaging sampling rate. This idea was practically applied by redirecting both beams using an electro-optic crystal (Z. Jiang and X. C. Zhang, 1999). This parallel detection mechanism was recently used to extract the image of an object by applying wide spectral bandwidth THz pulses (0.1-1.5 THz) (Ushakov et al., 2018). This scheme can also maintain all the advantages of the THz time-domain imaging such as temporal propagation speed and spectroscopic imaging. System requirements, such as amplified fs lasers to drive the charge-coupled device (CCD) camera, are one of the disadvantages of the parallel detection technique. Despite this bottleneck, video-rate THz imaging can be significantly improved by using this scheme. Rates of image acquisition can also be enhanced by the compressed sensing phenomena (Chan et al., 2008; Chan et al., 2009; Guerboukha, Nallappan, and Skorobogatiy, 2018). Sequential spatial modulation using spatial masking can manipulate the THz wavefront. This beamforming mechanism can enormously improve data acquisition speed compared to the conventional scanning technique (Huang, Y. Shen, and J. Wang, 2022). The re-shaped THz beam propagates from an object to a single-point detector. This

compressed sensing technique can retrieve both structural and chemical maps of a sample (Y. C. Shen et al., 2009). The realization of such a high imaging rate using the compressed sensing technique requires developments in equivalently fast multi-pixel THz modulators, that can be independently all-electronically controllable. Improvements in dynamic metamaterial-based THz spatial modulators could be key to accelerating the development of compressed THz imaging for practical applications besides the research laboratories (Watts et al., 2014a).

1.2.2 Communications

Nowadays, the THz communication community is shifting gears for the realization of faster data transmission speed above 100 Gbps. Undergoing research and developments in communication systems are now concentrated on the next generations of wireless communication systems such as 6G and beyond. Advances in THz communication can accelerate the developments in a variety of applications including augmented reality (AR), biological imaging, nanoscale communications (e.g., in supercomputers), radar systems, automotive and satellite communications, kiosk downloading, indoor links (L. Zhang et al., 2020a; Tadao Nagatsuma, Guillaume Ducournau, and Cyril C Renaud, 2016; Elayan et al., 2020). Developments of THz devices require an increase in their operational frequency where there are more unallocated waves in the spectrum. Despite the tremendous efforts in THz science and technology, there is still a lack of THz circuitry operating with high speed, high efficiency, and capability for pixel-to-pixel programmable coding (Han et al., 2022; L. Zhang et al., 2020b; T. Nagatsuma, G. Ducournau, and C. C. Renaud, 2016; Elayan et al., 2020; Huang, Y. Shen, and J. Wang, 2022; Zeng et al., 2021). Indoor and outdoor communications are significantly influenced by water absorption, which can reach up to 10-100 dB/km (Riccardo Degl'Innocenti, H. Lin, and Navarro-Cía, 2022). In nanoscale communication, the THz frequencies can be used in a variety of applications including device-to-device, different objects, or integrated electronic/optoelectronic components. Moreover, technologies that require extensive data throughput, fast modulation speed, kiosk down-leading, new unallocated frequencies bandwidth, and fast response are some of the key characteristics for revolutionizing the next-generations of telecommunication systems (Elayan et al., 2020; Riccardo Degl'Innocenti, H. Lin, and Navarro-Cía, 2022; Huang, Y. Shen, and J. Wang, 2022). Wireless communications beyond 5G are being deployed for mid- and near-field applications for ground communications, due to atmospheric absorption, on the promise of wide unallocated bandwidth and ultrafast communication (100 Gb-1 TB/s). Theoretical bottleneck of communication systems with capacity (C) is determined by the Shannon-Hertlet formalism as follows (Fujishima, 2021):

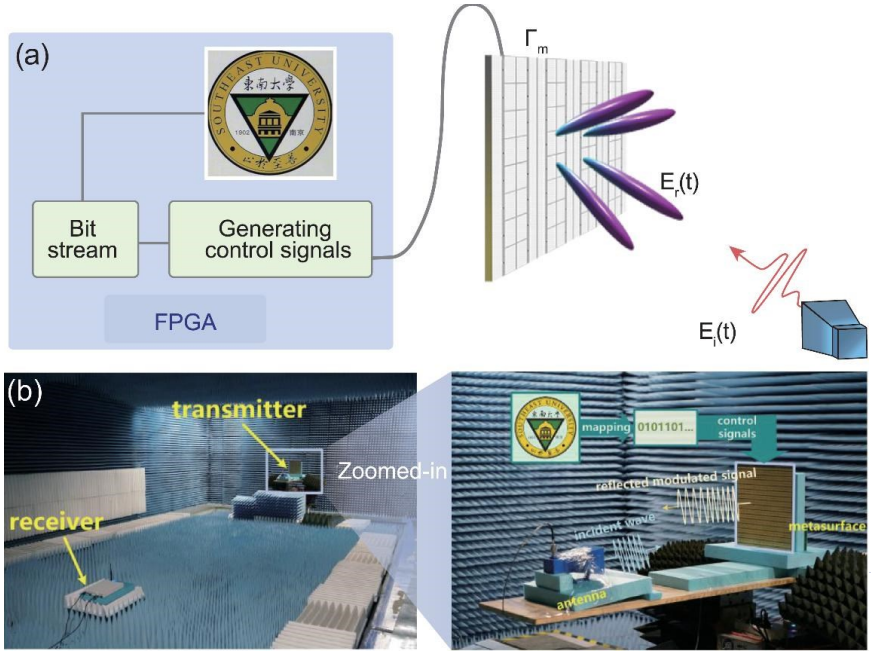

Figure 1.3: Time-domain digital-coding MMs for wireless communication demonstrations (Jin et al., 2017).

$$C = B \log_2 \left(1 + \frac{S}{N}\right), \tag{1.1}$$

where the frequency range is B, the received signal power is S, and the system's channel noise power is N. The received power by an antenna is proportional directly to the antenna's effective area and inversely to the squared of the propagating wavelength (Fujishima, 2021). Therefore, an increase in the operational frequency would enhance the system's signal-to-noise ratio (SNR) while reducing the total effective area (Riccardo Degl'Innocenti, H. Lin, and Navarro-Cía, 2022; Fujishima, 2021). This latter fact makes the THz frequencies more favorable over the microwave band (Fujishima, 2018).

Amongst various approaches to achieve these milestones, only a few technologies seem to overcome these obstacles such as 2D materials, semiconductors, phase-change materials, and micro-electromechanical systems (MEMS), Complementary Metal Oxide Semiconductor (CMOS), resonant tunnelling diode (RTD) lasers. The metamaterial (MM) approach, thanks to its versatility, efficiency, and miniaturization capabilities, is rapidly establishing itself as the privileged paradigm for the realization of integrated THz modulators (Josep Miquel Jornet and Akyildiz, 2013; Zeng et al., 2021). The increased light-matter interaction in the MMs along with their scalable

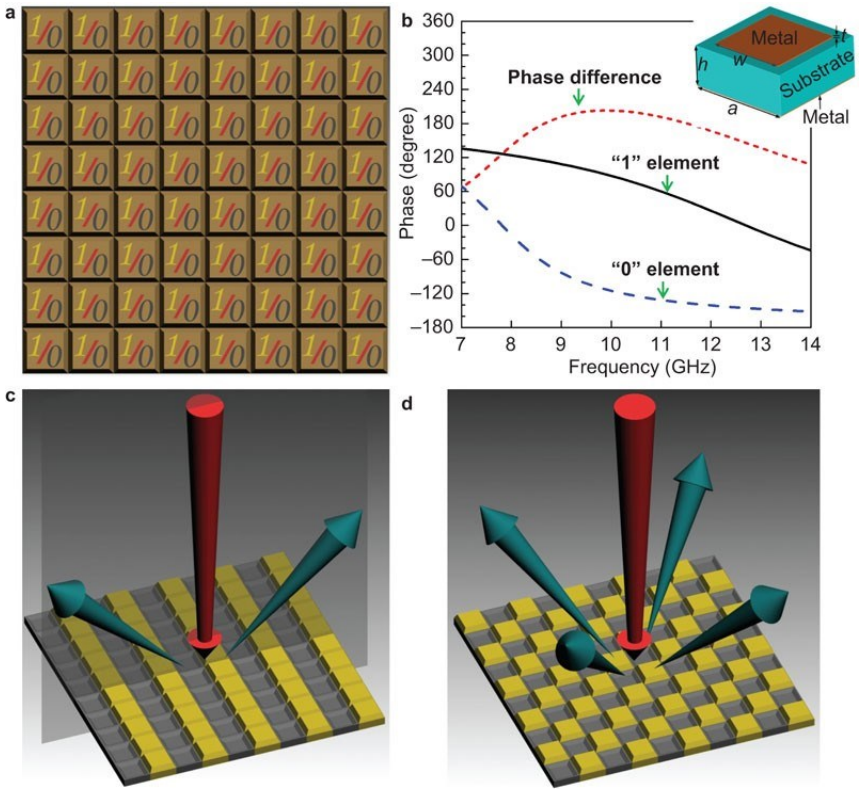

Figure 1.4: Digital coding of MMs and their application for 1-bit data transmission (Cui et al., 2014).

capability leads to low operational power (Riccardo Degl'Innocenti, H. Lin, and Navarro-Cía, 2022). The flexibility of operational frequency as well as the broad range of configuration arrangements make this approach well-suited for THz wireless systems. Several demonstrations of programmable and digitally coded devices were reported for applying the MMs techniques in wireless communication schemes. In (Jin et al., 2017), the EM waves were modulated using time-domain digitally programmed MMs by actively acting on the local phase of the surface reflectivity as illustrated in fig. 1.3. In fig. 1.4, a phase of the EM field was manipulated using controllable MMs operating at frequencies up to 14 GHz (Cui et al., 2014). Although the programmable devices are working at the microwave regime, the same concept can also be applied to THz frequencies (Fu et al., 2020). The salient feature of this approach is to achieve all-electrical control of a large number of MMs arrays separately for a variety of applications such as beam steering devices, spatial light modulators, phase modulators, and wave-forming gated MMs arrays. In Josep Miquel Jornet and Akyildiz, 2013, pixel-by-pixel arrays of MEMS split-ring resonators were reported with separate electrical controls. In this device, the Fano resonance mechanism was

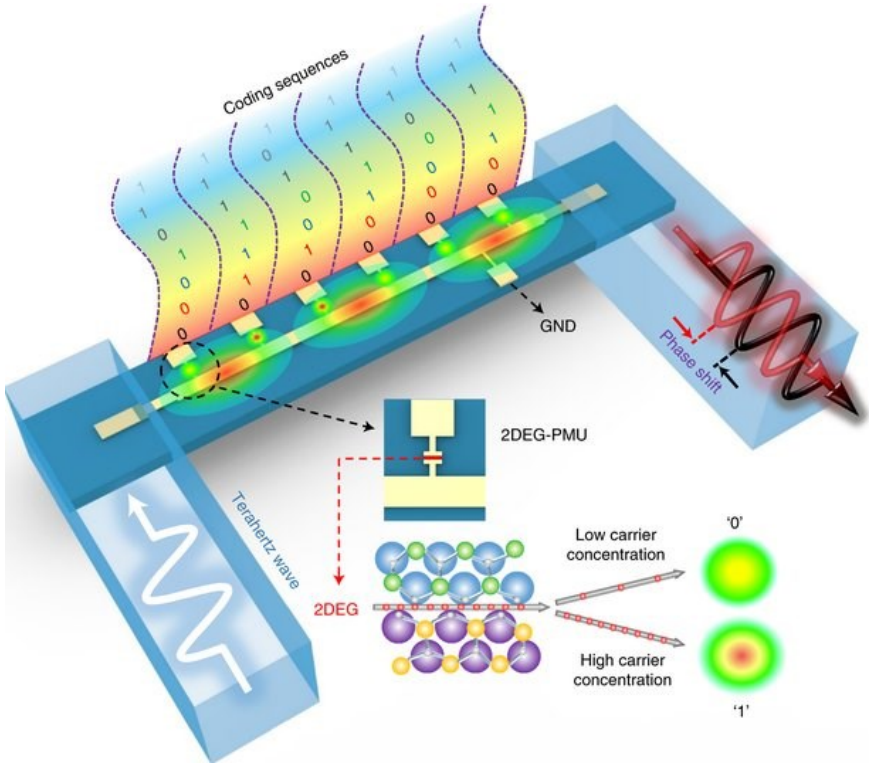

Figure 1.5: Phase coding at THz frequencies based on integrated MMs and 2DEG (Zeng et al., 2021).

deployed performing various digital logic gates such as XOR, XNOR, and NAND. The working principles of this approach further highlight its versatility factor for sending coded information through communication channels. Phase encoding was also achieved by independently coding the MMs as mentioned in (Zeng et al., 2021). In this work, a single-line transmission was combined with multichannel capacitive MMs integrated with 2DEG as plotted in fig. 1.5. This particular arrangement allows for achieving a robust phase control with minimal amplitude modulations, while the low RC constant provides high reconfiguration speeds.

1.3 Challenges

1.3.1 Atmospheric absorption

Severe atmospheric conditions, such as clouds and fog, limit the use of the THz band to medium and near-field applications. Propagation loss is one of the major

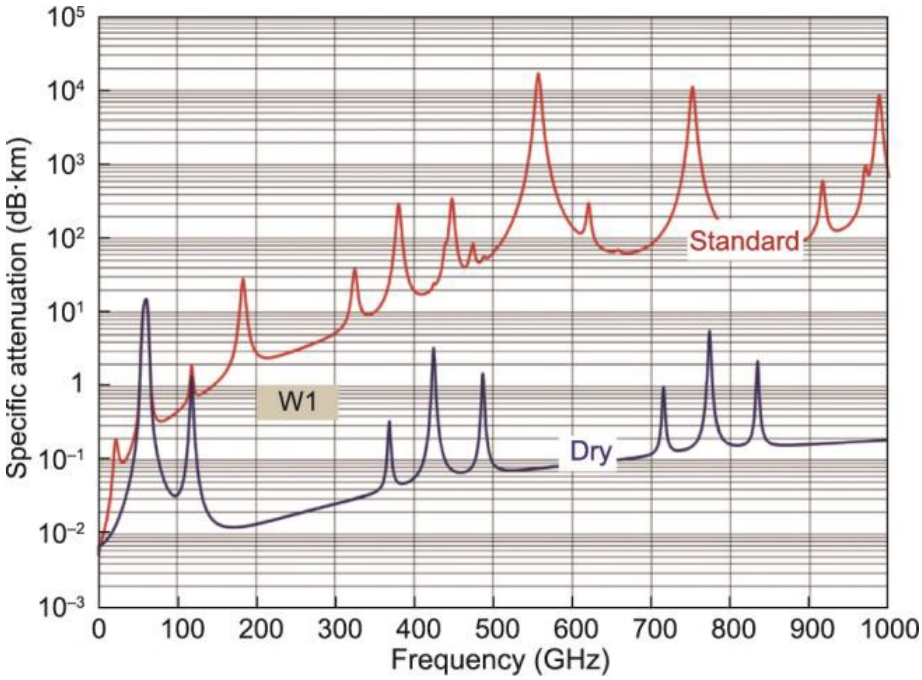

Figure 1.6: Mean of THz waves losses up to 1 THz for O_2 and H_2O sensitive environment representing the sea-level and dry air absorption (Tataria et al., 2021).

concerns in transmission. It is directly proportional to the square of frequency (f) and penetration distance (d), i.e. the free-space path loss (FSPL) (Pozar, 2011). Additionally, the transmission of specific THz frequencies experiences high power losses mainly because of H_2O and O_2 (Tataria et al., 2021). Frequencies with high power attenuation take place at 120, 183, 325, 380, 450, 550, and 760 GHz shown in fig. 1.6. Some low absorption regions in the THz band can be more useful for relatively far-field propagation. The region between 200-300 has almost flat and low power losses, hence more research and developments have been concentrated in this region. Unlike the RF/microwave region, THz waves encounter more power losses when propagating inside a medium such as reflection, scattering, and diffraction in small environmental structures due to their smaller wavelengths (Han et al., 2022). Compensation methods for atmospheric attenuation may include an increase of power depending on the availability of high-power THz generation devices, line-of-sight (LoS) and non-line-of-sight (NLoS) propagation path, and/or nanoscale communications such as device-to-device communications (Kürner, D. Mittleman, and Tadao Nagatsuma, 2021). Additionally, energy-concentrated directive beam transmission is crucial for the THz network for propagation loss compensation. The NLoS path concept is based on the beam scattering over broad angles, which will reinforce the need for beam forming and steering devices as illustrated by

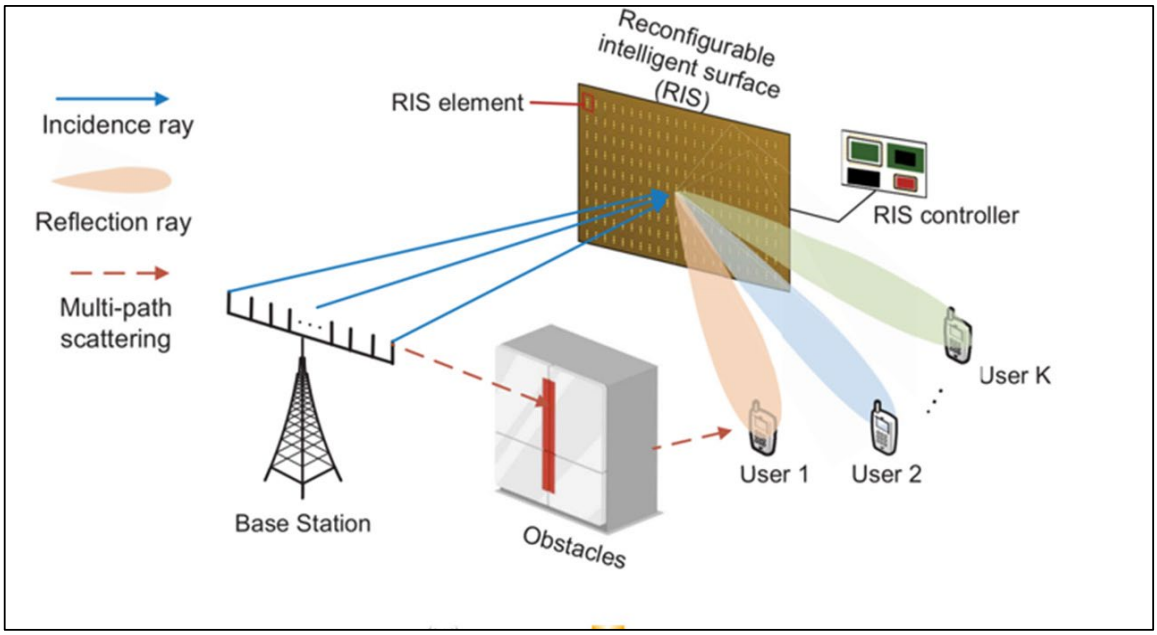

Figure 1.7: Beam forming, steering, or coding for THz channel modelling. Source (F. Yang, Pitchappa, and N. Wang, 2022).

fig. 1.7. Reconfigurable intelligent surfaces (RISs) are widely used to passively or actively optimize the THz beam path (F. Yang, Pitchappa, and N. Wang, 2022). A variety of tuning approaches have been proposed such as electronic mechanism (complementary metal-oxide-semiconductor (CMOS) transistors, Schottky diodes, high electron mobility transistors (HEMTs), and graphene), the optical mechanism (photoactive semiconductor materials), phase-change materials (vanadium dioxide, chalcogenides, and liquid crystals), and microelectromechanical systems (MEMS) (F. Yang, Pitchappa, and N. Wang, 2022).

1.3.2 All-electronic approach

On top of the environmental issue, there is an intrinsic one due to the fact that the so-called THz gap lies between electronics and photonics. Meaning that historically we have been trying to reach this range from both sides, but both approaches have their limitations. Complementary metal-oxide-semiconductor (CMOS) is an efficient solution for the bottom region of the THz band, i.e. <300 GHz. This approach is easily integrable due to advances in CMOS nanotechnology, has small footprints, and has relatively low cost with high resolution and flexibility (Elayan et al., 2020). In Venkatesh et al., 2020, a CMOS active transistor with a metasurfaces device operating at 0.3 THz was fabricated using a 65 nm CMOS nanoscale process. This

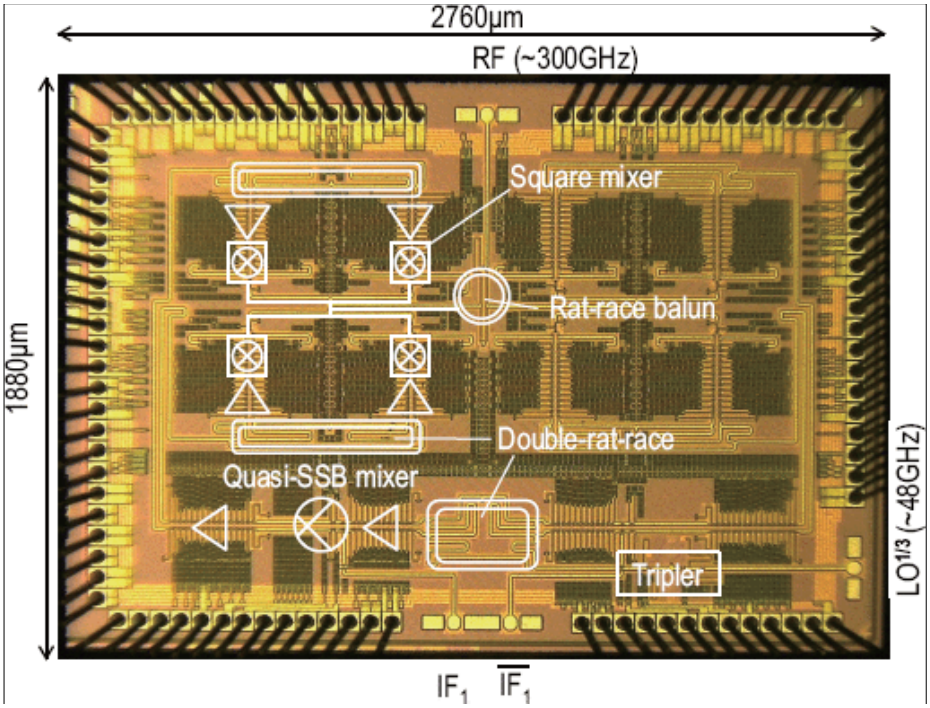

Figure 1.8: CMOS technology breaking the 100 Gbps of throughput speed (Takano et al., 2017).

CMOS/metasurface device was reported to achieve 25 dB of amplitude modulation depth, phase modulation, and active beam-steering by ±30°. As shown in fig. 1.8, CMOS complex technologies have reached up to 105 Gbps of data transmission speed operating at 300 GHz of the carrier frequency (Takano et al., 2017). Integration of a large number of nanoscale transistors may increase the operational frequencies. The high-speed oscillation of such transistors can be realized with a combination of transistor gate scaling for parasitic reduction and epitaxial material enhancements for improved electron transport properties (Elayan et al., 2020). Various methods of monolithic microwave integrated circuits (MMIC) have been realized such as heterojunction bipolar transistors (HBT) and high electron mobility transistors (HEMT). The HBTs devices can operate with high oscillation frequencies, biasing conditions, and with reduced parasitic capacitance through the substrate (Houston, 2000). These devices can be fabricated on a variety of platforms such as Si, GaAs, and InP, which makes them integrable with other optoelectronic devices operating at 10.3-1.5 μm including lasers or photodiodes (Elayan et al., 2020). Several HEMT fabricated on InP substrate devices were reported to operate with a carrier frequency of up to 1 THz (Elayan et al., 2020; H. Liu, Lu, and X. R. Wang, 2017). Manipulation of EM waves at above 300 GHz frequencies requires the development

of a high switching speed mechanism, where stand-alone electronics will not be able to maintain a high speed towards the milestone of achieving >Tbps. Consequently, devices based on electron diffusion tend to experience performance degradation when operating above 300 GHz (Elayan et al., 2020; Riccardo Degl'Innocenti, H. Lin, and Navarro-Cía, 2022). Continues miniaturization towards THz wavelengths and possible integration with other Si-based platforms could increase the difficulties in the CMOS and Monolithic microwave integrated circuit (MMIC) technologies, which makes it even harder to break the limits of Tbps data rates required by THz measurements and next-generations of wireless communication. The complexity of their operational principles and design is hardening the practicality of the all-electronic mechanism at the THz regime. The frequency change from RF/microwaves to the THz band results in a shorter operational wavelength and a wide range of hardware and software issues, including smaller sizes and more complex propagation characteristics.

Unlike the RF/microwave devices, the fabrication of THz devices is not mature. Basic diodes and transistors do not yet work efficiently in the THz band. Increasing the operating frequency of semiconductor devices up to the THz band, the semiconductor materials, and the distributed parameter of device packaging directly influence the circuit and system performance. Specifically, the fabrication of THz amplitude modulators is very challenging because of their small size. Modulation speed and modulation depth encounter even higher difficulties. It is well known that intrinsic materials can not effectively and rapidly modulate THz radiations; hence, it reinforces the need for an appropriate material and/or structure to fulfill the high-speed manipulation of THz waves. For this, 2DEG composite materials (e.g., GaN HEMT) and 2D materials (e.g., graphene) have been used in THz modulators. Thus, in the future, artificial materials with a response time of less than 1 picosecond in the THz band have attracted tremendous attention for device fabrication in light of expansion towards a high THz spectrum.

1.3.3 Photonic approach

Photonic-based THz transmitters with sufficient energy levels are feasible using resonant tunneling diodes (RTD), uni-traveling-carrier (UTC) photodiodes, or quantum-cascaded lasers (QCLs) (C. Lin and G. Y. L. Li, 2016; Kürner, D. Mittleman, and Tadao Nagatsuma, 2021; Stephen J. Kindness et al., 2020a). Their intensity can then be modulated using all-optical components, electro-optic, or electro-absorption techniques. Photonic-based technology has broadened the explorations of the THz band by unlocking various aspects such as wider spectral bandwidth, implementations of different data transmission modulation techniques like multichannel modulation frequency division multiplexing, and increase of the carriers frequency (Song, 2021). Photonic devices have a role in realizing high-speed data rates above 10 Gbps using

the on-off keying (OOK) scheme as reported by (Hirata et al., 2012). Unlike all-electronic, photonic components can be directly linked to not only the THz band technologies but also the optical communication community. For instance, fiber-optic communications operating with optical coherent network systems require ultra-wide bandwidth, high modulation depth, and fast reconfiguration speed of amplitude, phase, and polarization modulations (Tadao Nagatsuma, Guillaume Ducournau, and Cyril C Renaud, 2016).

Optoelectronic THz devices have enhanced the ability to convert from optical to THz conversions, which offer a higher level of miniaturization above 500 GHz. Experimental demonstrations using the optoelectronic approach reported achieving a data transmission rate of up to 260 Gb/s using carrier frequencies of 300-500 GHz (Tadao Nagatsuma, Guillaume Ducournau, and Cyril C Renaud, 2016). Therefore, optoelectronic devices operating over the whole THz range are essential toward achieving >100 Gbps required in the next-generation communication systems as illustrated by fig. 1.9. In standard electro-optical modulators, the required voltage to achieve π retardation denoted by V_π has a linear dependence on the wavelength, which

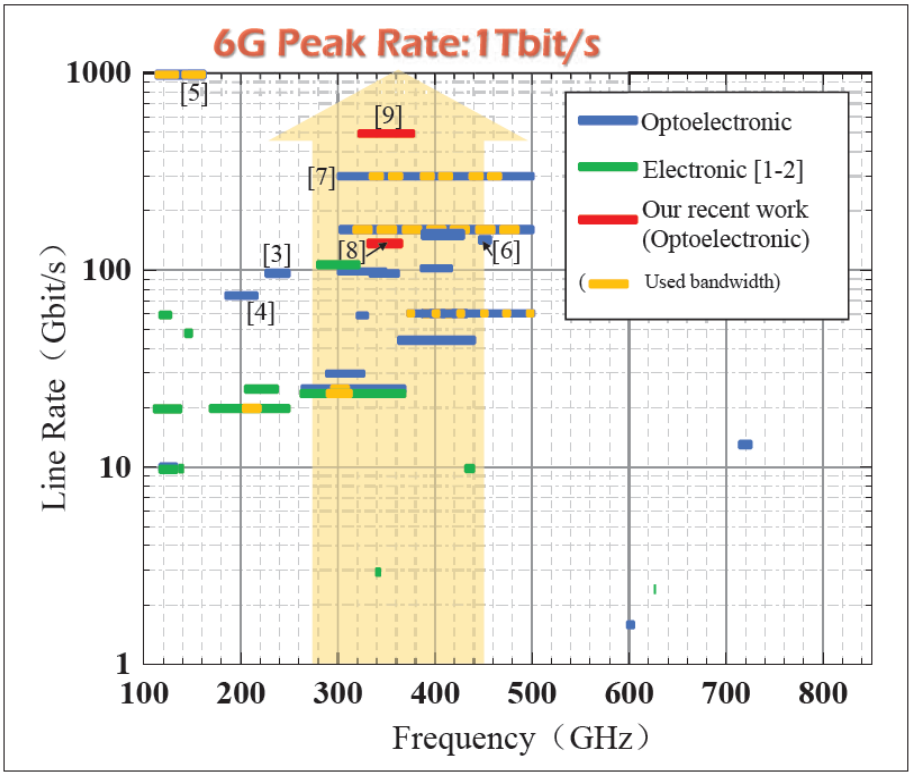

Figure 1.9: Different approaches have experimentally demonstrated high data transmission rates at the THz regime. Source (L. Zhang et al., 2020b).

makes the use of standard electro-optical modulators impractical at these wavelengths (Yariv, 1989). Optical to THz energy conversion efficiency may hinder the practical application of optoelectronic elements (Huang, Y. Shen, and J. Wang, 2022). To overcome some of these limitations, various approaches for flexible and integrable THz modulators have been proposed including 2D electron gases (2DEG) (Yaxin Zhang et al., 2015; Y. Zhao et al., 2019a; Kleine-Ostmann et al., 2004a), semiconductors (Pitchappa et al., 2019), or 2D surface plasmon/metamaterial based platforms (S. Lee et al., 2020; Riccardo Degl'Innocenti, H. Lin, and Navarro-Cía, 2022).

1.4 Our approach

As an approach to breaking the limits of high modulation speed, we propose an ultrafast and compact platform comparable with large-size industrial fabrication techniques, e.g. chemical vapour deposition (CVD) of graphene. Large monolayer and large-size area continuous films are playing a major role in emerging industrial applications, thanks to the developments in the CVD of graphene (Burton et al., 2019). The properties of a graphene monolayer and its integration with split-resonators devices are briefly described in Chapter 2. The simulated response for THz frequencies, fabrication steps, and cut-off frequency analysis are discussed in Chapter 3. Optoelectronic behavior is scrutinized as presented in Chapter 4. All-optical measurements on the complex structure determine the intrinsic upper limits of the modulation speed as presented in Chapter 5. Rotating the incident E-field provides the ability to actively control the polarization state of THz waves as illustrated in Chapter 6. Finally, this work will end with summarizing, research trends, and future work as in Chapter 7.

Chapter 2

Metamaterial active THz devices

2.1 General metamaterials definition, design, and properties

The realization of a fast, efficient, optoelectronic platform operating over the whole THz range requires a novel approach, which need to be versatile, efficient, and compatible with all applications described in the previous chapter. Our approach is based on active metamaterials. Most natural materials do not interact effectively with THz frequencies, hence the need for a new approach is required (Song and Tadao Nagatsuma, 2015). An artificially designed structure can be engineered to exhibit tailored resonances in the electromagnetic (EM) response, e.g. artificial resonance in the permittivity and/or permeability; this structure is called metamaterial (MM), meta-atom, or metasurface (Carpintero et al., 2015; S. H. Lee et al., 2012; He et al., 2018). The MMs can be designed in sub-wavelength components capable of manipulating the EM waves in the entire THz regime, which could lead to new physical phenomena e.g. artificial complex permittivity (ϵ) and/or permeability (μ) (S. H. Lee et al., 2012; Riccardo Degl'Innocenti, H. Lin, and Navarro-Cía, 2022). In order to achieve an effective homogeneous medium, a single unit cell of the MMs array must be much smaller than the targeted oscillating wavelength. Meta-atoms can support several resonance modes to oscillate under an external EM wave excitation. This resonance frequency (f_{res}) depends on the geometry and size of the meta-atoms rather than the material of choice. These devices can operate with approximately the same efficiency over the whole THz range just by increasing or reducing the size. Depending on the choice of the design, MMs can support different modes and exhibit different photonic properties, such as even and odd higher-order modes, Fano resonances, electromagnetically induced transparency (EIT), plasmon-induced transparency (PIT) influenced resonances, and resonances in chiral and toroidal

metamaterials (Banerjee, Pal, and Chowdhury, 2020). Further to this, the utilization of MMs at THz frequencies has unlocked access to unique physical principles namely negative and ultra-high refractive indices (Veselago, 1967; J. T. Shen, Catrysse, and S. Fan, 2005).

2.2 History and literature review

2.2.1 Passive THz matematerials

THz metamaterials can be grouped into passive and active devices based on their ability to manipulate the properties of EM radiation. These properties include resonant frequency (f_{res}) tuning, transmitted or reflected amplitude and/or phase, absorption factor, and index of refraction as summarized in fig. 2.1 (Song and Tadao Nagatsuma, 2015). The EM waves incident on passive MM devices cannot be modified by an external source of energy after fabrication. Unlike passive devices, the properties of dynamic metamaterials could be altered by external stimuli such as optical, electrical, thermal, or mechanical sources of energy. Integration of active medium with MMs has a huge impact on the EM wave manipulation capabilities.

In MMs with negative refractive index, the propagation of EM waves is determined

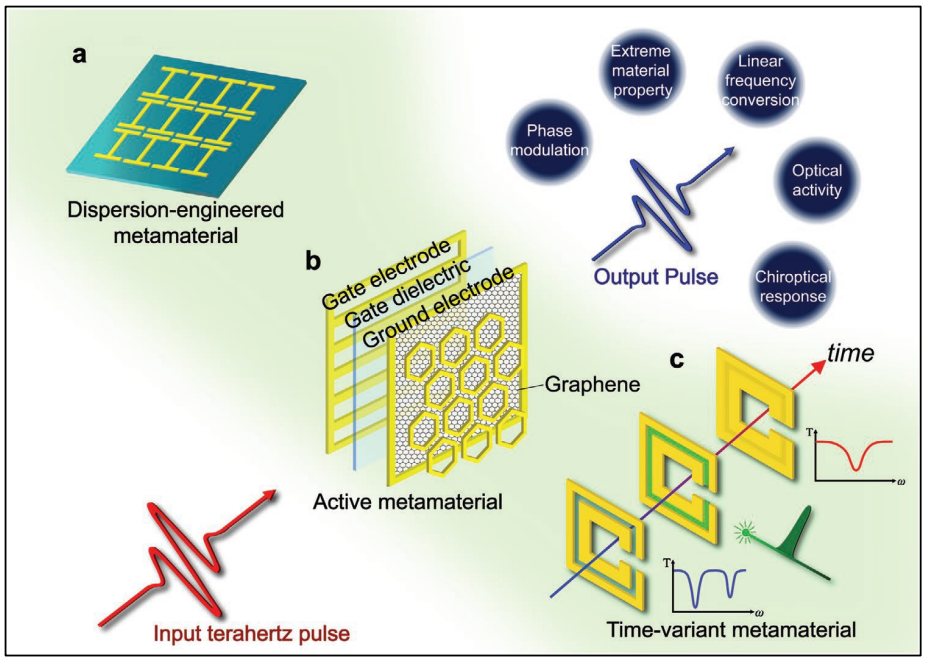

Figure 2.1: Various types of metamaterial devices including passive (a), active (b), and frequency conversion. Source (S. Lee et al., 2020).

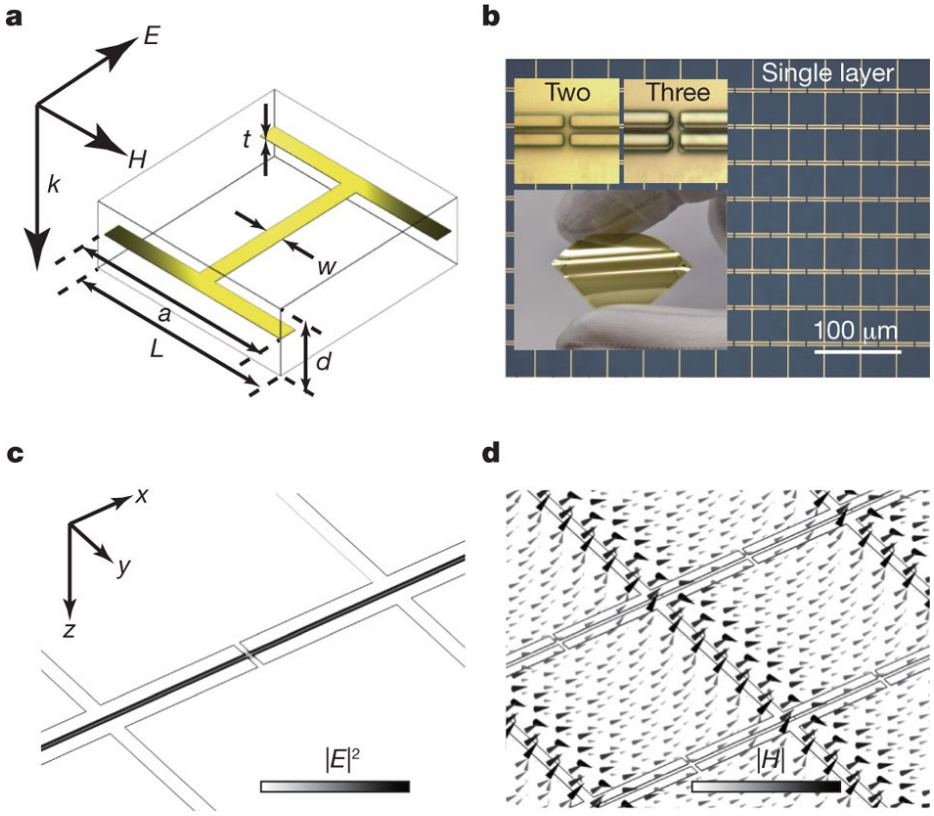

Figure 2.2: Passive MMs device exhibiting high refractive index (M. Choi et al., 2011).

by the sign of both permeability and permittivity ($\pm\sqrt{\epsilon\mu}$). A theoretical study of the negative refractive index MMs was first introduced using metallic wires array (J. B. Pendry et al., 1998) and split-ring resonators (SRR) array in (J. Pendry et al., 1999). A combination of two different SRRs into a single metamolecole was reported to be a left-handed medium (Smith et al., 2000). These devices have stronger beamforming and design flexibility capabilities. Early theoretical study on ultrahigh-index MMs was reported by (Shin, J.-T. Shen, and S. Fan, 2009; J. T. Shen, Catrysse, and S. Fan, 2005), but its complex 3D structure makes its practical implementations difficult.

2.2.2 Active THz matematerials

Active manipulation of THz radiation is a key element for research and developments targeted by the electronic and photonic communities. The metamaterials approach, thanks to its versatility, efficiency, and miniaturization capabilities, is rapidly establishing itself as the privileged paradigm for the realization of THz devices (Al-Naib and Withayachumnankul, 2017; S. Lee et al., 2020; J. Li et al., 2020; Yaxin

et al., 2020; Zuojia Wang et al., 2016; Hou-Tong Chen, Taylor, and N. Yu, 2016; Yoo and Park, 2019; Fu et al., 2020; S. Shen et al., 2022; Riccardo Degl'Innocenti et al., 2018; ZT Ma et al., 2019; Low and Avouris, 2014). Integrating active elements with MMs has been intensively studied reporting more effective control of the EM wave properties because of their powerful oscillation capability at THz frequencies. The lack of efficient and fast THz circuitry reinforces the need for active optical and electronic components such as switches, filters, and modulators. Acting on the active elements integrated with MM devices can be realized either optically, electrically, or mechanically.

All-optical control of a THz radiation device was demonstrated using an indium antimonide (InSb) grating (J. B. Pendry et al., 1998). In this work, the switching mechanism was based on the photoexcitation of the free electrons. In In Padilla et al., (2006), SRRs made of metals were fabricated on a semi-insulating gallium arsenide (Si-GaAs) substrate and tested by optically exciting, and THz probing, the MMs. In this experiment, the photo-inducing optical pulse significantly changed the absorption coefficient damping the resonance of the SRRs because of the domination of the photoexcited substrate. Using an all-optical experiment, continuous tuning

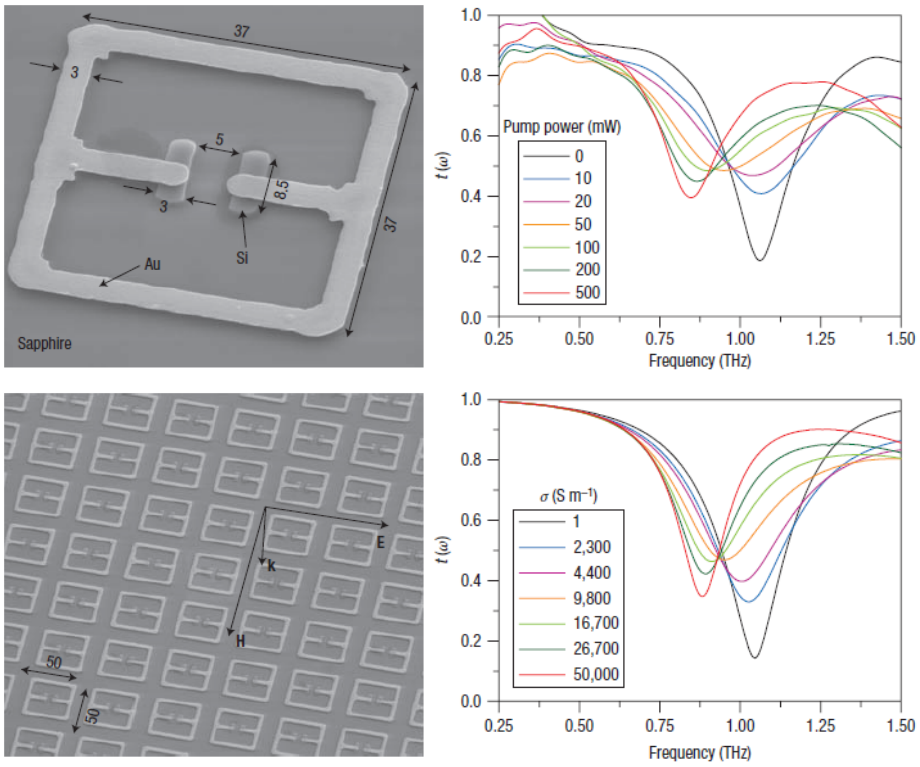

Figure 2.3: Active MMs device by photoexcited electrons (H.-T. Chen et al., 2008).

of f_{res} by 20% was at THz frequencies achieved by fabricating SRRs made of Si on a quartz platform (H.-T. Chen et al., 2008). In this design, manipulation of the capacitive gap mechanism was altered using different optical pump fluence, hence f_{res} was dynamically blueshifted. Its scanning electron microscope (SEM) picture as well as simulated and experimental frequency tuning results are illustrated in fig. 2.3.

A more practical technique for controlling the THz wave is required, i.e. electrically tunable THz metamaterials for practical applications, e.g. wireless communications. The physical properties of the THz frequencies, including amplitude (Hou-Tong Chen et al., 2006), phase (H.-T. Chen et al., 2009), and wavefront (Chan et al., 2009), were controlled by electrically biasing the MMs. The THz spatial light modulator (SLM) in (Chan et al., 2009) was tested in THz-TDS setup achieving ∼3 dB of amplitude modulation depth with an applied voltage of only 16 V at room temperature. The speed of mobility is the key element that determines the switching speed of THz devices. Therefore, different strategies have been developed in order to include active materials in the MM designs, thus achieving high modulation depth and speed. Amongst these, the most popular methodologies use semiconductors (Hou-Tong Chen et al., 2006; Pitchappa et al., 2019; Venkatesh et al., 2020) or 2D materials such as graphene (S. H. Lee et al., 2012; Stephen J. Kindness et al., 2020a; Zaman et al., 2023). A MM/graphene in a hybrid resonator was reported achieving ∼40 MHz of modulation speed at a resonance of about 5 THz (P. Q. Liu et al., 2015). Metallic plasmonic antennas shunted by graphene patches reported a reconfiguration speed as high as ∼115 MHz (Jessop et al., 2016). Gated MM resonators shunted by graphene have been deployed to actively modulate the beam of THz light, i.e. amplitude, phase, and polarization, with the potential of achieving a high speed of modulation (Stephen J. Kindness et al., 2019; Stephen J. Kindness et al., 2020a; Stephen J. Kindness et al., 2018; Riccardo Degl'Innocenti et al., 2016).

Other mechanisms for EM wave manipulation include VO_2 (Kats et al., 2013; Ivanov et al., 2021) or phase-changing materials such as liquid crystals (Ji et al., 2019a) or two-dimensional electron gases (2DEGs) (Yaxin Zhang et al., 2015; Y. Zhao et al., 2019a; Yaxin Zhang et al., 2015; Y. Zhao et al., 2019b). Despite the high robustness and efficiency of these approaches, they would not be able to keep up with the high modulation speed required by many strategical applications.

2.3 Electrical properties of materials

We focus our attention on metallic metamaterials, basically 2D metasurfaces. The conventional approach for understanding the electrical response of metals is expressed by a frequency-dependent, complex permittivity (ϵ), and a complex conductivity (σ) (Carpintero et al., 2015). The ϵ describes polarization responses inside the medium based on the material's molecular electron structure. The σ is related to the electron

mobility under the EM field excitation. However, polarization and conductivity of materials become strongly dependent on the frequency at the THz range since then the Drude model works better (Carpintero et al., 2015). In this case, the dielectric function of metals is best described by the Drude model in the frequency domain as (Song and Tadao Nagatsuma, 2015; Carpintero et al., 2015):

$$\epsilon(\omega) = 1 - \frac{\omega_p^2}{\omega^2 + i\Gamma\omega}, \tag{2.1}$$

where Γ is the collision (damping) frequency. The plasma frequency ω_p is expressed as $\omega_p = (n_e e^2/\epsilon_0 m_{eff})^{1/2}$ corresponding to the material's properties including the electron density n_e, electron charge e, vacuum permittivity ϵ_0, and effective electron mass m_{eff} (Song and Tadao Nagatsuma, 2015; Carpintero et al., 2015). Under an applied AC field oscillating with $f = \omega/2\pi$, the material's conductivity is a frequency variant complex value as follows (Carpintero et al., 2015):

$$\sigma(\omega) = \frac{\sigma_0}{1 + j\omega\tau} = \frac{\sigma_0}{1 + (\omega\tau)^2} - j\omega\tau\frac{\sigma^2}{1 + (\omega\tau)^2}, \tag{2.2}$$

where τ is the carrier relaxation lifetime and equals $1/\Gamma$, and σ_0 is the DC conductivity.

2.4 Graphene monolayer

Graphene is a 2D material used extensively as an active material due to its unique properties in optics and electronics. At a finite level of doping, graphene has frequency-dependent absorption and optical transition characteristics. When excited with less than double its Fermi-level energy, free electron-hole recombination occurs due to intraband absorption as illustrated in fig. 2.4. These energy levels correspond to the THz band and mid-IR region where the graphene conductivity follows a Drude peak (Low and Avouris, 2014). From near to visible light, interband free electrons recombination takes place with an absorption coefficient ($\sigma\pi$) of approximately 2.3%. The salient feature of using a monolayer of graphene is because of its fast responses in the THz band due to its symmetrical gapless conical shape of the bandgap energy (Low and Avouris, 2014). Graphene also offers a wide range of carrier mobility in the order of 70,000 $\mathrm{cm}^2/(\mathrm{V}\cdot\mathrm{s})$ with a broad carrier concentration that can reach about $10^{14}/\mathrm{cm}^2$ at room temperature reported for industrially relevant chemical vapor deposition techniques (Riccardo Degl'Innocenti, H. Lin, and Navarro-Cía, 2022). At the mid-IR due to Pauli blocking, there is a minimum absorption. At the THz range, however, the absorption is mainly due to intraband and disorder mediated where its conductivity is directly proportional to the square of the carrier's concentration. The THz regime absorption is commonly modeled with the Drude model as a first

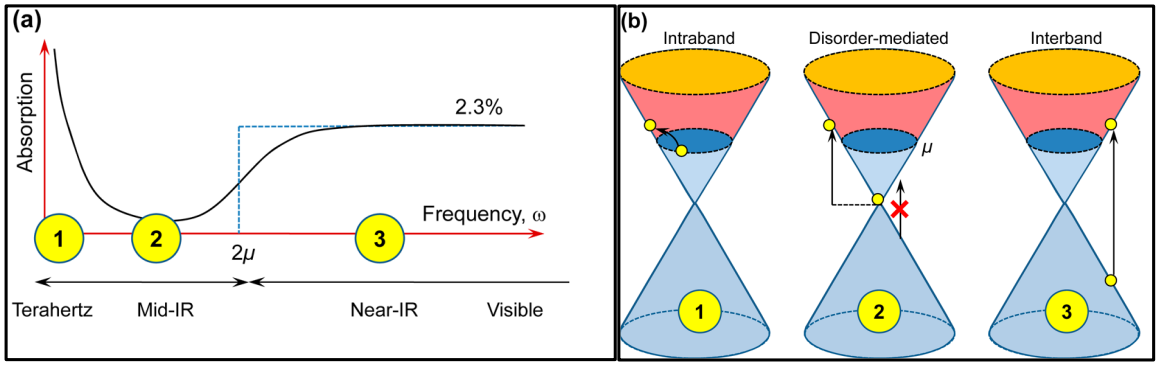

Figure 2.4: a) The absorption coefficient for doped graphene for each frequency region. (b) Allowed free carriers concentration in the bandgap of doped graphene. Source (Low and Avouris, 2014).

approximation, or using the Kubo formula (X. Chen et al., 2020; R. Lin et al., 2021) by neglecting the interband contribution as follows:

$$\sigma_{intra} = i \cdot \frac{e^2 k_B T}{\pi \hbar^2 (\omega + \frac{i}{\tau})} \cdot \left[\frac{E_F}{k_B T} + 2 \ln(e^{-\frac{E_F}{k_B T}} + 1) \right], \tag{2.3}$$

where the Boltzmann constant is denoted by k_B, reduced Planck's constant is $\hbar$, temperature T is usually assumed 300 K, electron charge is e, Fermi-level energy is E_F, and momentum relaxation constant τ is in the order of 10s of fs. The Fermi energy of graphene can be tuned either via electrostatic gating or optical pumping.

The unique properties of graphene as an active medium at the THz band have attracted a wide range of research experimentally. It is well known that graphene has a strong matter interaction with the propagation of surface plasmonic polariton (SPP) (T. Watanabe et al., 2013). Therefore, graphene exhibits: (1) strong interactions with oscillating plasma THz waves, (2) high electrical manipulations of the properties of SPP radiations, and (3) active 2D medium capable of converting and guiding the SPP waves into free-space (J. M. Jornet, Knightly, and D. M. Mittleman, 2023). All these latter advantages of graphene are still valid at the sub-wavelength size. Advances toward passive MMs have increased the need for active manipulation elements to improve practical implementations. Thus, many techniques have been introduced to integrate graphene as an active component with the MM designs. Depending on the integration mechanism, graphene conductivity can be controlled either by thermal, optical, or electrical excitation (Sun et al., 2020; Zaman et al., 2022b; Zaman et al., 2022a; Zaman et al., 2023; S. Lee et al., 2020). The ultrafast interband electron-hole recombination rates of epitaxial graphene were first studied by using optical-pump terahertz-probe spectroscopy yielding to a couple of ps time-scale (George et al.,

2008). The operational approach in semiconductors is mainly using the flow of charge carriers injected electrically. Despite the wide range of carriers concentration, the accessible conductivity range of unpatterned graphene is still practically insufficient and limited. As a way of compensation, graphene is usually patterned and integrated with plasmonic, metals, or dielectric resonators. Ion-gel allows chemical doping of graphene Fermi energy significantly larger than electrostatic doping, but it is not compatible with a >GHz, all-electronic reconfiguration speed as in this device; they normally have kHz-10's kHz speed, a few orders of magnitude slower than this gated/SRs device.

2.5 Active electromagnetic induced transparency (EIT) devices

Active polarization state manipulations of electromagnetic (EM) radiations have a wide range of applications. Historically, controlling the EM waves polarization was achieved via the Faraday effect, $\lambda/2$ or $\lambda/4$ waveplates, liquid crystal, and so on (Zhu and Dong, 2022; Yariv, 1989). The linear dependence on the wavelength makes use of standard electro-optical modulators impractical at THz frequencies. The implementations of the EIT effect can effectively manipulate the polarization states of THz waves. From a practical viewpoint, the design of EIT MMs devices has been constructed with various active materials such as 2D materials (e.g. graphene), optically sensitive elements, phase change components, and MEMS devices. The high mobility and atmospheric stability of a monolayer of graphene are among many advantages, which make graphene a solid choice for modern THz technologies. The Fermi-energy of graphene provides a low carrier density at its Dirac point and can be modified by external stimuli, hence changing its conductivity (Stephen J. Kindness et al., 2018; Zhu and Dong, 2022). Chemical doping of graphene can widen the range of graphene conductivity accessible experimentally, hence adding extra advantages for active manipulations of the EIT effect (H. Zhao et al., 2020). Integration of double C-shape resonators achieved dynamic frequency tuning by electrostatic bias in the metasurface shunted by graphene as shown in fig. 2.5. This EIT-based graphene device has reported continuous frequency tuning by up to 120 GHz operating at about 2 THz. The interplay switch between the coupled bright and dark resonators has reported the ability to control the group delay by approximately 0.5 ps. The active control of dispersion of the graphene-based EIT devices allows them to be ready for integration with THz sources. Despite the incredible performances of the active EIT devices, their reconfiguration speed has been reported in the order of tens of MHz till now. Although EIT-based metamaterials have achieved high sensitivities with high figure-of-merit values and Q factors, the modulation speed of these devices is still

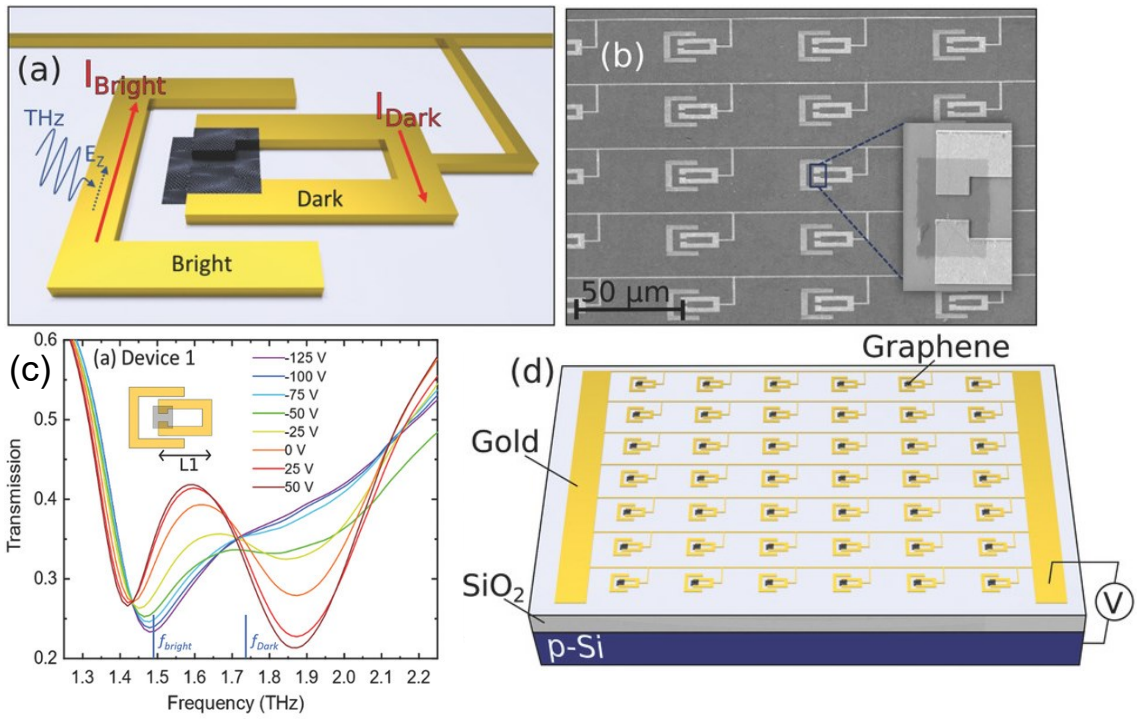

Figure 2.5: Graphene integrated EIT metamaterial resonators (Stephen J. Kindness et al., 2018).

within the MHz speed.

2.6 Metamaterial/graphene split resonators approach

Dynamic modulation of the absorption of collective charge plasmon was enhanced by using patterned graphene (J. T. Shen, Catrysse, and S. Fan, 2005). This latter phenomenon demonstrated the ability to manipulate the amplitude of THz waves using metallic bow-tie antennas shunted by a graphene monolayer as shown in fig. 2.6. In this THz modulator, active amplitude manipulation was reported to achieve 20-30% in modulation depth and ∼115 MHz in reconfiguration speed. For further improvements, the integration of graphene with MMs has significantly enhanced the modulation depth of THz modulators to about 60% with a measured reconfiguration speed of up to 40 MHz (P. Q. Liu et al., 2015; Yao et al., 2014). However, the modulation speed of these graphene/MMs devices is estimated to reach up to 20 GHz (P. Q. Liu et al., 2015). Till this point, the GHz modulation speed of THz modulators

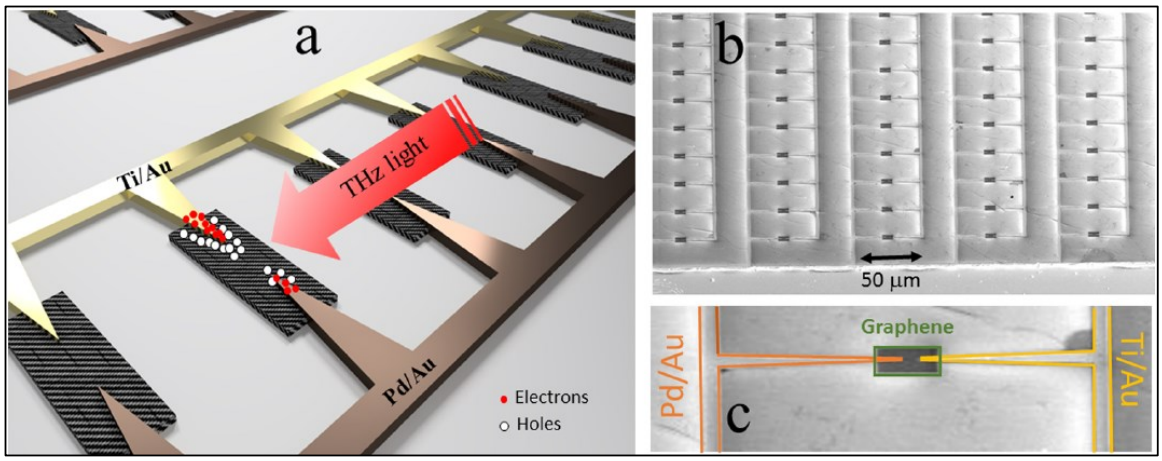

Figure 2.6: Electrically controllable graphene-hybridized metasurfaces amplitude modulator (Jessop et al., 2016).

is mainly limited by the modulation mechanism and the overall capacitance and resistance values. Improving the modulation speed could be achieved by reducing the total footprint size and the number of unit cells. In general, these two solutions become practically difficult as the operating frequency increases at the THz regime, especially in free-space applications. Consequently, a more effective modulation mechanism is required to further enhance the reconfiguration speed of THz modulators. In Wong et al., 2020, the integration of metallic patches with VO_2 stripes can selectively transmit or reflect the desired E-field polarization by independently applied voltages, as shown in fig. 2.7. Polarization conversion can also be achieved with different strategies, e.g. (Stephen J. Kindness et al., 2019; Zaman et al., 2023), but they require a high extinction ratio in amplitude modulation.

To further highlight the capability of achieving high-speed THz modulation, a new modulation mechanism is deployed using graphene integrated with metamaterial resonators. In Yaxin Zhang et al., 2015; Y. Zhao et al., 2019a, the single meta-atom state with condensed SPP modes is utilized by fabricating identical dual-resonators shunted by graphene as a variable resistance and double-gated by top and back gates. The collective state is realized by fabricating the resonators in nested and interdigitated schemes to form a complete array with four independent electrical connections, i.e. source, drain, top-gate, and back-gate. Dimensions of the dipoles are carefully designed to operate at around 0.8 THz, where THz generation technology is working sufficiently. The interplay between collective to individual states is demonstrated using this structure. The ability to switch between single to collective modes can nearly 99% shift the f_{res} due to the flexible distribution of these resonant modes throughout the entire metamaterials, hence modifying the transmission of THz

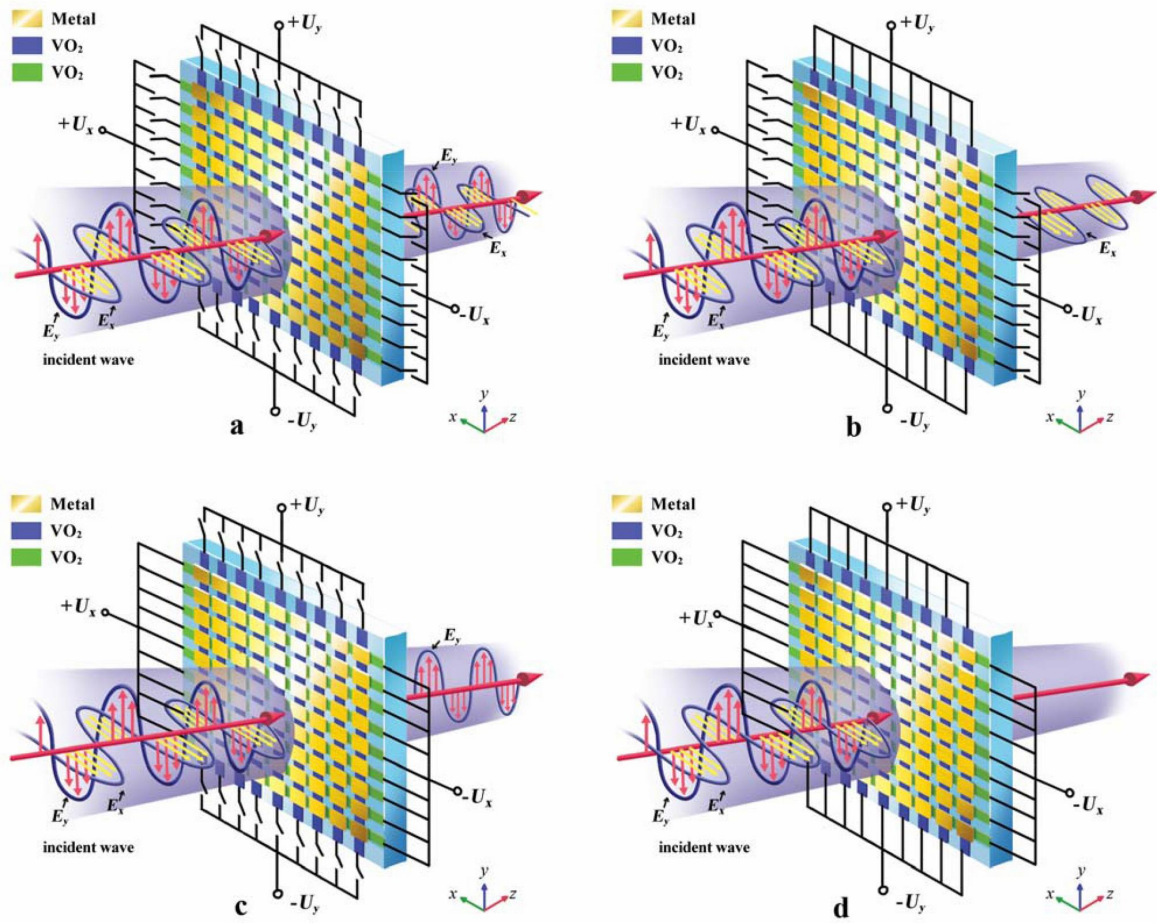

Figure 2.7: Tuneable polarization switching using integrated VO_2/MMs by reflecting the E-field component along the direction of the DC bias in a, b, c, and d. Source (Wong et al., 2020)

spectra. Additionally, the interplay mechanism has significantly reduced the parasitic resonances and overall capacitance values in this composition. Consequently, ultrafast modulation of a THz metamaterial/graphene array integrated device is demonstrated in both simulations and experiments.

Finally, the high performance of the device is achieved without affecting the measured reconfiguration speed which is reported to reach at least 3 GHz, limited only by the available instrumentation. This represents a progress of 30 times higher reconfiguration speed compared with previous similar all-electronic THz devices integrating graphene as a functional material. These results represent a breakthrough for many applications where fast and efficient THz circuitry is required, such as THz wireless communication or quantum electronics for active modelocking of QCLs.

2.7 Fabrication methodologies for THz metamaterials

The fabrication process of devices operating with THz carrier frequencies is one of the crucial and fundamental challenges. Technologies from RF/microwave are working with high reliability, robustness, and precision, but they are most likely to fail as the operational frequency keeps increasing toward the THz regime. Photonic-based modulators have the advantage of scaling their footprint size with low cost compared to all-electronics technology. Advances in nanotechnology could allow for the full integration of THz transmitters, modulators, amplifiers, and receivers. Monolithic integration of laser sources on InP, Si, and GaAs platforms have been already demonstrated in THz communication systems (Tadao Nagatsuma, Guillaume Ducournau, and Cyril C Renaud, 2016). Integration and fabrication imperfections have a direct impact on the performance of the THz devices. The required small footprint is undoubtedly not an easy task when increasing the operational frequency. The material of choice is an essential part that determines the modulation speed and depth of such a THz modulator. As a result, active functional materials have been included in the design of THz devices such as 2-dimensional electron gas (2DEG) (e.g. GaN HEMT (Yaxin Zhang et al., 2015; Y. Zhao et al., 2019a)) or 2D materials (e.g. graphene (Riccardo Degl'Innocenti, H. Lin, and Navarro-Cía, 2022; S. Lee et al., 2020)).

A variety of optoelectronic devices working as an external THz modulator have been tested with different THz sources for the potential of possible integration (Stephen J. Kindness et al., 2019). The latter group demonstrated the ability to apply an external THz modulator with QCLs in a test-bed setup as a proof-of-concept for the potential of integration. The individual units of the MMs array should be patterned in a micrometer-scale to satisfy the homogeneity, e.g. 1 THz corresponds to about 300 μm. Various nano-fabrication techniques have been applied to push the design of metamaterial toward the THz regime. One of the most widely deployed methodologies is the fabrication techniques for integrated circuits (ICs) and microelectromechanical systems (MEMS) (Song and Tadao Nagatsuma, 2015). In general, the MMs are constructed by dielectric and metals on a variety of substrate materials. The substrate of choice could be solid-state bulk material or flexible polymers. Fabrication of MMs mainly depends on the photolithographic technique, which is capable of constructing two-dimensional (2D) planar THz metasurfaces. Three-dimensional (3D) MMs can be fabricated using multi-layer structures, despite their fabrication complexity. Recently, advances in the nano-fabrication process have had a great influence on the realization of 3D THz metamaterials. Some of the new technologies that have been widely used are direct laser writing, x-ray lithography (e.g. Lithographie, Galvanik, and Abformung (LIGA) process), femtosecond laser microlens

array (fs-MLA) lithography, multilayers electroplating (MLEP), laser printing, E-beam lithography, and stereolithography (Song and Tadao Nagatsuma, 2015). More details on the fabrication techniques are described in Chapter 3.

For graphene based metamaterial, it is common to implement chemical vapour deposition (CVD) grown graphene rather than exfoliate, as this latter one has size not compatible with typical mm-size THz devices. The graphene integrated into the metamaterial devices described in this thesis is grown using CVD. This process uses a methane gas flow which passes by a heated copper catalyst where the graphene flakes self assemble (Hofmann, Braeuninger-Weimer, and Weatherup, 2015). The copper is then etched away in HCL leaving a graphene film which is transferred onto the Si/SiO_2 substrate used to build the metamaterial array. To convert this static sheet of graphene on the substrate into an electrically tunable medium, source/drain pads are then formed by thermal evaporation of metals, e.g. Au and Ti. The graphene sheet is then encapsulated by a dielectric layer using atomic layer deposition technique (ALD). Finally, top-gate stripes are formed using metal evaporation. Further description on the fabrication of our devices are reported in Chapter 3.

Chapter 3

Simulation and fabrication of the gated MMs/graphene resonators

There is extensive literature about graphene devices. Before starting this research, the record for graphene-based devices in the THz region was 100 MHz, which is too low for hungry data rate applications driving THz technology. Here, we have realized a >20 times improvement in speed for amplitude, phase, and polarization modulations. Moreover, our innovative polarization modulation scheme is based on a completely different approach from previous works (Stephen J. Kindness et al., 2019), and it yields an improvement of a few hundred times in reconfiguration speed (>115 MHz) reported in (Jessop et al., 2016).

Metamaterials shunted by graphene have been extensively studied in recent years aiming to realize fast effective reliable THz radiation manipulations. Double-layer of ring resonators were fabricated owing to the chirality of their structure to manipulate the polarization of incident THz radiations as reported in (Stephen J. Kindness et al., 2020a). Therefore, this gated split resonators (SRs) structure is adopted in this work to improve the overall performances of THz modulators, especially their reconfiguration speed. The SRs are shunted by graphene instead of 2DEG since graphene can provide high mobility, e.g. 70,000 $cm^2/(V \cdot s)$ (Riccardo Degl'Innocenti, H. Lin, and Navarro-Cía, 2022). The usage of top-gating instead of conventional back-gating is adding more advantages to the reconfiguration speed. The nested arrangement of the fabricated SRs is beneficial to reduce any cross-talk between the unit cells. This interdigitated design helps increasing the distance between consecutive unit-cells. This complex single unit-cells are simulated using the finite element method. The simulated 3D structure is meshed in order to solve the periodic boundary conditions. The simulated E-fields propagating through the unit-cells could help in estimating the resistance and capacitance values. These latter values are inserted into the reconstructed equivalent circuit model and solved via LTspice® to calculate the

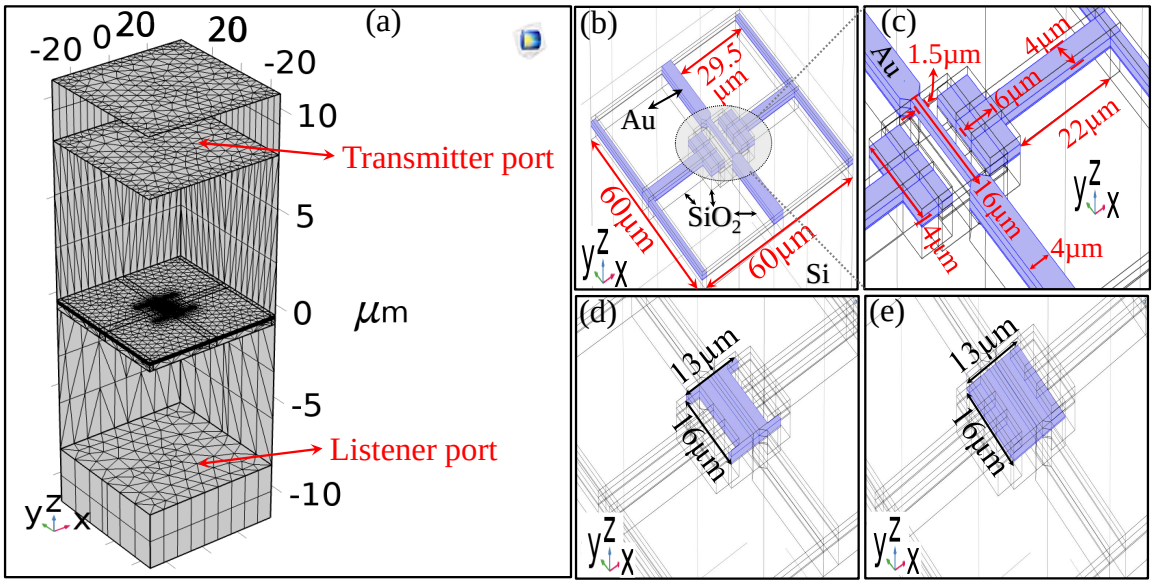

Figure 3.1: (a) 3D discretized model using tetrahedral elements. Simulated layers' composition and optimized dimensions of Au (b) and (c), dielectric (d), and graphene (e).

estimated cut-off frequency of the device.

3.1 Finite element method simulations

Various computational techniques for solving differential equations of Maxwell's electromagnetic (EM) equations have been developed such as the Fourier transform method (FTM) (Chapter 5 in Garg, 2008), finite-difference time-domain method (FDTD) (Chapter 8 in Garg, 2008), finite element method (FEM) (Chapter 10 in Garg, 2008), and method of moments (MoM) (Chapter 11 in Garg, 2008). Amongst all of these computational methods, the FEM has been extensively used to describe the physical behaviours of metamaterials (MMs) 3D structure, especially with graphene (Chandra et al., 2020). In the FEM, the physical 3D model structure is subdivided into small discrete elements where solutions of the propagating EM waves are then calculated at each element.

To better understand the physical behaviour of a single unit cell, a 3D model is developed and simulated using the RF module of COMSOL Multiphysics® software. Normally, the devices that we are using are composed of arrays with multiple identical unit cells. Simulating the whole design with FEM would require prohibitive RAM power and computer tools. What is normally done is to simulate at best a single

unit cell, where periodic lateral boundary conditions take into account the pitch of a complete array. This software can simulate the electromagnetic response of a single unit cell, which under the periodic boundary response is representative of the real array composed of hundreds of resonators. The optical conductivity of the graphene and Au layers are varied throughout these simulations as described by the frequency dependence Drude model as follows (S. Kindness, 2020):

$$\sigma_{AC}(f) = \frac{\sigma_{DC}}{1 + i2\pi f\tau}, \tag{3.1}$$

where σ_{DC} is the substrate resistivity of 100 Ωcm, while the Drude scattering time (τ) is 10 ps as reported in (S. Kindness, 2020). This software allows the retrieval of S_{11} and S_{21} parameters using the transmitter and receiver ports. The S_{11} component represents the reflected waves from the 3D structure (transmitter-to-transmitter signal), while the S_{21} parameter indicates transmitter-to-receiver waves passing through the 3D structure at port 2 as indicated by the meshed 3D model in fig. 3.1a. One of the fundamental properties of the FEM analysis is that simulation errors decrease with the increase of meshing density size to a minimum point before rising up again. Therefore, meshing size is more condensed inside the resonator's capacitive gap area to enhance the accuracy of simulations where the E-field is more concentrated. The thicknesses of each layer along with material properties are summarized in table 3.1. Additionally, all layers have a permeability of 1 H/m and permittivity (imaginary part) of 0 F/m. The single unit-cell dimensions are optimized in order to achieve the strongest damping in the spectral amplitude and phase at various THz frequencies as illustrated in figs. 3.1b-e. The optimum gap spacing of the split dipoles is found to be 7.5 μm which gives maximum depths of spectral amplitudes and phases according to the simulated results of various gap distances. In simulation, the minimum thickness to properly affect the propagating EM waves is found to be about 15 nm which is selected as the graphene layer's thickness. Also here, one should take into account the fact that it can not be possible to include the real thickness of the substrate, for the PC memory issues already explained, but it can be approximated.

Table 3.1: Optimized layers' thicknesses and materials' parameters used for simulation

Layer	**Thickness**	σ **(S/m)**	**Real** ϵ **(F/m)**
Graphene	15 nm	eq. 3.1	1
Au	80 nm	eq. 3.1	1
Al_2O_3	100 nm	0	9.1
SiO_2	300 nm	0	3.7636
Si	6 μm	0	6.8
Air	6 μm	0	1

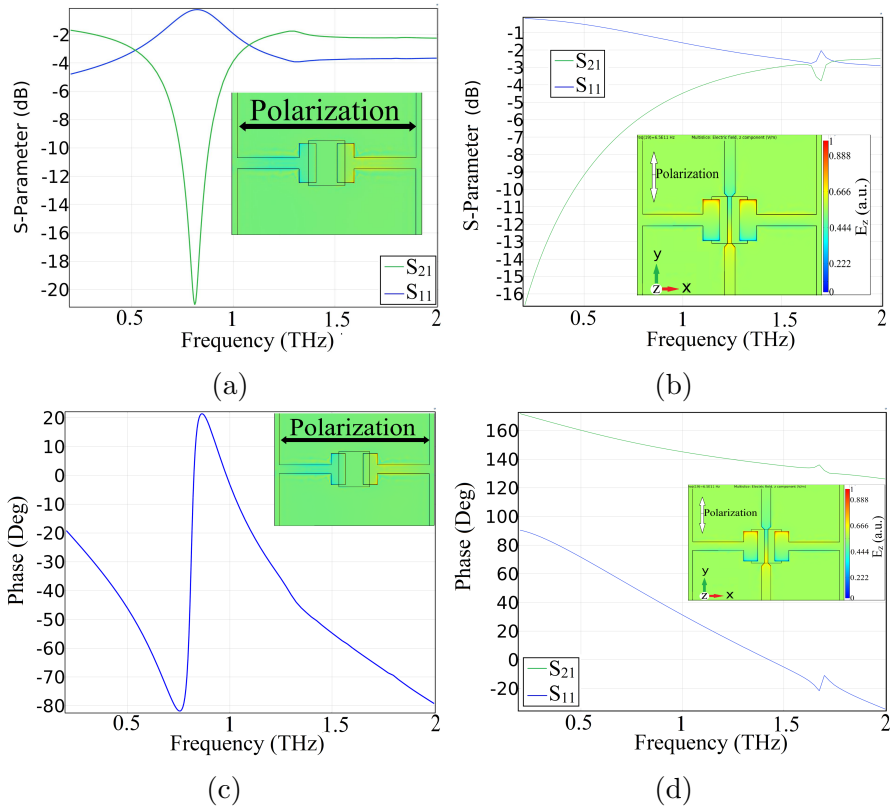

Figure 3.2: Simulated transmission (S_{21}) and reflection (S_{11}) spectral amplitudes (a) and (b) for both orthogonal polarizations. (c) Only S_{21} spectral phase. (d) S_{11} and S_{21} spectral phases for the cross-polarized incident field. The insets are the E-field norm along the z-direction calculated at the metallic surface.

In fact, the plasmonic modes have maximal values at the metal interface and are exponentially decaying inside the substrate. Therefore, the optimum EM propagation through the Si substrate is found to be ∼6 μm for a minimal computational time duration. The 3 μm boxes above the transmitter and below the receiver are perfectly matched layers (PML) or absorbing/scattering boundary conditions, which ensures continuous EM propagation and no back reflection for all frequencies, incident angles, and polarization. The transmitter's PML medium is air, while the receiver's one is Si.

In the first set of simulations, incident x-polarized plane EM waves are selected in correspondence with the resonators' parallel direction. The listener is also polarized the same as the transmitter. The selected frequency range is 0.2-2.5 THz with a resolution of 25 GHz which reduces to 5 GHz only between 0.65-0.90 THz for more precise calculations around the resonant frequency. The E-field resonance clearly

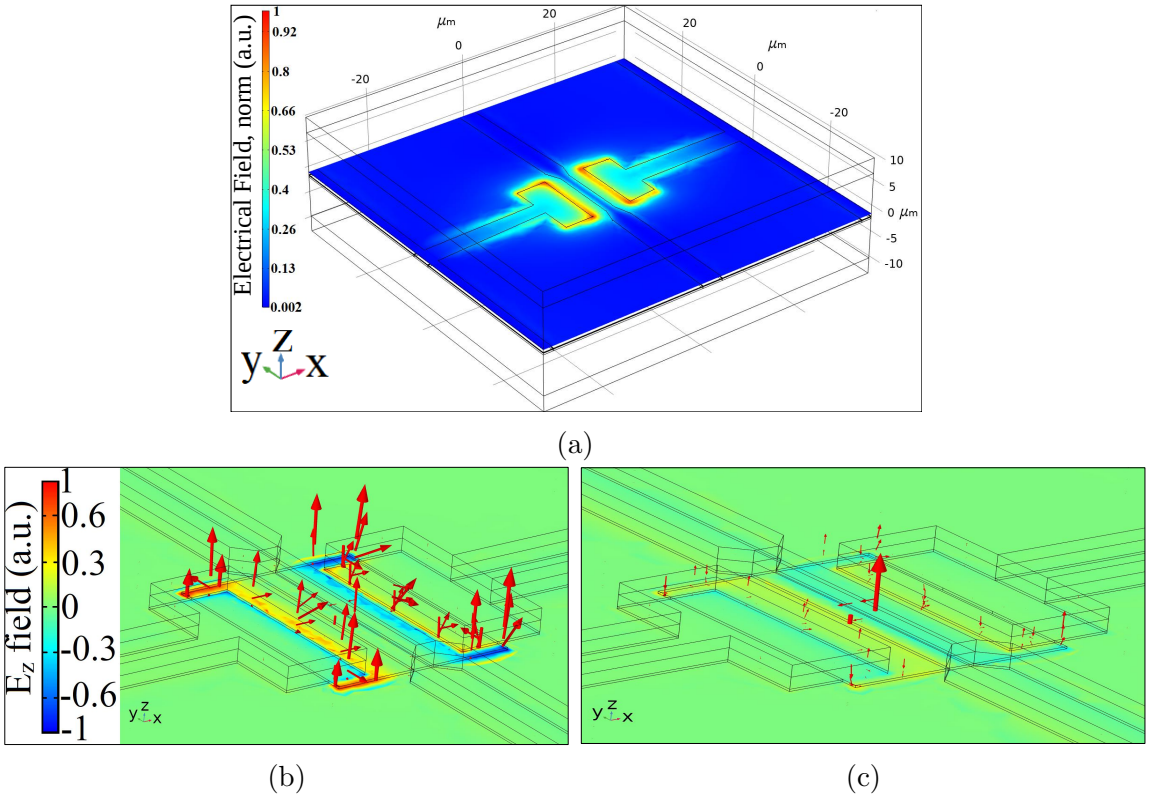

Figure 3.3: (a) Simulated normal E_z-field calculated at 500 nm above the top-gate Au stripe and the resonant frequency for $\sigma_{\text{graphene}} = 0.2$ mS. Using the same parameters as in (a), simulated E-field at z=-175 nm for $\sigma_{\text{graphene}} = 0.2$ mS (a) and 1.6 mS (b) indicating off- and on-states, respectively. Only E_z-field strength is indicated by colours, while E-field in all directions is shown by arrows. The incident field is x-polarized for all three plots.

appears at about 0.80 THz shown by the simulated transmission and reflection spectra plotted in fig. 3.2a. No resonances exist for incident E-fields polarized perpendicular to the SRs' orientation as shown in fig. 3.2b. The S_{21} has a spectral phase that follows a derivative-like shape as shown in fig. 3.2c, while S_{11} and S_{21} spectral phases are plotted in fig. 3.2d for the orthogonal polarization. A range of graphene conductivity (σ_{graphene}) is also swept between 0.2-1.6 mS with steps of 0.1 mS. This σ_{graphene} range does match very well with the same experimentally accessible range as previously demonstrated in (Stephen J. Kindness et al., 2019; Stephen J. Kindness et al., 2020a; Zaman et al., 2022a; Zaman et al., 2022b; Zaman et al., 2023). Based on the literature and testing experience of >100 devices realized in recent years, we are confident that the conductivity range accessible experimentally will be in this

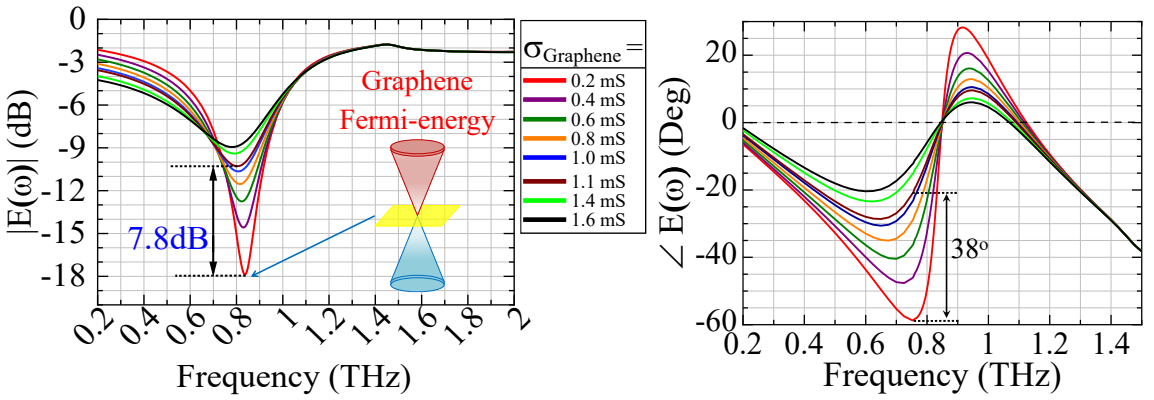

(a) (b)

Figure 3.4: S_{21} spectra of amplitudes (a) and phases (b) for various graphene conductivities ($\sigma_{graphene}$).

range. The two split capacitive dipoles are resonating when excited with external EM incident waves as illustrated by the normal E-field at resonance shown in fig. 3.3a. At σ_{graphene} = 0.2 mS, the resonating E-field is condensed in the capacitive parallel plates causing the strongest damping of the resonant frequency. At this σ_{graphene}, the graphene's conductivity reaches its Dirac point (minimum conductivity) where absorption of E-field is maximized. It is also referred to as an off-state throughout this thesis as presented in fig. 3.3b. On the other hand, an on-state occurs when σ_{graphene}=1.6 mS causing an undamped resonance while E-field is distributed amongst the entire graphene sheet as shown in fig. 3.3c. In this case, E-field strength is increased at the center of the graphene sheet and its conductivity is away from the Dirac point. S_{21} spectral amplitude can exceed a damping voltage depth of >7.8 dB at resonance between σ_{graphene} from 0.2 to 1.1 mS as shown in fig. 3.4a, which are experimentally accessible by acting on graphene. Over the same range of σ_{graphene}, S_{21} spectral phases are continuously tuned by >38° as shown in fig. 3.4b at 0.75 THz. Consequently, these simulation results strongly support the potential for achieving >80% in amplitude modulation depth and >45° in continuous phase shifts of transmitted THz spectra.

3.2 Frequency response using LTspice®

The equivalent circuit model is reconstructed in order to investigate the reconfiguration speed's bottleneck of this structure. A single unit-cell circuit has capacitance and resistance components as described in (Yaxin Zhang et al., 2015; Y. Zhao et al., 2019a) and shown in fig. 3.5a. Additionally, the parallel unit-cells lumped circuit model

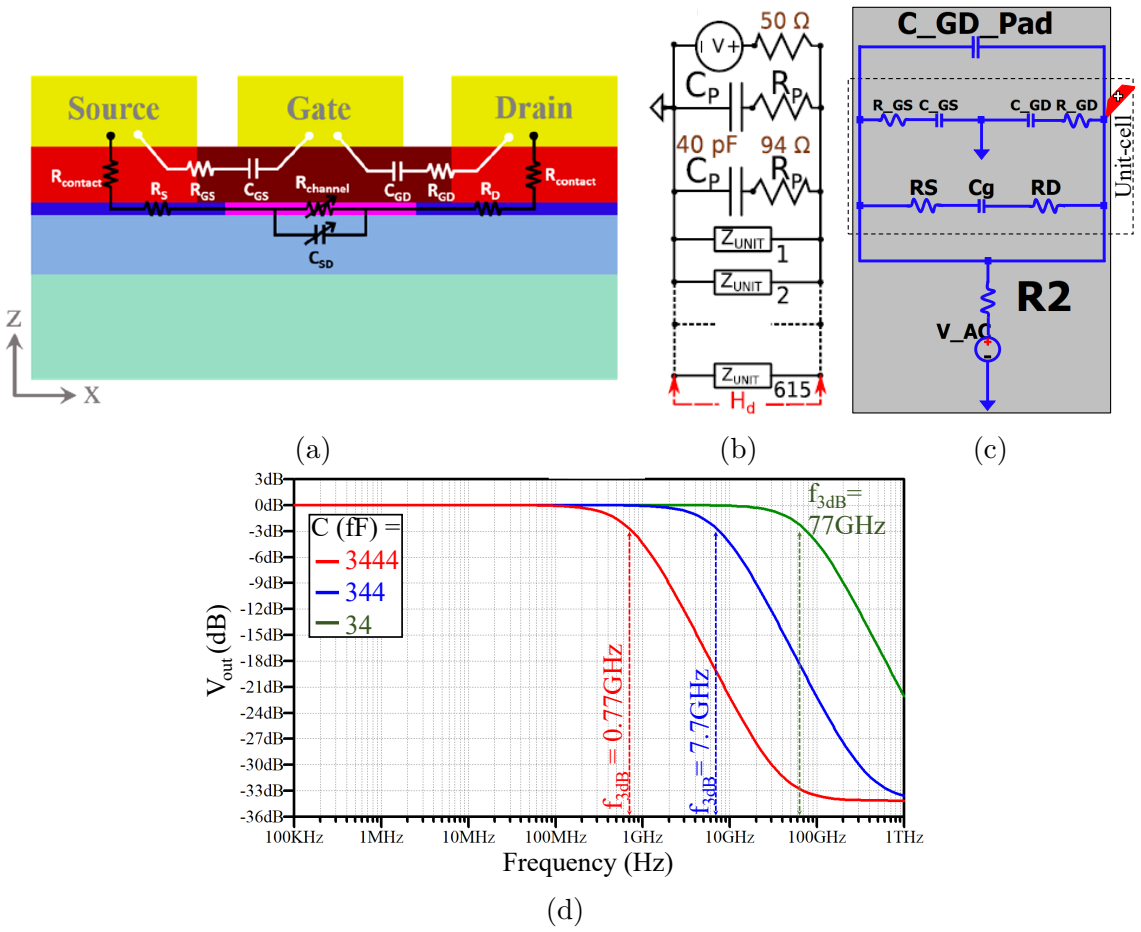

Figure 3.5: (a) Single unit-cell circuit for the 2DEG device in (Yaxin Zhang et al., 2015; Y. Zhao et al., 2019a). (b) parallel unit-cells lumped model as described in (Jessop et al., 2016). (c) Equivalent circuit model of the gated SRs/graphene device. (d) Simulated transfer function measured across a single resonator's gate-to-source capacitance for values of $C_{GS/GD}$ = 34 fF, 334 fF, and 3334 fF.

is calculated based on (Jessop et al., 2016) and as plotted in fig. 3.5b. Therefore, the gated SRs with graphene circuit is shown in fig. 3.5c. The R_S, C_g, and R_D variables are source-to-graphene resistivity, graphene layer capacitance, and graphene-to-drain resistivity, respectively. The second row in the circuit model consists of gate-to-source/drain resistivities ($R_{GS/GD}$) and gate-to-source/drain capacitors ($C_{GS/GD}$). COMSOL Multiphysics® software is used to extract the $C_{GS/GD}$ values as explicitly mentioned in (S. Kindness, 2020; Jessop et al., 2016). The entire array's parasitic capacitance ($C_{GD\text{-}Pad}$) is placed parallel to the unit-cell's circuit model following the method described in (Jessop et al., 2016). All of the circuit elements are biased by

Table 3.2: Equivalent circuit variables

Parameter	**Value (Unit)**
$C_{GD\text{-}Pad}$	1.25 fF
C_{GS}	34, 344, and 3444 fF
C_{GD}	34, 344, and 3444 fF
C_g	1200 fF
R_{GS}	1.2 Ω
R_{GD}	1.2 Ω
R_S	0.5 Ω
R_D	0.5 Ω
R_2	30 Ω

an AC voltage source with a 30 Ω output impedance. Different internal capacitance values for the gate to source/drain ($C_{GS/GD}$) are inserted to simulate the transfer function taken across $C_{GS/GD}$. All variables are summarized in table 3.2. The correspondence -3 dB cut-off frequencies are simulated to be 0.77 GHz, 7.7 GHz, and 77 GHz as shown by the transfer function for $C_{GS/GD}$ = 3444, 344, 34 fF, respectively, as plotted in fig. 3.5d.

3.3 Optical lithography mask design

AutoCAD 2019 software is used to write the required features to realize the patterns of the double-gated SRs modulator. Different layers in the AutoCAD drawings, indicated by different colours, correspond to metallic or non-metallic regions in the final fabricated chrome mask. In the final production, a fully covered area by chrome is to be inside for the green layer or outside for the red layer of any closed shape (see fig. 3.6). The uncovered areas are to be transparent quartz glass. Based on the fabrication steps, different features are prepared along with a large graphene patch covered with a dielectric square layer to be fabricated on the same chip as illustrated in fig. 3.6a. The SRs are arranged in a nested scheme where the graphene and dielectric rectangular patches are to be positioned within the center of the SRs' gap during fabrication as shown in fig. 3.6b. The top-gate array is prepared in a separate AutoCAD file, which can be uploaded directly to the E-beam machine as shown in fig. 3.6c. It is designed in such a way to pass around the source and drain dipoles in a zigzag fashion in order to minimize the fabrication steps where the whole gated SRs device can be prepared in a single layer instead of a double-layer structure as illustrated in fig. 3.6d. It will be aligned afterward to the center of the SRs' gap where its width shrinks from 4 μm to 1.5 μm when passing through the SRs' gap

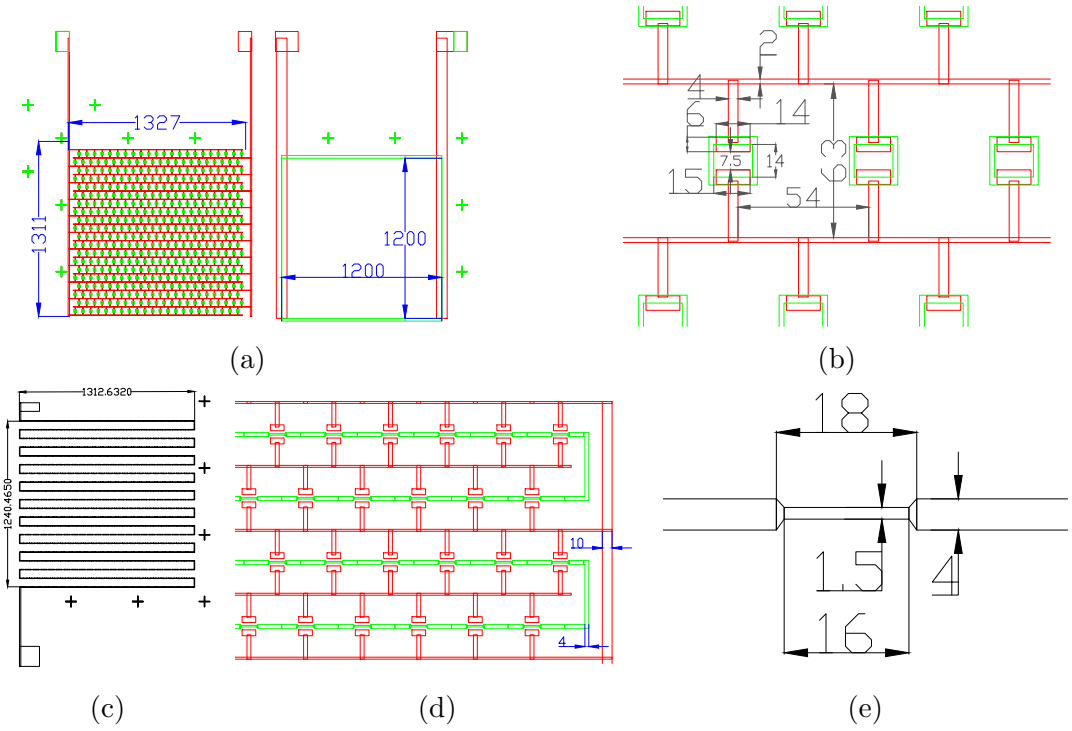

Figure 3.6: AutoCAD drawings for optical lithography mask showing (a) a complete array (left) and graphene patch (right), (b) SRs dimensions (red) with graphene and dielectric features (green), (c) top-gate array dimensions, (d) SRs (red) in a nested scheme and top-gate (green) in a zigzag loop, and (e) top-gate stripe dimensions when passes through the center of the SRs' gap. Note: all dimensions are in μm.

as plotted in fig. 3.6e. The final prepared drawings for the optical mask were sent for production by Compugraphics Photomasks Inc. The optical mask was fabricated using an electron beam (E-beam) lithography system with a resolution of 250 nm. The lithographic mask's features are made of chrome on a 4 $\times$ 4 inches quartz glass.

3.4 Fabrication procedure

3.4.1 Graphene growth and patterning

The fabrication process was accomplished in collaboration with the Cavendish Laboratory and the Department of Engineering at the University of Cambridge, Cambridge, United Kingdom. Part of the fabrication process was done in the Quantum Technology Cleanroom (QTC) at the Physics Department at Lancaster University. The QTC has two rooms of classifications which are ISO 5 (Class 100)

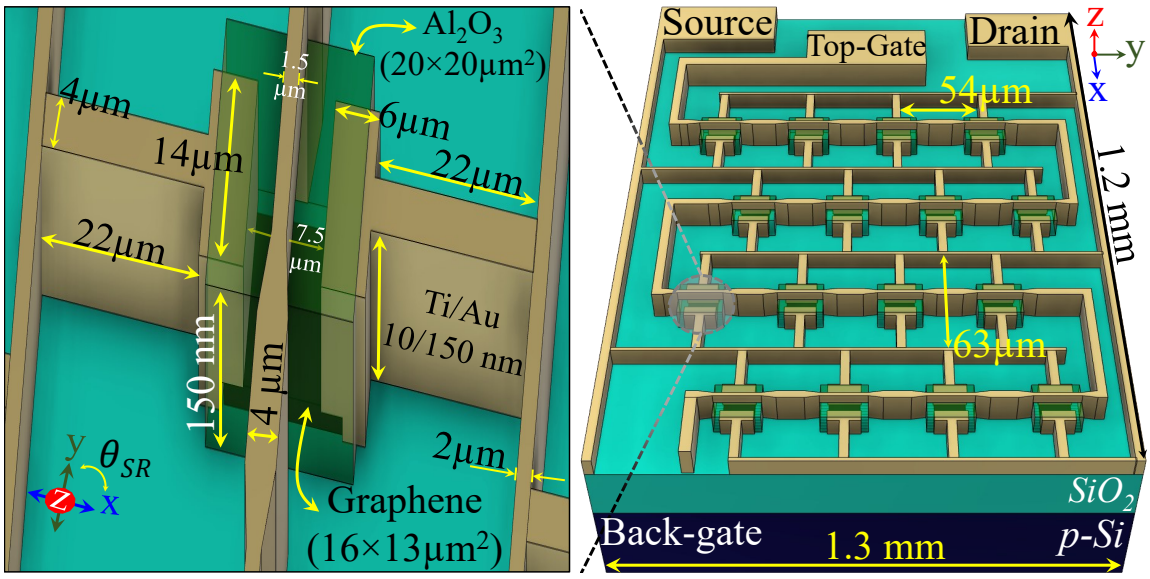

(a) (b)

Figure 3.7: Schematic pictures of a single unit-cell (a) and a complete array (b) showing their dimensions.

and ISO 6 (Class 1000). The monolayer of graphene was grown by Prof. Stephan Hofmann's group at the University of Cambridge. A monolayer of graphene was grown via the chemical vapor deposition (CVD) technique on commercial Cu foil membranes before being transferred onto about 5×5 mm^2 SiO_2/p-Si samples. Using H_2 annealing could help reduce the oxidization of graphene as described in (Burton et al., 2019). The substrate of choice was a commercially available 500 μm thick slightly p-doped (boron dopant) Si. The doping level of the substrate can be increased to enhance the switching speed, but it would introduce more losses to the transmitted THz waves. Thus, the doping level is compromised to allow for back-gating and minimal power attenuation. The substrate wafer comes with a pre-deposited 300 nm thickness of SiO_2 for electrical isolation. The gated resonators are fabricated with total dimensions as illustrated in fig. 3.7a. One complete array consists of 20 (columns) $\times$ 22 (rows) of resonators in an interdigitated arrangement with a total size of 1.3×1.2 mm^2 as shown in fig. 3.7b. The fabrication process is summarized as follows:

- Graphene monolayer growth and transfer on about 5×5 mm^2 SiO_2/p-Si samples
- Alignment marks metals evaporation
- Graphene patches pattering for shunting the resonators
- Source and drain metals evaporation

- Al_2O_3 deposition and patterning for protection and isolation
- Top-gating stripes metals evaporation

3.4.1.1 Alignment mark metals

Alignment marks and surface-gate features are first fabricated. The first one is important as all the following steps are aligned in accordance with these plus-shape metallic marks. Surface-gate is a rectangular metallic feature connected directly to the p-Si substrate through the top layers for faster back-gating. These gates are realized by etching down through the graphene and SiO_2 layers via rectangular features of

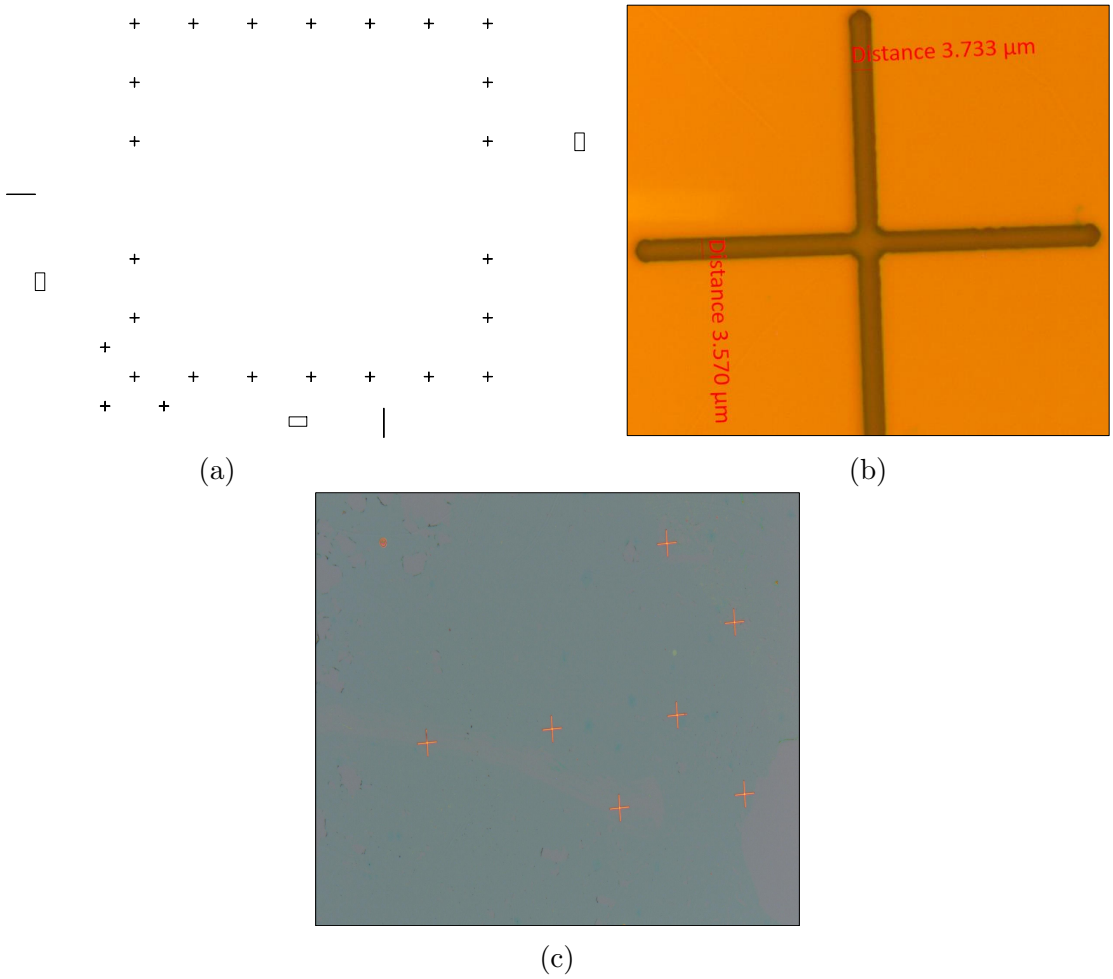

(a) (b)

(c)

Figure 3.8: Alignment marks and surface-gate features shown as (a) in the optical mask, (b) photoresist patterns, and (c) metallic features after the lift-off process.

150 × 80 μm^2 as shown in fig. 3.8a. The optical lithography step is first performed using SÜSS Microtec MJB4 mask-aligner as the following recipes:

- Spin-coating S1813 positive photoresist for 6000 rpm for 60 sec.
- Pre-baking on a hot plate at 115^{o}C for 4 min.
- UV exposure using the mask aligner for 2.5 sec at 22 mW of light intensity.
- Soaking samples in a photoresist developer (MF-CD 26 or MF-319) for ∼45 sec.
- Rinsing with DI water for ∼25 sec and drying with N_2.
- Post-baking on a hot plate at 115^{o}C for 4 min to harden the resist.

Spin-coating of resists creates a homogeneous polymer layer with about 1.3 μm of thickness. The pre-baking step is to harden the resist. Coated samples with resists are then exposed to a UV light operating with 365 nm wavelength. Samples are then soaked into a resist developer for a pre-optimized developing time. Both exposure and developing times are critical in order to have an optimum resists profile. A good lithographic process occurs when its size matches the one in the optical mask. Samples removed from the developer are rinsed with DI water to wash away any remaining developing solution. Post-baking is to harden more the resists to be used as a soft mask afterward. The two layers of graphene and SiO_2 are etched down via a reactive ion etcher (RIE) from Oxford Instruments, model PlasmaPro®NGP80, using the following recipes: duration time of 4 min using 100 sccm of CHF_3, 5 sccm of Ar, and 360 W of RF power. As a result, the Si substrate inside the alignment marks' features is now exposed as plotted in fig. 3.8b. Then, metal evaporation of Ti/Au (10 nm/80 nm) takes place followed by lift-off using an acetone bath on a hotplate at 80^{o}C for a couple of hours. The samples are then washed with acetone/isopropanol (IPA) and dried with N_2. The alignment marks and surface-gate metallic patterns are shown in fig.3.8c.

3.4.1.2 Graphene patterning

The graphene patches are patterned into about 16 × 13 μm^2 rectangular features which will fill the SRs' source/drain gap spacing afterward. This process begins with forming a soft mask of resists using graphene's features in the optical mask. The photolithographic recipes are the same ones mentioned previously (Section 3.4.1.1). The soft mask patterns for etching down the graphene layer are shown in fig. 3.9a. The graphene layer is then removed by O_2 plasma etching at 25 W repeated every 1 min to check the status of the photoresist under a microscope between each ashing step for a total time duration of about 7 min. The remaining photoresists are then washed

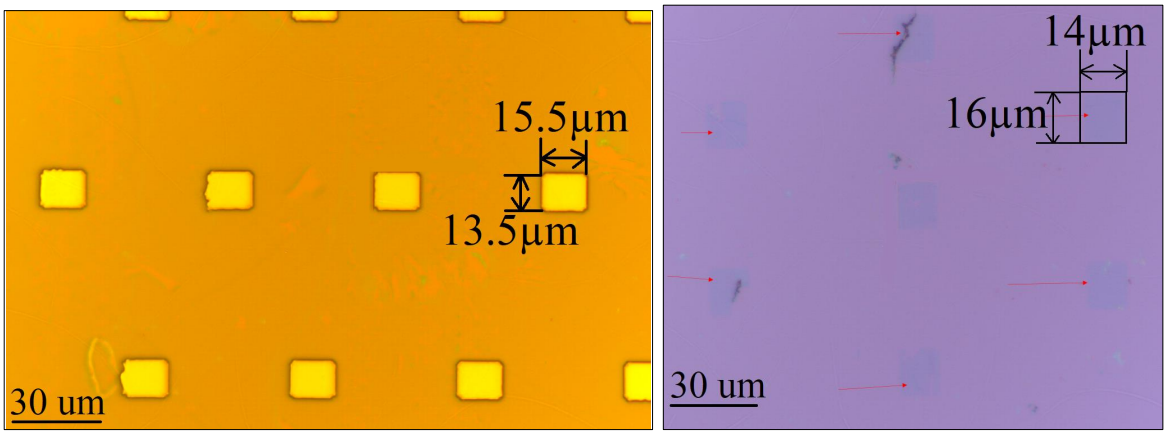

(a) (b)

Figure 3.9: (a) Photolithographic graphene features. (b) Graphene patches after resists removal.

away using an acetone bath on a hotplate at 80°C for about 5 min followed by rinsing with acetone/IPA and drying with N_2. The patterned graphene patches are shown in fig. 3.9b forming rectangles of about 16 × 14 μm^2. These graphene rectangles should be very well centralized with respect to the source/drain gap spacing of ∼7.5 μm as will be discussed in the next section.

3.4.2 Definition of metallic source and drain contacts

Ohmic contacts on the graphene patches are patterned to form the metallic source and drain dipoles. This process begins with transferring the resonators' features to photoresists as indicated by the red lines in fig. 3.6b. The photolithographic step is performed using the same recipes mentioned previously (Section 3.4.1.1). Here, the alignment part is extremely crucial and critical in order to properly position the graphene sheets at the central area of the SRs' gap. It requires high skills to be achieved since there is only about 4 μm of a degree of freedom to properly align graphene patches to touch both resonators. The SRs' photoresist features are centered with respect to the graphene sheets to a reasonable extent as shown by fig. 3.10a. Thermal evaporation of Ti and Au is performed with deposition thicknesses of about 10 nm and 150 nm, respectively. During the lift-off process, samples are soaked in an acetone bath on a hot plate at 80°C for a couple of hours followed by an ultrasonic bath for a couple of seconds only to help lifting-off. Metallic SRs patterns along with the array sample are shown in fig. 3.10b.

The use of a very aggressive recipe for lifting off is because of various reasons. First, S1813 positive photoresist could have been hardened to the extent that causes

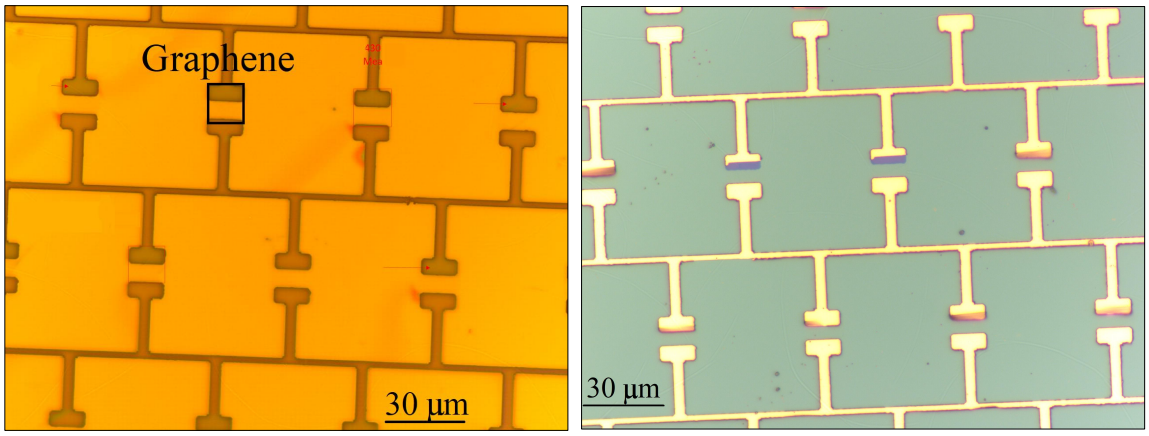

(a) (b)

Figure 3.10: Microscope pictures of the transferred resists of the SRs (a) and metallic SRs after lift-off (b).

difficulties during lift-off. Additionally, S1813 resist forms a vertical profile (90° sidewalls) when using the optimum exposure and developing times recipes. This vertical profile is not suited for lift-off. Therefore, a bi-layer undercut sidewall profile (sloped sidewalls) should be used with conventional positive resists, such as LOR, in order to achieve a discontinuous metals deposition as shown in fig. 3.11a. Moreover, NR7-1000PY negative photoresist creates negative slope sidewalls (opposite to the LOR's profile), which eases the lift-off process as illustrated by fig.3.11b.

3.4.3 Dielectric layer deposition and pattering

A dielectric layer is then deposited and patterned to serve many purposes. First, it acts as an electrical isolation of the resonators from the top-gate stripes. Additionally, encapsulating graphene by alumina is beneficial to reduce graphene's hysteresis and required voltage to reach its Dirac point (Alexander-Webber et al., 2016). The alumina layer is deposited covering the whole samples via atomic layer deposition (ALD) system, Veeco Savannah S100, with a thickness of ∼50 nm for devices fabricated in the QTC cleanroom at Lancaster University using pre-loaded recipes for Al_2O_3. The deposited dielectric layer is then patterned into square features of 20×20 μm^2 starting with transferring ALD features to resists via photolithography step as mentioned previously (Section 3.4.1.1). The ALD layer is then etched down via chemical wet etching recipes using 65% concentration of phosphoric acid (H_3PO_4) on a hot plate at 80°C with an etching rate of ∼33 nm/min. Thus, a 50 nm thickness of the ALD layer is etched down for a duration of about 2 min followed by rinsing with DI water for about 1 min to wash away in acid remaining and drying with N_2.

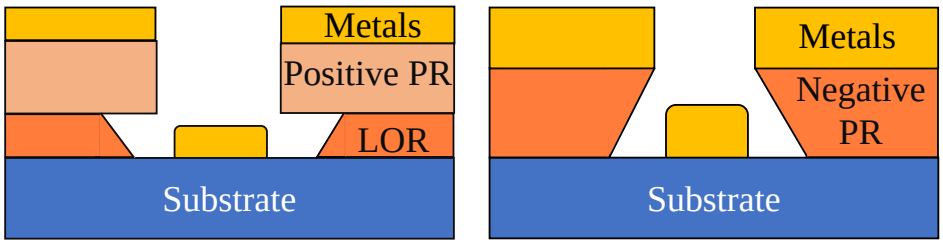

(a) (b)

Figure 3.11: (a) LOR lift-off resists profile being used with positive photoresists (PR). (b) NR7-1000PY negative PR sidewalls.

The remaining resists are then removed by soaking samples into an acetone bath on a hot plate at 80°C for ∼5 min followed by rinsing with acetone/IPA and drying with N_2.

Other devices fabrication were a collaboration by: 1) Prof. Stephan Hofmann's group for transferring graphene and deposition of ALD thicknesses of ∼150 nm and ∼95 nm following recipes mentioned elsewhere (Alexander-Webber et al., 2016), 2) myself (align marks, etc.), and 3) Dr Nikita W. Almond (E-beam, etc.).

3.4.4 E-beam lithography

Since the photolithography technique has a resolution of ∼2 μm when using soft contact, hence electron beam (E-beam) lithography or laser writer are better for finer features such as the ones in top-gate stripes. The smallest features in the top-gate array are as small as 4 μm, but it shrinks to 1.5 μm when passing through the center of the resonators' gap spacing. Further to this, precise alignment of the top-gate central features in the gaps of the SRs over 1×1 mm^2 patterns poses strict requirements to the alignment angles as well, which is beyond the control offered by optical lithographic systems. Due to limited and restricted access to the QTC cleanroom during the pandemic, devices were sent to Cambridge for processing top-gate stripes using the E-beam system by Prof. David A. Ritchie's group in the SP group of the Cavendish Laboratory. Double layers resist are performed using the following recipes:

- Spin-coating 495k PMMA A7 resist for 4000 rpm for 60 sec.
- Baking on a hot plate at 180°C for 10 min.
- Spin-coating 950k PMMA (1:5 MIBK) resist for 4000 rpm for 60 sec.
- Baking on a hot plate at 180°C for 10 min.
- Developing in IPA:MIBK:MEK with a ratio of 15:5:1 for 8-90 sec.

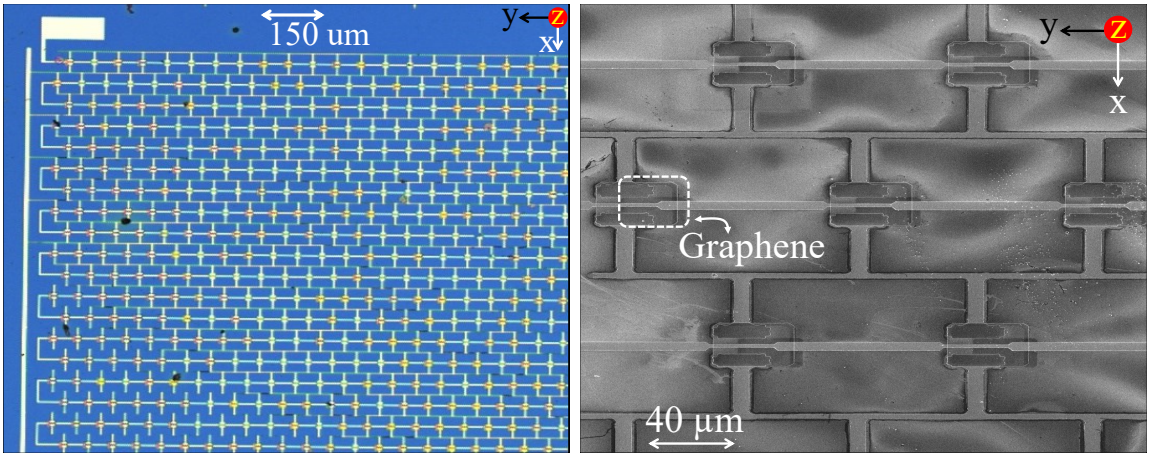

(a) (b)

Figure 3.12: (a) Microscopic using 5X objective and (b) scanning electron microscope (SEM) pictures of the fabricated double gated SRs modulator.

- Rinsing with IPA for ∼50 sec and drying with N_2.

Thermal evaporation of Ti/Au (10 nm/70 nm) is then performed followed by soaking samples in an acetone bath for lifting-off. The real fabricated double-gated SRs pictures are shown in fig. 3.12a and 3.12b.

3.4.5 Wire-bonding

To electrically drive these devices, they are mounted using silver pastes on high-speed boards model RO4000® series from Rogers Corporation and made of hydrocarbon/ceramic laminates that support high-speed frequencies above 70 GHz. The PCB circuit board is designed by EaglePCB commercial software and fabricated using an in-house PCB engraver. Its design and dimensions are shown in fig 3.13a. It also has a 5×5 mm^2 hole at its center to allow testing the mounted devices in a transmission configuration. Two SMA connectors are soldered to the two ends of the PCB design to apply high RF frequencies. To begin with the wire-bonding process, model HB05 Wedge and Ball Bonder from TPT Wire Bonder GmbH & Co. KG, the PCB board with a mounted sample are placed on a heater stage. The height of this stage must be about 76 mm. To place a bonding tip as shown in fig. 3.13b, the motorized wire clamp is opened and then moved manually and gently towards the left side away from the gold wire. A ceramic tool tip is then inserted into the bond head and screwed tightly with a torque wrench. A thin gold wire, coming from a gold wire spool with 25 μm thickness, is inserted into the tool-tip using a tweezer and simultaneously applying an ultrasound power (located on the moving stage mouse) to help it slide down smoothly.

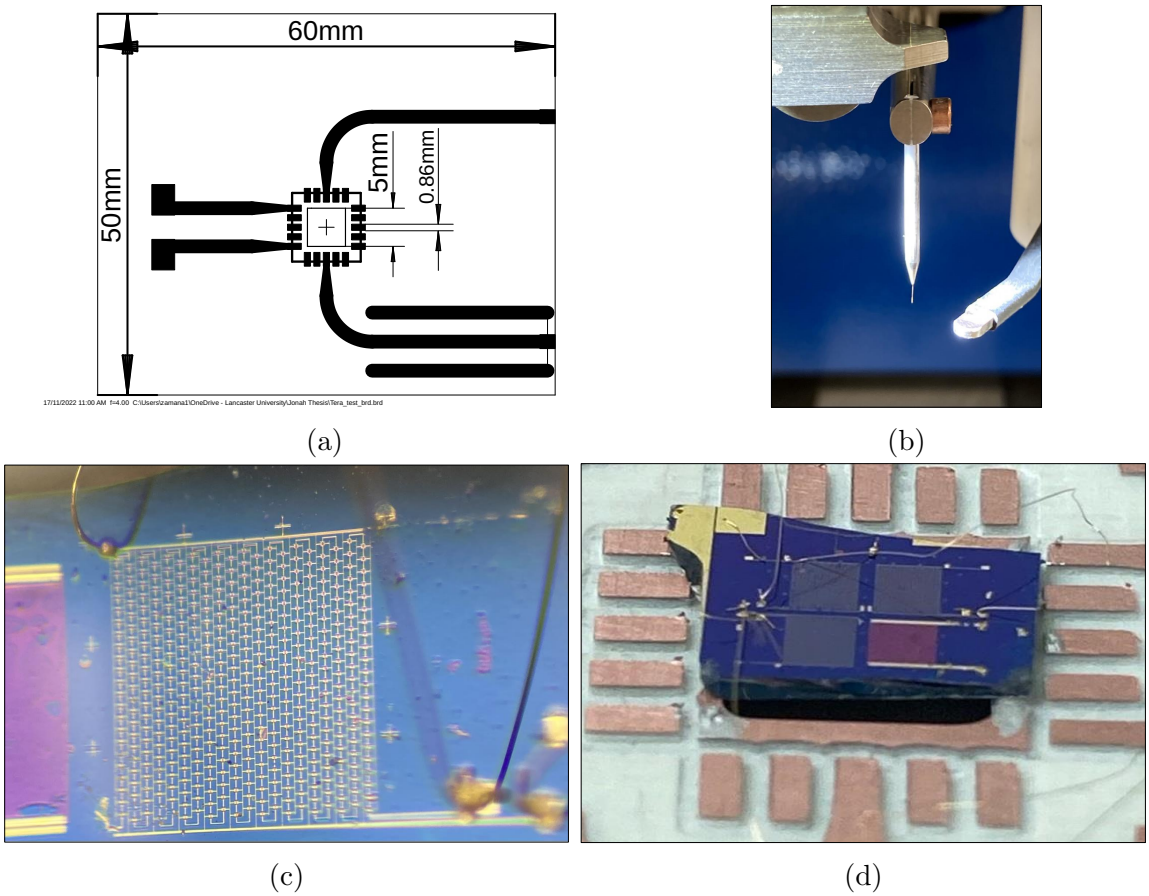

Figure 3.13: (a) PCB circuit design. (b) Inserted Au wire through a motorized wire clamp and ceramic tool tip. (c) Bonded array. (d) Bonded and mounted device.

The wire clamp can be returned back gently to its original position and closed to hold the Au wire, which can be controlled by the wire clamp. After that, the heater stage with a mounted sample is ready to be placed under the tool-tip. In the machine's settings screen, bonds 1 and 2 are set as detailed in table 3.3. In the beginning, lower force is recommended and then increased gradually if bonding on gold does not occur nor peel off. Usually, bond 1 is set to perform the Au ball bonding while bond 2 is for bonding on the circuit board leaving a wire tail of a 100 μm. An Au ball can be created by lifting up the lever's arm. The lever would hit the Au wire applying a high voltage simultaneously to melt the Au wire creating a ball. After setting the machine to a ball bonding method, the bonding process is performed with help of a microscope. A source/drain biasing line with a width of $\sim$10 μm is successfully bonded as shown in the upper right corner of fig.3.13c. Fig. 3.13d illustrates a bonded device showing three different arrays and a large on-chip graphene patch mounted on a high-speed

circuit board. The large graphene patch is used for post-processing of the acquired data, which will be discussed in the next Chapters (4). This bonded array is tested for analyzing its optoelectronic behaviour, MMs/graphene relaxation lifetime, and polarization modulation which will be discussed in the following chapters.

Table 3.3: Wire-bonding recipes for Au (high, medium, and low) and PCB board.

Parameter	**High**	**Medium**	**Low**	**Circuit Board**
Utrasonic power (W)	400	200	100	360
Bond Time (msec)	200	100	50	360
Bond Force (cN)	25-70	25-70	15-70	70-110

Chapter 4

THz waves spectral characterizations

4.1 THz time-domain spectroscopy

4.1.1 Measurement techniques

Since the beginning of the THz era, many experimental techniques have been developed from both photonic and all-electronic approaches. Enhancements in femtosecond (fs) pulses and semiconductor technologies have enabled developments for improving THz measurement techniques. Analysis of energy, wavelength, or frequency of photons or waves propagating through under-testing materials is well-known as spectroscopy (Neu and Schmuttenmaer, 2018). Various microscopic techniques emerged in the past decades such as in a-SNOM (Mitrofanov et al., 2016; Hale et al., 2020) and SNOM (Maissen et al., 2019; Huber et al., 2008). Vector network analyzer (VNA) spectrometers measure directly in the frequency domain and can scan over a broad range of frequencies. Fourier-transform infrared spectrometers (FTIRs) acquire measurements in the time domain using incoherent sources and then transform them into the frequency domain. Whilst it provides a large spectral range, it typically has a slow data acquisition speed and limited signal-to-noise ratio.

THz time-domain spectroscopy (THz-TDS) based on ultrashort fs pulses is well-known for its ability in characterizing 2D materials, semiconductors, superconductors, and standard dielectrics. Fig. 4.1 illustrates a THz-TDS setup in a transmission configuration. THz-TDS systems based on fs pulses provide a broadband coherent spectrum. The sampled signals are then detected using several techniques such as photoconductive switches or electro-optic sampling (Neu and Schmuttenmaer, 2018). it is also well-known for its low noise and for providing information on a wide frequency bandwidth typically between 0.1-4 THz. Further to this it is a coherent detection

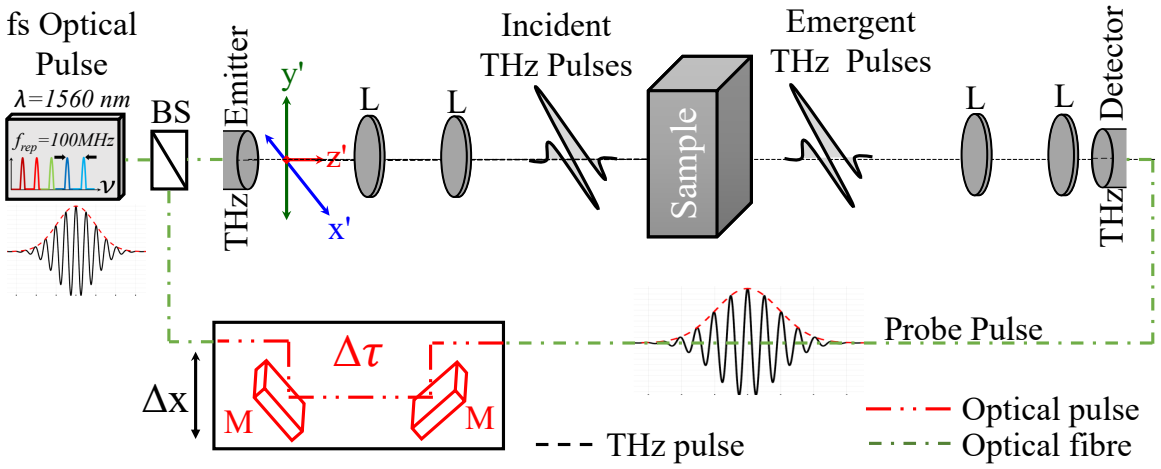

Figure 4.1: Schematic view of a THz-TDS setup in transmission configuration where L: lenses, M: mirrors, and BS: beamsplitter.

technique, thus allowing to acquire at the same time amplitude and phase of the THz E-field; e.g. for the retrieval of the complex refractive index of a material. Static properties of the tested materials allow using THz-TDS with enough efficiency to study molecular spectroscopy, quality control, biological studies, protein, crystalline, and aging variations of medicines (Patil et al., 2022). A typical THz-TDS system usually includes a THz emitter, samples in-contact configuration, amplifier responsively, and detection as explicitly reported in (Exter, Fattinger, and Grischkowsky, 1989).

4.1.2 Ultrashort pulse propagation

Although the intensity of THz pulses can easily be measured by detectors, extractions of the phase shifts are challenging and require more complicated techniques such as interferometers. The same generated fs pulse is used to extract the phase shift by delaying the same pulse. Autocorrelation of fs pulses arriving at a detector would reveal any accumulated phase differences. The mathematical representation of the fs optical pulses can be described as a Gaussian function. The time-domain pulse shape has the following formula (Y.-S. Lee and Y.-S. Lee, 2008):

$$E(t) = |E_0| e^{-\tau_0 t^2} e^{-i\omega_0 t}, \tag{4.1}$$

where temporal amplitude is $|E_0|$. The first exponential of E(t) carries information about the envelope of the optical pulses where the pulse duration is τ_0 and denoted by the dashed (red) line in fig. 4.2a. The second exponential of E(t) contains the sinusoidal oscillation with an angular frequency (ω_0) and is presented by the straight line (black) in fig. 4.2a. The autocorrelation function of E(t) provides the

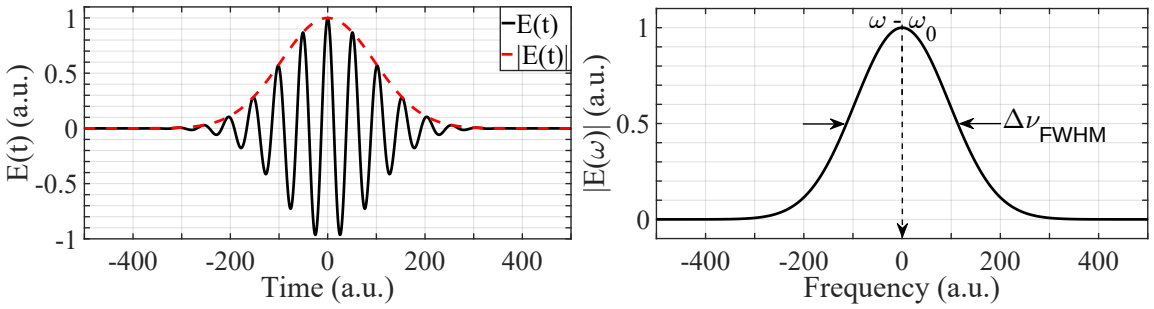

(a) (b)

Figure 4.2: (a) Temporal Gaussian pulse, and (b) its power spectrum density.

instantaneous intensity per unit area (W/cm^2) for pulses propagating in a linear medium as(Y.-S. Lee and Y.-S. Lee, 2008):

$$I(t) = \frac{\epsilon_0 cn}{T} \int_{t-T/2}^{t+T/2} E^2(t')\, dt' = \frac{1}{2}\epsilon_0 cn|E(t)|^2 = \frac{1}{2}\epsilon_0 cn|E_0|^2 e^{-2\tau_0 t^2}. \tag{4.2}$$

The permittivity of free space is ϵ_0, speed of light is c, waveform single period T, and refractive index of the medium is $n = \sqrt{\epsilon/\epsilon_0}$ for nonmagnetic transparent media. The pulse duration is usually calculated at the full width at half maximum (FWHM). Assuming a Gaussian pulse, the FWHM pulse duration is denoted by (τ_p) and given by (Y.-S. Lee and Y.-S. Lee, 2008):

$$\tau_p(t) = \sqrt{\frac{2ln(2)}{\tau_0}}. \tag{4.3}$$

The unique property of a Gaussian function is that its spectra takes also a Gaussian form with the following formula (Y.-S. Lee and Y.-S. Lee, 2008):

$$\mathbf{E}(\omega) = \mathcal{F}\{\mathbf{E}(t)\} = \int_{-\infty}^{+\infty} E(t)e^{-i\omega t}dt = |E(\omega)|e^{i\Phi(\omega)} = \sqrt{\frac{\pi}{\tau_0}}|E_0|e^{-\frac{(\omega-\omega_0)^2}{4\tau_0}}. \tag{4.4}$$

Both the time and spectra of the E-fields can be in complex representations. The spectral amplitude is $|E(\omega)|$, while the spectral phase is denoted by $\Phi(\omega)$.

4.1.3 THz emitters

THz waves can be generated using several physical techniques. One common mechanism is to excite a medium with fs optical pulses, which causes a current to flow. In regenerative amplifier lasers technology, however, a nonlinear process

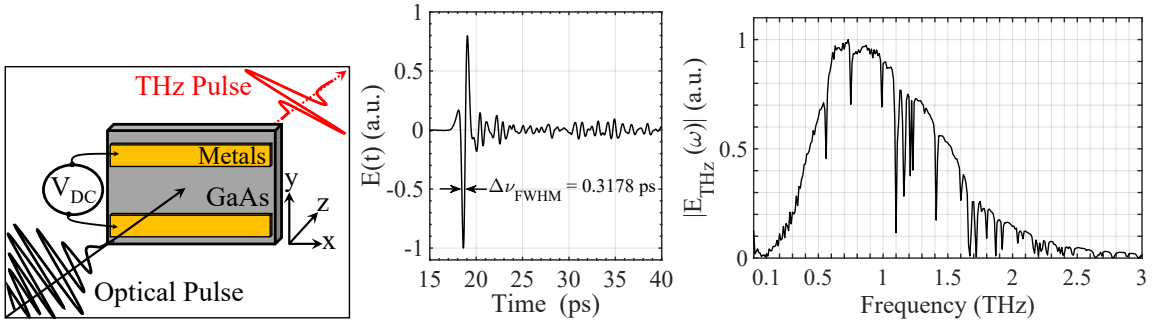

(a) (b) (c)

Figure 4.3: (a) PC antenna for THz generation (Y.-S. Lee and Y.-S. Lee, 2008). (b) Temporal THz pulse. (c) THz Spectra.

is used to emit THz radiations. Common characteristics of the THz emitters include THz spectral bandwidth and various laser technology compatibility. Laser oscillator technique generates THz pulses with up to 1 GHz of free spectral range ν_{FSR}, <150 fs pulses duration, and (∼nJ) pulses energy (Neu and Schmuttenmaer, 2018). By optical rectification method, THz pulses are generated with <10 kHz repetition rate, <150 fs pulse duration, and >10 μJ pulses energy (Wynne and Carey, 2005). THz pulses can be generated from fs optical pulses exciting a DC-biased photoconductive (PC) semiconductor antenna. The generated THz radiation is proportional to the induced current passing through the metallic antenna using the following formula (Y.-S. Lee and Y.-S. Lee, 2008; Neu and Schmuttenmaer, 2018):

$$E_{THz}(t) = \frac{\mu_0 \omega_0 \sin(\theta)}{4\pi r} \frac{d}{dt_r}[I_{PC}(t_r)]\hat{\theta} \propto \frac{dI_{PC}(t)}{dt}, \tag{4.5}$$

where the generated far-field (r$\gg \lambda_{\mathrm{THz}}$) E_{THz} takes an angle θ and the retarded time is $t_r = t - r/c$. Undoped semiconductors are used in PC antennas' metallic pads driven by a small DC voltage. The two metallic stripes are biased to accelerate the photogenerated carriers, thus providing an ultrafast current. The main factor is that it must allow fast recombination time as the leading edge in the THz pulse is given by the rising ultrafast current, but recombination time is the one determining the final part of the THz radiation pulse. Hence, low-temperature grown GaAs (LT-GaAS) is the material of choice. Exciting the bandgap energy of the substrate by an fs optical pulse with higher photon energy would induce carriers to flow through the semiconductor. A photon is absorbed generating an electron-hole pair, which are then driven toward the two metallic pads having opposite voltages. The THz pulse duration is determined by the fast photocurrent (I_{PC}), fs optical pulse width, and capacitance stored energy (Sze, Y. Li, and Ng, 2021). Electron scattering time and carrier lifetime of the semiconductor are some key factors to limit the photoinduced current. The

commonly used material for PC switching is low-temperature gallium arsenide (LT-GaAs) because of its short recombination time. The carrier lifetime of LT-GaAs is approximately 100 fs (Stellmacher et al., 1999), while the radiation-damaged silicon-on-sapphire (r-SOS) is the closest one with $\tau \approx 600$ fs (Doany, Grischkowsky, and Chi, 1987). Fig. 4.3a shows a schematic picture of THz wave generation using LT-GaAs substrate. Despite some disadvantages of the GaAs semiconductor for around 8.5 THz frequencies, the LT-GaAs THz transmitter has been widely used (Neu and Schmuttenmaer, 2018; Y.-S. Lee and Y.-S. Lee, 2008). A typical generated THz pulse using LT-GaAs technique is plotted in fig. 4.3b and its spectra in fig. 4.3c without nitrogen purging.

4.1.4 THz detectors

THz-TDS system is based on coherent detection techniques. To obtain most of the spectral contents, detectors with similar spectral gain and the best signal-to-noise ratio (SNR) should be taken into consideration. The detection mechanism in THz-TDS is based on sampling the wider THz pulse with a shorter fs optical pulse arriving simultaneously in the time domain. Thus, all detection methods measure the THz E-field and not intensity via the correlation operation (denoted by $\otimes$). The detected signal can be estimated as follows (Neu and Schmuttenmaer, 2018):

$$S(t) \propto I_{\text{optical}}(t) \otimes E_{\text{THz}}(t). \tag{4.6}$$

The optical intensity can be estimated as a delta function since it is much shorter than the THz E-field. At any given time, the detected signal can be approximated to be equal to only E_{THz}. Next is to delay the optical pulse to acquire the amplitude of the E_{THz}. In contrast to all other THz detection methods, the THz-TDS technique conducts measurements on the amplitude and phase of the THz E-field.

4.1.5 Our Menlo Systems setup

The TERA K15 fiber-coupled terahertz spectrometer is a device used for scientific THz applications. It offers fast broadband time-domain THz spectroscopy with a femtosecond laser source, fiber-coupled optical light path, THz wave path, control electronics, and data acquisition and evaluation software. It has a scan range of $\sim$600 ps and a spectral resolution below 1.67 GHz. It is suitable for various applications such as THz component testing, charge carrier dynamics investigation, and THz plasmonics. The THz-TDS setup is schematically shown in fig. 4.1 in the transmission configuration. The fiber laser operates at 1560 nm wavelength with $<$90 fs of temporal width and 100 MHz repetition rates. Both the emitter and receiver are pulsed terahertz modules made of mesa-structured InGaAs chips from Fraunhofer

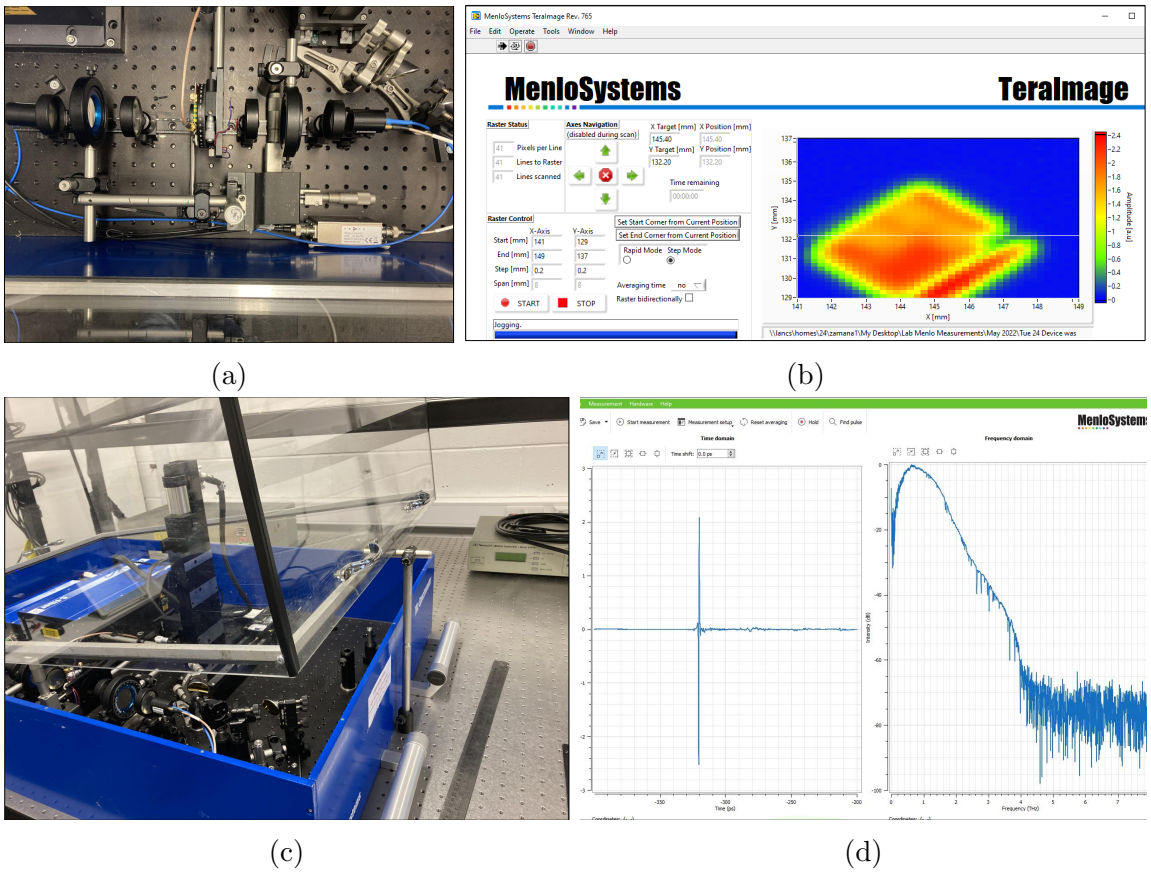

Figure 4.4: (a) picture of a THz-TDS spectrometer set in transmission mode. The system is a Tera k15 model from Menlo Systems. (b) PC-controllable stage software for the sample holder developed by Menlo Systems using the LabVIEW platform. (c) Setup arrangement. (d) Data acquisition software developed by Menlo Systems showing THz waveform and spectrum acquired with N_2 purging.

Heinrich Hertz Institute (Fraunhofer Institute for Telecommunications, n.d.) with a spectral range of 0.1-5 THz emitting a typical THz power of 25 μW. The emitted fs optical pulses are split into two by a beam splitter. One pulse is directed to a moving stage to introduce temporal delays ($\Delta\tau$). The second optical pulse propagates to a THz antenna generating only linearly polarized THz pulses. Both antenna's and receiver's mountings can be rotated, thus allowing for a simple change of the spectrometer polarization. Samples are placed at the focal point distance of the 4-f lenses system as shown by the picture of the setup in fig. 4.4a. Their rotational holder is positioned in an x-y electrically moving stage, which is controlled by PC software for precise spatial mapping measurements as shown in fig. 4.4b. The z-direction can

be altered manually via a micro-positioner for carefully positioning the sample in the focus of the optical system. Power attenuation is stronger at some THz frequencies due to atmospheric absorption which may affect the accuracy of measurements (Xin et al., 2006; Kürner, D. Mittleman, and Tadao Nagatsuma, 2021; C. Lin and G. Y. L. Li, 2016). Therefore, the Menlo setup is covered with an engineered packaging for purging with N_2 as shown by fig. 4.4c. The detected amplitude of E_{THz} in the time domain and its spectra are acquired using software developed by Menlo Systems as illustrated in fig.4.4d.

THz-TDS systems are known for their versatility. However, the transmission mode is the most commonly used. The optical system configuration, as well as the material of choice for lenses, reflective parabolic mirrors rather than TPX (Polymethylpentene) lenses play an important role in defining the final specifications in terms of power losses, frequency bandwidth, and error detection. Reflective optics, such as parabolic mirrors, provide larger bandwidth as they do not have absorption; but their alignment and stability in day-per-day operation are lower compared to standard optics (Withayachumnankul and Naftaly, 2014). Power losses are frequency dependent and increase for smaller frequencies (Withayachumnankul and Naftaly, 2014). The focal length and diameter of lenses are carefully selected based on the spatial profile of the generated THz beam. The generated THz waves are collected by a hyper-hemispherical HRFZ-Si lens directed to a 4-f lenses system as shown in fig. 4.4a. Four identical collimating lenses with 50 mm diameter are aligned in the transmission mode. These lenses have an effective focal distance of approximately 57.5 mm. The parameters of lenses and/or misalignment may change the THz beam's wavefront and direction leading to an increase in the detected power losses. The THz beam at the focal plane of the THz-TDS setup is estimated to be $\sim$1.2-1.3 mm in diameter. At the setup's focal plane, a pinhole is placed before the samples in order to control the THz beam waist. For a total array dimension of 1.3 mm $\times$ 1.2 mm, the pinhole's diameter is set to be approximately 1.1 mm based on Fresnel near-field formalism.

It is worth highlighting some preliminary characterizations of the THz-TDS system such as signal-to-noise ratio (SNR) and dynamic range (DR). Minimal changes in amplitude determine the sensitivity of detection, in other words, the SNR of the system. For optimization, detected E_{THz} amplitude can be divided by the root-mean-square of the temporal waveform noise. The noise floor can be obtained by blocking the THz beam path. Intensity fluctuations of the fs optical laser are a main source for stability reduction of the THz pulses. Averaging over multiple iterations of the acquired temporal waveforms improves the SNR since it reduces random noises of amplitude. The amplitude of temporal E_{THz} becomes sharper after averaging 1000 times as plotted in fig. 4.3b, while its spectra are shown in fig. 4.3c without samples nor purging. This averaging iteration would last about 2 min over 100 ps of scanning

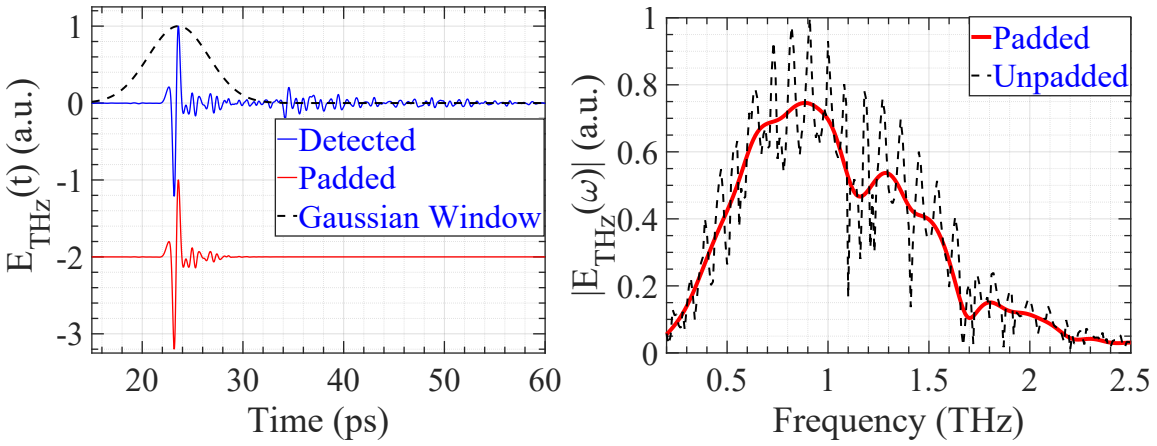

(a) (b)

Figure 4.5: THz E-field passing through the graphene reference in time-domain (a) and its spectra (b) averaged 500 times without purge. The padded temporal pulse is offset vertically for comparison purposes only.

time. Temporal uncertainty is one of the main causes of phase noise of THz radiation. Although the SNR of amplitude is acceptable for frequency above 1 THz, phase noise could be as large as $\pm 20^{o}$ (Neu and Schmuttenmaer, 2018).

The spectral resolution in a lossless system is determined by the fs optical pulse repetition rate and mechanical delay mirrors. The temporal delay can be calculated as the ratio between round-trip length to the speed of light (2L/c), where L corresponds to the total path length and the light make it twice back and forth. However, the system's SNR limits the frequency resolution practically. The commercialized Menlo System is designed to span over an optical path time up to 600 ps, which corresponds to about 9 cm of physical length. The inverse of the spanning time yields a frequency resolution of <2 GHz. Throughout this chapter, we acquire only 100 ps as we do not need a long scan that will not be adding any useful information but only make measurements longer. This time span is enough since the SNR of the system's amplitude remains almost unity at a certain point (Withayachumnankul and Naftaly, 2014), which corresponds to 10 GHz of frequency resolution. The DR can be measured in the frequency domain as a ratio between the maximum signal amplitude to noise floor amplitude at a given frequency. The DR is >90 dB for most frequencies <1 THz as plotted in fig. 4.4d. Although the DR decreases for frequencies >1 THz, measurements can be reasonably acceptable for frequencies up to 3 THz with the help of nitrogen purge. During signal processing, spectral features can be improved by applying a time-domain window to the acquired data and zero padding the rest to extend the temporal waveform. The padding effect on a 100 ps temporal waveform

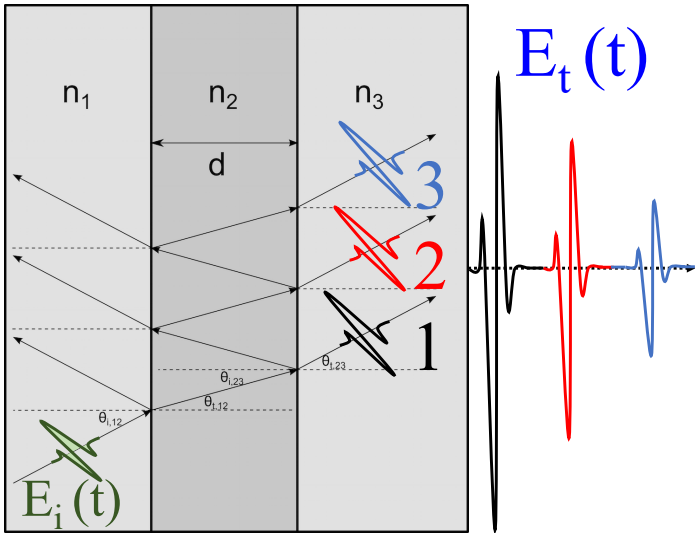

Figure 4.6: Multiple reflections/transmissions for wave propagation in a homogeneous medium.

is shown in fig. 4.5a using a Gaussian filter with 6 ps of FWHM and centered at the peak of the temporal pulse occurring at 23.6 ps. Additionally, padding the temporal waveforms is reducing the Fabry-Pèrot (FP) resonances and ringing in spectra as shown in fig. 4.5b. It is worth mentioning that the spectral resolution does not depend on the time-domain step size Δt, but on the total time-domain span $\mathrm{T} = 1/\Delta f$.

Fig. 4.6 illustrates the Fabry-Pèrot effect when electromagnetic (EM) waves propagate inside the substrate medium. Multiple reflections and transmissions occur inside a semiconductor substrate with refractive index n and thickness d. When taking into consideration the etalon effect, the transmitted EM waves through a sample can be described as follows (Son, 2020a; Neu and Schmuttenmaer, 2018):

$$E_{\mathrm{out}} = \sum_{i=1} E_{\mathrm{incident}} = t_{12} P_2 t_{23} F P_{123} E_{\mathrm{incident}}, \tag{4.7}$$

$$t_{\mathrm{jk}} = \frac{2n_{\mathrm{j}}}{n_{\mathrm{j}} + n_{\mathrm{k}}}, \tag{4.8}$$

$$P_2 = e^{-ik_0 d_2 n_2}, \tag{4.9}$$

$$F P_{\mathrm{jkl}} = \sum_{m=0}^{M} (r_{\mathrm{kl}} P_{\mathrm{k}} r_{\mathrm{jk}} P_{\mathrm{k}})^m, \tag{4.10}$$

$$r_{\mathrm{jk}} = \frac{n_{\mathrm{j}} - n_{\mathrm{k}}}{n_{\mathrm{j}} + n_{\mathrm{k}}}. \tag{4.11}$$

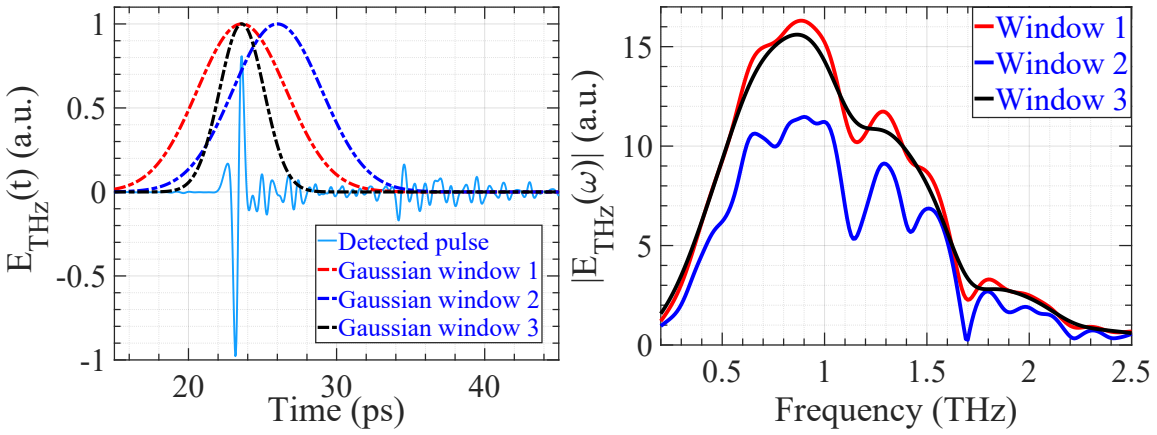

(a) (b)

Figure 4.7: THz E-field passing through the graphene reference in time-domain (a) and its spectra (b) averaged 500 times without purge for different applied Gaussian filters.

At each layer, the EM waves are altered by either a transmission coefficient (t_{jk}) or reflection coefficient (r_{jk}) based on Fresnel coefficients as given in eqs. 4.8 and 4.11, respectively. The EM waves are traveling through the sample (medium 2) with a propagation factor (P_2), the thickness of d, and refractive index n_2 as given by eq. 4.9. During signal processing, multiple reflections and transmissions can be eliminated by either applying a time-domain window or compensation of the Fabry-Pèrot (FP_{123}) effect (Son, 2020a; Neu and Schmuttenmaer, 2018). The FP resonances inside the substrate have an M number of reflections and are given by eq. 4.10.

4.1.6 Signal processing

The retrieval of spectral properties of THz pulses passing through metamaterials is explained in detail. Since the THz-TDS system conduct measurements in the time domain, the refractive index of under-testing materials can be extracted. However, our focus is on spectral parameters. THz waves passing through the semiconductor substrate at a normal incident angle including the etalon effect can be expressed as:

$$E_{sample}(\omega) = |E(\omega)|FP(\omega)e^{-i\phi(\omega)}, \tag{4.12}$$

where FP stands for Fabry-Pèrot effect. In addition to the transmission through the metamaterial array, THz pulses passing through the graphene reference must be acquired in order to cancel the effects of the spectrometer setup. Thus, having independent information about the metamaterials only. Eq. 4.12 holds for the reference E-fields as well, which will be denoted as (E_{ref}). Elimination of the FP

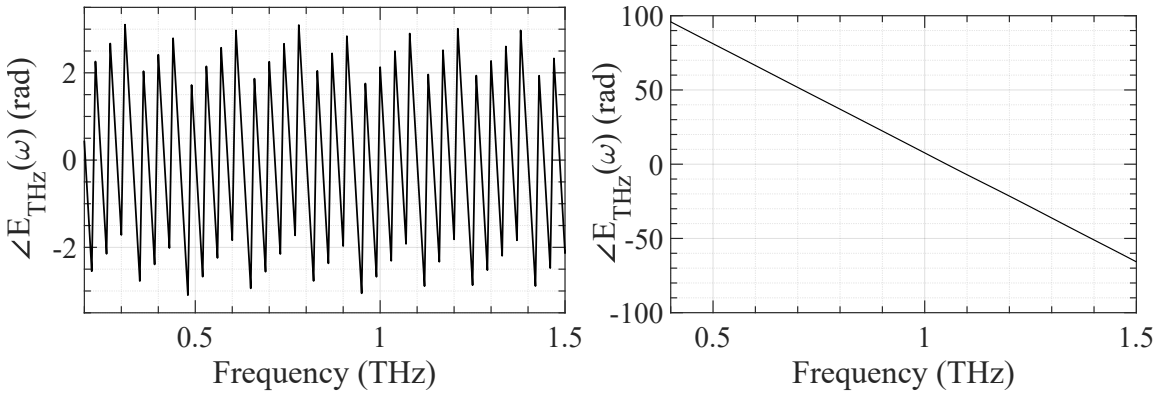

Figure 4.8: Spectral phase of THz E-field passing through the graphene reference when it is unwrapped (a) and wrapped (b).

resonances can be done experimentally by reducing the spanning time just right before the multiple reflection/transmission pulses, but we do it in post-processing since it is safer and can always selectively crop unwanted time-domain points. Multiplication of the temporal THz waveforms by a rectangle shape is translated into a convolution between the THz spectrum and *sinc* function in the frequency domain. Therefore, ripples of the *sinc* function cause ringing in the THz spectra. The Gaussian function could be the best option since its spectra are a Gaussian profile. Multiplication of THz spectra by a Gaussian window may broaden the metamaterials resonance, but it would eliminate the ringing issues. Temporal THz waveforms passing through the graphene reference are shown in fig. 4.5a. Multiple round-trip reflections are detected after about 11 ps from the first transmitted pulse corresponding to about 500 μm thickness of the Si substrate. Three different Gaussian filters are applied as shown in fig. 4.7a. Filters 1 and 2 are centered at the peak of the THz pulse (23.6 ps) with an FWHM of 3.5 ps and 7 ps, while the third filter is centered at 26 ps with an FWHM of 7 ps. Their Fourier transformed curves are shown in fig. 4.7b. Transition through a big patch of graphene fabricated on the same chip is used for reference to cancel out the effect of the substrate. Although transmission through the air can be used as a reference, it is better to use the same substrate without metals of metamaterial for normalization especially when testing complex and multi-layer structures. Equations being used during post-processing can be modified for completion as follows:

$$\begin{aligned} E_{\text{normalized}}(\omega) &= \left\{ \frac{FFT[Window(t) \times E_{\text{resonators}}(t)]}{FFT[Window(t) \times E_{\text{reference}}(t)]} \right\}, \\ &= \frac{|E_{\text{resonators}}(\omega)|}{|E_{\text{reference}}(\omega)|} e^{i\{\Phi_{\text{resonators}}(\omega) - \Phi_{\text{reference}}(\omega)\}}. \end{aligned} \tag{4.13}$$

Extraction of the spectral phase is one of the powerful advantages of the THz-TDS systems. The Fourier transform of the normalized THz E-field has complex representations. Phase is wrapping around itself between -π and π causing discontinuity. To eliminate the phase-jumping discontinuity, the following equation can be used:

$$\phi_{\text{wrapped}}(\omega) = \phi_{\text{unwrapped}}(\omega) - 2\pi M, \tag{4.14}$$

where M is an integer counting the number of phase jumping discontinuities. Fig. 4.8 illustrates the unwrapped and wrapped spectral phases. The wrapped phase takes the shape of a linear line.

4.2 Dynamic amplitude/phase tuning of the metamaterial/graphene modulator

4.2.1 Amplitude modulation

In this era of information, technologies for fast data rates are increasingly demanded by the next generations of wireless communications beyond 5G (Tadao Nagatsuma, Guillaume Ducournau, and Cyril C Renaud, 2016; Elayan et al., 2020; L. Zhang et al., 2020a; F. Fan et al., 2021a; Zeng et al., 2021). Therefore, research in the THz circuity is undoubtedly urgent and unavoidable. Amplitude and phase modulations are some basic properties for data transmissions in wireless communication such as in on-off keying (OOK) or quadratic amplitude modulation (QAM). Moving towards high frequencies, IQ modulation at source before the antenna emitter of electronic source become problematic, hence the need to develop a new approach based on external modulation platform. This approach is more versatile and allow to implement the same sources for a variety of functionalities. For external THz modulators, commonly referred to as a figure of merits, such as high modulation depth, fast reconfiguration speed, wall-plug efficiency, miniaturization, and power consumption. The modulation speed can be theoretically fitted to the -3dB cut-off frequency as follows:

$$H(f) = \frac{1}{\sqrt{1 + (\frac{f}{f_{3dB}})^2}}. \tag{4.15}$$

Since MMs design needs to be optimized with respect to the desired functionality, the following paragraph is dedicated to amplitude, phase, frequency, and polarization active MMs devices. Historically, amplitude modulation (AM) has been always the first selected mechanism to actively alter the properties of THz waves using the MMs approach (Hou-Tong Chen et al., 2006). Its implementation is considered

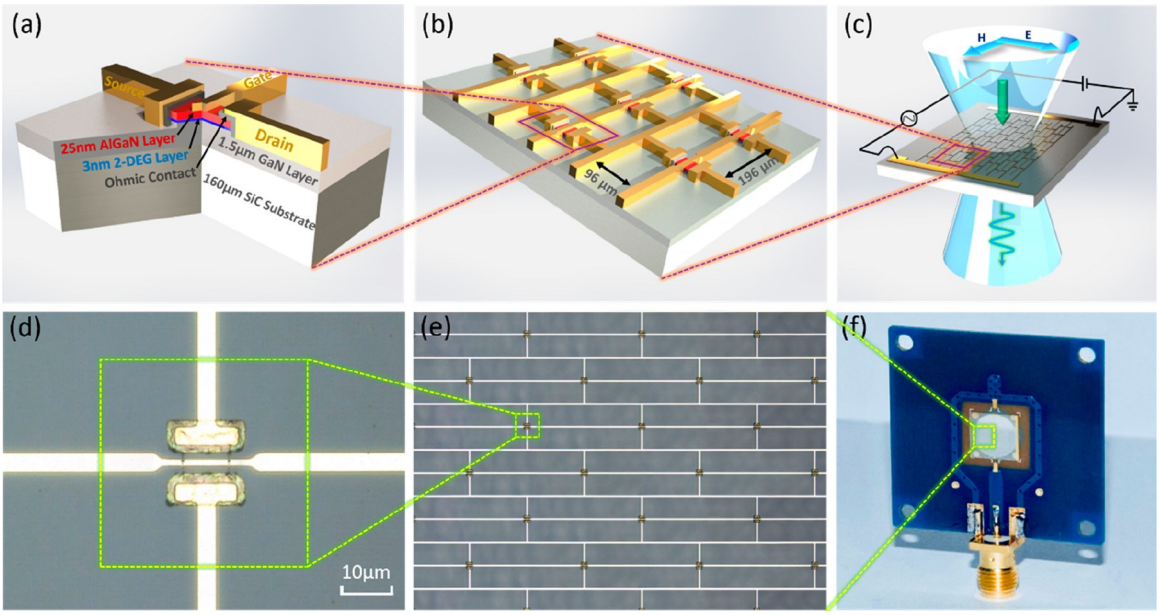

Figure 4.9: Active hybrid 2DEG/MMs optoelectronic THz modulator exhibiting wide amplitude modulation. Source (Yaxin Zhang et al., 2015)

much easier than the dynamic tuning of f_{res} or manipulation of polarization, where their design becomes more complex due to the existence of dispersive materials (Riccardo Degl'Innocenti, H. Lin, and Navarro-Cía, 2022). This modulation scheme is an essential element in any communication system including on-off keying (OOK), amplitude shift keying (ASK), or quadrature amplitude modulation (QAM) (Tadao Nagatsuma, Guillaume Ducournau, and Cyril C Renaud, 2016). Active AM has been achieved in both transmission and/or reflection configurations using a variety of active materials such as semiconductors, 2D materials including graphene or tungsten disulfide (WS2), carbon nanotubes, thermally change materials including vanadium oxide (VO_2) or MEMS, liquid crystals, and superconductors (Riccardo Degl'Innocenti, H. Lin, and Navarro-Cía, 2022). Improvements in THz modulators are mainly concentrated on the modulation speed and depth for both amplitude and/or phase (L. Wang et al., 2019). The speed of devices is another important factor for both communication and real-time imaging communities to bring their applications out of the research labs. Other difficulties that are worth mentioning include power consumption, wall-plug efficiency, footprint size, and fabrication complexity. Power consumption and driving voltages will determine the boundaries for designing future mobile devices.

A large extinction ratio in amplitude and phase was achieved by integrating 2DEG as an active element with a top-gated MMs array shown in fig. 4.9 (Yaxin Zhang et al.,

2015; Y. Zhao et al., 2019a). In this work, the operational transition capability between the single unit-cell to collective states was experimentally demonstrated reporting up to 93% in AM depth. This interplay scheme of states reduces the parasitic capacitance of dipole modes leading to a large depth of modulation. Reduction of parasitic capacitance and resistance values enhanced the modulation speed of this hybrid MMs structure to >GHz without changing the total dimension of the MMs array. These achievements had a positive impact on the practicality of this approach. Using the same materials but slightly modifying the MMs design, spectral phases at dual-f_{res} THz frequencies were continually tuned by >137$^{\text{o}}$ (Yaxin Zhang et al., 2019).

Several techniques and active materials have been investigated for the purpose of enhancing THz wave manipulations. Metallic metamaterials combined with semiconductors were demonstrated for THz wave amplitude modulations. The active material was either a bulk semiconductor (H.-T. Chen et al., 2006) or bi-dimensional electron gas (2DEG) (Kleine-Ostmann et al., 2004a). When using a bulk semiconductor as an active medium, amplitude modulation of THz waves was successfully achieved via electrostatic gating but with a modulation speed not exceeding several kHz. Top-gated metamaterials with 2DEG as an active medium were fabricated in a nested arrangement reporting about 93% of amplitude modulation (Yaxin Zhang et al., 2015; Y. Zhao et al., 2019a). This high extinction ratio is attributed to the collective contributions from all resonators as an array rather than the single unit-cell state. Electrical connections of the collective resonators were designed with the consideration of reducing the parasitic capacitance covering the same footprint. Consequently, the reconfiguration speed can reach a couple of GHz without affecting the spacial coupling of EM. Temperature-controlled MMs array designed on VO_2 reported achieving ∼35% of AM depth at f_{res} by varying the device's temperature. The same device was tested by THz pumping revealing the relaxation lifetime of the carriers in the order of a few ps, which makes this approach suitable for ultrafast reconfiguration speed. This latter fact suggests that the speed of THz modulators is limited by the material of the integrated active element rather than the total MMs array design. In (Yaxin Zhang et al., 2014), another hybrid MMs/VO_2 device was tested by photoexcitation using an external 808 nm CW laser pump achieving ∼80% of AM depth at a wide range of THz frequencies. When the CW laser pump was modulated by a square-wave voltage applied on an acoustic-optic modulator, the amplitude of the detected signal was significantly decreased at an RF frequency rate of ∼1 MHz.

4.2.2 Phase modulation

The THz-TDS measurements technique can reveal not only the spectral amplitude but also the phase changes of the transmitted THz light. Early demonstrations of THz

phase modulators had presented limitations with regard to operational temperature and reconfiguration speed (Hou-Tong Chen et al., 2009). In 2000, the earliest approach to establishing a THz phase shifter was accomplished by implementing a quantum well semiconductor device operating at cryogenic temperatures (Libon et al., 2000; Kersting, Strasser, and Unterrainer, 2000). Later in 2006, a THz phase modulator based on liquid crystal operating at low speed was demonstrated (Hsieh et al., 2006). Amongst the first attempts to implement the metamaterial for a realization of THz phase modulation was reported in (Hou-Tong Chen et al., 2009). Metallic split resonators (SRRs) metamaterial array fabricated on n-GaAs substrate achieving about $\pi/6$ rad of relative phase shifts with 16 V of a biasing voltage. Split-resonators (SRs) metamaterials shunted by two-dimensional electron gas (2DEG) were fabricated on top of a GaN substrate (Yaxin Zhang et al., 2015). This device can be biased by grounding the metallic SRs while grounding the top-gating stripes. This THz modulator achieved a relative phase shift of 1.19 rad with only 6 V of a gate voltage at 0.352 THz of a resonant frequency, but gases are well-known for their slow reconfiguration speed. Without using any metamaterial structure, graphene-based

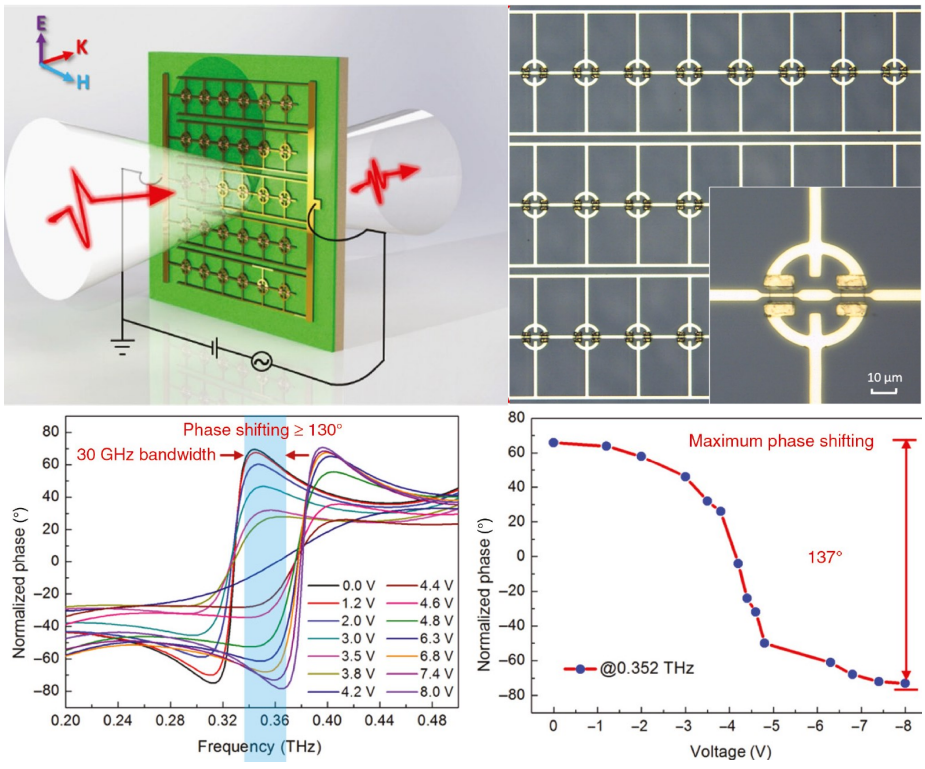

Figure 4.10: Active hybrid 2DEG/MMs optoelectronic THz modulator exhibiting wide phase tuning (Yaxin Zhang et al., 2019).

THz modulators were transferred on metals and isolated by an Ion-gel as reported in (Kakenov et al., 2018). This structure demonstrated the ability to achieve a complete π rad of relative phase shifts when driving the device between 0 V to only 2 V at a resonance of 1.2 THz. Consequently, electrostatic gating the graphene conductivity had attracted researchers because of its robustness, versatility, high mobility, and ultrafast responses.

Dynamic phase tuning can be achieved in a variety of different methods including heat effect or photoexcited approach. Remarkable amplitude and phase modulations were achieved using all-electronically controlled VO_2 integrated with MMs devices reporting almost 99% in amplitude modulation depth and 90° in relative phase shift (Hu et al., 2021; M. Jiang et al., 2021). These incredible performances are achieved by implementing different shapes of aluminum SRRs with silicon nitrite (Si_3N_4) as a dielectric layer fabricated on various substrates. Integration of Vanadium dioxide (VO_2) with MMs has also achieved a large active manipulation at THz frequencies due to large phase transitions of VO_2 when driving the device under controlled temperature as shown in fig. 4.10. Another phase change element that can be integrated with MMs is chalcogenides, namely $Ge_2Sb_2Te_5$ and abbreviated as GST. In (Pitchappa et al., 2019), a thin film of GST was integrated with asymmetric SRRs exhibiting Fano-like and wide dipole resonances in the THz regime. Both f_{res} are damped via thermal effect induced by the optical pump and electrically applied current. The achieved AM depth was reported almost 100% defined with respect to the peak-to-peak strength of the Fano resonance. The reconfiguration speed of this device was measured by optically pumping with a fluence of 636.6 μJ/cm^2 and THz probing reporting a recovery lifetime of approximately 19 ps. Consequently, the switching speed of GST/MMs devices is reported in the order of tens of GHz (Pitchappa et al., 2021a). Similarly, the fast carrier relaxation lifetime of Germanium (Ge) was found to be in the order of a few ps in the timescale. Therefore, the integration of the Ge with metallic closed-ring resonators (CRR) and two pairs of SRRs was fabricated in a MEMS device. This MEMS device was able to engineer the group velocity dispersion of the transmitted THz radiations by taking advantage of the THz waves transparency region between coupled dual-f_{res} (Sun et al., 2020). In this design, different polarization states would excite only one of the two resonators resulting in 4 different f_{res}. More details on active THz modulators are reported in (Riccardo Degl'Innocenti, H. Lin, and Navarro-Cía, 2022).

4.2.3 Our approach

Gated MM resonators shunted by graphene have been deployed to actively modulate the beam of THz light, i.e. amplitude, phase, and polarization, with the potential of achieving a high speed of modulation (Stephen J. Kindness et al., 2019; Stephen J.

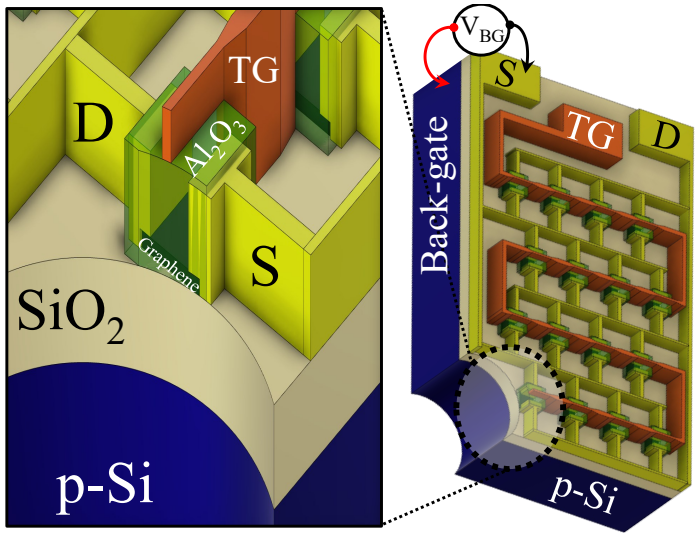

Figure 4.11: Schematic view of a single metamaterial/graphene resonator and a complete array structure.

Kindness et al., 2020a; Stephen J. Kindness et al., 2018). Recently, this approach has been used also with THz laser sources and for frequency combs stabilization (Burghoff et al., 2014; Rösch et al., 2015) due to its capability to control and alter the optical dispersion (F. Wang et al., 2017; Mezzapesa et al., 2019a). Our approach is to implement graphene and metamaterial fabricated on top of a SiO_2/p-doped Si substrate. Thus, the graphene conductivity can be altered by optical pumping or electrostatic gating. This novel structure consists of source and drain metallic SRs forming a capacitor-like shape along with a top-gate stripe centering the SRs' gap spacing. The salient feature of this structure is that it gives the advantage to decouple the three biasing connectors from each other, i.e. source, drain, and gates. These double-gated resonators can not only modulate THz radiations but also detect the modulated waves as well by carefully monitoring voltage or current changes across the graphene sheet. Thus, a detection technique can be used by fabricating the exact same structure with minimal differences in the electric configurations. In this section, we basically exploit the strong amplitude and phase anisotropy of this new architecture to achieve THz wave modulations by the electrical bias of the graphene sheet.

4.2.4 Static characterizations

A dipole resonance is always induced in a metallic wire based on the geometry of the metamaterial structure. In this section, spectral contents of the metamaterial loaded with graphene are first investigated without any applied voltages. In order to

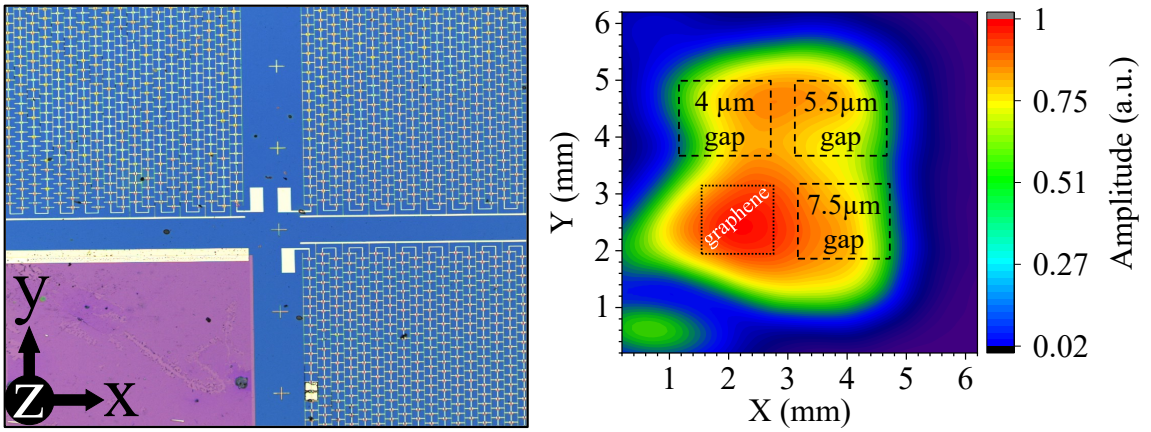

(a) (b)

Figure 4.12: (a) Optical microscopic picture of the tested metamaterials showing four different arrays. (b) Maximum E-field intensity for THz pulses transmitted through the device acquired whilst scanning the sample at the focus of the optical system.

maximize the modulation speed, particular attention was devoted to a preliminary optimization of the design by considering the reduction of capacitances, resistances, and footprint Y. Zhao et al., 2019a; Hou-Tong Chen et al., 2006; Nouman et al., 2016; P. Q. Liu et al., 2015. Our approach consists of designing double-gated MM/graphene devices fabricated on top of a commercially available SiO_2/p-doped Si (300 nm, 500 μm) substrate. The Si substrate is a slightly p-doped wafer, to allow back-gating. Details on the design and fabrication of the devices are explicitly described in Chapter 3 and plotted again in fig. 4.11 for completeness. The total size of an array is 1.3×1.2 mm^2, and it comprises 22×20 identical interdigitated SR units electrically connected in a nested arrangement. Three arrays were fabricated on the same chip with capacitive dipoles gap distances of 4, 5.5, and 7.5 μm. Additionally, three different devices were fabricated with ALD thicknesses of 50, 95, and 150 nm which are to be named as device 1, device 2, and device 3, respectively.

Device 3 shown in fig. 4.12a was tested with a THz-TDS setup in the transmission configuration as plotted in fig. 4.4a. The mounted device on a PCB board was placed on a rotational holder, which can be rotated by 360° with a 1° of rotational angle precision. Both the THz transmitter and detector are set to the horizontal polarization state, i.e. the x-axis. The device is positioned at the minimum spot size of the 4-f lenses system. It can be rotated with an angle θ with respect to the horizontal axis, i.e. the x-axis. Rotating the devices by $\theta = 0°$ would excite the LC dipoles resonance with co-polarized incident THz radiations along the x-axis. $\theta = 90°$ angle is to induce carriers with perpendicular polarization (cross-polarization) along the y-axis. The samples are first scanned spatially in order to locate the designated area

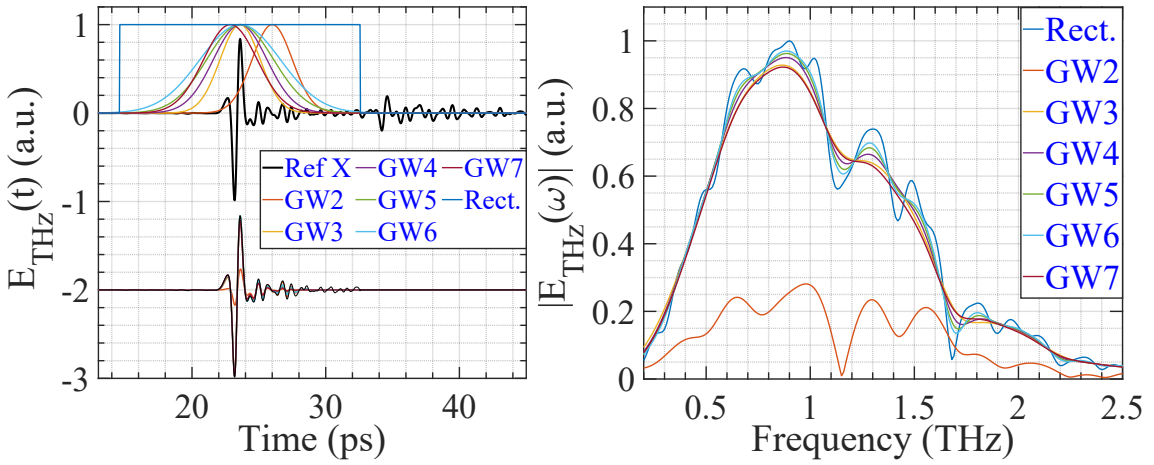

(a) (b)

Figure 4.13: THz E-field passing through the graphene reference for different applied filter profiles summarized in table 4.1 in the time-domain (a) and their corresponding spectra (b).

Table 4.1: Parameters of rectangular (Rect.) and Gaussian (GW) filters used for signal processing in the time domain. Widths of the Gaussian profiles are measured at the FWHM.

Name	**Centered Peak (ps)**	**Width (ps)**
Rect.	23.6	16
GW2	26	4
GW3	23.6	4
GW4	23.6	5
GW5	23.6	6
GW6	23.6	7
GW7	22.87	4

of the reference (graphene patch) and then the 7.5 μm gap spacing array. A large graphene patch covered with ALD fabricated on the same chip is used for referencing during post-processing. A 6×6 mm^2 area of the sample positioned at the focus of the optical system was scanned with a step size of 0.2 mm as shown in fig. 4.12b. The THz spot size was defined as approximately 1.3 mm by using a pinhole placed at the focal plane of the setup. The time-domain waveforms are acquired with a window of 100 ps corresponding to a 10 GHz frequency-domain resolution.

To eliminate the FP effect during post-processing, the first temporal pulses are selected by applying a unity rectangular filter (Rect.) or several Gaussian windowing (GW) following the parameters summarized in table 4.1. Additionally, the 100 ps width of the rectangular window can be applied to consider the entire temporal waveform. The time-domain traces of THz pulses are shown in fig. 4.13a propagating through the graphene sheet used for normalization without any bias or purge. The filtered temporal pulses are offset for comparison purposes only. The other lower amplitude pulses are approximately 11 ps away from the main pulse corresponding to reflections from the Si substrate thickness of about 500 μm. Spectral amplitudes of the THz E-fields used as a reference are plotted in fig 4.13b. The E-field amplitudes filtered by the rectangular function have a strong ringing in its spectra due to convolution with the *sinc* function in the frequency domain. Additionally, dips at >1 THz frequencies due to atmospheric absorption are enhanced. Moving to the 7.5 μm gap distance array, the resonators are tested with two rotational angles $\theta_{SR} = 0^o$ and 90^o to excite both the co- (E_x) and cross- (E_y) polarization waves as plotted in fig. 4.14a with no bias nor purge. The processed THz pulses in the time domain are offset for comparison purposes only. Peaks of the temporal THz pulses occurring at different moments are due to moving the device at different z-axis locations.

During post-processing, the acquired THz pulses are normalized to the reference and Fourier transformed to the frequency-domain following eq. 4.13. Regardless of the type of windowing used, a strong resonance clearly appears at 0.75 THz for the co-polarized E-field with about -19 dB of absorption strength as shown in fig. 4.14b.

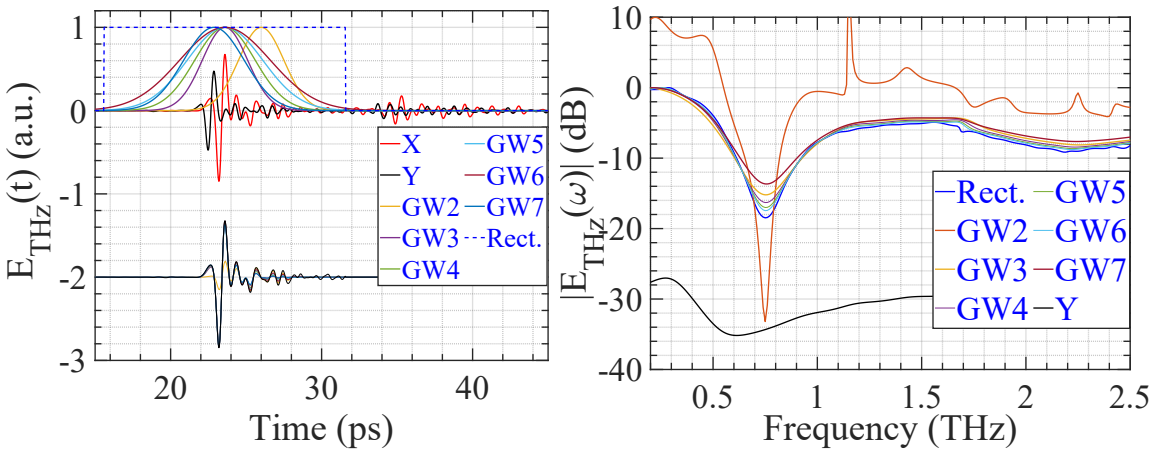

(a) (b)

Figure 4.14: THz E-field passing through the metamaterials for different applied processing filters and the co- and cross-polarizations (X and Y) in the time-domain (a) and their corresponding spectra normalized to the reference (b).

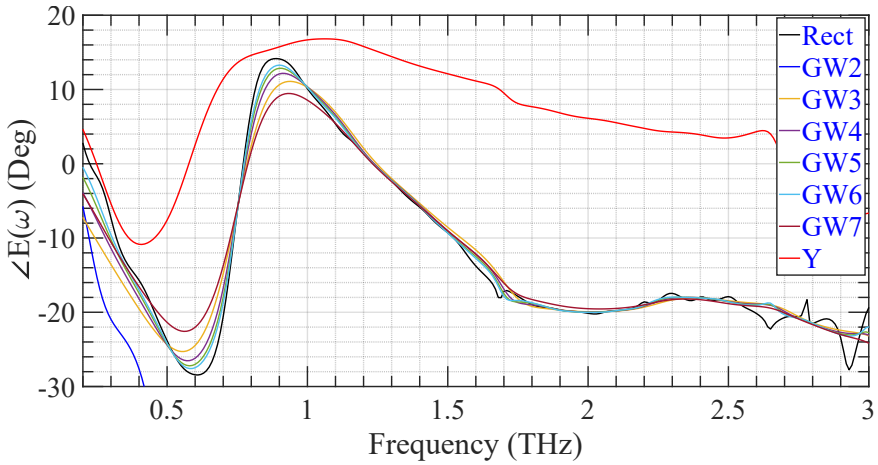

Figure 4.15: Extracted spectral phase shifts for the THz E-fields passing through the metamaterials for co- (all different colors but the red curve) and cross- (red curve and denoted by Y) polarized waves using different applied filters without any bias.

This resonant frequency is smaller than the simulated one by about 50-80 GHz, mostly due to unmanageable error margins during the fabrication. On the other hand, there is no distinguished resonance for the cross-polarization when the device is rotated by $\theta_{SR} = 90^{o}$ as it is expected and shown by the black curve in fig. 4.14b. The filter GW7 is applied for the cross-polarized THz E-field because of different time-domain peaks. When exciting the metamaterials with the co-polarization fields, frequencies smaller than the resonance accumulate smaller spectral phase shifts while the larger frequencies exhibit larger phases following the real part of refractive index as shown in fig. 4.15. The cross-polarization has a spectral phase that has a positive slope for frequencies above 0.4 THz till reaching its maximum at the resonant frequency of 0.75 THz, where then slowly decays as indicated by the red curve in fig. 4.15. Consequently, the maximum phase difference between the co- and cross-polarizations occurs at around 0.68 THz. The spectral phase is not significantly affected by the selected windowing profiles (different GW and Rect. curves in fig. 4.14a).

4.2.5 Dynamic modulation

Depletion of graphene conductivity separates the source and drain wires corresponding to a split dipole resonance in the shorter identical resonators. In contrast, increasing carrier concentration shifts the resonant frequency towards lower frequencies resulting in the manipulation of THz radiations. The double-gate metamaterial modulator has four independent electrical configurations, i.e. source, drain, top-gate, or back-gate. As mentioned before, source and drain pads are shunted by graphene to manipulate

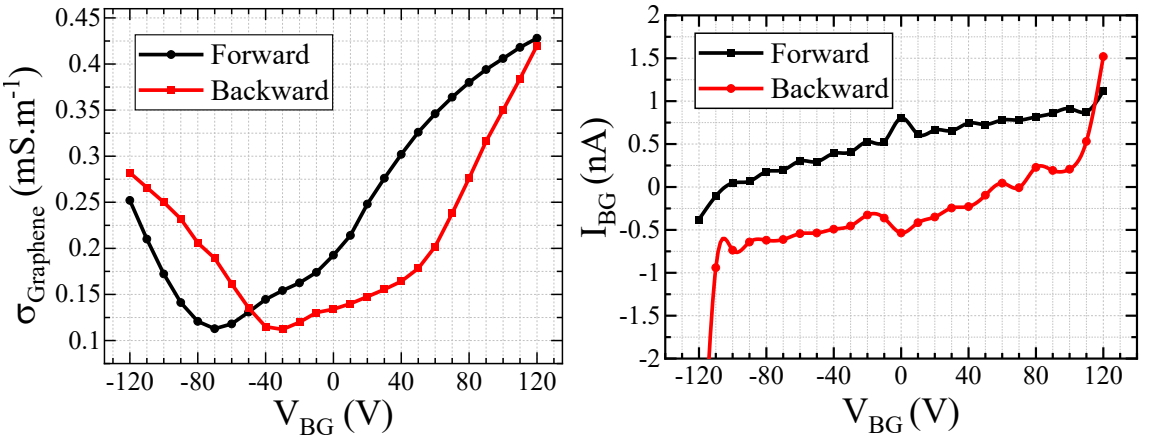

Figure 4.16: (a) Source/drain current through graphene sheet for different back-gate voltages. (b) Leakage current towards back-gate.

the graphene conductivity (σ_{graphene}) around its Dirac point affecting its Fermi-energy levels. The back and top gates principally work the same, but the key difference is the dielectric layer thicknesses. Graphene sheets to p-doped Si substrate (back-gate) are isolated by the SiO_2 thickness of about 300 nm, while graphene patch to top-gate stripe is encapsulated with different ALD thicknesses for the devices 1, 2, and 3. Biasing through the back-gate can support a wider range of applied voltages and is more robust, but it has higher risks of shortage. In contrast, driving metamaterials through the top gate can have access to the same range of $\sigma_{graphene}$ with less demanding conditions. Moreover, devices driven by the top gate are less susceptible to shortages and faster in speed which makes this electric configuration more favorable for fast data transmission in telecommunication applications. The range of $\sigma_{graphene}$ accessible experimentally is examined by applying a fixed voltage between source and drain (V_{SD}= 5 mV) while varying the applied voltages through the gates, which is denoted by V_{BG} for the back-gate configuration. Current passing between source to drain (I_{SD}) through the graphene sheet and leakage current towards the gates (I_{BG}) are carefully monitored by a DC power supply from Kethley, model 2450 source-meter-unit (SMU). Fig. 4.16a shows the absolute values of σ_{graphene} calculated using the following formula: $\sigma_{\text{graphene}} = (I_{\text{SD}} \cdot d)/(V_{\text{SD}} \cdot W)$, where both the source to drain distance (d) and width of the tested graphene patch (W) are identical (i.e. 1.2 μm). For various V_{BG}, continuous large patch of graphene conductivity ($\sigma_{graphene}$) is manipulated with an estimated Dirac point voltage (V_{Dirac}) of 60-70 V for forwards gating through the back-gating as illustrated by the black circled curve in fig. 4.16a using about a 50 nm thickness of ALD device. The asymmetrical Dirac curve is due to the differences in

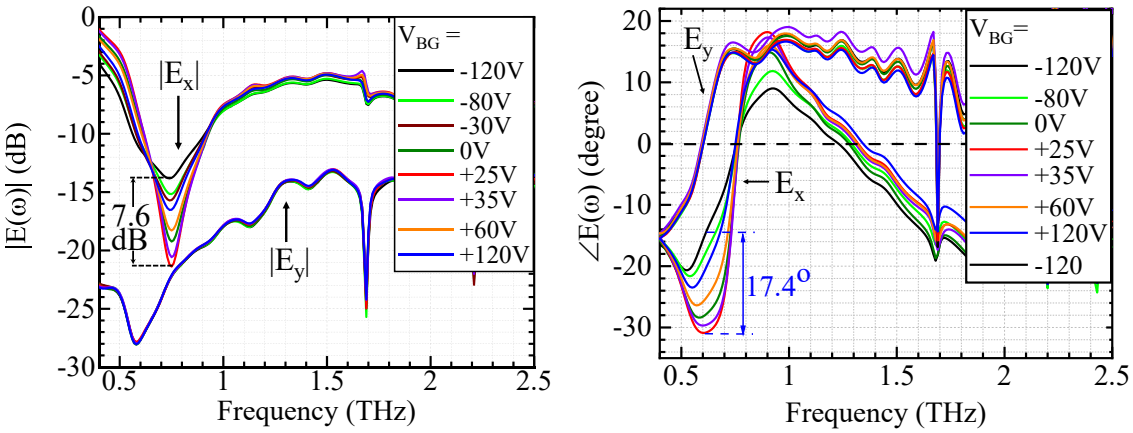

(a) (b)

Figure 4.17: THz-TDS experimental measurements of the transmitted E-field spectral amplitudes (a) and phases (b) at different V_{BG}.

the mobility of holes and electrons (Stephen J. Kindness et al., 2020a). Graphene patch driven with reverse bias voltages has a shifted V_{Dirac} to 30 V representing the graphene's hysteresis condition as indicated by the red squared curve in fig. 4.16a. This hysteresis in $\sigma_{graphene}$ is mainly due to trapped carriers in the dielectric layer (Alexander-Webber et al., 2016). Resistivity between source and drain (R_{SD}) varies with the applied back-gate voltages peaking at about 8.8 kΩ, which corresponds to the graphene conductivity at its Dirac point (minimum $\sigma_{graphene}$ = ∼0.1 mS). In separate all-electronic measurements discussed in the next section (4.3), the V_{Dirac} is found to be at approximately 10 V when driving the modulator through the top-gate using device 3 as mentioned in (Zaman et al., 2022a). This range of $\sigma_{graphene}$ and V_{Dirac} are very well aligned with measurements previously reported as in (Zaman et al., 2022a; Zaman et al., 2022b; Zaman et al., 2023). The I_{BG} is measured to be ∼100 times smaller than the I_{SD} leading to the back-gate resistivity (R_{BG}) of a couple of GΩs as shown in fig. 4.16b when biasing the graphene patch in forward and backward directions.

Active manipulation of incident THz waves is demonstrated by applying a range of different V_{BG} between -120 V to +120 V to electrostatic gating graphene conductivity around the Dirac point. The dynamic behaviour of device 3 is examined by a THz-TDS setup in the transmission mode as shown in fig. 4.4a and schematically in fig. 4.1. The source and drain pads are both connected to the negative port of an SMU while the back gate is connected to the positive terminal. This set of measurements was acquired without any N_2 purging. The detected THz pulses are normalized with the graphene patch reference following the post-processing steps mentioned previously

in Section (4.2.4). By considering only the first temporal pulses using the 16 ps rectangle window, an extinction ratio of >7.6 dB is achieved in the amplitude spectra at the resonant frequency of 0.75 THz as shown in fig. 4.17a. The strongest resonance occurs when the device is driven by +25 V, which can be estimated as the V_{Dirac} as mentioned in (Jessop et al., 2016). When the graphene conductivity reaches its Dirac point, the two SRs are completely decoupled causing the strongest resonance mode (off-resonance). However, these two SRs emerges to one wire dipole as σ_{graphene} increases causing a blueshifted resonant frequency (on-resonance). This blueshifted resonance leads to a strong amplitude modulation depth when altering the graphene conductivity by electric gating only. If top-gating is used, amplitude modulation can be achieved around only 10 V of V_{Dirac} with a damping depth of >80% in the spectral amplitude. Almost no change is observed in amplitudes of the cross-polarized waves ($\theta_{\text{SR}} = 90^{\text{o}}$). Altering the complex refractive index of the device also changes the spectral phase of incident THz radiation. A continuous phase tuning of the co- and cross-polarization fields are illustrated in fig. 4.17b. Maximum phase shift occurs at 0.68 THz with $>17.4^{\text{o}}$ and 0.90 THz with $>10^{\text{o}}$, while the phase of the resonant frequency remains almost unchangeable. Hence, spectral amplitudes and phases can be almost independently controlled for various THz frequencies. When considering all the transmission and reflection pulses using a 100 ps temporal window, FP resonances are observed in the spectra with a free spectral range (ν_{FSR}) of about 90 GHz. Consideration of the energies from all temporal pulses is enhancing the depth of AM to >10 dB at 0.74 THz. Similarly, spectral phase tuning is also improved to exceed 27^{o} at 0.62 THz when considering the entire time-domain waveform.

4.3 All-electronic characterization

Reconfiguration speed is one of the figure-of-merit for the communication community. Switching back and forth between the on- and off-resonant states would determine the achievable modulation speed. Modulating around the strongest slop of the graphene conductivity could be the most effective method for using the metamaterial as THz modulators. For example, applying a modulating signal around V_{Gate}= 0 V can be used for the demonstration of OOK or QAM schemes of communication. Moreover, modulation speed is intensively scrutinized using an all-optical technique discussed in the next chapter (5).

In a separate set of experiments, the device is mounted on a high-speed circuit board in order to investigate its reconfiguration speed as mentioned in Section 3.4.5. For practical applications, the device is driven through the top gate, instead of the back gate, to allow for lower biases and for more robustness with respect to shortage and leakage currents. Hence, a wider voltage range is accessible for characterization. An RF signal, generated with an Agilent RF generator model N9310A, is mixed

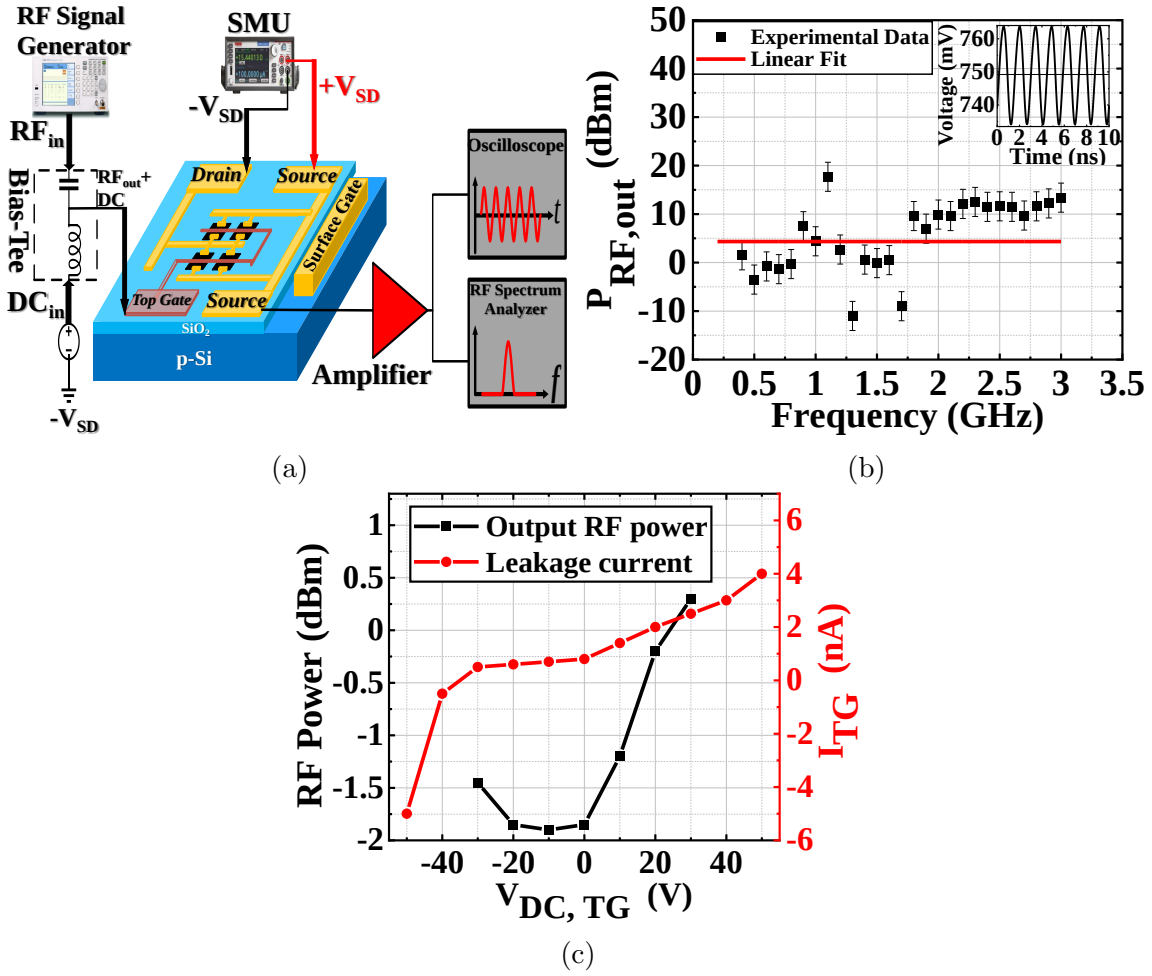

Figure 4.18: (a) Schematic of the RF electrical setup, (b) frequency response of the modulator (inset is the 700 MHz output waveform), and (c) output RF power for 750 MHz frequency and leakage current towards the top-gate for different DC biases.

with a DC voltage (V_{DC}) using a bias-tee (model ZX85-12G-S+ from Mini-Circuits). The importance of the applied DC voltage is to offset the input RF signal along the curve of Dirac point voltage. The $\mathrm{RF_{out}}$+DC signal is applied between the top gate and drain pads to modulate the graphene conductivity. The drain pad acts as a common ground throughout these measurements. The source ($+V_{\mathrm{SD}}$) and drain ($-V_{\mathrm{SD}}$) pads are connected separately to an SMU providing a fixed current of 700 nA. The modulated voltage between the source and drain pads is detected and fed to an external low-noise amplifier, model ZX60-83LN-S+ from Mini-Circuits, to boost its amplitude. The output RF signal is monitored by an oscilloscope and an RF spectrum analyzer from Rohde & Schwarz, model FS300. The RF electrical characterization

setup is illustrated in fig. 4.18a.

When driving the modulator with an input RF power of +20 dBm and an offset DC voltage (V_{DC}) of +20 V, the modulator shows a well-established response to all frequencies up to 3 GHz as plotted in fig. 4.18b. It should be noted that the output RF power fluctuations at different frequencies are due to impedance mismatch, and the speed limitations are subject to instrument availability. The output waveform for a frequency of 700 MHz is plotted as an inset in fig. 4.18b showing a DC voltage offset of ∼750 mV which corresponds to the potential voltage of source-drain. fig. 4.18c reports the modulator's response at a fixed frequency of 750 MHz for different input V_{DC} biases. The output RF power is decreasing as $V_{DC,TG}$ increases till reaching its minimum around the Dirac voltage, ∼10 V, providing a good agreement with the results reported previously in Section 4.2.5 and illustrated in fig. 4.18c. The output RF power attenuation with different input driving DC voltages is to be ascribed to the change of graphene conductivity. The Dirac voltage is found around 10 V with 150 nm thickness of Al_2O_3 gate dielectric which is consistent with the 25-30 V voltages required to reach Dirac point with the back gate where the SiO_2 dielectric thickness is 300 nm. Please note that the leakage current towards the top gate (I_{TG}) is ∼100 times smaller than the I_{SD} as shown in fig. 4.18c. It is important to mention that the RF signal generator, bias-tee, external amplifier, oscilloscope, and RF spectrum analyzer are only limited to a few GHz. This device could operate up to tens of GHz according to our model mentioned in Section 3.2, and therefore a different approach should be envisaged either all-optically or with high-frequency vector network analyzers (VNAs).

4.4 Conclusion and outline

In this chapter, we present an efficient and ultrafast modulator operating in the THz range based on an MM array loaded with graphene. A maximum amplitude modulation depth of >80% and phase modulation of >17° were reported around the resonant frequency of 0.8 THz. When considering all temporal pulses, the depth of amplitude and phase modulations increase to >90% and >27°, respectively. The high performance of the device was achieved without affecting the measured reconfiguration speed which was reported to reach at least 3 GHz, limited only by the available instrumentation. This represents a progress of 10 times higher reconfiguration speed compared with previous similar all-electronic THz devices integrating graphene as a functional material. These results represent a breakthrough for many applications where fast and efficient THz circuitry is required, such as THz wireless communication or quantum electronics for active modelocking of QCLs.

Purging the THz-TDS setup with dry air or nitrogen could improve the accuracy of the dynamic modulation depths. Overcoming the issue of multiple Fabry-Pèrot resonances is feasible, e.g. by implementing anti-reflection coating. On the other

hand, processing all transmission/reflection E-fields is similar to the case of exciting the metamaterial device with continuous wave (CW) THz sources such as UTC photodiodes or RTD lasers. Depths of modulations may be improved by increasing the number of resonators in the same array's area, in other words, designing an array with more condensed resonators covering the same area. Power insertion losses could be reduced by fabricating the metamaterials on an undoped Si substrate since this double-gated structure can be derived using the top-gate stripes only. Encapsulation materials of choice for the graphene sheet may play a major role in the range of graphene conductivity accessible experimentally.

Spectral phases are actively tuned by changing the real part of the refractive index (n). Thus, changes in the refractive index of the two identical split resonators (SRs) are essential in order to maximize the relative phase shifts. Since the graphene patch is not in complete contact with both dipoles as clearly measured by the resistivity between source-drain ($R_{\mathrm{SD}} =\sim 1M\Omega$) mentioned in Section 4.3, it is most likely that the graphene patch is affecting only one of the identical SRs limiting the achieved continuous tuning of the spectral phase. As a result, a significant difference between the simulated and practical phase modulation depths is clearly observed.

Chapter 5

Ultrafast modulation of the MMs/graphene modulator

5.1 Theory

5.1.1 Optical pump/THz probe experiments and setup

Light controlled by light is the main principle of an all-optical modulation scheme where signal processing allows for full-photonic manipulation. Using all-optical measurements can eliminate the need for electrical-to-optical conversion, hence it is a direct measurement without all the bottlenecks that might be provided by electronics, e.g. parasitic capacitance, delay time dephasing, etc. A variety of all-optical techniques have been presented such as optical doping, thermo-optic effect, and Kerr effect (Ziming Wang et al., 2021). The optical doping mechanism is based on photoinduce charges of the illuminated materials via light modulation. In semiconductors, carriers can be generated by photo-inducing when excited via photon energies larger than the bandgap. The dielectric constant of the illuminated semiconductors can be expressed by the Drude model (Ziming Wang et al., 2021). Thus, a change in electron-hole results in a tuning of modulation depth. At the same time, this large separation could reduce the response speed. A combination of large carrier density in 2D materials and photonic resonance elements has been widely implemented to investigate the fast modulation speed and achievable extinction ratio for various all-optical THz modulators. OPTP spectroscopy is a time-resolved technique and can therefore be used to probe charge carrier dynamics in contrast with THz-TDS.

In addition to the previous THz measurement techniques, optical pump THz-probe spectroscopy (OPTP) has been widely used to investigate the ultrafast relaxation lifetime and recombination dynamics of photo-excited carriers of various epitaxial

materials such as graphene (Jnawali et al., 2013; Winnerl et al., 2013; Pitchappa et al., 2021b; George et al., 2008; Shi et al., 2014). Optical pumping can be generated in the form of continuous, pulsed, optical rectification, transient currents, or mechanical excitation (Patil et al., 2022). In OPTP measurements, the THz E-field passing through a medium is detected for various delay times between pump and probe pulses. The decay of the photoexcited carriers gives the relaxation and recombination lifetime (Lloyd-Hughes and Jeon, 2012). Therefore, the OPTP technique is important to retrieve carrier dynamics of the active materials (e.g. graphene) to investigate the ultimate reconfiguration speed. Additionally, we wanted to find an intrinsic physical limits to our measurements. We wanted to verify what was reported in literature, the few ps speed. In literature, this was achieved only on large area and more of a material study. Here we are performing a device study, to see if after all the processing still graphene's ultimate limit is there. The OPTP setup is a modification of the THz-TDS system, but the fs optical radiation is redirected by a third beamsplitter (BS2) into the optical pump path (a third optical path). The optical pump propagates to under-testing materials by a second chopper (C2) and a moveable mechanical delay stage (D2). The third path is to introduce time delays between the optical pump and THz pulse (Joyce et al., 2016). A detailed description of the OPTP setup can be found in (Joyce et al., 2016; Ulbricht et al., 2011).

In this chapter, the optical pump THz probe (OPTP) measurements were conducted in a collaboration with Dr. Rostislav V. Mikhaylovskiy's group at the physics department at Lancaster University. In his laboratory, the fs laser source from Spectra-Physics, Solstice, is the light source for the OPTP setup as illustrated in fig. 5.1. The laser source has a ∼40 fs pulse duration with 1 kHz repetition rates at 800 nm operational wavelength. ZnTe with <110> crystal orientation and 1 mm thick is used for THz probe generation and time-resolved detection in the electro-optic sampling. Two mechanical delay stages control the pump-probe optical path to introduce various arrival times at the sample with a >1 ns time delay (t_{pp}) and 40 fs temporal resolution. 90° gold-coated parabolic mirrors direct the propagation of both the pump and probe beams. The pump spot size illuminating the sample was set to 2.1 mm diameter by using suitable irises, while the THz spot was measured to be approximately 1 mm. The THz focal point is dependent on the frequency. However, we measured the THz spot size by the knife-edge measurement, which cannot distinguish the frequency dependence. Therefore, the OPTP beam size was defined as an indicative number for a broadband THz pulse as is common in time-domain spectroscopy experiments. Knife-edge measurements were performed for different relative positions with respect to the second parabolic mirror (PM) and retrieved the corresponding radius as shown in fig. 5.2b. The diameter of the spot size is < 1 mm at the focus. This latter task is important due to the error in positioning the sample precisely, and because of the frequency dependence of the spot size we preferred to

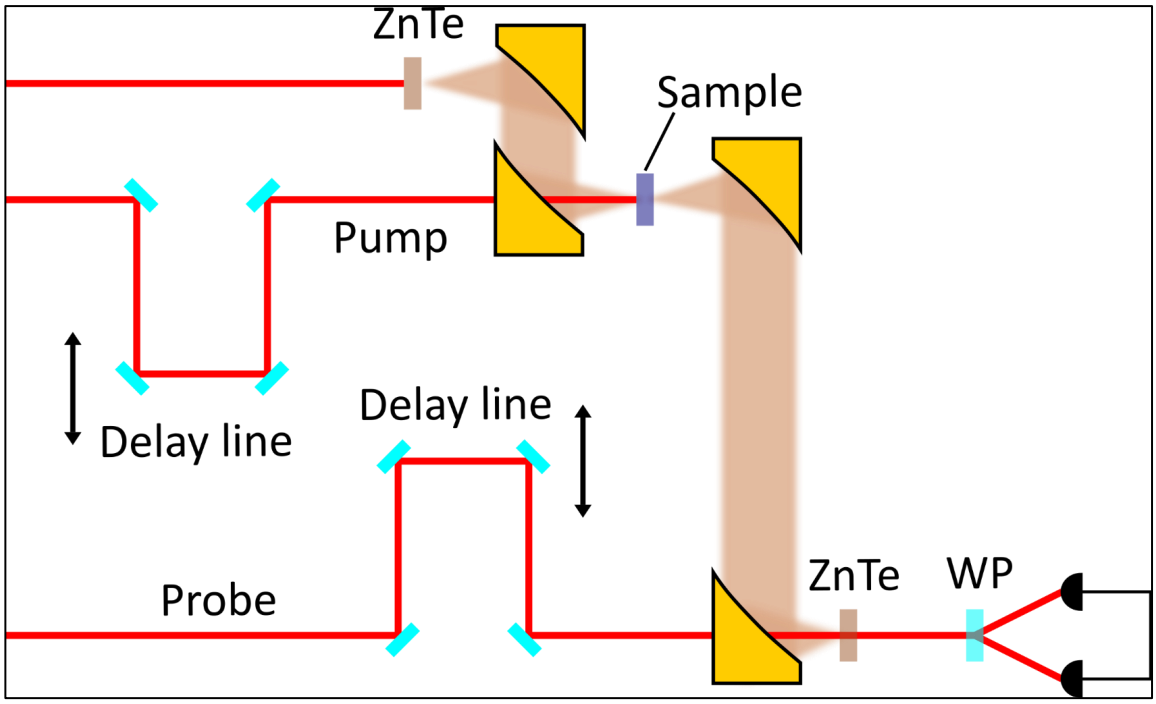

Figure 5.1: Schematic diagram of a typical optical pump/THz probe (OPTP) experimental setup, where WP is a Wollaston prism. It has been modified with permission from Yuichi Saito, Physics Department.

provide a value of approximately 1 mm.

The OPTP experimental apparatus is used to measure the photoconductivity induced at different pump/probe delays tpp, thus allowing the determination of the excitation/decay paths for the photogenerated carriers. To retrieve the entire THz waveform, the delay stage controlling the pump path remains fixed while varying the stage position of the probe. The THz probe measured by the OPTP system is plotted in fig. 5.2a, where the red line indicates the peak of the temporal THz pulse. The Fourier Transform of the THz temporal trace would reveal the spectral contents, as will be discussed in Section 5.2).

The measurements conducted in this chapter are: 1) standard THz pulse at different pump powers and fixed pump delay. It was done at different delays. 2) Fixed the time delay of the probe to the top and then perform a scan in the relative pump/probe delay.

The carrier dynamics of the double-gated graphene integrated with metamaterials are investigated using an OPTP setup. The modulator is fabricated on a p-doped Si platform. To break down this complex structure, photoexcitation lifetime in the Si is first introduced followed by the carrier dynamics in graphene. Finally, photogenerated

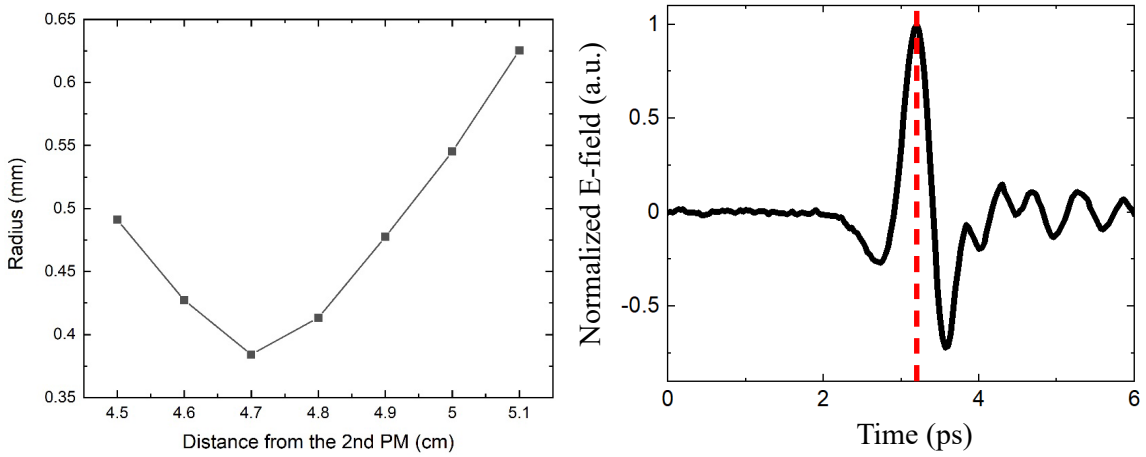

(a) (b)

Figure 5.2: (a) THz beam size measurements conducted by the knife-edge method. (b) Acquired temporal THz probe at a fixed photo-excitation delay showing its peak position.

carriers relaxation of the complex design is presented.

5.1.2 Silicon

The ultrafast carrier response study is of great importance for the semiconductor field, which is experiencing a continuous reduction in size towards the nanoscale regime. Electron diffusion speed can be in the order of a few ps in nanoscale transistors. This transit time scale is within the regime of electron and phonon scattering, as well as some of the bulk and surface photo-inducing processes. Various theoretical models have been introduced to explain the carrier dynamics in nanoscale devices such as Monte Carlo and hydrokinetic transport models (Sabbah and Riffe, 2002). It is well-known that hot-carrier diffusion is significantly influenced by the ratio of carrier momentum-relaxation time to energy-relaxation time. Carrier behaviour in crystalline Si has been extensively investigated by the ultrafast laser pump-probe approach. The study of carrier transmit time in Si has been demonstrated using several measurement modes such as transient reflectivity and/or transmission, transient-grating diffraction including two-beam self-diffraction, photothermal deflection, and time-resolved photo-emission (Sabbah and Riffe, 2002).

In all of these experiments, the electron-hole recombination occurs via excitation with strong laser radiation or two crossed pulses in the transient grating diffraction technique. The photo-excitation relaxation lifetime is then gradually recovered with a decay time tracked by a time-resolved probe. As a result, carrier recombination

lifetime in Si was studied. For the first time duration, <100 fs, phase states of the momentum-relaxing scattering and excited-carrier are separated due to carrier-carrier and carrier-phonon scattering (Sabbah and Riffe, 2002). The following time scale of approximately 100-300 fs is attributed to the carrier-carrier scattering defining electron/hole temperature. The following few hundred fs is a contribution of hot carriers because of electron-phonon scattering. Electrons-hole relaxation is fully recovered in bulk and surface recombination processes at longer time scales.

Details on the carrier dynamics of Si were investigated by (Sabbah and Riffe, 2002). The acquired photoinduced delays are shown in fig. 5.3a. Initially, there is a small, sharp increase in reflectivity (labeled A) followed by a much larger pulse-width limited decrease (B). After this fast decrease, the reflectivity continues to decrease, but at a much slower rate (C). The reflectivity then begins to recover approximately 500 fs after the initial excitation (D). Fig. 5.3b shows data obtained from three of the samples with 120-ps scans. These data indicate the range of variation in the recovery of the reflectivity back towards its initial value for the native-oxide terminated samples.

5.1.3 Graphene

Carriers' charge density changes the steady-state properties of graphene near its Fermi-energy level, while the high-speed carrier dynamics can transport using high-energy external fields. The electron-electron and electron-phonon interaction in a monolayer of graphene layer was first studied in (Breusing et al., 2011; Brida et al.,

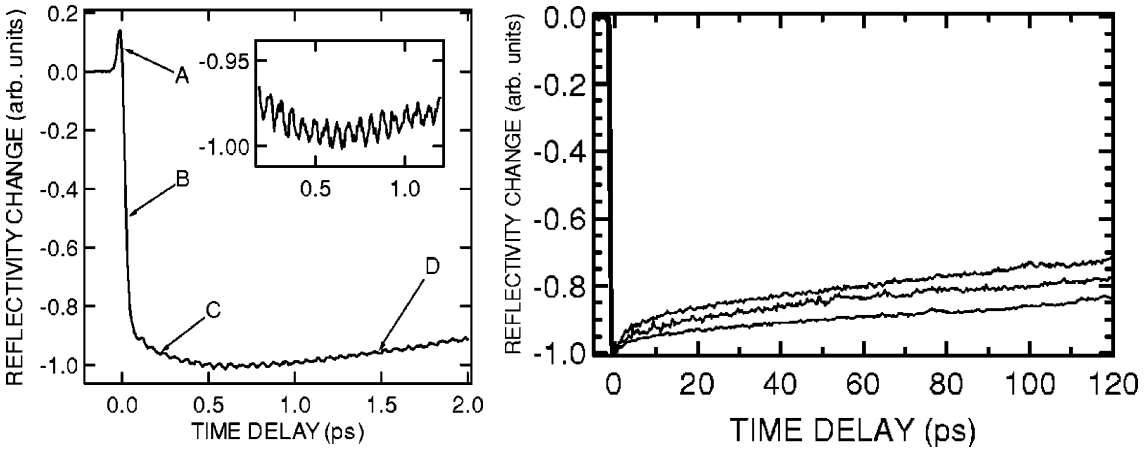

(a) (b)

Figure 5.3: Maximum of the THz temporal waveform at different t_{pp} from the optical pump for short (a) and long (b) delays. Inset in (a) illustrates coherent-phonon contribution to reflectivity (Sabbah and Riffe, 2002).

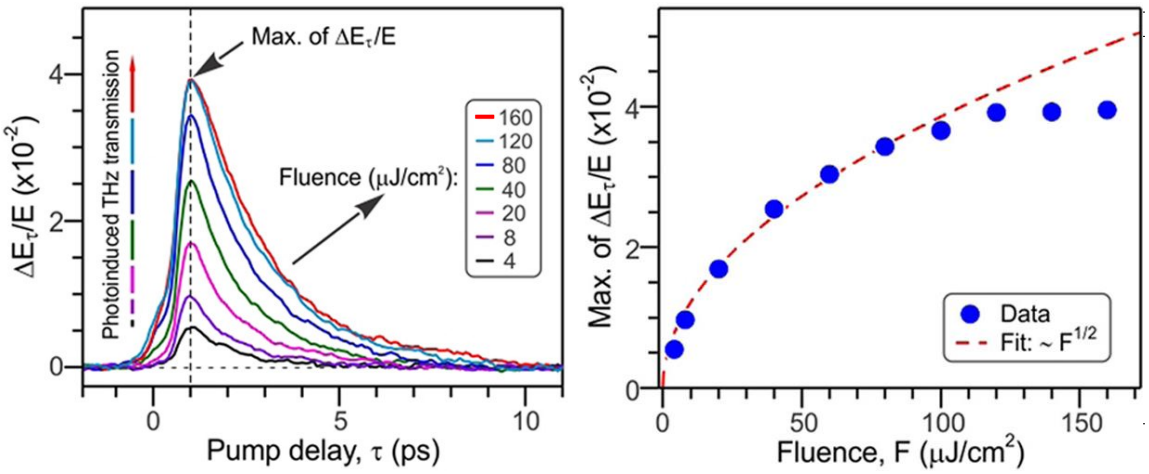

(a) (b)

Figure 5.4: (a) Temporal evolution of the change in the maxima of the transmitted THz waveforms normalized by the THz probe for different pump fluences. (b) The decay times are extracted by fitting the dynamics with a single exponential function. Source: (Jnawali et al., 2013).

2013; Gierz et al., 2013). Electrons dynamics of the interplay between interband and intraband defines the light absorption in a monolayer of graphene (Cinquanta et al., 2023).

The non-thermal distribution of carrier dynamics can induce interband absorption using an external excitation source of fs optical pulses and a CW laser light, and it depends on the Fermi energy position. The first stage of relaxation dynamics occurs due to thermalization with a defined temperature and a larger momentum spreading. This state takes place in <100 fs lifetime and can be described by electron-electron Coulomb scattering processes (Breusing et al., 2011; Brida et al., 2013; Gierz et al., 2013). This ultrafast carrier heating was first reported by (Gierz et al., 2013). In the following stage comes a cooling state with a quasi-equilibrium decay in terms of a hot temperature. With photoexcitation at the Fermi-energy <0.1 eV, interband ultrafast photoexcitation occurs increasing the THz absorption for intrinsic graphene. However, photoinduced carriers in doped graphene induced by Fermi-energy >0.1 eV reduce the THz absorption (Cinquanta et al., 2023). Increasing the doping level of graphene makes it more resistant to THz radiations, which is attributed to the hot-carrier multiplication. This latter phenomenon can also be expressed as an electron-electron scattering, which is faster than the electron-phonon scattering time as shown in fig. 5.4.

Thinner epitaxial graphene samples of monolayers and multilayers were grown on

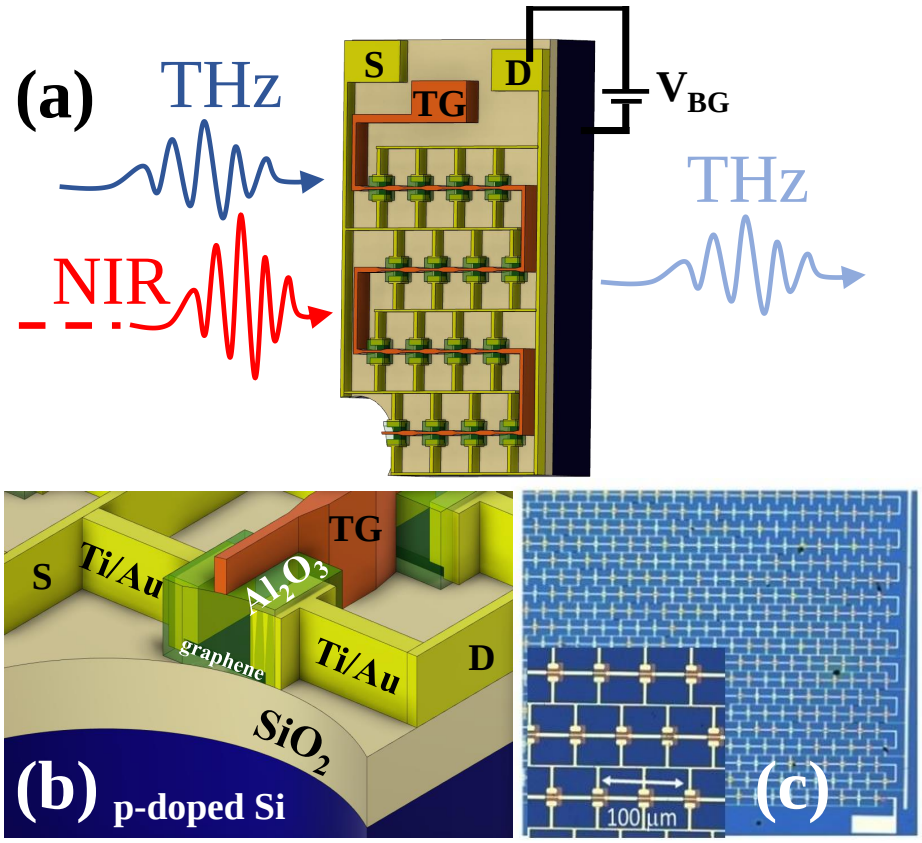

Figure 5.5: (a) Schematic of the OPTP experimental arrangement where the MM/graphene sample was kept at the Dirac point by acting on the back-gate voltage (V_{BG}). S, D, and TG represent the source, drain, and top gate of the device, respectively. (b) Cross section of the device and (c) optical picture of the top surface.

the Si-face of SiC wafers were reported by (H. Choi et al., 2009) observing a single exponential decay for the pump-induced conductivity. In the same measurements, it is found that the minority carriers dominate the pump-induced conductivity in highly n-doped graphene samples. Thus, the reported single exponential decay is attributed to the recombination of holes and a largely excitation-independent lifetime of 1.2 ps. This value of recombination time is consistent with Auger and phonon-mediated recombination (Rana et al., 2009).

5.2 Metamaterial/graphene based heterostructure

The challenge in this work is mainly the extraction of the carrier dynamic of photoinduced carriers in graphene small patches over a large background of the doped

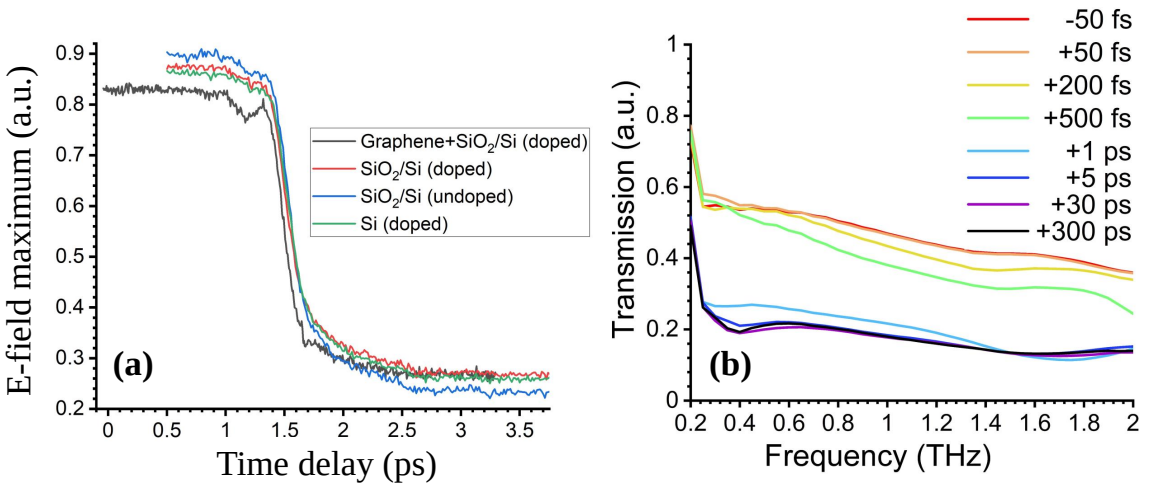

Figure 5.6: (a) Maximum THz E-field transmitted as a function of the time delay with respect to the pump pulse with fluence $\Phi = 0.18$ mJ/cm^2 for different materials. (b) THz transmission for the same pump fluence at different delays through the graphene uniform area on top of the SiO_2/Si substrate.

Si substrate because we want to be sure that after all the processing and fabrication we could observe the ultimate limit of graphene dynamics. Graphene patches integrated with MMs resonators are relatively small compared with the photoexcited spot size. The graphene/MM array is schematically plotted in fig. 5.5a and 5.5b, while fig. 5.5c shows an optical microscopic picture of the fabricated MM/graphene integrated array. After placing the device at the focal point of the OPTP system, a uniform graphene patch of 1.2×1.2 mm^2 is first investigated by fixing the THz probe pulse to its maximum peak and varying the optical pump delays. Fig. 5.6a shows the peak values of the THz temporal E-fields at different t_{pp} delays illuminated by the NIR pump with a fluence of 0.18 mJ/cm^2 compared with other substrates without graphene, e.g., SiO_2/Si (doped), SiO_2/Si (undoped), and Si (doped). All curves are shifted in time and normalized for comparison purposes only. Fast decays in the first sub-ps timescale are observed for all curves, but only the THz transmission through the graphene patch exhibits a complex and reproducible feature at a time scale below <2 ps on top of the predominant absorption in silicon. This complex behaviour is attributed to the presence of graphene. For the same NIR pumping fluence, the frequency-domain of all THz pulses at various t_{pp} are presented in fig. 5.6b passing through the graphene patch. The carriers' generation and relaxation lifetime of silicon is predominating the dynamic process, as expected. The fast decays in the THz probe intensity for the sub-ps timescale followed recovery lifetime exceeding 300 ps, not observed even after 1 ns as in other measurements, are in a great match with the OPTP measurements

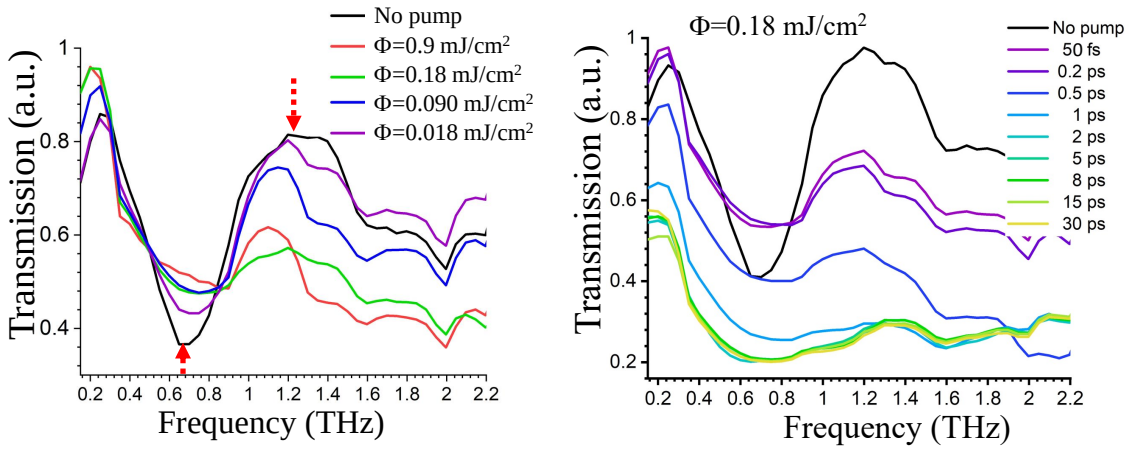

Figure 5.7: (a) MM/graphene THz transmission for different pump fluences, recorded at 200 fs time delay. (b) THz transmission curves acquired at different time delays with a pump fluence of 0.18 mJ/cm^2.

shown in literature and discussed previously in Section 5.1.2. These acquired data are being used as a reference for the signal processing of the THz pulses passing through the hybrid MM/graphene resonators.

The integrated MM/graphene device is electrically biased away from its Dirac point voltage, i.e. ∼80 V using Keithley (model 2450) source-meter, to ensure that the carrier transport is due to the optical pump. Various optical fluences are pumping the metamaterials ranging between $\Phi = 0.018$ to 0.9 mJ/cm^2 by swapping different neutral density filters. The spectral contents of the THz pulse passing through the array are shown in fig. 5.7a with a fixed $t_{pp} = 200$ fs and for various pump fluences. This time delay of t_{pp} is selected to appreciate the conductivity changes in both silicon and graphene. A clear resonance, at 0.75 THz, is observed without pumping the device while it gradually vanishes as the pump fluence increases. The photoinduced carrier dynamic in graphene significantly influences the resonance mode causing changes in graphene and Si conductivities, as well as Si absorption. The SR sub-wavelength mode is significantly overlapping with the substrate; therefore, the two effects are present at the same time, even though on a different timescale. For different t_{pp}, the spectral contents of the THz pulses passing through the hybrid metamaterials are shown in fig. 5.7b pumping with $\Phi = 0.18$ mJ/cm^2. The limited t_{pp} of 30 ps is only shown here since the resonance mode is fully damped after a few ps and the slow relaxation time afterward does not significantly add extra information.

Additionally, the entire THz spectrum experiences a similar but not exact behaviour after resonance damping. Fig. 5.8 reports the acquired optical pump/THz

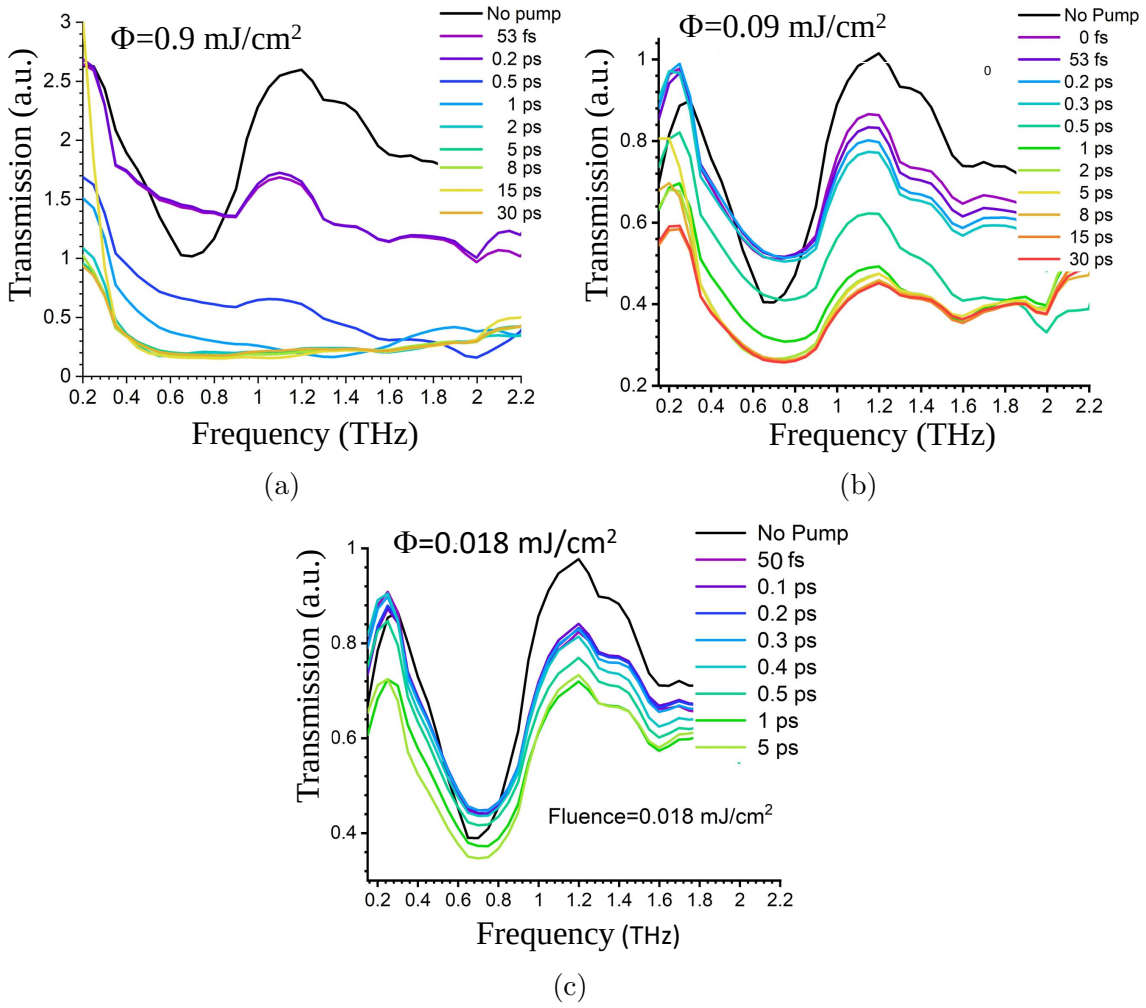

Figure 5.8: (a)-(c) THz transmission curves acquired at different time delays for different fluences.

probe normalized transmitted curves for the fluences Φ= 0.9, 0.090, and 0.018 mJ/cm^2. The largest fluence (Fig. 5.8a drastically affects the overall transmission, whilst the lowest fluence (reported in fig. 5.8c) is not sufficient to completely dampen the resonance and achieve limited absorption, also at saturation. The difference in THz spectral amplitudes between the resonant frequency and 1.2 THz, indicated by the red arrows in fig. 5.7a, has an extinction ratio of about 6 dB compared with no pump and with t_{pp} exceeding several ps as shown in fig. 5.8a. These spectrum curves are consistent with the set of measurements extracted by the THz-TDS setup previously reported in Chapter 4.

Differences in modulation depth at resonance are tracked at different pump energy

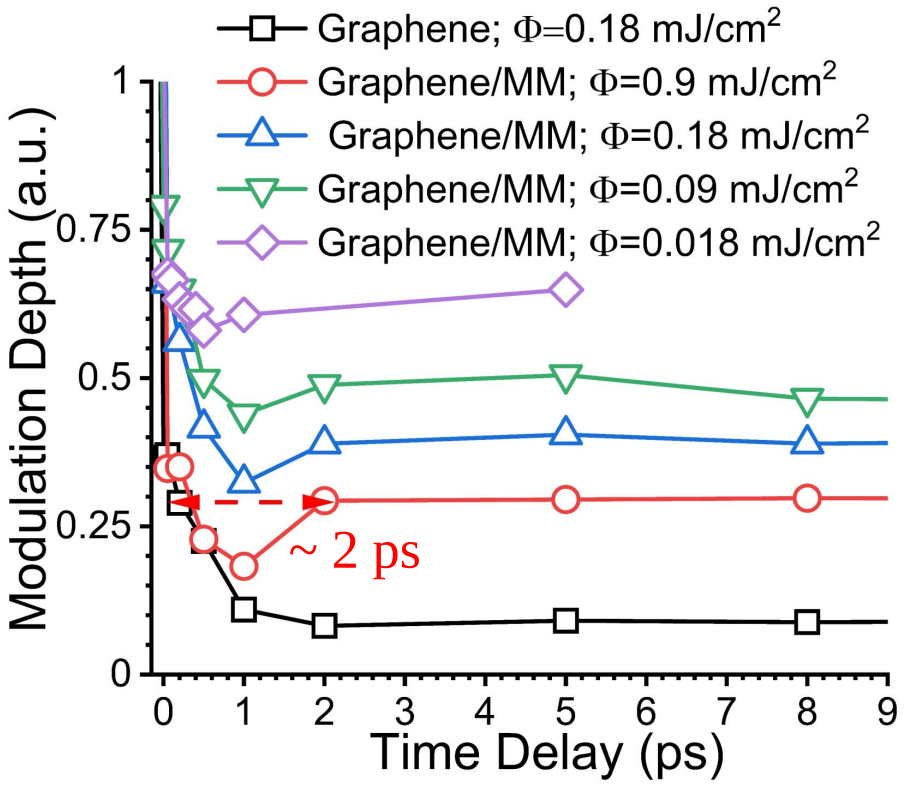

Figure 5.9: Modulation depths versus time delays calculated for different pump fluences.

to study the photoinduced carrier dynamics of graphene integrated with MMs as plotted in fig. 5.9. Photoinduced charges on the uniform graphene reference area are represented by the black trace, where the silicon substrate predominates the carrier dynamics. In contrast, the modulation depth in the hybrid MM/graphene device is clearly showing different behaviours within <2 ps of timescale due to the strong MMs resonance and their high susceptibility to any graphene conductivity changes. These curves are scaled for comparison only. Despite keeping the device electrically biased at the Dirac point of graphene, optical pumping can manipulate and alter the graphene conductivity. The retrieval of the precise time evolution due to the graphene effect requires precise modelling of the fluence-dependent silicon carriers' dynamics, graphene excitation, and recombination times, convoluted with the laser pulse width. Although feasible, this analysis requires a large number of diverse measurements in order to rule out the different effect and find the correct time delay/pump power sweet spots that allows the identification of graphene's contribution. Furthermore, the main objective of this study is more concentrated on the investigation of the ultimate time limit of a graphene-based MM device for THz ultrafast modulation. The modulation

depth results, shown by fig. 5.9, suggest the upper boundary of the carrier dynamics by graphene under the assumption of ultrafast excitation with a laser pulse limited width and fluence energy of $\sim$0.9 mJ/cm^2. An increase in amplitude extinction ratio is a result of a decrease in graphene conductivity, which recovers within approximately 2 ps showing a great match with the previously reported value of 1.9 ps by (Shi et al., 2014). Shorter cycles with almost sub-ps relaxation lifetimes are observed when reducing the pump fluences with the lowest ones occurring at 0.018 mJ/cm^2. The same observations were reported in (Jnawali et al., 2013; Winnerl et al., 2013). At the first hundreds of fs of recovery lifetime, the modulation depth exhibits an ultrafast decrease mainly due to the effect of ultrafast photoinduced charges of hot carrier distribution in graphene. The following stage of relaxation timescale is attributed to the carrier-phonon and electron-hole recombination scattering processes taking place within a timescale of $>$1 ps as also reported by (George et al., 2008). The strong E-field concentration in the split resonators has significantly enhanced the carrier dynamics of graphene observed on top of a large background of the photogenerated carrier by the substrate. It is worth mentioning that these measurements are realized on a complex design, which is composed of double-gated split resonators shunted by an encapsulated in the dielectric graphene layer. Despite the large photogenerated carriers in Si, the ultrafast carriers dynamic of graphene is still the main element of the optoelectronic response of the device. The properties of graphene do not seem to be significantly affected by the complex fabrication process as the OPTP measurements previously reported by (Shi et al., 2014; Jnawali et al., 2013; Winnerl et al., 2013)

The importance of using the OPTP measurements for testing THz optoelectronic devices is strongly supported as a result of these findings, which also suggest an upper intrinsic limit of the maximum modulation speed of the device. Finally, these results could highlight the implementation of graphene for ultrafast THz photonic applications such as the realization of the deep, strong light-matter regime for the investigation of exotic quantum phenomena (Halbhuber et al., 2020). In order to fully appreciate and model the device dynamics, it is envisaged that the contribution of silicon to the total induce conductivity should be drastically reduced. The first route consists in optical pumping below the Si gap, which would allow us to further increase the analysis on graphene optical pumping as well. An alternative solution consists in using a different substrate but would require changing the device architecture, novel device fabrication, and using a platform other than silicon.

Chapter 6

Dynamic polarization modulation of THz waves

6.1 Background and theory

Research in active controlling of EM waves polarizations is rapidly growing due to its strategic applications in polarization-sensitive fields of image sensing (W. Xu, Xie, and Ying, 2017; Peiponen, J. Axel Zeitler, and Kuwata-Gonokami, 2013; Born and Wolf, 1999; Barron, 2009), spectroscopy (S. Lee et al., 2020), communications (L. Zhang et al., 2020b; T. Nagatsuma, G. Ducournau, and C. C. Renaud, 2016; Elayan et al., 2020), and quantum electronics (Liang et al., 2017; L. Xu et al., 2017; B. Wei et al., 2018; Fang et al., 2019; Wen, T. Xu, and Y.-S. Lin, 2021; Mezzapesa et al., 2019b; Almond et al., 2020; Jeannin et al., 2020). polarization modulation is normally describing two different effects, namely optical activity (OA) and circular dichroism (CD). OA is the changes of polarization plane defined by $\overrightarrow{k}$ vector and E-field's components, while CD is a change in the polarization ellipticity (Riccardo Degl'Innocenti, H. Lin, and Navarro-Cía, 2022; Ji et al., 2021). Orthogonal E-field components of the incoming beam entering a medium and seeing a different real part of the refractive index, will experience at the output OA. The OA is illustrated by the emergent E-fields rotated by Φ angle in fig. 6.1 (top). Linearly-polarized lights can be quantified as a superposition of two identical circularly-polarized waves propagating with the same amplitude and phase, but having different helicity. On the other hand, changes in the imaginary parts of n alter the absorption coefficient. Therefore, linear to circular polarizations (LP and CP) conversion and ellipticity modifications occur leading to what is well-known as circular dichroism (CD) (Riccardo Degl'Innocenti, H. Lin, and Navarro-Cía, 2022; S. Wang, Kang, and Werner, 2018; Ji et al., 2021; R. Lin et al., 2021). CD is due to different absorption., e.g different imaginary part of the refractive index seen by the two orthogonal components of the incoming E-field.

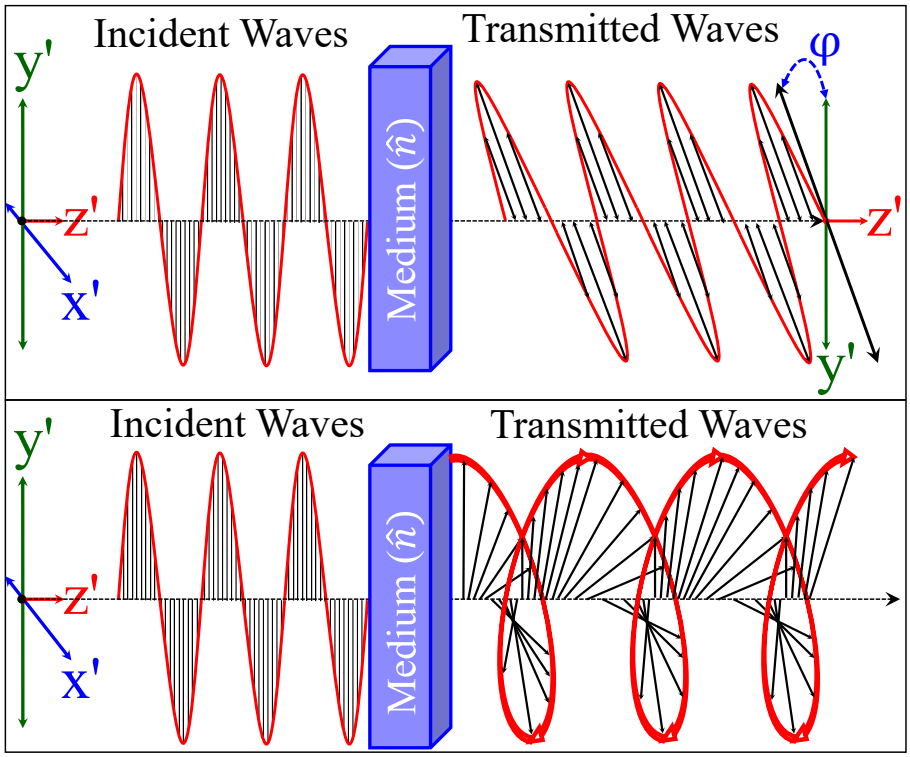

Figure 6.1: Schematic view of a linearly-polarized EM field propagating through a polarization-sensitive medium resulting in rotations of optical activity (top) and/or changes in circular dichroism (bottom).

Circularly-polarized waves have a perfectly circular cross-section of the helix, while the elliptical cross-section of the helix is an indication of the elliptical polarization E-fields. Clockwise spin state refers to right-handed CP, whilst left-handedness waves rotate counterclockwise. Dynamic manipulations of one of the decomposed components of the CP would introduce changes in ellipticity ratio, hence changes in the CD as schematically described by the transmitted EM waves in fig. 6.1 (bottom). Independent control of the OA and CD is a key element for achieving more degrees of freedom for polarization modulators, even though it is difficult to achieve the two effects independently.

The theoretical frame from (S. Wang, Kang, and Werner, 2018; Ji et al., 2021; R. Lin et al., 2021) was used to better investigate and describe the performance of this device when operated as a polarization modulator. Alternative more comprehensive theoretical frames can be used to model these results, e.g. using the Poincare sphere (Cai et al., 2021). Poincare's sphere formalism is indeed required to describe a complex 3D wavefront/polarization tuneable metadevice, which is based on the

interplay between two different dielectric metamaterial elements having different phase and polarization profiles as for (Cai et al., 2021). For the case of flat metasurfaces with a well-defined polarization input state and wave-vector perpendicular direction as in this case, however, a commonly used modelling based on Jones matrices is commonly adopted (Zaman et al., 2023; Zaman et al., 2022a; Stephen J. Kindness et al., 2020a; Stephen J. Kindness et al., 2020b). Polarization of light propagating in an anisotropic dielectric medium has three main operation principle mechanisms, which are atomic polarization, orientation polarization, or space-charge polarization (Iizuka, 2002). Polarization E-field (P) has an opposite direction from the original charge (D) as follows (Iizuka, 2002):

$$\mathbf{E} = \frac{\mathbf{D}}{\epsilon_0} - \frac{\mathbf{P}}{\epsilon_0}, \tag{6.1}$$

where ϵ_0 is free space permittivity. The E-field propagation in a linear range of polarization and in an isotropic medium can be simplified to $\mathbf{P} = \epsilon_0 \chi \mathbf{E}$ and, where χ is the electric susceptibility. As a result, the charge density becomes as $\mathbf{D} = \epsilon_0 \mathbf{n^2 E}$, where $n^2 = \epsilon_r = 1 + \chi$. The later equations must be calculated for the same frequency. In anisotropic medium, the susceptibility χ can vary in three dimensions as follows (Iizuka, 2002):

$$\begin{pmatrix} P_\mathrm{x} \\ P_\mathrm{y} \\ P_\mathrm{z} \end{pmatrix} = \epsilon_0 \begin{pmatrix} \chi_{11} & \chi_{12} & \chi_{13} \\ \chi_{21} & \chi_{22} & \chi_{23} \\ \chi_{31} & \chi_{32} & \chi_{33} \end{pmatrix} \begin{pmatrix} E_\mathrm{x} \\ E_\mathrm{y} \\ E_\mathrm{z} \end{pmatrix}. \tag{6.2}$$

The tensor matrix is orientations dependent on the dielectric material. It also can be converted into a diagonal matrix only by selecting coordinate directions parallel to the eigenvectors yielding a much simplified on-diagonal matrix as follows (Iizuka, 2002):

$$\begin{pmatrix} P_\mathrm{x} \\ P_\mathrm{y} \\ P_\mathrm{z} \end{pmatrix} = \epsilon_0 \begin{pmatrix} \chi_{11} & 0 & 0 \\ 0 & \chi_{22} & 0 \\ 0 & 0 & \chi_{33} \end{pmatrix} \begin{pmatrix} E_\mathrm{x} \\ E_\mathrm{y} \\ E_\mathrm{z} \end{pmatrix}. \tag{6.3}$$

As a result, the refractive index tensor can also be reduced to (Iizuka, 2002):

$$\begin{pmatrix} D_\mathrm{x} \\ D_\mathrm{y} \\ D_\mathrm{z} \end{pmatrix} = \epsilon_0 \begin{pmatrix} n_\mathrm{x}^2 & 0 & 0 \\ 0 & n_\mathrm{y}^2 & 0 \\ 0 & 0 & n_\mathrm{z}^2 \end{pmatrix} \begin{pmatrix} E_\mathrm{x} \\ E_\mathrm{y} \\ E_\mathrm{z} \end{pmatrix}. \tag{6.4}$$

Modulation of THz wave polarization properties plays an essential role in many polarization-dependent applications. For light propagating through a medium, OA represents the polarization plane rotation, while CD expresses changes in the ellipticity of circularly polarized waves. Different states of polarization of the molecules in

an anisotropic medium cause circular polarization rotating according to the right- or left-hand rules, abbreviated as RCP and LCP, respectively. Polarization states usually encounter weak interactions with intrinsic chirality materials and require long penetration distances at THz frequencies. Technologies of THz polarization modulators are considered immature and underdeveloped due to insufficient dynamic elements. MM approach has established itself as a paradigm for achieving efficient THz modulators because of its high efficiency, versatility, miniaturization capability, and ease of integration. A multi-stacking structure metadevices were constructed and reported great performances in integration-friendly platforms. The superposition of two identical linearly-polarized EM waves with equal amplitudes can describe the circular transmission of RCP and LCP. These two circular components propagating in a polarization-sensitive medium accumulate different complex refractive indices, either n_+ or n_- accordingly. Consequently, the emergent coefficients are complex and denoted by either T_+ or T_- based on the hand rule direction. The real components of $n_\pm$ can modify the rotations of OA, while the imaginary components of $n_\pm$ convert the CD from linear to elliptical can the absorption coefficient manipulations (Riccardo Degl'Innocenti, H. Lin, and Navarro-Cía, 2022).

Linearly polarized light propagating through an anisotropic medium is projected into two perpendicular components $\mathrm{E_x}$ and $\mathrm{E_y}$ along the two symmetry axes as shown in fig. 6.1. Thus, linear to circular or elliptical polarization conversion takes place, hence causing different interactions for the cross-polarized transmitted E-field vectors. The transmitted linearly polarized coefficients can be converted into circular ones by following Jones formalism as follows (S. Wang, Kang, and Werner, 2018; Ji et al., 2019b; Ji et al., 2021; R. Lin et al., 2021; F. Fan et al., 2021b; Zaman et al., 2022a; Zaman et al., 2023):

$$\begin{pmatrix} E_{RCP}(\omega) \\ E_{LCP}(\omega) \end{pmatrix} = \frac{1}{\sqrt{2}} \begin{pmatrix} 1 & i \\ 1 & -i \end{pmatrix} \begin{pmatrix} E_x(\omega) \\ E_y(\omega) \end{pmatrix} = \frac{1}{\sqrt{2}} \begin{pmatrix} 1 & i \\ 1 & -i \end{pmatrix} \begin{pmatrix} |E_x(\omega)| e^{i\angle E_x(\omega)} \\ |E_y(\omega)| e^{i\angle E_y(\omega)} \end{pmatrix}, \quad (6.5)$$

where $\mathrm{E_x}$ and $\mathrm{E_y}$ complex components are the linear transmitted vectors projected along x or y axes, while $\mathrm{E_{RCP}}$ and $\mathrm{E_{LCP}}$ represent the spin rotation direction for circularly-polarized radiations. Both linear and circular components are used to describe either the OA (denoted by Ψ) or CD (denoted by η) as follows (S. Wang, Kang, and Werner, 2018; Ji et al., 2019b; R. Lin et al., 2021; F. Fan et al., 2021b; Zaman et al., 2022a; Zaman et al., 2023):

$$\Psi(\omega) = \frac{1}{2} \cdot \tan^{-1}\{\tan[2 \cdot \frac{|E_x(\omega)|}{|E_y(\omega)|}] \cdot \cos[\angle E_x(\omega) - \angle E_y(\omega)]\}, \quad (6.6)$$

$$\eta(\omega) = \frac{|E_{RCP}(\omega)| - |E_{LCP}(\omega)|}{|E_{RCP}(\omega)| + |E_{LCP}(\omega)|}, \quad (6.7)$$

where $\Psi(\omega)$ and $\eta(\omega)$ units are in degrees and dimensionless, respectively. E_{RCP} and E_{LCP} complex values, in eq. 6.7, are calculated using eq. 6.5. The linear scale of η indicates the ratio between the major and minor axes of polarization ellipses, hence complete linear or perfect circular polarization states correspond to 0 or ± 1, respectively. Enlarging the phase modulation depths in one of the orthogonal waves (E_x or E_y) would increase the continuous rotation range of the polarization plane. In contrast, enhancing the amplitude extinction ratio would increase the dynamic changes of ellipticity. An arbitrary state of polarization can be retrieved from the crossed linear coefficients. The quadratic equation describing the polarization state in cartesian components is as follows (Ji et al., 2019b; F. Fan et al., 2021b; Zaman et al., 2022a; Zaman et al., 2023):

$$\frac{E_{x'}^2}{|E_x|^2} - 2 \cdot \frac{E_{x'}E_{y'}}{|E_x||E_y|} \cdot \cos(\angle E_x - \angle E_y) + \frac{E_{y'}^2}{|E_y|^2} = \sin^2(\angle E_x - \angle E_y), \tag{6.8}$$

where E_x and E_y are the major and minor axes of an elliptically polarized wave. Visualization of transmitted polarization states in polar coordinates (r, θ) could be easier as follows:

$$\frac{r^2\cos^2(\theta)}{|E_x|^2} - \frac{2r^2\cos(\theta)\sin(\theta)}{|E_x||E_y|} \cdot \cos(\angle E_x - \angle E_y) + \frac{r^2\sin^2(\theta)}{|E_y|^2} = \sin^2(\angle E_x - \angle E_y), \tag{6.9}$$

where $x = r\cos(\theta)$, $y = r\sin(\theta)$, and θ ranges from 0 to 2π. The two solutions of eq.6.9 with respect to the ellipse's radius as a function of the rotational angle (θ) are:

$$r(\theta) = \pm \frac{|E_x||E_y|\sin(\Delta\Phi)}{\sqrt{\{|E_x|^2\cos^2(\theta)\} + \{|E_y|^2\sin^2(\theta)\} - \{2|E_x||E_y|\cos(\Delta\Phi)\cos(\theta)\sin(\theta)\}}}, \tag{6.10}$$

where $\Delta\Phi = \angle E_x - \angle E_y$ in radian. Prior to plotting the retrieved state of polarization, the radius $r(\theta)$ is normalized with respect to its maximum value.

Decoupling the control of OA and CD could enrich the polarization-sensitive applications, despite its difficulties. Generally, maximization of the off-diagonal components in the transmission matrix could enhance the tuning range of OA. When targeting a wide range of CD, MMs structure must consider a 90° phase accumulation between the co-polarized radiations. Therefore, various MMs devices were constructed from several layers to enhance the linear to circular conversion. Mechanical movements have been implemented when designing the MMs using MEMS devices to achieve active polarization. Another approach is integrating dynamic materials with MMs such as in phase change elements utilizing thermal effect using VO_2 or liquid crystals, and 2D materials via graphene, 2DEG, or Si.

Amongst many approaches, only a few selected ones seem to provide flexibility, efficiency, and reconfiguration speed required by the disruptive technologies driven by the next-generation wireless communication scenarios. Optoelectronic techniques offer a higher level of miniaturization and efficiency above 500 GHz. The metamaterial (MM) approach, thanks to its versatility, efficiency, and miniaturization capabilities, is rapidly establishing itself as the privileged paradigm for the realization of integrated THz modulators Low and Avouris, 2014; Hou-Tong Chen, Taylor, and N. Yu, 2016; Zuojia Wang et al., 2016; Al-Naib and Withayachumnankul, 2017; ZT Ma et al., 2019; Riccardo Degl'Innocenti et al., 2018; Yoo and Park, 2019; J. Li et al., 2020; S. Lee et al., 2020; Yaxin et al., 2020; Fu et al., 2020; S. Shen et al., 2022. This approach has proved to be particularly efficient for achieving a continuous tuning of the polarization state of THz radiation, especially when combined with active materials such as phase change materials. Different strategies have been developed in order to include active materials in the MM designs, thus achieving a modulation. Amongst these, the most popular methodologies use phase-changing materials such as VO_2 (Kats et al., 2013; Ivanov et al., 2021), semiconductors (Hou-Tong Chen et al., 2006; Pitchappa et al., 2019), liquid crystals (LC) Ji et al., 2019a; D. Xiao et al., 2018, 2D materials such as graphene (S. H. Lee et al., 2012; Stephen J. Kindness et al., 2019; Stephen J. Kindness et al., 2020a; Masyukov et al., 2020; Zaman et al., 2022a; Zaman et al., 2022b), two-dimensional electron gases (2DEGs) (Yaxin Zhang et al., 2015; Y. Zhao et al., 2019a; Yaxin Zhang et al., 2015; Y. Zhao et al., 2019b), or in MEMS arrangement metasurfaces (Longqing Cong et al., 2019b; R. Xu et al., 2021).

In this chapter, the demonstration of an ultrafast versatile polarization modulator based on the interplay between graphene and metamaterials is discussed in detail. Fermi-energy levels of a graphene monolayer can be altered either chemically or by electrostatic gating (Shafraniuk, 2015). MMs/graphene polarization modulator was extensively investigated using gated double layers of graphene sheet reporting up to 95% of polarization conversion efficiency (Yin Zhang, Feng, and J. Zhao, 2020). Ion-gel gating technique was deployed to allow chemical doping of graphene Fermi-energy which is significantly larger than electrostatic doping (Q. Li et al., 2022), but it is not compatible with high all-electronic reconfiguration speed (>GHz). Yin Zhang, Feng, and J. Zhao, 2020 reported dynamic polarization manipulation of EM waves for a wide range of THz frequencies from 1.64 to 2.26 THz by gating a graphene sheet with up to 93% of polarization conversion efficiency, while graphene/metamaterial with Ion-gel was implemented and reported achieving V_{ext} of 5.5 V as described in (Yaxin Zhang et al., 2015). The two mentioned articles (Yin Zhang, Feng, and J. Zhao, 2020; Q. Li et al., 2022) are indeed very interesting but are also addressing beam steering which is not the main target of this work. Mostly, these articles are based on the ion-gel gating technique. These asymmetries in the $E_{x/y}$ amplitude and phase, which vary with the device rotational angle and incident frequency, can be exploited into

an active polarization device that highlights the CD or OA depending on the user's selected configuration. The physical principle resembles the standard electro-optic modulator arrangement with crossed polarizers in the visible light as in (Yariv, 1989) or ultraviolet (R. Degl'Innocenti et al., 2007) range but without the need for long crystals which would be impractical at these wavelengths. Other active metamaterial architectures demonstrated a similar mechanism by combining phase change materials (VO_2) with metamaterial arrays (Kats et al., 2013; Ivanov et al., 2021). Whilst this approach is effective in yielding large modulation of polarization states, it can not match the ultrafast speed demonstrated by graphene-based modulators. Additional details on the recent progress on MMs polarization modulators are summarized in table 6.1.

Table 6.1: Maximum polarization modulation depths (MDs) for some recent MMs devices operating at different resonant frequency ($f_{res.}$).

Platform	**Method**	**MDs (unit)**	**$f_{res.}$ (THz)**	**Speed**	**Reference**
Conjugated Z MMs	Graphene/ electronic	$\Delta\Psi = 10^o$ $\Delta\eta \simeq 0.82$	1.4 1.1	//	T.-T. Kim et al., 2017
Conjugated MMs	Graphene/ electronic	$\Delta\Psi = 10^o$ $\Delta\eta \simeq 0.82$	1.9 2.1	//	Stephen J. Kindness et al., 2020a
EIT meta-materials	Graphene/ electronic	$\Delta\Psi = 20^o$	1.75	>MHz	Stephen J. Kindness et al., 2019
Conjugated graphene multilayers	Graphene/ optical	$\Delta\eta = 20^o$	0.76	//	Masyukov et al., 2020
SRRs on Silicon	Silicon/ optical	$\Delta\eta \simeq 30^o$	0.84	//	L. Cong et al., 2018
Grid polarizers	VO_2/ electronic	$\Delta\Psi = 90^o$	∼0.33-0.4	//	Wong et al., 2020
L-shape cantilevers	MEMS/ electronic	$\Delta\Psi = 22^o$ $\Delta\eta \simeq 30^o$	0.4 0.65	//	Longqing Cong et al., 2019a
MMs/ graphene split-resonators	Graphene/ optoelectronic	$\Delta\Psi > 21.5^o$ $\Delta\eta > 0.3$	0.71 0.71	>3 GHz electrically and <500 GHz optically	Zaman et al., 2023

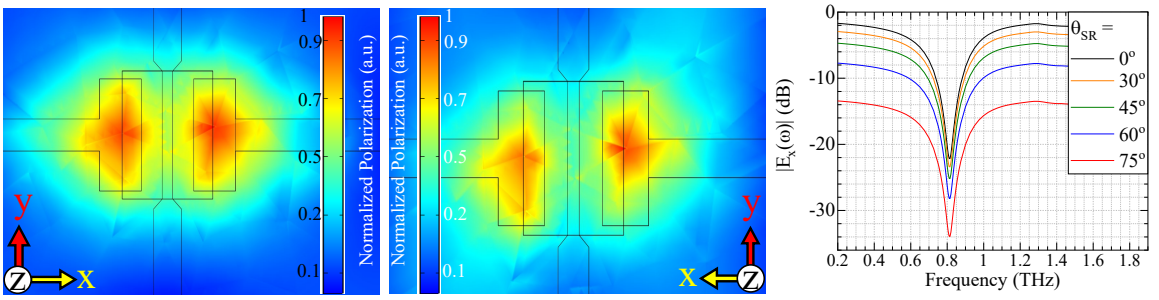

(a) (b) (c)

Figure 6.2: Simulated normalized E_x polarization calculated at Z=-8 μm inside the substrate at a rotated listener port by 0° (a) and 75° (b). (c) Simulated amplitudes of S_{21} for different x-polarized listener's angles.

6.2 Operation principles and fabrication

This complex design described explicitly in (Zaman et al., 2023) is reminiscent of the nested architecture proposed by (Y. Zhao et al., 2019a) using 2DEG as an active material. The polarization mechanism is more similar to a tuneable metallic grid polarizer where the E-field polarized along its wires is rejected, rather than based on an engineered chiral response (Stephen J. Kindness et al., 2020a) or EIT analogy (Stephen J. Kindness et al., 2019). The remarkable performances as a polarization modulator are accompanied by the fast reconfiguration speed (>3 GHz) as mentioned in (Zaman et al., 2022a) and carriers relaxation time of the graphene sheet (∼500 GHz or <2 ps) as described in (Zaman et al., 2022b). More details on simulation and fabrication are previously reported in (Zaman et al., 2022a; Zaman et al., 2022b; Zaman et al., 2023) and extensively in Chapter 3. Polarization dependence of the device is simulated by exciting the unit-cell with both $E_{x/y}$-polarized plane waves weighted differently. E_x amplitude is multiplied by $\cos(\theta_{SR})$ whilst E_y amplitude is multiplied by $\sin(\theta_{SR})$. The listener port is only x-polarized and weighted by $\cos(\theta_{SR})$ to receive the polarization along the resonators' plane. Normalized polarization calculated at Z = -8 μm below the metallic surface is plotted for the listener's rotations of 0° and 75° as shown in figs. 6.2a and 6.2b, respectively. Rotating the plane of the incident reduces the amount of power projected into the oscillating dipoles causing less radiated power for the x-polarized E-field component as represented by the simulated S21 amplitudes in fig. 6.2c. The simulated phases of S_{21} for E_x-polarized receiver (not shown here) have identical phases for all excitation angles.

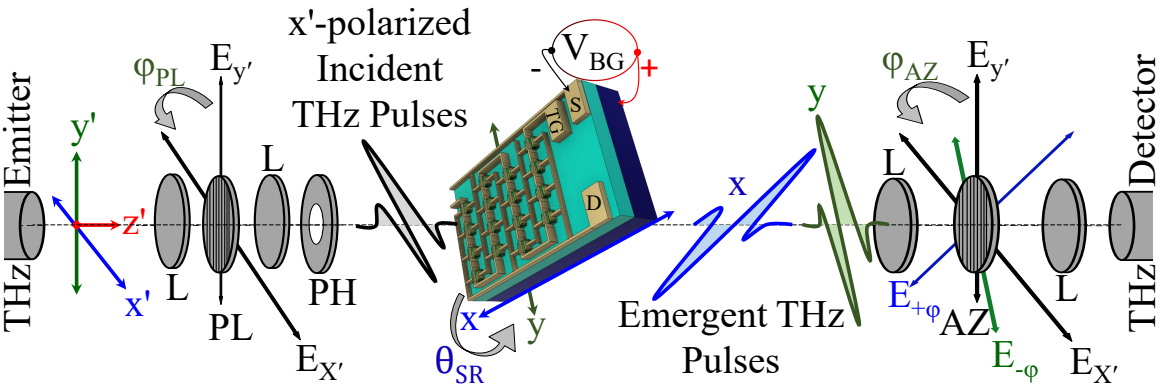

Figure 6.3: Schematic view of the modified THz-TDS setup where where θ_{SR} and Φ are rotational angles with respect to the x' or y' axes, respectievly. L: lenses, PL: polarizer, PH: pinhole (iris), V_{GND}: the ground connection that is always in contact with the graphene patches through the source and drain pads, V_{BG}: top- or back-gates, and AZ: analyzer.

6.3 Experimental results

The double-gated MMs/graphene devices working as polarization modulators are investigated by the TERA K15 fiber-coupled terahertz spectrometer from Menlo Systems. The THz-TDS system is aligned in the transmission configuration and modified with two grid polarizers. The polarizers are from Nearspec, made of metallic grids, and positioned before and after the sample as illustrated in fig. 6.3. The THz emitter is always kept at the horizontal polarization state (i.e. along the x'-axis) throughout the entire measurements in this Chapter (6). Similarly, the first polarizer (PL) is always set at $\Phi_{PL} = 0^o$ with respect to the y'-axis, i.e. vertical grids and full transmission, to ensure transmission of only $E_{x'}$. The incident polarization state into the THz detector is then independently selected by rotating the analyzer's (AZ's) grids by an angle Φ_{AZ} with respect to the vertical axis, i.e. the y'-axis. Lastly, transmitted waves through the AZ are detected by a THz receiver that is always set to the horizontal polarization state along the x'-axis. During post-processing, the projection of E-fields on the receiver is taken into account by dividing the detected waves by $\sin / \cos$ (Φ_{AZ}) based on the AZ's orientation.

Eventual crosstalk between the co- and cross-polarizations is not avoidable. The crosstalk is measured by rotating the PL's angle to allow for full transmission of the incoming $E_{x'}$-polarized light while rotating the AZ to $\Phi_{PL} = 90^o$ to completely block the incident $E_{x'}$-field into the detector with no samples. The time-domain waveforms are acquired with a total span of 500 ps without N_2 purging corresponding to a spectral resolution of ~2 GHz. Fig. 6.4b shows only a 100 ps time span of the detected THz-

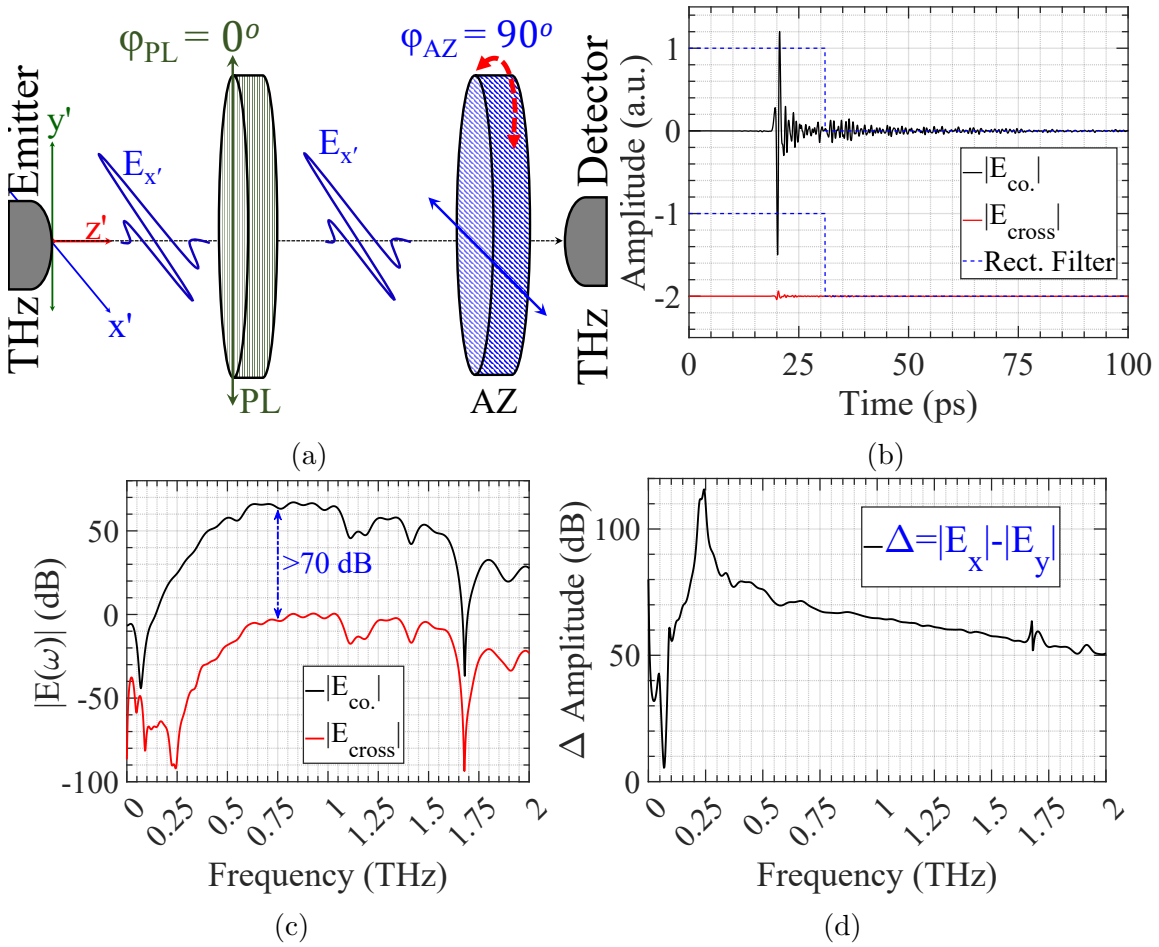

Figure 6.4: (a) Schematic view of the cross-polarization THz-TDS setup arrangement. Detected THz pulses passing through the co and cross polarizers in the time-domain (b) and their spectra (c). (d) Measured differences of crosstalk between the co and cross-polarizations. Temporal $|E_{\text{cross}}|$ and its filter in (b) are offset for comparison.

TDS pulses. $E_{\text{co.}}$ is the EM waves passing through the two vertically aligned PL and AZ ($\Phi_{\text{PL}} = \Phi_{\text{AZ}} = 0^{\text{o}}$), while E_{cross} is for the crossed polarizers ($\Phi_{\text{PL}} = 0^{\text{o}}$ and $\Phi_{\text{AZ}} = 90^{\text{o}}$). The $E_{\text{co.}}$ waves have the full power of the transmitted THz pulses received at the detector since both PL and AZ are set to the full transmission mode. However, the cross-polarized E-filed is barely detected. During post-processing only, a rectangular window centered at zero time with 63 ps of pulse duration is used for filtering the first temporal pulses as indicated by the dashed-blue lines in fig. 6.4b. Their spectral amplitudes are illustrated in fig. 6.4c. Differences between the co and cross polarizations exceed 70 dB in amplitude as plotted in fig. 6.4d. The crosstalk waveform ($|E_{\text{cross}}|$) can be used to correct the received E-fields at the detector.

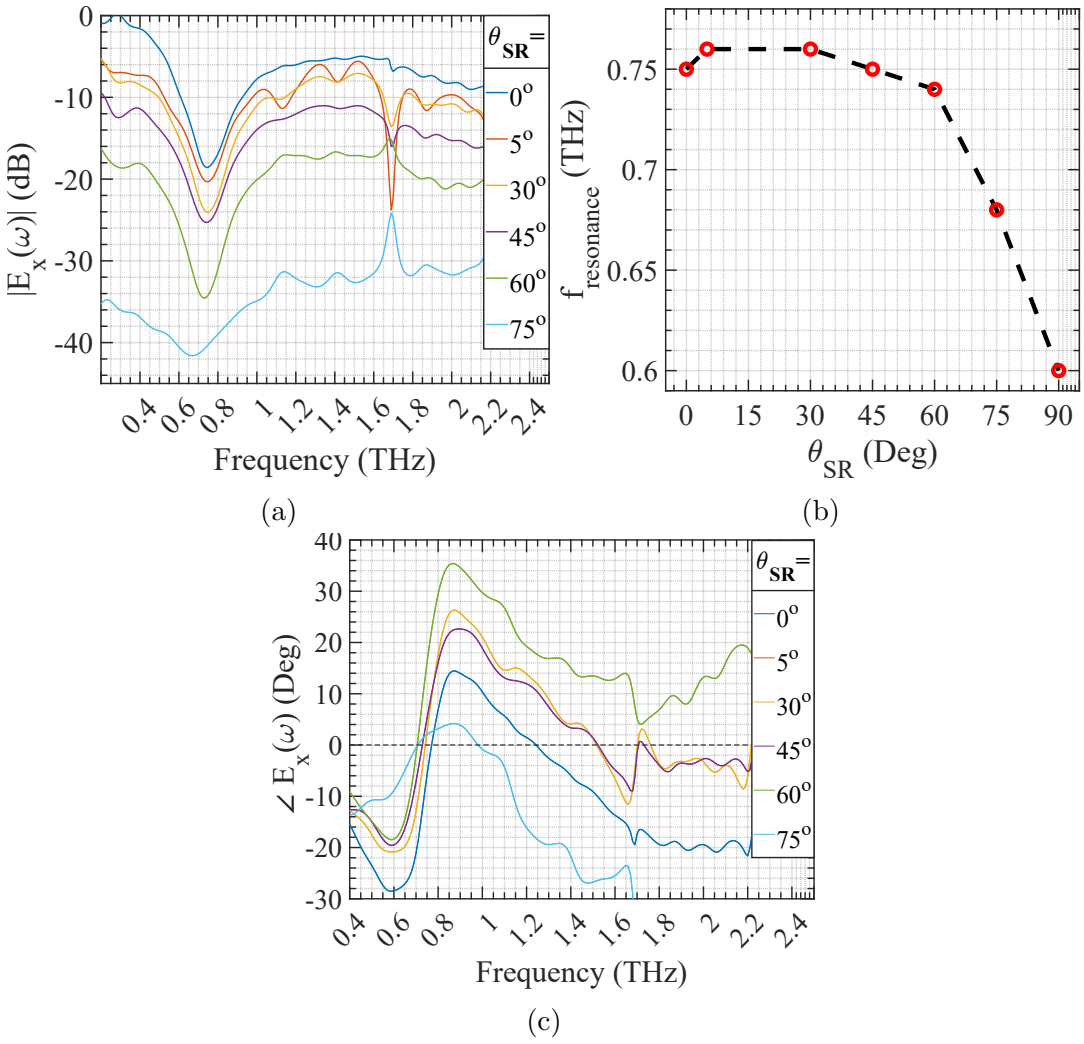

Figure 6.5: (a) Spectral amplitudes of E_x polarization normalized to the reference, (b) tracking of the strongest dip frequency of amplitudes, and (c) spectral phases of the x'-polarized waves. These THz-TDS measurements are for pulses passing through the SRs, various rotational angles θ_{SR}, no bias, and with N_2 purging.

6.4 Measurements and discussion

6.4.1 Preliminary measurements

Device 2, 95 nm Al_2O_3 thick of dielectric layer encapsulating the graphene patch, is inserted at the focal plane of the polarization-sensitive THz-TDS setup. After passing through a pinhole (1.1 mm diameter), the device is mounted on a rotational moving stage which can be rotated by θ_{SR}= 360° with respect to the horizontal (x'-) axis

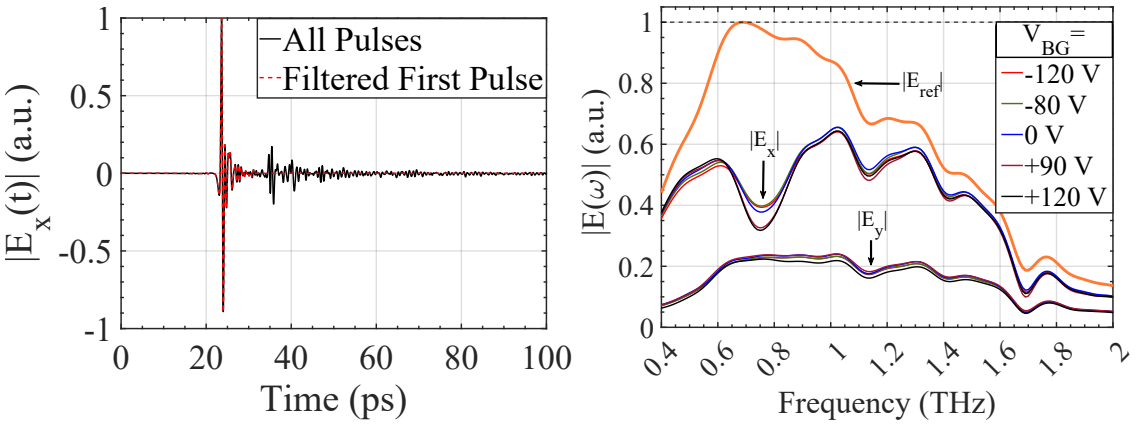

Figure 6.6: (a) Temporal THz E_x-fields normalized to the maximum value of the filtered first pulse with N_2 purge. (b) Fourier transformation of the detected E-fields before normalization for different biasing conditions.

allowing to excite both symmetry axes of the device (named x and y in fig. 6.3). θ_{SR} can be rotated with a step resolution of 1°. A component of the incident E-field is projected parallel to the SR's plane of the incident (E_x), while the other is perpendicular to the SR's plane of the incident (E_y). Φ_{AZ} is rotated by different angles in accordance with the SRs' orientations (θ_{SR}). Both the PL and AZ can be independently rotated by angles Φ_{PL} and Φ_{AZ} with respect to the y'-axis.

It is important that the two polarizers have finite selectivity as the polarization-sensitive THz emitter and detector units. Polarization states are first examined without any applied voltages while rotating the SRs by several θ_{SR} angles as follows: $\theta_{SR} = \{5°, 30°, 45°, 60°, \text{and } 75°\}$. Consequently, horizontally polarized incident waves are projected into two orthogonal E-fields to excite either the LC capacitive resonances or the top-gate dipoles along the x or y axes. As θ_{SR} becomes larger, the projected power toward the capacitive gap (x-axis) decreases while more power goes toward the perpendicular vector (y-axis). The correspondence AZ angles would be Φ_{AZ} = {-5°, +85°, -30°, +60°, ±45°, -60°, +30°, -75°, and +15°} in order to select either the E_x or E_y to pass to the detector. The rotated E-fields are incident to the horizontally polarized detector, thus they are being projected again with respect to the detection orientation (i.e. the x'-axis). To compensate for this vector projection, the acquired E-fields have been divided accordingly by either $\cos\{\theta_{SR}\}$ or $\cos\{90 - \theta_{SR}\}$ during post-processing. Additionally, unity rectangle windowing centered at the peaks of the first pulses is used during filtering the first temporal pulses with a temporal duration of 17 ps. Different E_{Ref} passing through the graphene patch is acquired each time the device is rotated by θ_{SR} with both Φ_{PL} and Φ_{AZ} set to vertical grids to allow for full

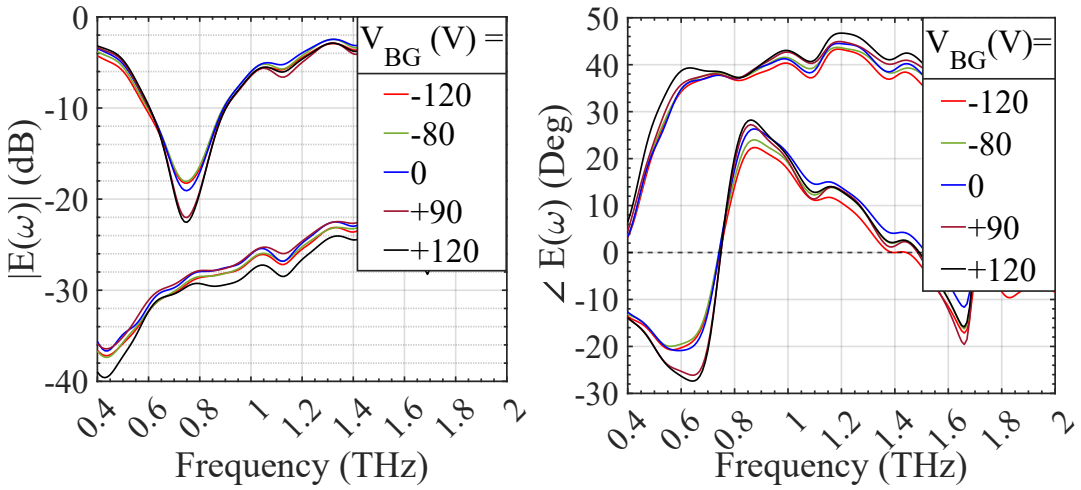

(a) (b)

Figure 6.7: Spectral amplitudes (a) and relative phases (b) normalized to a reference and considering only the first temporal pulses at different V_{BG} when θ_{SR}= 30° and Φ_{AZ} = -30° and +60°.

transmission. The time-domain traces are acquired with a temporal span of 100 ps with N_2 purging. As θ_{SR} increases, E_x amplitudes generally exhibit power losses for all THz frequencies below 1 THz, as expected and shown in fig. 6.5a. An unwanted dip at frequencies around 1.70 THz is due to atmospheric absorption. The resonance frequency remains almost unchanged with the rotation till exceeding above 60° of θ_{SR} where it starts blueshifting towards the $f_{res.}$ of 0.60 THz as plotted in fig. 6.5b. Spectral phases of the x'-polarized lights have three interesting regions. Around 0.65 and 0.87 THz frequencies, spectral phases remain almost the same. The spectral phases of E_x are crossing the zero line at around the resonance frequency. These zero-crossing frequencies decrease from 0.77 to 0.71 THz as the SR's angle increases leading to about 50 GHz of blueshift as plotted in fig. 6.5c. Modulation depth (MD) is a key factor to determine the quality performance of such a modulator. Generally, the MD is defined as the normalized maximal excursion in amplitude (A) under an external stimulus as follows:

$$MD = A_{max} - A_{min}, \tag{6.11}$$

where A_{max} and A_{min} represent the maximum and minimum values.

Graphene conductivity is dynamically modified by electrostatic gating, and therefore absorption of the incoming radiations at resonance is modified. The device is electrically biased by connecting the graphene's areas through the SRs' elements (V_{GND}), whereas the back-gate is connected to the positive terminal of a

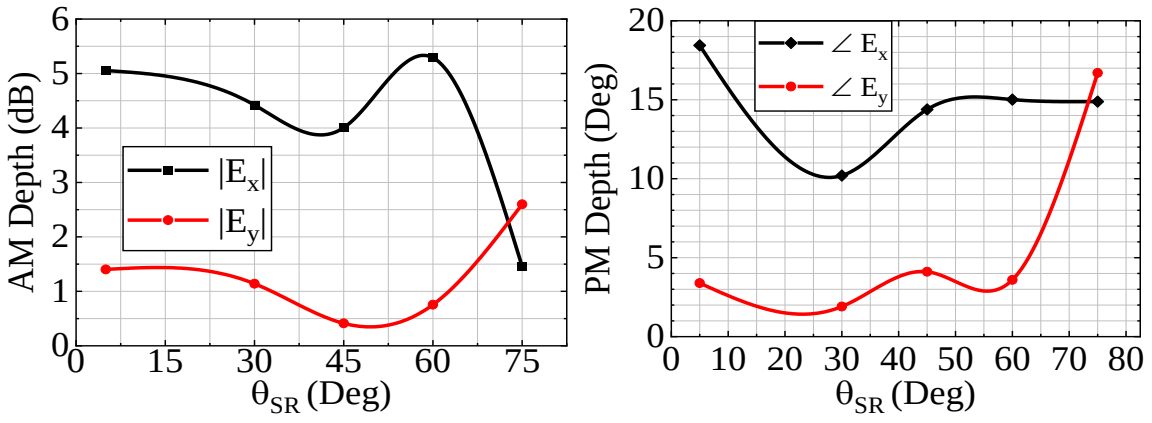

Figure 6.8: Depth of AM at 0.74 THz (a) and PM at 0.68 THz (b) of THz spectra when rotating the SRs by various angles and processing only the first temporal pulses.

DC power supply from a Kethely model 2450 source meter unit (SMU). These sets of measurements are acquired by using the back-gate electrical configuration since it is more robust than the top-gate and allows a larger biasing range without risking incurring any shortages. Top-gating is instead readily accessible and requires a lower voltage range, but it is more susceptible to shortage mostly for wide biasing ranges. Therefore, it is faster and compatible with fast data transmission applications. The device is driven with gate voltages (V_{BG}) varying between -160 V to +160 V to alter the graphene conductivity around the Dirac point while measuring the gate leakage current (I_{BG}). The Dirac voltage is estimated to be around 20-35 V, but it is not clear with device 2 due to an excess amount of the leakage current in the order of 700 μA. Here, this device's architecture was tested all-electronically demonstrating a reconfiguration speed of >3 GHz, only limited by available electronics as previously presented in (Zaman et al., 2022a; Zaman et al., 2022b). During post-processing, the acquired temporal THz pulses are filtered either with a 17 ps unity rectangular window centered at the first pulse's peak or with a full (100 ps) unity rectangular window to consider all transmission and reflection E-fields arising from multiple reflections at the air/sample boundaries (Fabry-Pèrot resonances) as illustrated in figure 6.6a. Single pulse transmission analysis provides altogether comparison with the simulations and yields direct evidence of the resonance supported by the SRs. By considering all the Fabry-Pèrot resonances, it is possible to infer the device's behaviour under a THz continuous wave source. Pulses passing through a 1.2×1.2 μm^2 uniform graphene patch fabricated on-chip without any SRs metal features are used for normalization, i.e. $E_{ref.}$. Unwanted absorption for frequencies above 1 THz clearly appears in the spectral amplitudes of $E_{ref.}$, E_x, and E_y as shown in figure 6.6b. Upon filtering

temporal pulses, the acquired E-fields are normalized by referencing their spectral amplitudes to $E_{ref.}$'s amplitude, as shown in figure 6.7a. At the same time, the extracted spectral phases are normalized by subtracting the spectral phase of $E_{ref.}$, as plotted in figure 6.7b. Separate $E_{ref.}$ waveforms were acquired each time the device was rotated while orienting both the PL and AZ to vertical grids (full transmission) position. A component of the incident E-field is parallel to the SR's plane of the incident (E_x), while the other is perpendicular to the SR's plane of the incident (E_y).

Fig. 6.8 reports the AM and PM modulation depths calculated for different device angles (θ_{SR}), from 5° to 75°. The MD is extracted for each θ_{SR} angels taking into consideration only the first temporal pulse following equations explicitly mentioned in Chapter 4. The MDs of E_y polarization gradually shift towards smaller frequencies in order to match a dipole resonance along the orthogonal direction (the y-axis). When focusing on 0.74 THz, E_x polarized waves encounter a sharp decrease in their spectral amplitude MDs when rotating the SRs by 75° with an average of ∼5 dB as shown in fig. 6.8a. At the same frequency, orthogonal waves (E_y) encounter a sharp reduction in their MD values as expected when exciting the SRs with orthogonal polarization. Although rotating the SRs' by an angle introduces different interactions with incident THz radiations, other factors should be taken into account; e.g. principally power attenuation. It comes with the drawback of excessive power losses. A summary of several MDs achieved considering only the first temporal pulse is reported in table 6.2. When taking into account the entire temporal waveform during post-processing, E_x polarized lights have an enhanced spectral amplitude MD of >7.5 dB at 0.75 THz in correspondence with a device rotational angle (θ_{SR}) of 5°. Moreover, the E_y polarized radiations have a spectral amplitude MD that exceeds 6 dB at 0.61 THz when θ_{SR}= 75° as summarized in table 6.2 for considerations of the entire temporal waveforms.

Table 6.2: Maximum modulation depth (MD) with and without considering multiple reflections.

Signal processing	**Type of MD**	**E-field component**	**θ_{SR} from x'-axis**	**Frequency (THz)**	**Active MD**
Without considering multiple reflections	AM	E_x	5°	0.74	>5.5 dB
		E_y	75°	0.62 & 0.63	>3.75 dB
	PM	E_x	5°	0.68	>18°
		E_y	75°	0.80	>22.5°
Computing all temporal pulses	AM	E_x	5°	0.75	>7.5 dB
		E_y	75°	0.61	>6 dB
	PM	E_x	45°	0.70	>25°
		E_y	30°	0.60	>10°

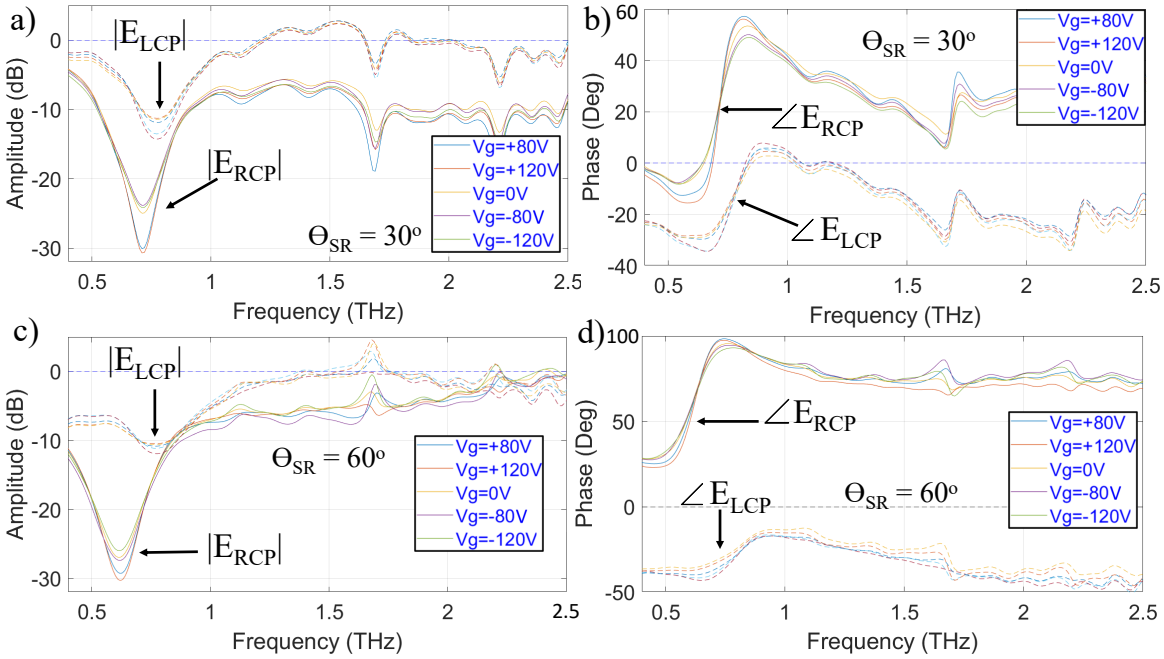

Figure 6.9: (a-d) Spectral amplitudes and phases of the circular polarization E-fields passing through the resonators rotated by different angles at various biasing conditions considering only the first transmitted pulse.

Active changing of graphene conductivity also changes the phase of the supported resonant mode. By applying the 17 ps rectangle filter, E_x polarization reports a continuous change of $\sim$18.5° in MD of spectral phase at 0.68 THz when θ_{SR}= 5°. These results are also summarized in table 6.2. At 0.80 THz, E_y polarization reaches its peak of MD with $\sim$22.5° of continuous phase tuning when the SR is rotated by 75°. When focusing on 0.64 THz as presented in fig. 6.8b, E_x polarized waves have an average spectral phase MD of $\sim$15° regardless of the SR's rotational angle. At the same frequency, E_y polarized spectral phases are continuously tuned by >17° when θ_{SR}= 75°. Considerations of the entire 100 ps acquired waveform, E_x polarized waves have a continuous spectral phase tuning of >25° when θ_{SR} = 45° at 0.70 THz. Additionally, E_y polarization has a spectral phase MD that reaches >10° when θ_{SR} = 30° at 0.60 THz as summarized in table 6.2.

6.4.2 Single pulse processing

For each applied voltage, both cross-polarization waves transmitted from the device are consecutively acquired by rotating the analyzer with the correct Φ_{AZ} angle based on the SR's orientations. During post-processing throughout this section, the first

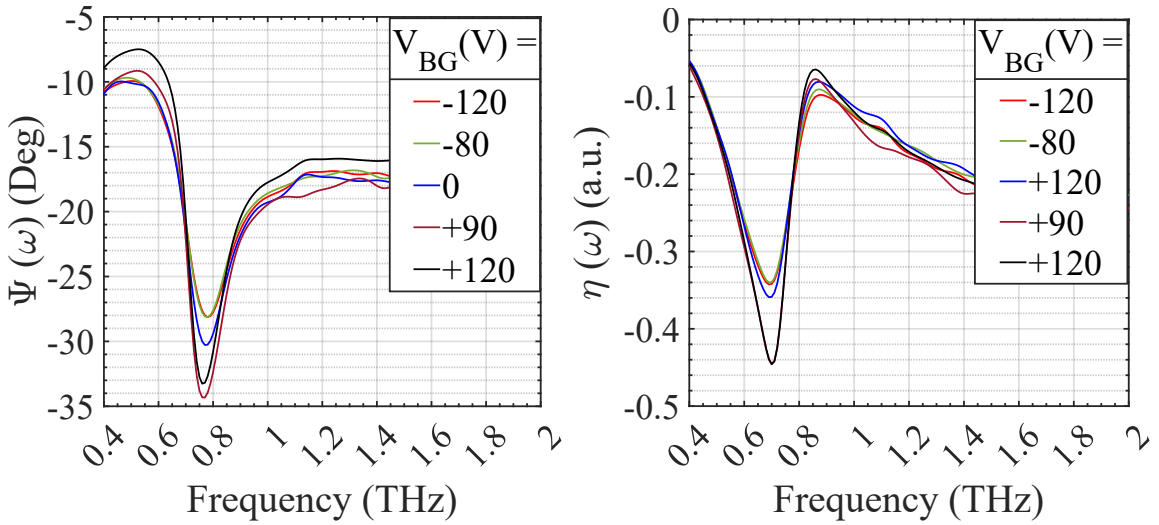

Figure 6.10: OA (a) and ellipticty ratio (b) at different biasing conditions when θ_{SR}= 30° and Φ_{AZ} = -30° and +60°.

temporal pulse is filtered using a unity rectangle window with 17 ps of width as plotted in fig. 6.6a. The transmitted linearly polarized waves $E_{x/y}$ are converted into circularly polarized radiations ($E_{RCP/LCP}$) by following eq. 6.5. The spectral amplitudes and phases of $E_{RCP/LCP}$ are calculated for all rotational angles of the SRs, but only θ_{SR} = 30° and 60° are plotted in fig. 6.9a-d as an example to present. Both OA and CD are calculated following eqs. 6.6 and 6.7, respectively. The linear scale of η indicates the ratio between the major and minor axes of polarization ellipses, hence complete linear or perfect circular polarization states correspond to 0 or ±1, respectively. Enlarging the phase modulation depths in one of the orthogonal waves (E_x or E_y) would increase the continuous rotation range of the polarization plane. In contrast, enhancing the amplitude extinction ratio would increase the dynamic changes of ellipticity. Fig. 6.9 shows the spectral amplitudes and phases of the LCP and RCP at different back-gate biasing conditions when rotating the SRs by 30° and 60°. Continuous rotation of Ψ by ∼6.5° is observed at 0.75 THz when rotating the device by θ_{SR} = 30° and for a voltage sweep between -120 V to +120 V as shown in fig. 6.10a. The maximum difference between the amplitudes of E_{RCP} and E_{LCP} is resulting in maximum modifications of η at 0.72 THz from ∼0.33 to ∼0.45 as illustrated in fig. 6.10b.

Larger phase differences between the two circular polarizations lead to maximized rotation of OA. Consequently, maximum modulation depth of Ψ is found to be >12° of continuous tuning at 0.68 THz when θ_{SR} is 5° as summarized in table 6.3. Fig. 6.11a

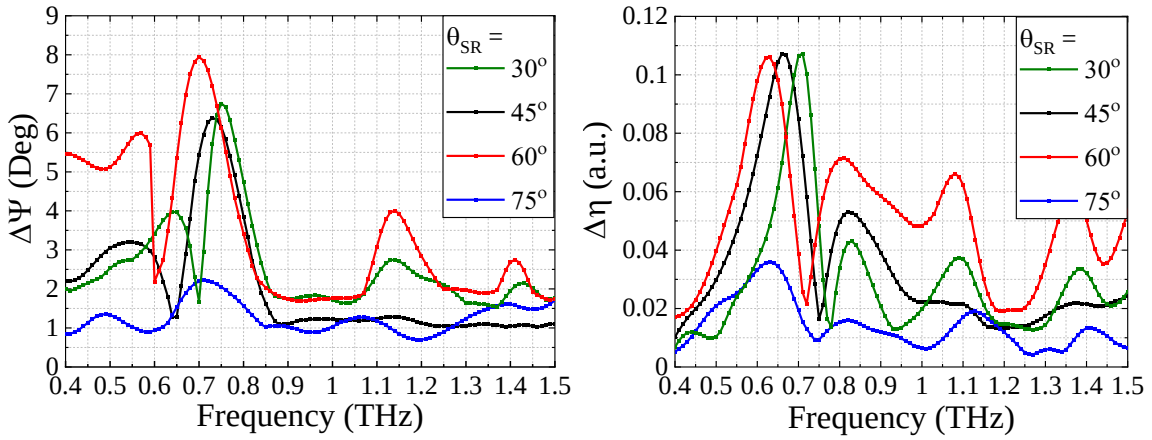

(a) (b)

Figure 6.11: Active modulation depths of OA (a) and CD (d) for various θ_{SR} angles. These values have been calculated by considering only the first temporal pulse.

illustrates the active modulations of OA for each THz frequency where the peaks of $\Delta\Psi$ are blueshifted with the increase of the SR's rotational angle. $\Delta\Psi$ peaks start degrading sharply for all θ_{SR} above 75°. Similarly, the depth of ellipticity changes ($\Delta\eta$) is maximized with the ratio $|E_x|/|E_y|$ changes by 0.16 when the SRs are rotated by 5° at 0.72 THz as summarized in table 6.3. Dynamics of $\Delta\eta$ remain almost steady for all SRs' angles ranging from 30° to 60° with an average $\Delta\eta$ of 0.11 at different frequencies as plotted in fig. 6.11b. Active changes of $\Delta\eta$ are sharply decreased when rotating the SRs by 75°. Another interesting observation is that the peaks of dynamic tuning of $\Delta\Psi$ and $\Delta\eta$ keep shifting gradually towards smaller frequencies when increasing the SRs' angle from 30° to 60°. Polarization ellipses, shown in fig. 6.12a-h and calculated using eqs. 6.8 and 6.9, further highlight the independent control of OA and CD for different applied back-gate voltages. When rotating the device by 45°, for example, the maximum $\Delta\eta$ of 0.11 occurs at 0.65 THz with a minimal change in the $\Delta\Psi$ by only 1.3°. On the other hand, maximum tuning of Ψ by 6.4° takes place at 0.73 THz with a minimal $\Delta\eta$ of 0.04. The same observation is reported for other rotational angles of θ_{SR} at different frequencies. Depending on the sample rotational angle and incoming frequency, it is possible with this approach to selectively enhance either OA or CD independently. This is of great importance with polarization spectroscopy (W. J. Choi et al., 2019), polarization imaging (S. Watanabe, 2018), or THz applications in the pharmaceutical (Markl et al., 2018) or biomedical fields, e.g. (Son, 2020b). It is worth mentioning that η is reversing its sign at 0.86 THz when rotating the device by θ_{SR} = 60° with its ellipticity becomes almost zero when $|E_{RCP}|/|E_{LCP}| \simeq 0$ at the applied voltage of -80 V as plotted in fig. 6.9. This ultrafast switching of the light handedness

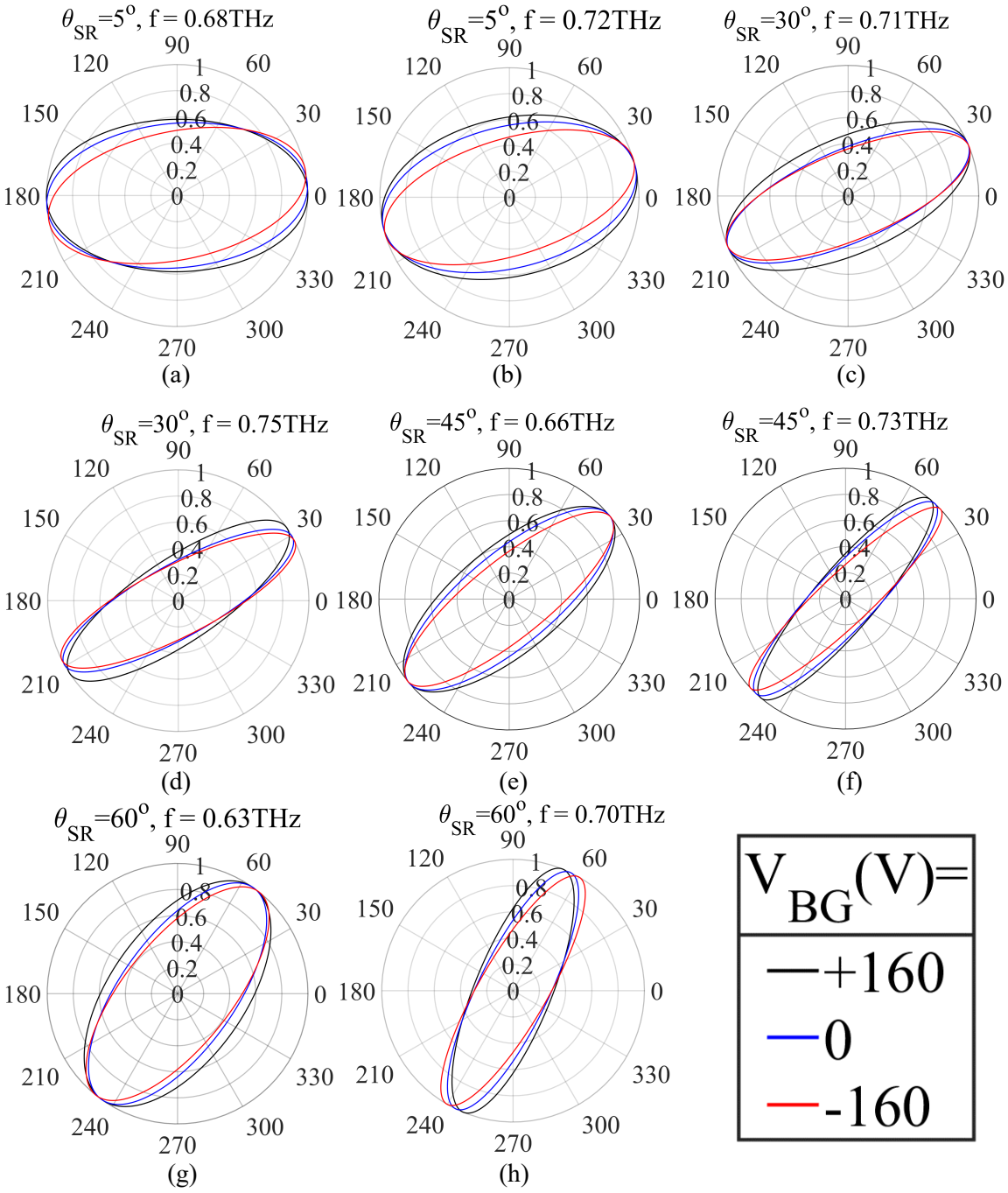

Figure 6.12: **(A-H)** Polarization state ellipses for different SR's angles considering the first transmitted temporal pulse.

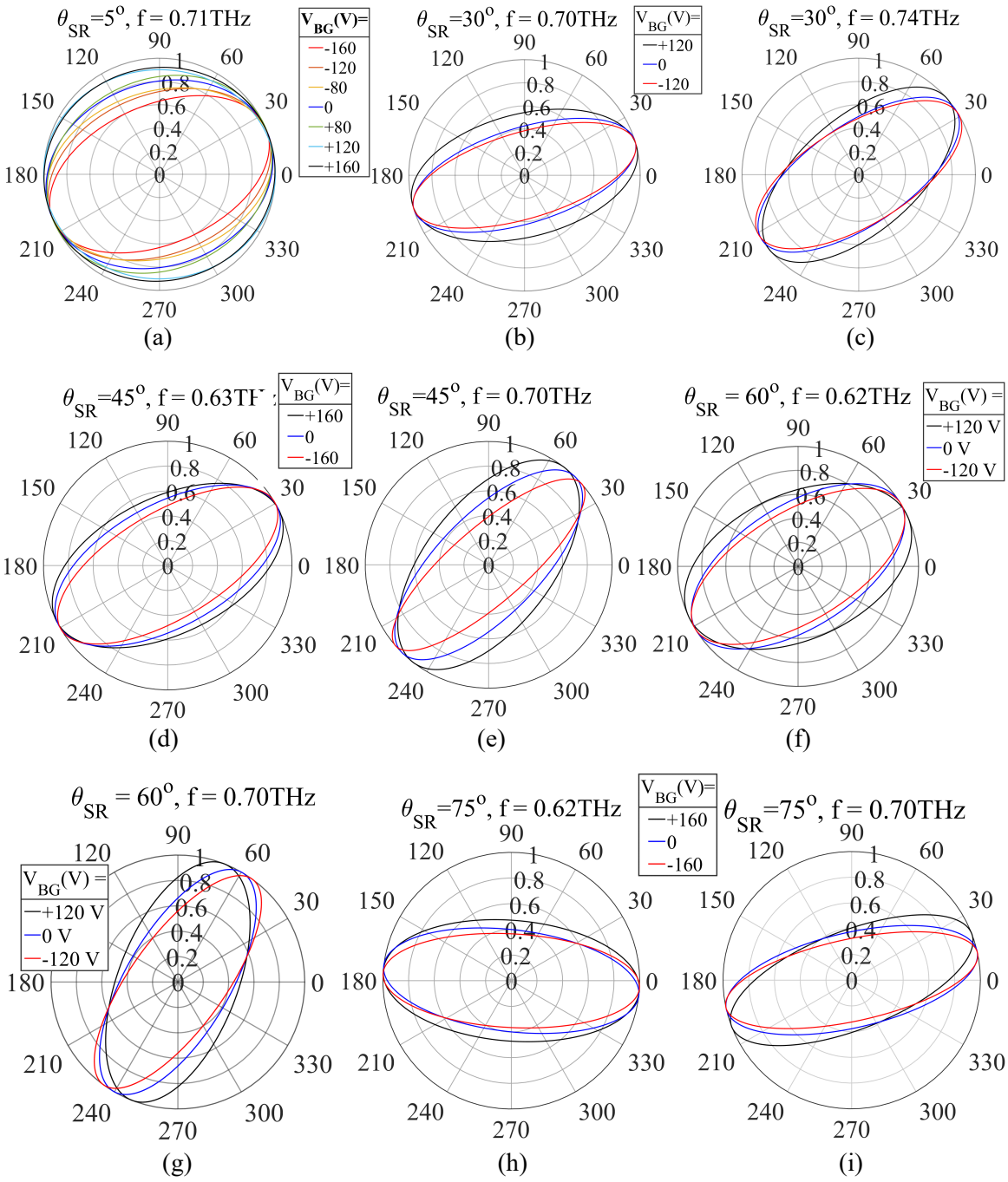

Figure 6.13: **(A-I)** Polarization ellipses for different SR's angles considering all transmitted temporal pulses.

finds application in spintronics or characterization of topological materials (Bader and Parkin, 2010; Y. Liu et al., 2020; Papaioannou and Beigang, 2021; C. Liu et al., 2021; Plank and Ganichev, 2018).

6.4.3 All pulses processing

The inclusion of all temporal pulses during post-processing, however, offers a further opportunity to enhance the modulation of the polarization state at the same frequencies. For example, integration of the MMs/graphene as a polarization modulator with a CW laser source requires the consideration of the etalon effect in case no anti-reflection coating of the back facet is utilized. This task is done by applying a unity rectangular window with a duration of 100 ps. The multiple transmission/reflection pulses in the substrate are shown by the black trace in fig. 6.6a. At $\theta_{\mathrm{SR}} = 30^{\mathrm{o}}$, the depth of CD is increased from 0.11 to 0.16 at resonance. When increase θ_{SR} to 60^{o}, $\Delta\Psi$ is enhanced from 8^{o} to 15^{o} whilst $\Delta\eta$ is increased from 0.11 to 0.15 at different THz frequencies. Almost perfect circular polarization is observed when rotating the SRs by 5^{o} at the Dirac point voltage as plotted in fig. 6.13a at 0.71 THz. The dynamic changes of Ψ and η exceed 21.5^{o} and 0.3, respectively, at 0.71 THz and $\theta_{\mathrm{SR}} = 5^{\mathrm{o}}$ as presented by the polarization ellipses in fig. 6.13a for various back-gate voltages. Moreover, decoupling of OA and CD is observed when rotating the SRs by any other angle besides $\theta_{\mathrm{SR}}= 5^{\mathrm{o}}$ as shown in figs. 6.13b-k and reported in table 6.3. When $\theta_{\mathrm{SR}}= 45^{\mathrm{o}}$, dynamics of $\Delta\eta$ are also maximized to >0.21

Table 6.3: Maximum modulation depth (MD) of OA and CD with/without considerations of the Fabry-Pêrot effect.

Signal processing	**Type of MD**	**θ_{SR} from x'-axis**	**Frequency (THz)**	**Active MD**
without considering of multiple reflections	$\Delta\eta$	5^{o}	0.72	>0.16
	$\Delta\Phi$	5^{o}	0.68	$>12^{\mathrm{o}}$
computing all temporal pulses	$\Delta\eta$	5^{o}	0.71	>0.3
		30^{o}	0.70	>0.16
		45^{o}	0.70	>0.21
		60^{o}	0.62	>0.15
		75^{o}	0.62	>0.11
	$\Delta\Phi$	5^{o}	0.71	$>21.5^{\mathrm{o}}$
		30^{o}	0.74	$>10^{\mathrm{o}}$
		45^{o}	0.70	$>12^{\mathrm{o}}$
		60^{o}	0.70	$>15^{\mathrm{o}}$
		75^{o}	0.70	$>9^{\mathrm{o}}$

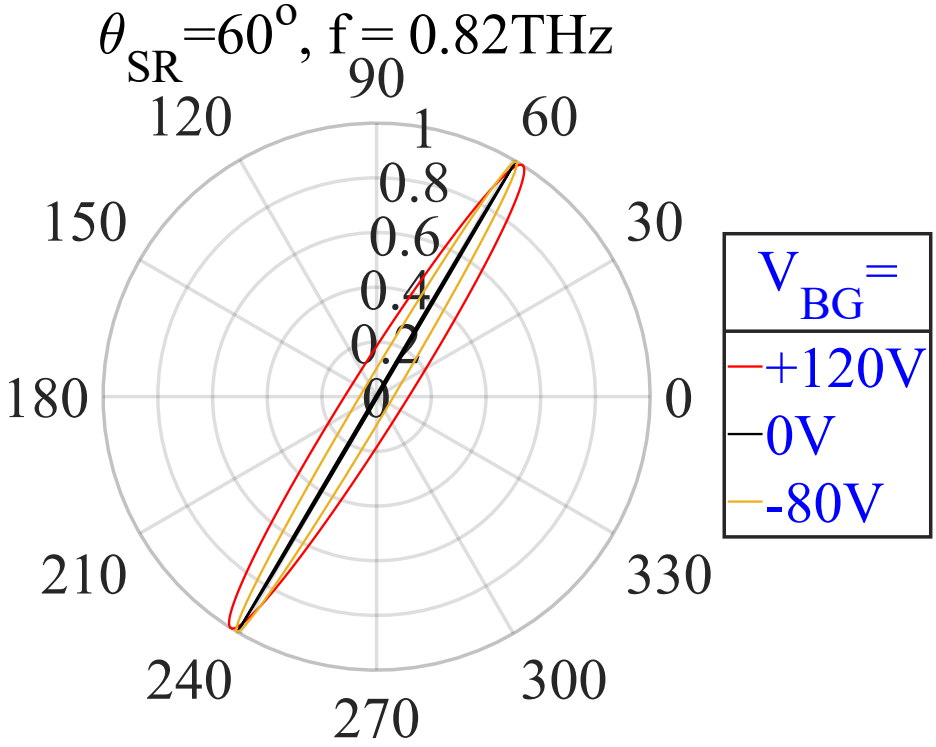

Figure 6.14: Almost perfect LP to CP conversion when applying different back-gate voltages and rotating the device for all pulses processing.

at 0.70 THz while continuous tuning of Ψ is exceeding >12° as shown in fig. 6.13b and 6.13c; respectively. It is worth mentioning that η is reversing its sign at 0.82 THz when rotating the device by $\theta_{SR} = 60°$ with its ellipticity becomes almost zero when $|E_{RCP}|/|E_{LCP}| \simeq 0$ at the applied voltage of 0 V as plotted in fig. 6.14.

6.5 Conclusion and outline

External integrated optoelectronic polarization modulators based on the interplay between graphene and metallic metamaterial arrays have been investigated using THz-TDS setup for applications such as GHz-speed communication, spectroscopy, and imaging. By electrostatic gating, the double-gated MMs/graphene resonators, polarization modulation was reported with dynamic conversions from linear to elliptical polarization states. An extensive study of the polarization behaviour of the device was presented in this chapter for various rotational angles and biasing conditions. Considerations of only the first temporal pulse during signal processing reveal an active tuning of OA by 12° at 0.68 THz and $\theta_{SR} = 5°$. At the same

angle, the modulation depth of ellipticity was dynamically changed by >0.16 at 0.72 THz. When processing all temporal pulses, almost perfect linear to circular polarization conversion was reported when rotating the device by 5° at 0.71 THz. At the same angle, maximum modulation depths of CD and OA were continuously manipulated by 0.3 and 21.5°, respectively. Almost independent control of CD and OA was demonstrated for all different rotational angles at distinct frequencies. These remarkable performances along with >GHz switching speed all-electronically represent a step forward toward various applications such as in next-generation wireless communication, spectroscopy, and imaging.

Achieved polarization modulation of OA is limited by the phase difference between the two circularly-polarized waves and the graphene conductivity range accessible experimentally. Due to fabrication dysfunction, continuous tuning of the spectral phase could be doubled as suggested by the simulated phase for different graphene conductivity if the graphene patch was aligned in contact with both resonators. Consequently, the modulation depth of OA could also be doubled reaching >25° for the first temporal pulses and >45° for the entire waveform when introducing an angle of 5°. The active modulation depth of CD can be improved by enhancing the graphene sheet absorption. This task could be accomplished by increasing the E-field concentration in the capacitive gap by reducing its distance. Enlarging the graphene rectangle shunting the two resonators may also be beneficial to increase dynamic manipulations of polarization states. Investigations of the cross-polarizers reveal some interesting findings. It could be there is an indirect coupling between the LC resonators and top-gate dipole causing a sharp absorption/peak in the spectra. Simulations of the phase using a cross-polarized transmitter and listener show that a sharp switching in phase already exists and does change significantly with different graphene conductivity at a frequency of about 50 GHz blueshifted from the resonance. Hence, more experiments on the cross polarizers should be conducted to explore the potential of having an electromagnetic induced transparency (EIT) phenomenon in this double-crossed dipole structure.

These remarkable performances of this device as a polarization modulator are coupled with a reconfiguration speed exceeding at least 3 GHz, which can be safely considered the fastest THz modulator to the best of our knowledge so far and 1000 times faster than the chiral or EIT polarization modulators done previously by our group in Stephen J. Kindness et al., 2020a; Stephen J. Kindness et al., 2019; Stephen J. Kindness et al., 2018. Moreover, this fast modulation speed is not affecting significantly the other figures of merits of the device's performance. Additionally, the selection of two different LC resonators' lengths instead of identical ones may reveal a sharp absorption or peak in the spectra since two resonances will be oscillating. This device's structure is already designed for independent biasing configurations to the two identical SRs through separate electrical lines (source/drain pads). This

independent electrical control of the source/drain pads allows using this device not only as a modulator but as a detector as well.

Polarization jitter should be controlled when using the device in coherent communication systems. The severe presence of the jitter decreases the signal-to-noise ratio during signal detection. Fluctuations in the applied voltages would cause phase noise, hence OA drifts. Therefore, the feedback loop can be utilized using all-electronic for polarization control to enhance the system's stabilization and accuracy.

Chapter 7

Conclusion and future work

7.1 Conclusion

Fast and integrated devices operating in the THz range with GHz reconfiguration speed have been demonstrated. This is a world record for graphene-based all-electronic driven at these frequencies. First, the THz frequencies were introduced in Chapter 1 highlighting some of the challenges and applications. This work represents an important milestone for metamaterial research as well. This approach has proved to be particularly efficient for achieving a continuous tuning of the polarization state of THz radiation.

In Chapter 2, a broad historical overview, as well as some of the theories describing these resonances, were discussed. Graphene as an active element has unique optical and electrical properties. It offers a wide range of carriers and a ps of relaxation lifetime. Previously, the performance of these integrated circuitry has been investigated by using FEM software and other simulation tools.

In Chapter 3, the THz modulator was designed and developed using a variety of tools. First, a 3D structure of a single unit cell was simulated by the RF module of COMSOL Multiphysics® software. The simulated amplitude and phase have supported the experimental optoelectronic behaviour. The frequency response of the modulator's equivalent circuit model was simulated via LTspice®, which had shown an estimated all-electronic cutoff frequency. Additionally, the fabrication procedure was explicitly discussed. For instance, simulated modulation depth can exceed 7 dB within the range of graphene conductivity accessible experimentally.

In Chapter 4, an efficient and ultrafast modulator operating in the THz range based on an MM array loaded with graphene was presented. A maximum amplitude modulation depth of >80% and phase modulation of >17° were reported around the resonant frequency of 0.8 THz. When considering all temporal pulses, the depth of amplitude and phase modulations increase to >90% and >27°, respectively.

Additionally, the ellipticity and rotational angle changes exceed 60% and 20°, respectively. Finally, the high performance of the device was achieved without affecting the measured reconfiguration speed which was reported to reach at least 3 GHz, limited only by the available instrumentation. This represents a progress of 30 times higher reconfiguration speed compared with previous similar all-electronic THz devices integrating graphene as a functional material. These results represent a breakthrough for many applications where fast and efficient THz circuitry is required, such as THz wireless communication or quantum electronics for active modelocking of QCLs.

In Chapter 5, this work reported the ultrafast modulation of a metamaterials array loaded with graphene at the resonance frequency of ∼0.8 THz by using the OPTP laser system (available at the Physics Department) and controlling electronically at the same time the graphene's Fermi level at the Dirac point. The modulation depth reported, ∼6 dB in power, is in very good agreement with the >7 dB reported all-electronically. By suitably calibrating the impinging fluence of the optical pump, it was possible to discern the induced conductivity dynamics in the silicon substrate from the graphene ones, which were recorded to be ∼2 ps representing a great match with previous literature reported on graphene. These results reinforce the use of metamaterial/graphene optoelectronic devices for the ultrafast modulation of THz waves.

In Chapter 6, external integrated optoelectronic polarization modulators based on the interplay between graphene and metallic metamaterial arrays have been investigated by terahertz time-domain spectroscopy. The amplitude modulation allowed the development of a novel experimental arrangement aiming at the achievement of polarization modulation. By electrostatic gating the graphene/metamaterials split resonators, polarization modulation was reported with dynamic conversions from linear to elliptical polarization states. When processing only the first temporal pulse, the amplitude extinction ratio was demonstrated achieving >5.5 dB at 0.74 THz for the E_x polarized waves. The spectral phase could be actively tuned by >22° at 0.63 THz for the E_y polarization. The modulation depths of η were dynamically changed by >0.16 in ellipticity ratio at 0.72 THz while Ψ were continuously rotated by >12° at 0.68 THz. When processing all temporal pulses, the amplitude modulation depths were enhanced to exceed 7.5 dB at the resonant frequency for the E_x polarization. The spectral phase was dynamically manipulated by >25° at 0.70 THz for the E_x polarization. Almost independent control of CD and OA was demonstrated achieving $\Delta\eta$= >0.3 and $\Delta\Psi$= >21.5°, respectively, at 0.71 THz. These remarkable performances along with >GHz switching speed all-electronically represent a step forward toward various applications such as in next-generation wireless communication, spectroscopy, and imaging.

7.2 Future work

7.2.1 RF measurements up to 100 GHz speed

Because of the high conductivity and short optical response time of graphene, this top-gated integrated graphene THz device can be used as a very fast modulator/detector. We experimentally verified that the response time of our device is larger than 3 GHz (Chapter 4), which is limited by the available instrumentation. The generated RF frequency was limited to only 3 GHz by the function generator. Before sending the RF signal to the modulator, it was mixed with a DC source meter from Kethley by a bias-tee operating up to 12 GHz. The RF power at the output port of the bias-tee degrades for frequencies >12 GHz. The output signal from the modulator is fed to an external amplifier, which is limited to 8 GHz. For characterizations of the output RF signal, the oscilloscope is limited to 0.5 GHz only, hence a spectrum analyzer was used for frequencies above 0.5 GHz. The spectrum analyzer is also limited to 3 GHz. In addition to the limited range of operations, the cost of all-electronic instruments would dramatically increase as the operating frequency increases.

The phase of the sinusoidal signal was not controlled, hence the phase of the RF signal reaching each individual split resonator is ambiguous. Controlling the phase of the RF signal feeding the modulator may help reducing the parasitic capacitances and cross-talk between the individual unit cells, which could enhance the modulation speed. The interdigitate arrangement of the single-unit cell in an array is already designed to reduce the effect of parasitic capacitance, thus the next step would be feeding the modulator with a well-determined phase of the RF signal. Additionally, improvements to the operating speed could be achieved by reducing the overall footprint to near λ size of about 200×200 μm. The source/drain pads play a significant role in determining the reconfiguration speed. Therefore, reducing their size and increasing the thickness of the insulating layer underneath the contact pad would enhance the modulation speed.

All the other components, e.g. integrated amplifier and bias-tee, needed to perform these measurements operate till a certain range and are expensive and work only in a limited range. Further to this, synchronization of all MM units, optimization of the boards and waveguides, impedance matching starts playing a role at high frequencies, making the exact determination of the final cut-off frequency challenging from the technical point of view.

7.2.2 Vector Network Analyzer measurements

A vector network analyzer (VNA) is one of the key measurement techniques based on continuous waves (CW) sources. It can obtain the frequency contents of under-testing devices by recording and analyzing the incident and response signals in both

magnitude and phase (Ding et al., 2022). Researchers use VNA to test chips, devices, and systems operating in the microwave, terahertz, or optics region.

All-electronic response of the device (A) is tested via a VNA as schematically plotted in fig. 7.1. The input RF frequency is swept from 1 to 20 GHz. The VNA transmission (S_{21}) is first calibrated without the modulator as shown by the black line in fig. 7.2. The RF transmission is then connected through the top gate while grounding the drain pad. The RF transmission is mixed with a DC component via a bias-tee operating up to 12 GHz. The DC offset is important to control the doping level of the graphene sheet. The RF output is then taken across the source and drain pads. The top-gate voltage (V_{TG}) is swept between -50 to +50 V, while the voltage between source/drain pads (V_{SD}) is fixed to 0.7 V both using a Kethley source meter unit. The current is also monitored and recorded to be about 0.7 μA for I_{SD}, while only a few nA of I_{TG} are measured similar to the leakage current measured in Chapter 7.2.1. The frequency response of the integrated graphene modulator is showing a well-established response for the entire range with a mean RF magnitude of about -28 dB. Due to impedance mismatch, the output RF amplitude has strong fluctuations. About 3 dB of amplitude modulation is observed at about 4 GHz, which can be used for data transmission measurements as indicated by the inset of fig. 7.2. The measured impedance of the transmission through the modulator shows an average resistivity of approximately 2 $k\Omega$ as plotted in fig. 7.3a. The strongest change in resistivity is observed by $\Delta R = \sim 0.4$ $k\Omega$ at around 4.23 GHz. The overall

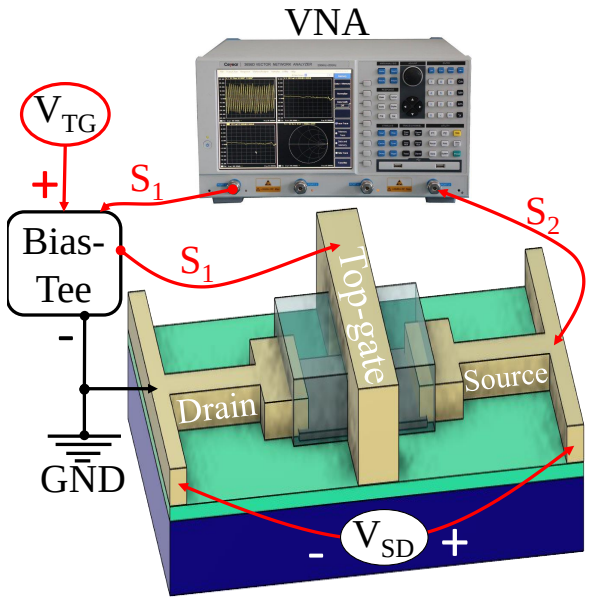

Figure 7.1: Schematic view of the all-electronic VNA setup operating up to 20 GHz.

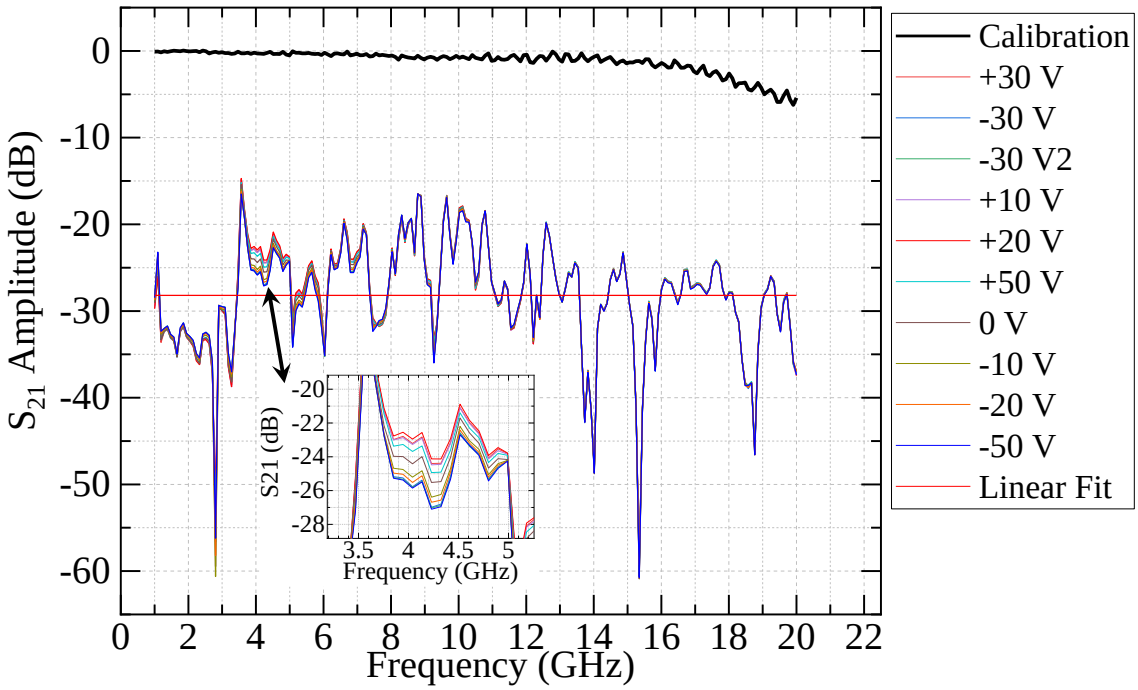

Figure 7.2: Measured frequency response through RF cables (calibration line) and integrated graphene/MMs modulator (various colors). The inset is a zoomed-in picture indicating the most significant amplitude modulation.

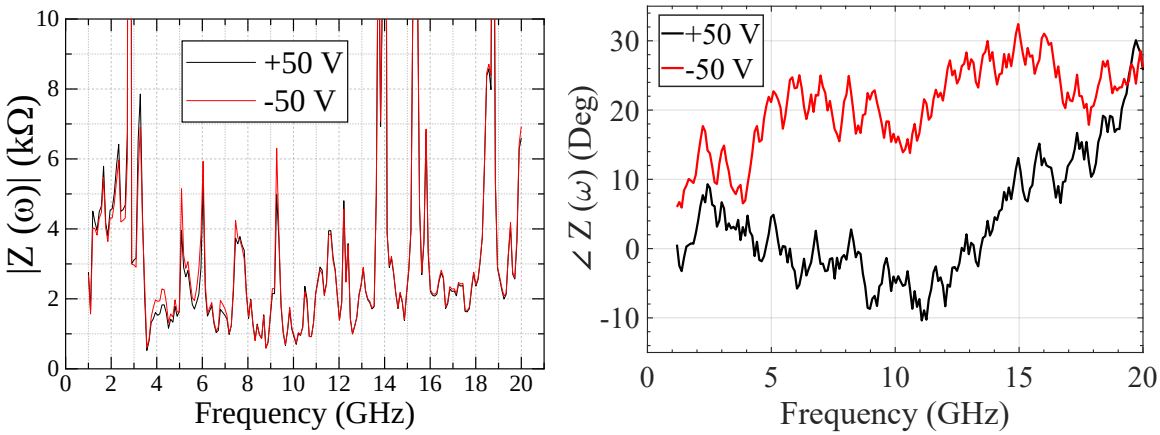

(a) (b)

Figure 7.3: Measured impedances of the integrated graphene/MMs device by the VNA (S_{21} port) at two applied top-gate voltages representing the overall system's resistivity (a) and wrapped phase shifts (b).

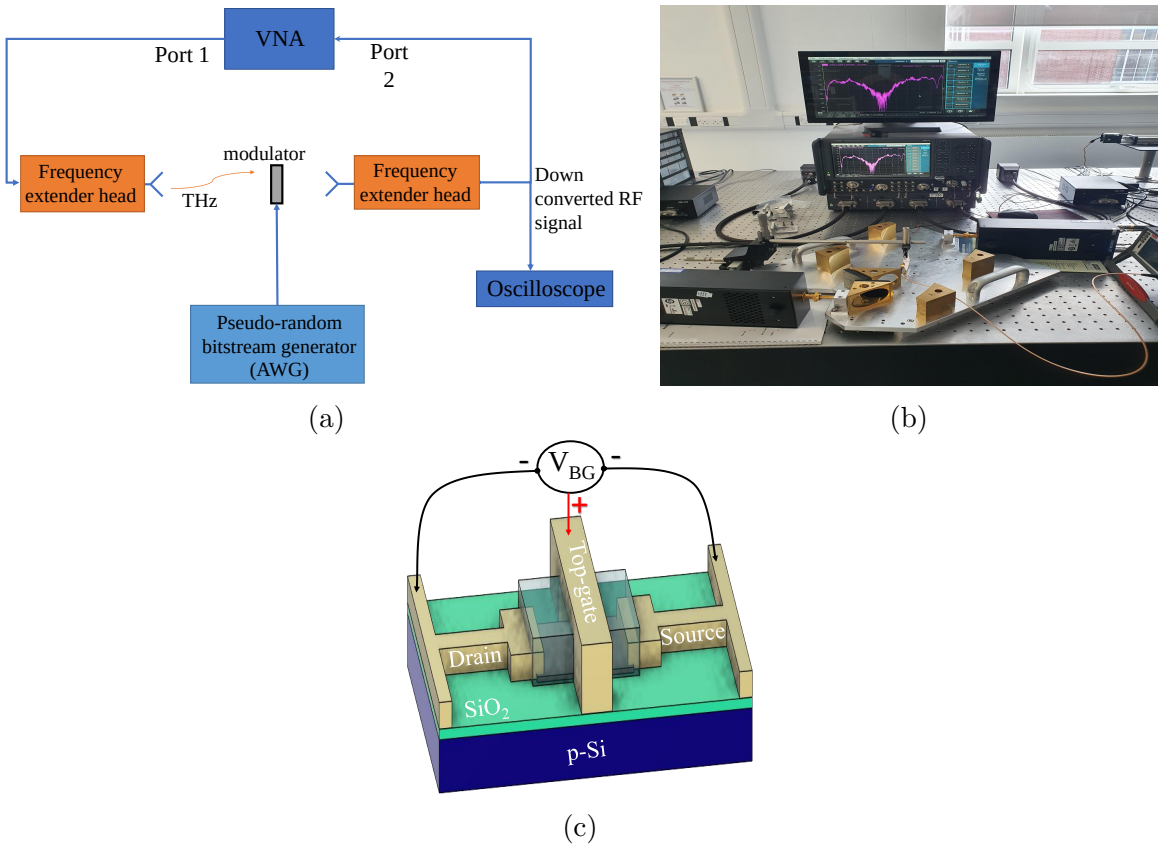

Figure 7.4: Schematic diagram (a) and benchtop setup (b) of the quasi-optic VNA system. (C) Electrical bias configuration.

system's phase is shifted by >20° when applying different voltages through the top gate as shown in fig. 7.3b. These measurements could be helpful for the careful designing of impedance mismatch compensations. It is hard to simulate and design a prior impedance-matched device, e.g. graphene conductivity is not known exactly.

7.2.3 Real setup for data transmissions communications at 700-800 GHz carrier frequency

The first demonstration of coded metamaterials was represented by (Cui et al., 2014). The digitally coded metamaterials were programmed to manipulate the emergent EM waves at a speed of 14 GHz. After this pioneering work, numerous metamaterial designs have been constructed aiming to realize various applications, such as beam-steering, beam-forming, imaging, and holography (Zeng et al., 2021). These works have shown the capability to actively program the metamaterials with distinct coding

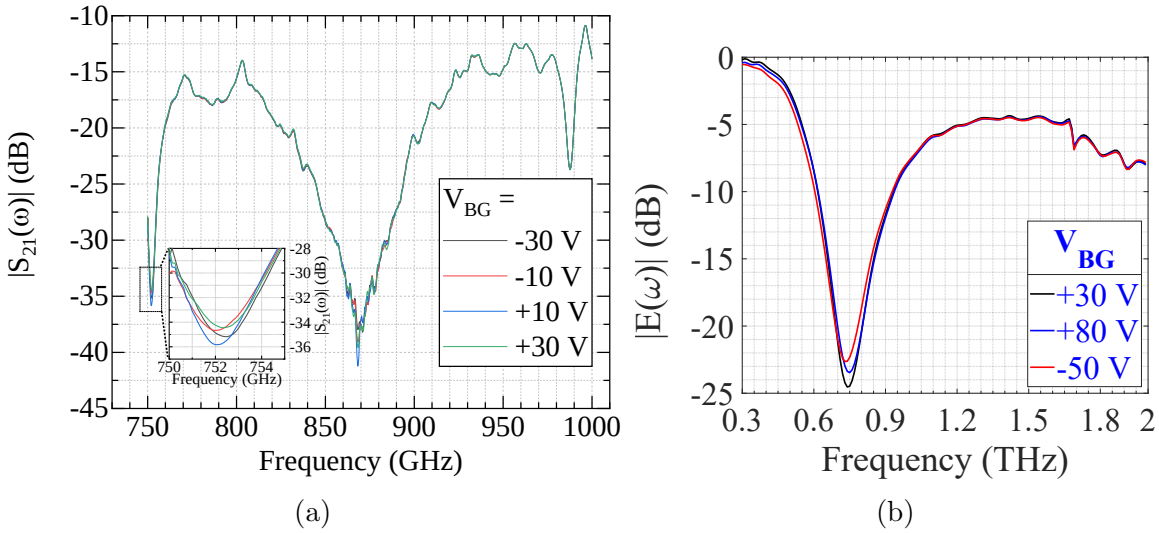

(a) (b)

Figure 7.5: (a) Continuous waves (CW) of a THz source passing through the integrated graphene/MMs modulator (S_{21}) for different back-gate voltages. (b) THz-TDS measurements of the graphene/MMs integrated array.

frames. The coding speed and precision are gradually increasing with advances in THz technologies. Deployments of THz modulators have so far been characterized based on quasi-optic systems.

The hybrid graphene modulator is tested in a quasi-optic system in a collaboration with Dr. Stephen Hanham at Birmingham University. Fig 7.4a and 7.4b represent the schematic diagram and the real testbed setup. A pair of frequency extenders are connected to the VNA, which enabled the measurements in the waveguide band between 0.75 to 1.1 THz. The graphene/MMs modulator is positioned at the focal point of the system with a focused transmitted beam a few millimeters in diameter. The modulator is electrically controlled by a Kethely source meter connected to the back gate while grounding the source/drain pad as illustrated in fig. 7.4c. For the range of several back-gate voltages (V_{BG}), the amplitude of the THz source passing through the modulator can be controlled as shown in fig. 7.5a. The device was partially damaged prior to conducting these tests as shown by the THz-TDS preliminary measurements shown in fig. 7.5b. This testbed experiment represents great progress toward the demonstration of data streaming using communication schemes, e.g. OOK, ASK, or QAM, by modulating THz carrier frequencies. This is the correct direction but these measurements need to be done more systematically, the sample started to be damaged, and we were close to an absorption line.

7.3 Perspective

Advances in terahertz devices will increase the pace to bridge the technology and application gap of the THz frequencies. Power generation, energy dissipation, and chip miniaturization are some of the key components to motivate efforts toward more developments in the upcoming years. Exploring THz science and technology using both electronic and photonic methodologies have obtained more attention ranging from fundamental research to reliable and practical technologies. Some of the brainstorming ideas could be commercialized if there are enough efficient and robust devices operating in the THz regime. The great progress in recent years towards THz instrumentation could be motivated by achieving compact and user-friendly benchtop systems with relatively low costs (Daniel M. Mittleman, 2017). After the successful execution and demonstration of the 5G wireless cellular systems, intensive attention is being directed toward the next generations of wireless communication as illustrated by fig. 7.6. All of these hungry information strategical applications have triggered the exploration of THz frequencies looking for a wider unallocated bandwidth in the spectrum, despite all of the limitations of THz waves such as small directional beam sizes and short traveling lengths. New technologies for the field of wireless communications are required since most RF/microwave techniques are no longer applicable. Demand for speed and bandwidth of data throughputs is rapidly increasing with an unfeasible end to this need. Moreover, hot topic areas may

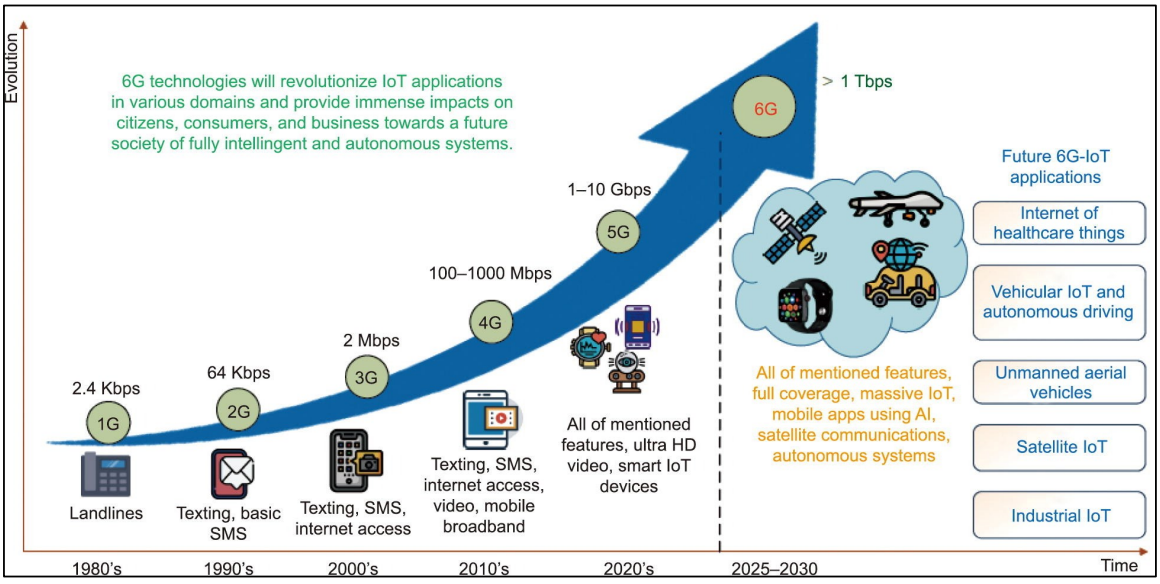

Figure 7.6: Revolutions of wireless communication systems. Source (Huang, Y. Shen, and J. Wang, 2022).

cover frequency tuning, GHz modulation speed, only electronically driven devices, power loss compensation, scalability, reduced wall-plug efficiency, reduced complexity of integration and fabrication processes, robustness, and reliability. Devices operating at >100 GHz are being extensively investigated for successful manipulations of THz radiations. The early demonstration of THz modulators (K. Unterrainer, 2000; Kleine-Ostmann et al., 2004b; L. Zhang et al., 2020b) has enabled accomplishments of high modulation speed and depth as well as a reduction in insertion loss (Hou-Tong Chen et al., 2006; Nouman et al., 2016; P. Q. Liu et al., 2015).

Other important elements in THz systems that could be the center of research and development include splitters (Pandey, Kumar, and Nahata, 2010; Reichel, R. Mendis, and D. M. Mittleman, 2016), beam forming/steering (Monnai et al., 2013a; Steinbusch et al., 2014), multiplexer (Karl et al., 2015; J. Ma et al., 2017a), spatial light modulators (Watts et al., 2014b; J. Ma et al., 2017b; Zaman et al., 2022a; Jessop et al., 2016), frequency tuning (Stephen J. Kindness et al., 2018), polarization modulator (Stephen J. Kindness et al., 2019; Stephen J. Kindness et al., 2020a; Zaman et al., 2023), and filters (Libon et al., 2000; Rajind Mendis et al., 2010). Recently, active all-electronic controllable beam forming focusing and steering devices have been demonstrated with the capability to dynamically manipulate the THz light wavefront (Monnai et al., 2013a; Steinbusch et al., 2014; Monnai et al., 2013b; K. Liu et al., 2017). Progress in this technology is a great benefit for various applications such as next-generation wireless communications, quasi-optical links, and kiosk down-leading.

Different active elements have been integrated with THz devices to enhance the ability to manipulate THz wave properties such as Ion-gel, 2DEG, graphene, perovskites, and 3D Dirac materials. Similar to the band-gap energy of graphene and Weyl semimetals, the 3D Dirac materials have a linear gapless dispersion (W. J. Lee et al., 2022; Riccardo Degl'Innocenti, H. Lin, and Navarro-Cía, 2022). The wide range of implementations of these active materials is mainly due to their remarkable physical interactions with optoelectronic devices including an ultra-wide range of carrier mobility in the order of $\sim$7200 $cm^2/(Vs)$ (Efetov and P. Kim, 2010; De Fazio et al., 2019), absorption saturation, and ultrafast relaxation lifetime within a couple of ps. The remarkable properties of these active elements when integrated with optoelectronic devices will shape the future of EM wave manipulations in the THz gap.

Since optoelectronic devices can be scaled down as the carrier frequency increase, several arrays can be designed in microscale pixel arrangements with independent biasing controls. This feature is an important key to unlocking a wide range of applications such as coded THz radiations and logic gates for both holographic and communication communities. Additionally, multi-pixel of THz sources can work as a phased array capable of re-engineering the THz wave's wavefront (Assefzadeh and Babakhani, 2017; Wu and Sengupta, 2017). Integration of subwavelength sensing

components near the THz source transmitter can enhance the technology of ultra-wide range of spectroscopy detection and sensing (Wu and Sengupta, 2016). Real-time imaging is an essential technology for the medical and chemical communities. Advances in THz imaging would reveal more information regarding skin or even under-skin pictures. Because of non-ionization properties, THz waves have the potential to cover many aspects of medical imaging because of their coherency, time-domain resolution, and relatively low noise imaging. Advances in the THz imaging field require more improvements in the spatial and axial resolutions, depths of propagation inside an under-testing material, and high data acquisition techniques. Progress in THz imaging depends on advances and developments in THz generations, THz light manipulation, and THz detection.

The recent advancements in the use of metamaterials have been implemented for logic gates in the terahertz spectrum. Different types of metamaterials such as MEMS-based metallic metasurfaces and coded metamaterials have been demonstrated for logical operations like XOR, XNOR, and NAND. The next generation of THz metamaterial modulators will focus on further integration of different functionalities such as active beam forming and steering, real-time controllable phase gradients or distributions, and active wavefront control. Integrated elements capable of reproducing logic gates such as AND and OR together with coding metamaterials are hot topics in the THz field, and metamaterials offer the efficiency, miniaturization, and integration scalability to address these challenges. These key features enhance the potential use of metamaterials for wireless communication in the terahertz spectrum. The modulation depth and reconfiguration speed of the devices are key parameters that play a fundamental role in many applications such as wireless communication or real-time imaging. The power consumption, driving voltage, packaging, and fabrication technological hurdles are key factors of concern for specific applications/experiments. The potential of coded metamaterials for implementing logic gates and programmable metasurfaces can be extended to holographic and communication applications.

The importance of terahertz beam steering technologies are in various applications such as terahertz radars, wireless communication, and imaging systems. Conventional terahertz beam steering technologies include electromechanical scanning, phased array, frequency scanning, and multifeed switching, as well as newer technologies utilizing metamaterials and metasurfaces. Various methods for beam steering in the terahertz frequency range such as mechanical scanning, structured MEMS surfaces, phased-array technology, electronic device-based phase shifters, optical technology-based phase shifters, and tunable material-based phase shifters. Alternative materials for designing terahertz phase shifters can be achieved using LC, graphene, and vanadium dioxide (VO_2). Different materials and technologies have been proposed for reconfigurable terahertz metasurfaces, including phase-transition materials such as

GST and VO_2, electrically tunable materials such as LC and graphene, and MEMS technology. These materials and technologies allow for tunable and reconfigurable metasurfaces that can achieve beam steering and other functionalities. These advancements include the development of metasurfaces for applications such as holography, imaging, sensing, and communication, as well as the exploration of new materials and fabrication techniques. For instance, the reflective element was made up of Au antennas/graphene, a silicon spacer, and Ag/Al reflective film shown in fig. 7.7. The same article, (Fu et al., 2020), highlights the potential of metasurfaces for future technologies such as quantum computing and 5G communication. Overall, the article provides a comprehensive overview of terahertz beam steering technologies and their potential applications.

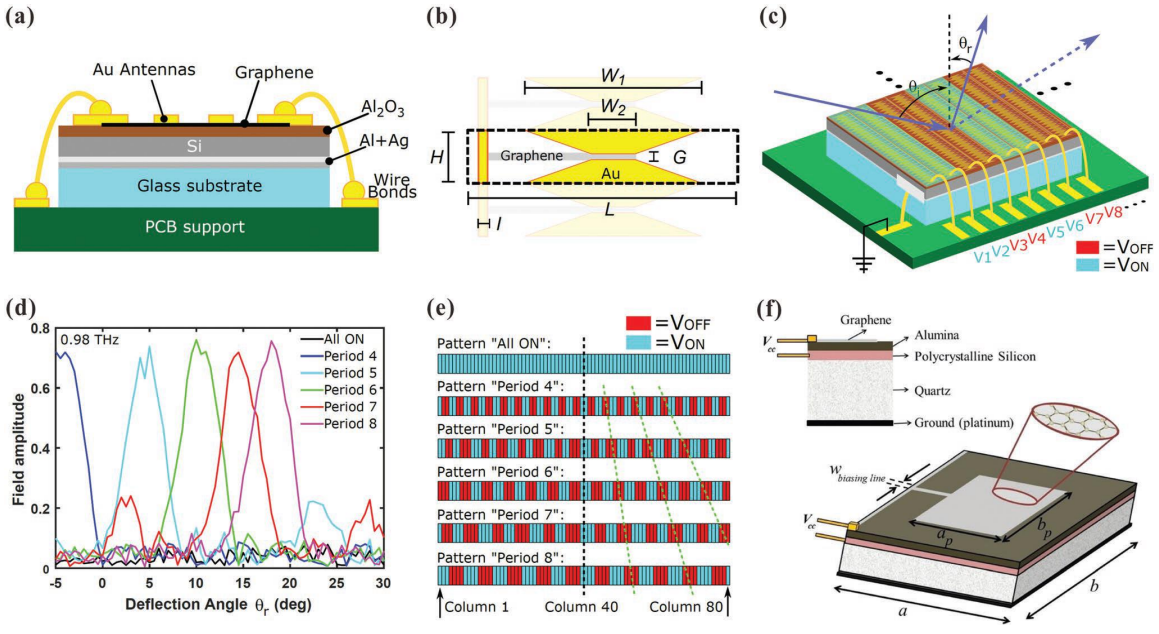

Figure 7.7: Electrically tunable beam steering devices (Fu et al., 2020).

Appendix A

A.1 THz waves propagation

Most EM wave propagation is described by Maxwell's formalism, which is a set of questions governing the interrelationship between Components of the EM waves such as electric field E (V/m), magnetic field strength H (A/m), and magnetic flux density B (Wb/m^2 = Vs/m^2). The electric and magnetic properties are generated by the electric charge density ρ (C/m^3 = As/m^3), and electric current density J (A/m^3). The EM wavefront propagating inside a medium is manipulated following the material's permittivity ϵ (F/m = As/Vm) and permeability μ (H/m = Vs/Am). ϵ relates both E and D, while μ connects H to B. Based on Maxwell's equations, changes in B produce E while changes in both current (J) and D generate H. In an antenna, a flow of current creates H resulting in changes to E and vice versa. Mediums with constant ϵ and μ are referred to as homogeneous and isotropic, where the propagation properties of EM waves are location independent in all directions. Additionally, the EM field power does not influence the physical principles of linear mediums (Carpintero et al., 2015). Lossy mediums have generally complex values of ϵ and μ where the relative ϵ and μ depend on the material's structure (ϵ_r and μ_r) and free space propagation constants (ϵ_0 and μ_0).

THz frequencies propagating in free space have a relatively large beam size compared with their wavelength, hence careful consideration of beam diffraction is required. Propagation at THz frequencies can be described spatially as quasi-optics (Carpintero et al., 2015). The Gaussian profile is a natural choice for analyzing quasi-optical beams propagating in a well-defined direction. In practice, the lowest-order Gaussian mode often suffices for a good description of a propagating beam. In free space, components of monochromatic and spatially coherent waves can be described by the complex E-field E(x,y,z) traveling in the z-direction. Hence, the time-independent (Helmogoltz) wave equation can be applied (Carpintero et al., 2015). For a large-collimated beam, the Helmogoltz equation can be further simplified leading to the paraxial wave formula. This latter equation has a simple solution that describes the

spatial propagation of the Gaussian beam after normalization as follows (Carpintero et al., 2015):

$$E(x,y,z) = \sqrt{\frac{2}{\pi \mathrm{w}^2(z)}} \cdot \exp\left[-\left(\frac{(x^2+y^2)}{\mathrm{w}^2(z)}\right)\right] \cdot \exp\left[-j\left(\frac{k(x^2+y^2)}{2R(z)} + kz + \phi_0(z)\right)\right], \tag{A.1}$$

where the Gaussian beam phase $\phi_0(z)$, or Guoy phase, can be described as (Carpintero et al., 2015):

$$\phi_0(z) = \tan^{-1}\left(\frac{\lambda z}{\pi \mathrm{w}_0^2(z)}\right). \tag{A.2}$$

The beam waist is reaching its minimum at w_0 at distance z=0. After traveling distance z, the Gaussian beam broadens its radius (w) and its curvature radius (R) as follows (Carpintero et al., 2015):

$$\mathrm{w}(z) = \mathrm{w}_0\sqrt{\left[1+\left(\frac{\lambda z}{\pi \mathrm{w}_0^2}\right)^2\right]}, \tag{A.3}$$

$$R(z) = z + \frac{1}{z}\left(\frac{\pi \mathrm{w}_0^2}{\lambda}\right)^2. \tag{A.4}$$

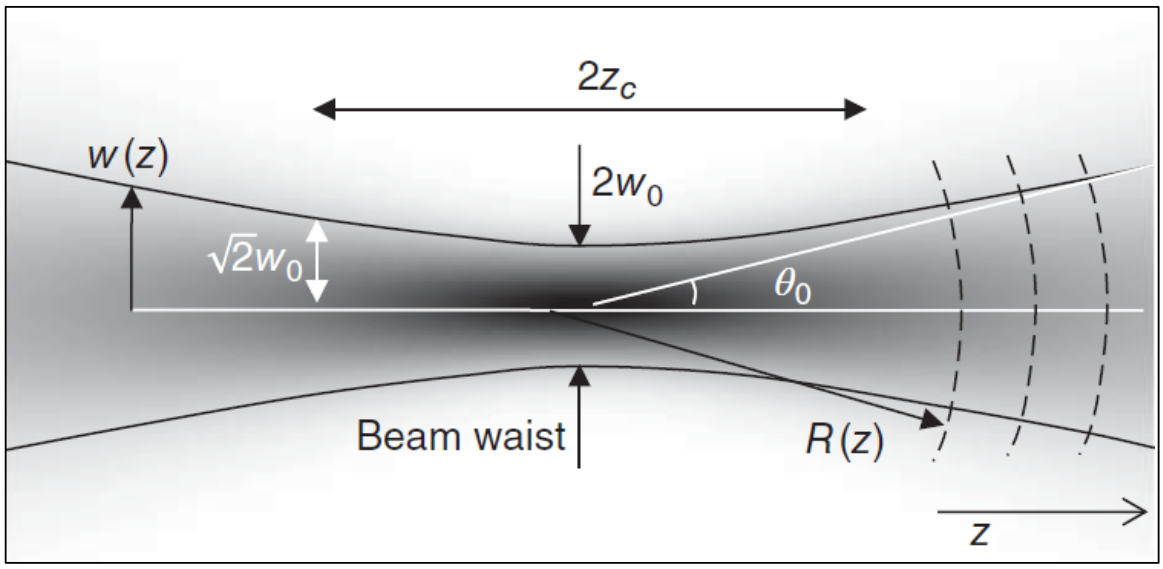

Figure A.1: A Gaussian beam profile for spatial propagation (Carpintero et al., 2015).

As the beam diffracts away from w_0, its amplitude decreases and its curvature radius broadens. As a result, the beam remains almost quasi-collimated within a range of $-z_c < z < z_c$. The confocal length (z_c) or Rayleigh distance can be calculated as $z_c = \pi w_0^2/\lambda$ (Carpintero et al., 2015). The beam propagation distances can be categorized into near or far fields. A near-field is when the traveling distance is much smaller than the confocal distance, while a far-field is when propagating much longer than the Rayleigh range. When $z \ll z_c$, the diffraction angle of the beam radius increase linearly with z and can be approximated as $\theta_0 = \tan^{-1}\{\lambda/(\pi w_0)\}$ (Carpintero et al., 2015). As the THz wavelength becomes smaller, the beam's radius w(z) is smaller while R(z) and θ_0 are larger. Fig. A.1 illustrates the characteristic elements of a propagating Gaussian beam.

References

Abdullah M. Zaman et al. (2021). "Graphene-based External Optoelectronic Terahertz Modulators for High Speed Wireless Communications". In: *2021 14th UK-Europe-China Workshop on Millimetre-Waves and Terahertz Technologies (UCMMT)*, pp. 1–3. DOI: 10.1109/UCMMT53364.2021.9569931.

Abdullah M. Zaman et al. (2022a). "Active Polarization Modulation of Terahertz Radiation Using Metamaterial/Graphene-Based Optoelectronic Devices". In: *2022 47th International Conference on Infrared, Millimeter and Terahertz Waves (IRMMW-THz)*, pp. 1–3. DOI: 10.1109/IRMMW-THz50927.2022.9895720.

Abdullah M. Zaman et al. (2022b). "Terahertz Metamaterial Optoelectronic Modulators with GHz Reconfiguration Speed". In: *IEEE Transactions on Terahertz Science and Technology* 12.5, pp. 520–526. DOI: 10.1109/TTHZ.2022.3178875.

Abdullah M. Zaman et al. (2022c). "Towards Ultrahigh Modulation Speed of Terahertz Optoelectronic Devices Based on Metamaterial/Graphene Split-Ring Resonators". In: *2022 9th International Conference on Optical Terahertz Science and Technology (OTST2022), held at Mercure Budapest Castle Hill Hotel, Budapest, Hungary, June 19-24, 2022*. URL: https://www.otst2022.hu/.

Abdullah M. Zaman et al. (2022d). "Ultrafast modulation of a THz metamaterial/graphene array integrated device". In: *Appl. Phys. Lett.* 121.9, p. 091102. DOI: https://doi.org/10.1063/5.0104780.

Abdullah M. Zaman et al. (2023). "Versatile and active THz wave polarization modulators using metamaterial/graphene resonators". In: *Front. in Nanotechnol.* 5. ISSN: 2673-3013. DOI: 10.3389/fnano.2023.1057422. URL: https://www.frontiersin.org/articles/10.3389/fnano.2023.1057422.

Alexander-Webber, Jack A et al. (Dec. 2016). "Encapsulation of graphene transistors and vertical device integration by interface engineering with atomic layer deposited oxide". In: *2D Materials* 4.1. doi: 10.1088/2053-1583/4/1/011008, p. 011008.

Almond, Nikita W. et al. (2020). "External cavity terahertz quantum cascade laser with a metamaterial/graphene optoelectronic mirror". In: *Appl. Phys. Lett.* 117.4, p. 041105. DOI: https://doi.org/10.1063/5.0014251.

Assefzadeh, M. Mahdi and Aydin Babakhani (2017). "Broadband Oscillator-Free THz Pulse Generation and Radiation Based on Direct Digital-to-Impulse Architecture".

In: *IEEE Journal of Solid-State Circuits* 52.11, pp. 2905–2919. DOI: 10.1109/JSSC.2017.2739180.

Bader, S.D. and S.S.P. Parkin (2010). "Spintronics". In: *Annual Review of Condensed Matter Physics* 1.1, pp. 71–88. DOI: 10.1146/annurev-conmatphys-070909-104123.

Banerjee, Sabyasachi, Bishnu P. Pal, and Dibakar Roy Chowdhury (2020). "Resonance phenomena in electromagnetic metamaterials for the terahertz domain: a review". In: *Journal of Electromagnetic Waves and Applications* 34.10, pp. 1314–1337. DOI: 10.1080/09205071.2020.1713227.

Barron, L.D. (2009). *Molecular Light Scattering and Optical Activity*. Cambridge University Press. ISBN: 9781139453417. URL: https://books.google.co.uk/books?id=rTx7aG18854C.

Beck, M. et al. (Apr. 2019). "High-speed THz spectroscopic imaging at ten kilohertz pixel rate with amplitude and phase contrast". In: *Opt. Express* 27.8, pp. 10866–10872. DOI: 10.1364/OE.27.010866. URL: https://opg.optica.org/oe/abstract.cfm?URI=oe-27-8-10866.

Berry, C. W. et al. (Mar. 2013). "High-speed THz spectroscopic imaging at ten kilohertz pixel rate with amplitude and phase contrast". In: *Nat Commun* 4.1, p. 1622. DOI: 10.1038/ncomms2638.

Born, Max and Emil Wolf (1999). *Principles of optics: electromagnetic theory of propagation, interference and diffraction of light*. Seventh (Expanded). Cambridge, UK: University of Cambridge.

Breusing, M. et al. (Apr. 2011). "Ultrafast nonequilibrium carrier dynamics in a single graphene layer". In: *Phys. Rev. B* 83 (15), p. 153410. DOI: 10.1103/PhysRevB.83.153410. URL: https://link.aps.org/doi/10.1103/PhysRevB.83.153410.

Brida, D. et al. (June 2013). "Ultrafast collinear scattering and carrier multiplication in graphene". In: *Nat Commun* 4 (1), p. 1987. DOI: 10.1038/ncomms2987. URL: https://doi.org/10.1038/ncomms2987.

Burghoff, David et al. (May 2014). "Terahertz laser frequency combs". In: *Nature Photon* 8.6. doi: https://doi.org/10.1038/nphoton.2014.85, pp. 462–467.

Burton, Oliver J. et al. (June 2019). "The Role and Control of Residual Bulk Oxygen in the Catalytic Growth of 2D Materials". In: *J. Phys. Chem. C* 123.26. doi: 10.1021/acs.jpcc.9b03808, pp. 16257–16267.

Cai, Xiaodong et al. (2021). "Dynamically controlling terahertz wavefronts with cascaded metasurfaces". In: *Advanced Photonics* 3.3, p. 036003. DOI: 10.1117/1.AP.3.3.036003. URL: https://doi.org/10.1117/1.AP.3.3.036003.

Carpintero, G et al. (2015). *Semiconductor TeraHertz Technology: Devices and Systems at Room Temperature Operation*. Available from: ProQuest Ebook Central. New York, UNITED STATES: John Wiley & Sons, Incorporated. URL:

https://ebookcentral.proquest.com/lib/lancaster/detail.action?docID=4039863.

Chan, Wai Lam et al. (May 2008). "Terahertz imaging with compressed sensing and phase retrieval". In: *Opt. Lett.* 33.9, pp. 974–976. DOI: 10.1364/OL.33.000974. URL: https://opg.optica.org/ol/abstract.cfm?URI=ol-33-9-974.

Chan, Wai Lam et al. (2009). "A spatial light modulator for terahertz beams". In: *Applied Physics Letters* 94.21, p. 213511. DOI: 10.1063/1.3147221. eprint: https://doi.org/10.1063/1.3147221. URL: https://doi.org/10.1063/1.3147221.

Chandra, Y. et al. (2020). "Advances in finite element modelling of graphene and associated nanostructures". In: *Materials Science and Engineering: R: Reports* 140, p. 100544. ISSN: 0927-796X. DOI: https://doi.org/10.1016/j.mser.2020.100544. URL: https://www.sciencedirect.com/science/article/pii/S0927796X20300024.

Chen, H.-T. et al. (2006). "Active terahertz metamaterial devices". In: *Nature* 444.7119, pp. 597–600. DOI: 10.1038/nature05343. URL: https://doi.org/10.1038/nature05343.

Chen, H.-T. et al. (Apr. 2008). "Experimental demonstration of frequency-agile terahertz metamaterials. Nature Photonics". In: *Nature Photon* 2 (5), pp. 295–298. DOI: 10.1038/nphoton.2008.52.

Chen, H.-T. et al. (Feb. 2009). "A metamaterial solid-state terahertz phase modulator". In: *Nature Photonics* 3 (3), pp. 148–151. DOI: 10.1038/nphoton.2009.3.

Chen, Hou-Tong, Antoinette J Taylor, and Nanfang Yu (June 2016). "A review of metasurfaces: physics and applications". In: *Reports on Progress in Physics* 79.7. doi: 10.1088/0034-4885/79/7/076401, p. 076401.

Chen, Hou-Tong et al. (Nov. 2006). "Active terahertz metamaterial devices". In: *Nature* 444.7119. doi: https://doi.org/10.1038/nature05343, pp. 597–600.

Chen, Hou-Tong et al. (2009). "A metamaterial solid-state terahertz phase modulator". In: *Nature photonics* 3.3, pp. 148–151.

Chen, Xieyu et al. (2020). "Electrically Tunable Perfect Terahertz Absorber Based on a Graphene Salisbury Screen Hybrid Metasurface". In: *Advanced Optical Materials* 8.3, p. 1900660. DOI: https://doi.org/10.1002/adom.201900660.

Choi, H. et al. (2009). "Broadband electromagnetic response and ultrafast dynamics of few-layer epitaxial graphene". In: *Appl. Phys. Lett.* 94.17, p. 172102. DOI: 10.1063/1.3122348. eprint: https://doi.org/10.1063/1.3122348. URL: https://doi.org/10.1063/1.3122348.

Choi, M. et al. (May 2011). "A terahertz metamaterial with unnaturally high refractive index". In: *Nature* 470 (7334), pp. 369–373. DOI: 10.1038/nature09776. URL: https://doi.org/10.1038/nature09776.

Choi, W. J. et al. (2019). "Terahertz circular dichroism spectroscopy of biomaterials enabled by kirigami polarization modulators". In: *Nat. Mater.* 18.8, pp. 820–826. DOI: https://doi.org/10.1038/s41563-019-0404-6.

Cinquanta, Eugenio et al. (2023). "Charge carrier dynamics in 2D materials probed by ultrafast THzspectroscopy". In: *Advances in Physics: X* 8.1, p. 2120416. DOI: 10.1080/23746149.2022.2120416. eprint: https://doi.org/10.1080/23746149.2022.2120416. URL: https://doi.org/10.1080/23746149.2022.2120416.

Cong, L. et al. (2018). "All-optical active THz metasurfaces for ultrafast polarization switching and dynamic beam splitting". In: *Light Sci Appl* 7.1, p. 28. DOI: 10.1038/s41377-018-0024-y.

Cong, Longqing et al. (2019a). "Electrically Programmable Terahertz Diatomic Metamolecules for Chiral Optical Control". In: *Research* 2019. DOI: 10.34133/2019/7084251. eprint: https://spj.science.org/doi/pdf/10.34133/2019/7084251. URL: https://spj.science.org/doi/abs/10.34133/2019/7084251.

— (2019b). "Electrically programmable terahertz diatomic metamolecules for chiral optical control". In: *Research* 2019, p. 11. DOI: https://doi.org/10.34133/2019/7084251.

Cui, T. J. et al. (2014). "Coding metamaterials, digital metamaterials and programmable metamaterials". In: *Light Sci Appl* 3.10. DOI: 10.1038/lsa.2014.99. URL: https://doi.org/10.1038/lsa.2014.99.

De Fazio, Domenico et al. (July 2019). "High-Mobility, Wet-Transferred Graphene Grown by Chemical Vapor Deposition". In: *ACS Nano* 13.8. doi: 10.1021/acsnano.9b02621, pp. 8926–8935.

Degl'Innocenti, R. et al. (2007). "Ultraviolet electro-optic amplitude modulation in β-BaB_2O_4 waveguides". In: *Appl. Phys. Lett.* 91.5, p. 051105. DOI: 10.1063/1.2761484.

Degl'Innocenti, Riccardo, Hungyen Lin, and Miguel Navarro-Cía (2022). "Recent progress in terahertz metamaterial modulators". In: *Nanophotonics* 11.8, pp. 1485–1514. DOI: 10.1515/nanoph-2021-0803. URL: https://doi.org/10.1515/nanoph-2021-0803.

Degl'Innocenti, Riccardo et al. (2016). "Fast Room-Temperature Detection of Terahertz Quantum Cascade Lasers with Graphene-Loaded Bow-Tie Plasmonic Antenna Arrays". In: *ACS Photonics* 3.10. doi: 10.1021/acsphotonics.6b00405, pp. 1747–1753.

Degl'Innocenti, Riccardo et al. (Oct. 2018). "All-integrated terahertz modulators". In: *Nanophotonics* 7.1. doi: 10.1515/nanoph-2017-0040, pp. 127–144.

Dexheimer, Susan L. (2008). *Terahertz spectroscopy: principles and applications*. USA: CRC Press, Taylor & Francis Group.

Ding, Min et al. (2022). "Wideband Vector Network Analyzer Based on Direct Microwave Photonic Digitization". In: *Journal of Lightwave Technology* 40.14, pp. 4581–4588. DOI: 10.1109/JLT.2022.3168044.

Doany, F. E., D. Grischkowsky, and C.-C. Chi (1987). "Carrier lifetime versus ion-implantation dose in silicon on sapphire". In: *Applied Physics Letters* 50.8, pp. 460–462. DOI: 10.1063/1.98173. eprint: https://doi.org/10.1063/1.98173. URL: https://doi.org/10.1063/1.98173.

Efetov, Dmitri K. and Philip Kim (Dec. 2010). "Controlling Electron-Phonon Interactions in Graphene at Ultrahigh Carrier Densities". In: *Phys. Rev. Lett.* 105 (25). doi: 10.1103/PhysRevLett.105.256805, p. 256805.

Elayan, Hadeel et al. (2020). "Terahertz Band: The Last Piece of RF Spectrum Puzzle for Communication Systems". In: *IEEE Open Journal of the Communications Society* 1, pp. 1–32. DOI: 10.1109/OJCOMS.2019.2953633.

Exter, Martin van, Ch. Fattinger, and D. Grischkowsky (Oct. 1989). "Terahertz time-domain spectroscopy of water vapor". In: *Opt. Lett.* 14.20, pp. 1128–1130. DOI: 10.1364/OL.14.001128.

Fan, Fei et al. (Sept. 2021a). "Magnetically Induced Terahertz Birefringence and Chirality Manipulation in Transverse-Magnetized Metasurface". In: *Adv. Optical Mater.* 9.24. doi: https://doi.org/10.1002/adom.202101097, p. 2101097.

— (2021b). "Magnetically Induced Terahertz Birefringence and Chirality Manipulation in Transverse-Magnetized Metasurface". In: *Adv. Optical Mater.* 9.24, p. 2101097. DOI: https://doi.org/10.1002/adom.202101097. eprint: https://onlinelibrary.wiley.com/doi/pdf/10.1002/adom.202101097. URL: https://onlinelibrary.wiley.com/doi/abs/10.1002/adom.202101097.

Fang, Ming et al. (Jan. 2019). "Nonlinearity in the Dark: broadband Terahertz Generation with Extremely High Efficiency". In: *Phys. Rev. Lett.* 122 (2), p. 027401. DOI: 10.1103/PhysRevLett.122.027401. URL: https://link.aps.org/doi/10.1103/PhysRevLett.122.027401.

Fraunhofer Institute for Telecommunications Heinrich-Hertz-Institut, HHI (n.d.). *Pulsed Terahertz Emitter and Receiver Modules*. URL: https://www.hhi.fraunhofer.de/en/departments/pc/technologies-and-solutions.html.

Fu, Xiaojian et al. (2020). "Terahertz Beam Steering Technologies: From Phased Arrays to Field-Programmable Metasurfaces". In: *Adv. Optical Mater.* 8.3. doi: https://doi.org/10.1002/adom.201900628, p. 1900628.

Fujishima, Minoru (2018). "Key Technologies for THz Wireless Link by Silicon CMOS Integrated Circuits". In: *Photonics* 5.4. ISSN: 2304-6732. DOI: 10.3390/photonics5040050. URL: https://www.mdpi.com/2304-6732/5/4/50.

— (Feb. 2021). "Future of 300 GHz band wireless communications and their enabler, CMOS transceiver technologies". In: *Jpn. J. Appl. Phys.* 60.SB, SB0803. DOI: 10.35848/1347-4065/abdf24.

Garg, Ramesh (2008). *Analytical and Computational Methods in Electromagnetics*. Norwood, UNITED STATES: Artech House. URL: http://ebookcentral.proquest.com/lib/lancaster/detail.action?docID=456916.

George, Paul A. et al. (2008). "Ultrafast Optical-Pump Terahertz-Probe Spectroscopy of the Carrier Relaxation and Recombination Dynamics in Epitaxial Graphene". In: *Nano Lett.* 8.12. PMID: 18989983, pp. 4248–4251. DOI: 10.1021/nl8019399. eprint: https://doi.org/10.1021/nl8019399. URL: https://doi.org/10.1021/nl8019399.

Gierz, I. et al. (Oct. 2013). "Snapshots of non-equilibrium Dirac carrier distributions in graphene". In: *Nature Mater* 12 (12), pp. 1119–1124. DOI: 10.1038/nmat3757. URL: https://doi.org/10.1038/nmat3757.

Guerboukha, Hichem, Kathirvel Nallappan, and Maksim Skorobogatiy (Feb. 2018). "Exploiting k-space/frequency duality toward real-time terahertz imaging". In: *Optica* 5.2, pp. 109–116. DOI: 10.1364/OPTICA.5.000109. URL: https://opg.optica.org/optica/abstract.cfm?URI=optica-5-2-109.

Halbhuber, M. et al. (Aug. 2020). "Non-adiabatic stripping of a cavity field from electrons in the deep-strong coupling regime". In: *Nat. Photonics* 14 (11), pp. 675–679. DOI: 10.1038/s41566-020-0673-2. URL: https://doi.org/10.1038/s41566-020-0673-2.

Hale, Lucy L. et al. (2020). "Noninvasive Near-Field Spectroscopy of Single Subwavelength Complementary Resonators". In: *Laser & Photonics Reviews* 14.4, p. 1900254. DOI: https://doi.org/10.1002/lpor.201900254. eprint: https://onlinelibrary.wiley.com/doi/pdf/10.1002/lpor.201900254. URL: https://onlinelibrary.wiley.com/doi/abs/10.1002/lpor.201900254.

Han, Chong et al. (2022). "Terahertz Wireless Channels: A Holistic Survey on Measurement, Modeling, and Analysis". In: *IEEE Communications Surveys & Tutorials* 24.3, pp. 1670–1707. DOI: 10.1109/COMST.2022.3182539.

He, Qiong et al. (2018). "High-Efficiency Metasurfaces: Principles, Realizations, and Applications". In: *Advanced Optical Materials* 6.19, p. 1800415. DOI: https://doi.org/10.1002/adom.201800415. eprint: https://onlinelibrary.wiley.com/doi/pdf/10.1002/adom.201800415. URL: https://onlinelibrary.wiley.com/doi/abs/10.1002/adom.201800415.

Hirata, Akihiko et al. (2012). "120-GHz-Band Wireless Link Technologies for Outdoor 10-Gbit/s Data Transmission". In: *IEEE Transactions on Microwave Theory and Techniques* 60.3, pp. 881–895. DOI: 10.1109/TMTT.2011.2178256.

Hofmann, Stephan, Philipp Braeuninger-Weimer, and Robert S. Weatherup (2015). "CVD-Enabled Graphene Manufacture and Technology". In: *J. Phys. Chem. Lett.* 6.14. PMID: 26240694, pp. 2714–2721. DOI: 10.1021/acs.jpclett.5b01052. eprint: https://doi.org/10.1021/acs.jpclett.5b01052. URL: https://doi.org/10.1021/acs.jpclett.5b01052.

Houston, P.A. (Oct. 2000). "High-frequency heterojunction bipolar transistor device design and technology". English. In: *Electronics & Communication Engineering Journal* 12 (5), 220–228(8). ISSN: 0954-0695. URL: https://digital-library.theiet.org/content/journals/10.1049/ecej_20000504.

Hsieh, Cho-Fan et al. (2006). "Voltage-controlled liquid-crystal terahertz phase shifter and quarter-wave plate". In: *Optics letters* 31.8, pp. 1112–1114.

Hu, Fangrong et al. (Apr. 2021). "Electrically Controlled Terahertz Binary Coder Based on Hysteresis of Vanadium Dioxide Embedded Modulator". In: *J. Lightwave Technol.* 39.8, pp. 2476–2481. URL: https://opg.optica.org/jlt/abstract.cfm?URI=jlt-39-8-2476.

Huang, Yi, Yaochun Shen, and Jiayou Wang (2022). "From Terahertz Imaging to Terahertz Wireless Communications". In: *Engineering*. ISSN: 2095-8099. DOI: https://doi.org/10.1016/j.eng.2022.06.023. URL: https://www.sciencedirect.com/science/article/pii/S2095809922006361.

Huber, A. J. et al. (2008). "Terahertz Near-Field Nanoscopy of Mobile Carriers in Single Semiconductor Nanodevices". In: *Nano Letters* 8.11. PMID: 18837565, pp. 3766–3770. DOI: 10.1021/nl802086x. eprint: https://doi.org/10.1021/nl802086x. URL: https://doi.org/10.1021/nl802086x.

Iizuka, K. (2002). *Elements of Photonics, Volume I: In Free Space and Special Media*. Wiley Series in Pure and Applied Optics. Wiley. ISBN: 9780471839385. URL: https://books.google.co.uk/books?id=CRfDHdahgz0C.

Ivanov, Alexey V. et al. (Oct. 2021). "Fabrication of Epitaxial W-Doped VO_2 Nanostructured Films for Terahertz Modulation Using the Solvothermal Process". In: *ACS Appl. Nano Mater.* 4.10. doi: 10.1021/acsanm.1c02081, pp. 10592–10600.

Jeannin, Mathieu et al. (2020). "High temperature metamaterial terahertz quantum detector". In: *Appl. Phys. Lett.* 117.25, p. 251102. DOI: 10.1063/5.0033367.

Jessop, David S et al. (2016). "Graphene based plasmonic terahertz amplitude modulator operating above 100 MHz". In: *Applied Physics Letters* 108.17, p. 171101. DOI: https://doi.org/10.1063/1.4947596.

Ji, Yunyun et al. (Feb. 2019a). "Manipulation enhancement of terahertz liquid crystal phase shifter magnetically induced by ferromagnetic nanoparticles". In: *Nanoscale* 11.11. doi: https://doi.org/10.1039/C8NR09259A, pp. 4933–4941.

— (Feb. 2019b). "Manipulation enhancement of terahertz liquid crystal phase shifter magnetically induced by ferromagnetic nanoparticles". In: *Nanoscale* 11.11, pp. 4933–4941. DOI: https://doi.org/10.1039/C8NR09259A.

Ji, Yunyun et al. (Aug. 2021). "Active terahertz spin state and optical chirality in liquid crystal chiral metasurface". In: *Phys. Rev. Materials* 5 (8), p. 085201. DOI: 10.1103/PhysRevMaterials.5.085201.

Jiang, Mingzhu et al. (2021). "Electrically Triggered VO2 Reconfigurable Metasurface for Amplitude and Phase Modulation of Terahertz Wave". In: *Journal of Lightwave Technology* 39.11, pp. 3488–3494. DOI: 10.1109/JLT.2021.3068395.

Jiang, Zhiping and X. C. Zhang (Nov. 1999). "2D measurement and spatio-temporal coupling of few-cycle THz pulses". In: *Opt. Express* 5.11, pp. 243–248. DOI: 10.1364/OE.5.000243. URL: https://opg.optica.org/oe/abstract.cfm?URI=oe-5-11-243.

Jin, Qi et al. (2017). "Observation of broadband terahertz wave generation from liquid water". In: *Applied Physics Letters* 111.7, p. 071103. DOI: 10.1063/1.4990824. eprint: https://doi.org/10.1063/1.4990824. URL: https://doi.org/10.1063/1.4990824.

Jnawali, Giriraj et al. (2013). "Observation of a Transient Decrease in Terahertz Conductivity of Single-Layer Graphene Induced by Ultrafast Optical Excitation". In: *Nano Letters* 13.2, pp. 524–530. DOI: 10.1021/nl303988q.

Jornet, J. M., E. W. Knightly, and D. M. Mittleman (Feb. 2023). "Wireless communications sensing and security above 100 GHz". In: *Nat Commun* 14.841. DOI: https://doi.org/10.1038/s41467-023-36621-x.

Jornet, Josep Miquel and Ian F. Akyildiz (2013). "Graphene-based Plasmonic Nano-Antenna for Terahertz Band Communication in Nanonetworks". In: *IEEE Journal on Selected Areas in Communications* 31.12, pp. 685–694. DOI: 10.1109/JSAC.2013.SUP2.1213001.

Joyce, Hannah J et al. (Sept. 2016). "A review of the electrical properties of semiconductor nanowires: insights gained from terahertz conductivity spectroscopy". In: *Semicon. Sci. Technol.* 31.10, p. 103003. DOI: 10.1088/0268-1242/31/10/103003. URL: https://dx.doi.org/10.1088/0268-1242/31/10/103003.

Kakenov, Nurbek et al. (2018). "Graphene based terahertz phase modulators". In: *2D Materials* 5.3, p. 035018.

Karl, N. J. et al. (2015). "Frequency-division multiplexing in the terahertz range using a leaky-wave antenna". In: *Nature Photon* 9.11, pp. 717–720. DOI: 10.1038/nphoton.2015.176.

Kats, Mikhail A. et al. (Feb. 2013). "Thermal tuning of mid-infrared plasmonic antenna arrays using a phase change material". In: *Opt. Lett.* 38.3, pp. 368–370. DOI: 10.1364/OL.38.000368.

Kersting, R, G Strasser, and K Unterrainer (2000). "Terahertz phase modulator". In: *Electronics Letters* 36.13, pp. 1156–1158.

Kim, Teun-Teun et al. (2017). "Electrical access to critical coupling of circularly polarized waves in graphene chiral metamaterials". In: *Sci. Adv.* 3.9, e1701377. DOI: 10.1126/sciadv.1701377. eprint: https://www.science.org/doi/pdf/10.1126/sciadv.1701377. URL: https://www.science.org/doi/abs/10.1126/sciadv.1701377.

Kindness, Stephen (2020). "Graphene Integrated Metamaterial Devices for Terahertz Modulation". PhD thesis. University of Cambridge.

Kindness, Stephen J. et al. (2018). "Active control of electromagnetically induced transparency in a terahertz metamaterial array with graphene for continuous resonance frequency tuning". In: *Adv. Optical Mater.* 6.21, p. 1800570.

Kindness, Stephen J. et al. (May 2019). "Graphene-Integrated Metamaterial Device for All-Electrical Polarization Control of Terahertz Quantum Cascade Lasers". In: *ACS Photonics* 6.6, pp. 1547–1555. DOI: https://doi.org/10.1021/acsphotonics.9b00411.

Kindness, Stephen J. et al. (Aug. 2020a). "A Terahertz Chiral Metamaterial Modulator". In: *Adv. Optical Mater.* 8.21, p. 2000581. DOI: https://doi.org/10.1002/adom.202000581.

Kindness, Stephen J. et al. (July 2020b). "Active metamaterial polarization modulators for the Terahertz frequency range". In: *J. Phys.: Conf. Ser.* 1571.1. dio: 10.1088/1742-6596/1571/1/012003, p. 012003.

Kleine-Ostmann, T. et al. (2004a). "Room-temperature operation of an electrically driven terahertz modulator". In: *Applied Physics Letters* 84.18, pp. 3555–3557. DOI: 10.1063/1.1723689. eprint: https://doi.org/10.1063/1.1723689. URL: https://doi.org/10.1063/1.1723689.

— (2004b). "Room-temperature operation of an electrically driven terahertz modulator". In: *Applied Physics Letters* 84.18, pp. 3555–3557. DOI: 10.1063/1.1723689. eprint: https://doi.org/10.1063/1.1723689. URL: https://doi.org/10.1063/1.1723689.

Kürner, Thomas, D Mittleman, and Tadao Nagatsuma (2021). *THz Communications: Paving the Way Towards Wireless Tbps*. doi: https://doi.org/10.1007/978-3-030-73738-2. Springer.

Lee, Seojoo et al. (Mar. 2020). "Metamaterials for Enhanced Optical Responses and their Application to Active Control of Terahertz Waves". In: *Adv. Mater.* 32.35. doi: https://doi.org/10.1002/adma.202000250, p. 2000250.

Lee, Seung Hoon et al. (Sept. 2012). "Switching terahertz waves with gate-controlled active graphene metamaterials". In: *Nature Mater* 11.11, pp. 936–941. DOI: https://doi.org/10.1038/nmat3433.

Lee, W. J. et al. (2022). "Possible permanent Dirac- to Weyl-semimetal phase transition by ion implantation". In: *NPG Asia Materials* 14.1, p. 31. DOI: 31.10.1038/s41427-022-00380-w.

Lee, Yun-Shik and Yun-Shik Lee (2008). *Principles of Terahertz Science and Technology*. New York, NY: Springer.

Li, Jie et al. (Aug. 2020). "Metal-graphene hybrid active chiral metasurfaces for dynamic terahertz wavefront modulation and near field imaging". In: *Carbon* 163. doi: https://doi.org/10.1016/j.carbon.2020.03.019, pp. 34–42. ISSN: 0008-6223.

Li, Qiushi et al. (2022). In: *Nanophotonics* 11.9, pp. 2085–2096. DOI: doi:10.1515/nanoph-2021-0801. URL: https://doi.org/10.1515/nanoph-2021-0801.

Liang, Guozhen et al. (2017). "Monolithic Semiconductor Lasers with Dynamically Tunable Linear-to-Circular Polarization". In: *ACS Photonics* 4.3, pp. 517–524. DOI: 10.1021/acsphotonics.6b00703. eprint: https://doi.org/10.1021/acsphotonics.6b00703. URL: https://doi.org/10.1021/acsphotonics.6b00703.

Libon, I. H. et al. (2000). "An optically controllable terahertz filter". In: *Applied Physics Letters* 76.20, pp. 2821–2823. DOI: 10.1063/1.126484. eprint: https://doi.org/10.1063/1.126484. URL: https://doi.org/10.1063/1.126484.

Lin, Cen and Geoffrey Ye Li Li (Dec. 2016). "Terahertz Communications: An Array-of-Subarrays Solution". In: *IEEE Communications Magazine* 54.12. doi: 10.1109/MCOM.2016.1600306CM, pp. 124–131.

Lin, Rong et al. (Sept. 2021). "Multiple interference theoretical model for graphene metamaterial-based tunable broadband terahertz linear polarization converter design and optimization". In: *Opt Express* 29.19, pp. 30357–30370. DOI: 10.1364/OE.438256.

Liu, Changqin et al. (Oct. 25, 2021). "Active spintronic-metasurface terahertz emitters with tunable chirality". In: *Advanced Photonics* 3.5, p. 056002. DOI: https://doi.org/10.1117/1.AP.3.5.056002.

Liu, Hongwei, Junpeng Lu, and Xiao Renshaw Wang (Dec. 2017). "Metamaterials based on the phase transition of VO_2". In: *Nanotechnology* 29.2, p. 024002. DOI: 10.1088/1361-6528/aa9cb1. URL: https://dx.doi.org/10.1088/1361-6528/aa9cb1.

Liu, K. et al. (Jan. 2017). "Wide Field-of-view and Broadband Terahertz Beam Steering Based on Gap Plasmon Geodesic Antennas". In: *Opt. Express* 7.1, p. 41642. DOI: 10.1038/srep41642.

Liu, Peter Q et al. (Nov. 2015). "Highly tunable hybrid metamaterials employing split-ring resonators strongly coupled to graphene surface plasmons". In: *Nat Commun* 6.1. doi: https://doi.org/10.1038/ncomms9969, pp. 1–7.

Liu, Yongshan et al. (Dec. 2020). "Generation of tailored terahertz waves from monolithic integrated metamaterials onto spintronic terahertz emitters". In: *Nanotechnology* 32 (10), p. 105201. DOI: https://doi.org/10.1088/1361-6528/abcc98. URL: https://doi.org/10.1088/1361-6528/abcc98.

Lloyd-Hughes, J. and T.-I. Jeon (May 2012). "A Review of the Terahertz Conductivity of Bulk and Nano-Materials". In: *Journal of Infrared, Millimeter, and Terahertz Waves* 33.9, pp. 871–925. DOI: 10.1007/s10762-012-9905-y. URL: https://doi.org/10.1007/s10762-012-9905-y.

Low, Tony and Phaedon Avouris (2014). "Graphene Plasmonics for Terahertz to Mid-Infrared Applications". In: *ACS Nano* 8.2. PMID: 24484181, pp. 1086–1101. DOI:

10.1021/nn406627u. eprint: https://doi.org/10.1021/nn406627u. URL: https://doi.org/10.1021/nn406627u.

Ma, J. et al. (2017a). "Frequency-division multiplexer and demultiplexer for terahertz wireless links". In: *Nat Commun* 8.1, p. 729. DOI: 10.1038/s41467-017-00877-x.

— (June 2017b). "Frequency-division multiplexer and demultiplexer for terahertz wireless links". In: *Nat Commun* 8.1, p. 729. DOI: 10.1038/s41467-017-00877-x.

Ma, Zhenzhe et al. (2022). In: *Nanophotonics* 11.9, pp. 1847–1862. DOI: doi:10.1515/nanoph-2021-0714. URL: https://doi.org/10.1515/nanoph-2021-0714.

Ma, ZT et al. (May 2019). "Modulators for terahertz communication: The current state of the art". In: *Research* 2019. doi: https://doi.org/10.34133/2019/6482975, p. 22.

Maissen, Curdin et al. (2019). "Probes for Ultrasensitive THz Nanoscopy". In: *ACS Photonics* 6.5, pp. 1279–1288. DOI: 10.1021/acsphotonics.9b00324. eprint: https://doi.org/10.1021/acsphotonics.9b00324. URL: https://doi.org/10.1021/acsphotonics.9b00324.

Markl, Daniel et al. (2018). "Characterisation of pore structures of pharmaceutical tablets: a review". In: *International Journal of Pharmaceutics* 538.1, pp. 188–214. ISSN: 0378-5173. DOI: https://doi.org/10.1016/j.ijpharm.2018.01.017. URL: https://www.sciencedirect.com/science/article/pii/S0378517318300231.

Masyukov, M. et al. (2020). "Optically tunable terahertz chiral metasurface based on multi-layered graphene". In: *Sci Rep* 10.1, p. 3157. DOI: 10.1038/s41598-020-60097-0.

Mendis, Rajind et al. (2010). "A tunable universal terahertz filter using artificial dielectrics based on parallel-plate waveguides". In: *Applied Physics Letters* 97.13, p. 131106. DOI: 10.1063/1.3495994. eprint: https://doi.org/10.1063/1.3495994. URL: https://doi.org/10.1063/1.3495994.

Mezzapesa, Francesco P. et al. (July 2019a). "Tunable and compact dispersion compensation of broadband THz quantum cascade laser frequency combs". In: *Opt. Express* 27.15. doi: 10.1364/OE.27.020231, pp. 20231–20240.

— (July 2019b). "Tunable and compact dispersion compensation of broadband THz quantum cascade laser frequency combs". In: *Opt Express* 27.15, pp. 20231–20240. DOI: 10.1364/OE.27.020231. URL: https://opg.optica.org/oe/abstract.cfm?URI=oe-27-15-20231.

Mitrofanov, Oleg et al. (2016). "Near-Field Spectroscopy and Imaging of Subwavelength Plasmonic Terahertz Resonators". In: *IEEE Transactions on Terahertz Science and Technology* 6.3, pp. 382–388. DOI: 10.1109/TTHZ.2016.2549367.

Mittleman, Daniel M. (2017). "Perspective: Terahertz science and technology". In: *Journal of Applied Physics* 122.23, p. 230901. DOI: 10.1063/1.5007683. eprint: https://doi.org/10.1063/1.5007683. URL: https://doi.org/10.1063/1.5007683.

Monnai, Yasuaki et al. (Jan. 2013a). "Terahertz beam steering and variable focusing using programmable diffraction gratings". In: *Opt. Express* 21.2, pp. 2347–2354. DOI: 10.1364/OE.21.002347. URL: https://opg.optica.org/oe/abstract.cfm?URI=oe-21-2-2347.

— (Jan. 2013b). "Terahertz beam steering and variable focusing using programmable diffraction gratings". In: *Opt. Express* 21.2, pp. 2347–2354. DOI: 10.1364/OE.21.002347. URL: https://opg.optica.org/oe/abstract.cfm?URI=oe-21-2-2347.

Nagatsuma, T., G. Ducournau, and C. C. Renaud (2016). "Advances in terahertz communications accelerated by photonics". In: *Nat. Photon.* 10.6, pp. 371–379. DOI: 10.1038/nphoton.2016.65.

Nagatsuma, Tadao, Guillaume Ducournau, and Cyril C Renaud (May 2016). "Advances in terahertz communications accelerated by photonics". In: *Nat. Photon.* 10.6. doi: https://doi.org/10.1038/nphoton.2016.65, pp. 371–379.

Al-Naib, Ibraheem and Withawat Withayachumnankul (Mar. 2017). "Recent progress in terahertz metasurfaces". In: *J Infrared Milli Terahz Waves* 38.9, pp. 1067–1084. URL: https://doi.org/10.1007/s10762-017-0381-2.

Neu, Jens and Charles A. Schmuttenmaer (2018). "Tutorial: An introduction to terahertz time domain spectroscopy (THz-TDS)". In: *Journal of Applied Physics* 124.23, p. 231101. DOI: 10.1063/1.5047659.

Nouman, Muhammad Tayyab et al. (May 2016). "Terahertz modulator based on metamaterials integrated with metal-semiconductor-metal varactors". In: *Sci Rep* 6.1. doi: https://doi.org/10.1038/srep26452, pp. 1–7.

Pandey, Shashank, Gagan Kumar, and Ajay Nahata (Oct. 2010). "Slot waveguide-based splitters for broadband terahertz radiation". In: *Opt. Express* 18.22, pp. 23466–23471. DOI: 10.1364/OE.18.023466. URL: https://opg.optica.org/oe/abstract.cfm?URI=oe-18-22-23466.

Papaioannou, Evangelos Th. and René Beigang (2021). "THz spintronic emitters: a review on achievements and future challenges". In: *Nanophotonics* 10.4, pp. 1243–1257. DOI: 10.1515/nanoph-2020-0563. URL: https://doi.org/10.1515/nanoph-2020-0563.

Patil, Mangesh R. et al. (2022). "Terahertz Spectroscopy: Encoding the Discovery, Instrumentation, and Applications toward Pharmaceutical Prospectives". In: *Critical Reviews in Analytical Chemistry* 52.2. PMID: 32772866, pp. 343–355. DOI: 10.1080/10408347.2020.1802219. eprint: https://doi.org/10.1080/10408347.2020.1802219. URL: https://doi.org/10.1080/10408347.2020.1802219.

Peiponen, Kai-Erik, J. Axel Zeitler, and Makoto Kuwata-Gonokami (2013). *Terahertz spectroscopy and imaging*. Berlin: Springer.

Pendry, J B et al. (June 1998). "Low frequency plasmons in thin-wire structures". In: *Journal of Physics: Condensed Matter* 10.22, p. 4785. DOI: 10.1088/0953-8984/10/22/007. URL: https://dx.doi.org/10.1088/0953-8984/10/22/007.

— (1999). "Magnetism from conductors and enhanced nonlinear phenomena". In: *IEEE Transactions on Microwave Theory and Techniques* 47.11, pp. 2075–2084. DOI: 10.1109/22.798002.

Pitchappa, Prakash et al. (2019). "Chalcogenide Phase Change Material for Active Terahertz Photonics". In: *Adv. Mater.* 31.12, p. 1808157. DOI: https://doi.org/10.1002/adma.201808157.

Pitchappa, Prakash et al. (2021a). "Volatile Ultrafast Switching at Multilevel Nonvolatile States of Phase Change Material for Active Flexible Terahertz Metadevices". In: *Advanced Functional Materials* 31.17, p. 2100200. DOI: https://doi.org/10.1002/adfm.202100200.

— (2021b). "Volatile Ultrafast Switching at Multilevel Nonvolatile States of Phase Change Material for Active Flexible Terahertz Metadevices". In: *Advanced Functional Materials* 31.17, p. 2100200. DOI: https://doi.org/10.1002/adfm.202100200. eprint: https://onlinelibrary.wiley.com/doi/pdf/10.1002/adfm.202100200. URL: https://onlinelibrary.wiley.com/doi/abs/10.1002/adfm.202100200.

Plank, Helene and Sergey D. Ganichev (2018). "A review on terahertz photogalvanic spectroscopy of Bi_2Te_3- and Sb_2Te_3-based three dimensional topological insulators". In: *Solid-State Electronics* 147, pp. 44–50. ISSN: 0038-1101. DOI: https://doi.org/10.1016/j.sse.2018.06.002. URL: https://www.sciencedirect.com/science/article/pii/S0038110118302478.

Pozar, David M (2011). *Microwave Engineering*. John wiley & sons.

Rana, Farhan et al. (Mar. 2009). "Carrier recombination and generation rates for intravalley and intervalley phonon scattering in graphene". In: *Phys. Rev. B* 79 (11), p. 115447. DOI: 10.1103/PhysRevB.79.115447. URL: https://link.aps.org/doi/10.1103/PhysRevB.79.115447.

Reichel, K. S., R. Mendis, and D. M. Mittleman (2016). "A Broadband Terahertz Waveguide T-Junction Variable Power Splitter". In: *Sci Rep* 6.1, p. 28925. DOI: 10.1038/srep28925.

Rieh, Jae-Sung (2020). *Introduction to Terahertz Electronics*. Cham, Switzerland: Springer Nature.

Rösch, Markus et al. (Nov. 2015). "Octave-spanning semiconductor laser". In: *Nature Photon* 9.1. doi: https://doi.org/10.1038/nphoton.2014.279, pp. 42–47.

Sabbah, A. J. and D. M. Riffe (Oct. 2002). "Femtosecond pump-probe reflectivity study of silicon carrier dynamics". In: *Phys. Rev. B* 66 (16), p. 165217. DOI: 10.1103/PhysRevB.66.165217. URL: https://link.aps.org/doi/10.1103/PhysRevB.66.165217.

Saeedkia, Daryoosh (2013). *Handbook of terahertz technology for imaging, sensing and communications*. Cambridge, UK: Woodhead Publishing limited.

Shafraniuk, Serhii (2015). *Graphene : fundamentals, devices, and applications*. Jenny Stanford Publishing. ISBN: 0-429-06884-0. DOI: http://ebookcentral.proquest.com/lib/lancaster/detail.action?docID=1726100.

Shen, J. T., Peter B. Catrysse, and Shanhui Fan (May 2005). "Mechanism for Designing Metallic Metamaterials with a High Index of Refraction". In: *Phys. Rev. Lett.* 94 (19), p. 197401. DOI: 10.1103/PhysRevLett.94.197401. URL: https://link.aps.org/doi/10.1103/PhysRevLett.94.197401.

Shen, Suling et al. (2022). "Recent Advances in the Development of Materials for Terahertz Metamaterial Sensing". In: *Adv. Optical Mater.* 10.1. doi: https://doi.org/10.1002/adom.202101008, p. 2101008.

Shen, Y. C. et al. (2009). "Terahertz pulsed spectroscopic imaging using optimized binary masks". In: *Applied Physics Letters* 95.23, p. 231112. DOI: 10.1063/1.3271030. eprint: https://doi.org/10.1063/1.3271030. URL: https://doi.org/10.1063/1.3271030.

Shen, Yao-Chun and Philip F. Taday (2008). "Development and Application of Terahertz Pulsed Imaging for Nondestructive Inspection of Pharmaceutical Tablet". In: *IEEE Journal of Selected Topics in Quantum Electronics* 14.2, pp. 407–415. DOI: 10.1109/JSTQE.2007.911309.

Shi, S.-F. et al. (2014). "Controlling Graphene Ultrafast Hot Carrier Response from Metal-like to Semiconductor-like by Electrostatic Gating". In: *Nano Lett.* 14.3, pp. 1578–1582. DOI: https://doi.org/10.1021/nl404826r.

Shin, Jonghwa, Jung-Tsung Shen, and Shanhui Fan (Mar. 2009). "Three-Dimensional Metamaterials with an Ultrahigh Effective Refractive Index over a Broad Bandwidth". In: *Phys. Rev. Lett.* 102 (9), p. 093903. DOI: 10.1103/PhysRevLett.102.093903. URL: https://link.aps.org/doi/10.1103/PhysRevLett.102.093903.

Smith, D. R. et al. (May 2000). "Composite Medium with Simultaneously Negative Permeability and Permittivity". In: *Phys. Rev. Lett.* 84 (18), pp. 4184–4187. DOI: 10.1103/PhysRevLett.84.4184. URL: https://link.aps.org/doi/10.1103/PhysRevLett.84.4184.

Son, Joo-Hiuk (2020a). *Terahertz Biomedical Science & Technology*. First. CRC Press.

— (2020b). *Terahertz Biomedical Science & Technology*. 1st. Boca Raton, Florida: London: CRC Press.

Song, Ho-Jin (2021). "Terahertz Wireless Communications: Recent Developments Including a Prototype System for Short-Range Data Downloading". In: *IEEE Microwave Magazine* 22.5, pp. 88–99. DOI: 10.1109/MMM.2021.3056935.

Song, Ho-Jin and Tadao Nagatsuma (2015). *Handbook of Terahertz Technologies : Devices and Applications*. 1st. Boca Raton, Florida, USA: CRC Press.

Steinbusch, T. P. et al. (Nov. 2014). "Active terahertz beam steering by photo-generated graded index gratings in thin semiconductor films". In: *Opt. Express* 22.22, pp. 26559–26571. DOI: 10.1364/OE.22.026559. URL: https://opg.optica.org/oe/abstract.cfm?URI=oe-22-22-26559.

Stellmacher, Max et al. (1999). "Photoconductivity investigation of the electron dynamics in GaAs grown at low temperature". In: *Applied Physics Letters* 74.9, pp. 1239–1241. DOI: 10.1063/1.123511. eprint: https://doi.org/10.1063/1.123511. URL: https://doi.org/10.1063/1.123511.

Su, Ke, Yao-Chun Shen, and J. Axel Zeitler (2014). "Terahertz Sensor for Non-Contact Thickness and Quality Measurement of Automobile Paints of Varying Complexity". In: *IEEE Transactions on Terahertz Science and Technology* 4.4, pp. 432–439. DOI: 10.1109/TTHZ.2014.2325393.

Sun, Hao et al. (Mar. 2020). "Ultrafast polarization-dependent all-optical switching of germanium-based metaphotonic devices". In: *Photon. Res.* 8.3, pp. 263–270. DOI: 10.1364/PRJ.380446. URL: https://opg.optica.org/prj/abstract.cfm?URI=prj-8-3-263.

Sze, Simon M, Yiming Li, and Kwok K Ng (2021). *Physics of semiconductor devices*. John wiley & sons.

Takano, Kyoya et al. (2017). "17.9 A 105Gb/s 300GHz CMOS transmitter". In: *2017 IEEE International Solid-State Circuits Conference (ISSCC)*, pp. 308–309. DOI: 10.1109/ISSCC.2017.7870384.

Tataria, Harsh et al. (2021). "6G Wireless Systems: Vision, Requirements, Challenges, Insights, and Opportunities". In: *Proceedings of the IEEE* 109.7, pp. 1166–1199. DOI: 10.1109/JPROC.2021.3061701.

Tu, Wanli et al. (2016). "Nondestructive testing of marine protective coatings using terahertz waves with stationary wavelet transform". In: *Ocean Engineering* 111, pp. 582–592. ISSN: 0029-8018. DOI: https://doi.org/10.1016/j.oceaneng.2015.11.028. URL: https://www.sciencedirect.com/science/article/pii/S0029801815006502.

Ulbricht, Ronald et al. (June 2011). "Carrier dynamics in semiconductors studied with time-resolved terahertz spectroscopy". In: *Rev. Mod. Phys.* 83 (2), pp. 543–586. DOI: 10.1103/RevModPhys.83.543. URL: https://link.aps.org/doi/10.1103/RevModPhys.83.543.

Unterrainer, K. (June 2000). "Terahertz phase modulator". English. In: *Electronics Letters* 36 (13), pp. 1156–1158. ISSN: 0013-5194. URL: https://digital-library.theiet.org/content/journals/10.1049/el_20000837.

Ushakov, Aleksandr et al. (May 2018). "Broadband in-line terahertz 2D imaging: comparative study with time-of-flight, cross-correlation, and Fourier transform data processing". In: *J. Opt. Soc. Am. B* 35.5, pp. 1159–1164. DOI: 10.1364/

JOSAB.35.001159. URL: https://opg.optica.org/josab/abstract.cfm?URI=josab-35-5-1159.

Venkatesh, Suresh et al. (Dec. 2020). "A high-speed programmable and scalable terahertz holographic metasurface based on tiled CMOS chips". In: *Nat Electron* 3.12. doi: https://doi.org/10.1038/s41928-020-00497-2, pp. 785–793.

Veselago, Viktor G (1967). "Electrodynamics of substances with simultaneously negative ϵ and μ". In: *Usp. fiz. nauk* 92.7, p. 517.

Wallace, Vincent P. et al. (Oct. 2006). "Terahertz Pulsed Spectroscopy of Human Basal Cell Carcinoma". In: *Appl. Spectrosc.* 60.10, pp. 1127–1133. URL: https://opg.optica.org/as/abstract.cfm?URI=as-60-10-1127.

Wang, Feihu et al. (July 2017). "Short Terahertz Pulse Generation from a Dispersion Compensated Modelocked Semiconductor Laser". In: *Laser & Photonics Reviews* 11.4. doi: https://doi.org/10.1002/lpor.201700013, p. 1700013.

Wang, Lan et al. (2019). "A Review of THz Modulators with Dynamic Tunable Metasurfaces". In: *Nanomaterials* 9.7. ISSN: 2079-4991. DOI: 10.3390/nano9070965. URL: https://www.mdpi.com/2079-4991/9/7/965.

Wang, Shengxiang, Lei Kang, and Douglas H Werner (Jan. 2018). "Active terahertz chiral metamaterials based on phase transition of vanadium dioxide (VO_2)". In: *Sci Rep* 8.1, pp. 1–9. DOI: https://doi.org/10.1038/s41598-017-18472-x.

Wang, Ziming et al. (2021). "Recent progress in terahertz modulation using photonic structures based on two-dimensional materials". In: *InfoMat* 3.10, pp. 1110–1133. DOI: https://doi.org/10.1002/inf2.12236. eprint: https://onlinelibrary.wiley.com/doi/pdf/10.1002/inf2.12236. URL: https://onlinelibrary.wiley.com/doi/abs/10.1002/inf2.12236.

Wang, Zuojia et al. (Sept. 2016). "Optical chiral metamaterials: a review of the fundamentals, fabrication methods and applications". In: *Nanotechnology* 27.41. doi: 10.1088/0957-4484/27/41/412001, p. 412001.

Watanabe, Shinichi (2018). "Terahertz Polarization Imaging and Its Applications". In: *Photonics* 5.4. ISSN: 2304-6732. DOI: https://doi.org/10.3390/photonics5040058. URL: https://www.mdpi.com/2304-6732/5/4/58.

Watanabe, Takayuki et al. (July 2013). "The gain enhancement effect of surface plasmon polaritons on terahertz stimulated emission in optically pumped monolayer graphene". In: *New Journal of Physics* 15.7, p. 075003. DOI: 10.1088/1367-2630/15/7/075003. URL: https://dx.doi.org/10.1088/1367-2630/15/7/075003.

Watts, C. M. et al. (2014a). "Terahertz compressive imaging with metamaterial spatial light modulators". In: *Nature Photon* 8.8, pp. 605–609. DOI: 10.1038/nphoton.2014.139.

— (June 2014b). "Terahertz compressive imaging with metamaterial spatial light modulators". In: *Nature Photon* 8.8, pp. 605–609. DOI: 10.1038/nphoton.2014.139.

Wei, B. et al. (2018). "Amplitude stabilization and active control of a terahertz quantum cascade laser with a graphene loaded split-ring-resonator array". In: *Appl. Phys. Lett.* 112.20, p. 201102. DOI: 10.1063/1.5027687.

Wen, Yao, Tao Xu, and Yu-Sheng Lin (2021). "Design of electrostatically tunable terahertz metamaterial with polarization-dependent sensing characteristic". In: *Results in Physics* 29, p. 104798. ISSN: 2211-3797. DOI: https://doi.org/10.1016/j.rinp.2021.104798. URL: https://www.sciencedirect.com/science/article/pii/S2211379721008536.

Winnerl, S et al. (Jan. 2013). "Time-resolved spectroscopy on epitaxial graphene in the infrared spectral range: relaxation dynamics and saturation behavior". In: *J. Phys.: Condens. Matter* 25.5, p. 054202. DOI: 10.1088/0953-8984/25/5/054202. URL: https://dx.doi.org/10.1088/0953-8984/25/5/054202.

Withayachumnankul, Withawat and Mira Naftaly (2014). "Fundamentals of Measurement in Terahertz Time-Domain Spectroscopy". In: *J Infrared Milli Terahz Waves* 35, pp. 610–637. DOI: https://doi.org/10.1007/s10762-013-0042-z.

Wong, H. et al. (2020). "Active meta polarizer for terahertz frequencies". In: *Sci. Rep.* 10.1, p. 15382. DOI: 10.1038/s41598-020-71990-z.

Wu, Xue and Kaushik Sengupta (2016). "On-Chip THz Spectroscope Exploiting Electromagnetic Scattering With Multi-Port Antenna". In: *IEEE Journal of Solid-State Circuits* 51.12, pp. 3049–3062. DOI: 10.1109/JSSC.2016.2597845.

— (2017). "Dynamic Waveform Shaping With Picosecond Time Widths". In: *IEEE Journal of Solid-State Circuits* 52.2, pp. 389–405. DOI: 10.1109/JSSC.2016.2616349.

Wynne, Klaas and John J. Carey (2005). "An integrated description of terahertz generation through optical rectification, charge transfer, and current surge". In: *Optics Communications* 256.4, pp. 400–413. ISSN: 0030-4018. DOI: https://doi.org/10.1016/j.optcom.2005.06.065. URL: https://www.sciencedirect.com/science/article/pii/S0030401805006565.

Xiao, Dong et al. (2018). "Liquid-crystal-loaded chiral metasurfaces for reconfigurable multiband spin-selective light absorption". In: *Opt. Express* 26.19, pp. 25305–25314. DOI: https://doi.org/10.1364/OE.26.025305.

Xin, X. et al. (2006). "Terahertz absorption spectrum of para and ortho water vapors at different humidities at room temperature". In: *Journal of Applied Physics* 100.9, p. 094905. DOI: 10.1063/1.2357412. eprint: https://doi.org/10.1063/1.2357412. URL: https://doi.org/10.1063/1.2357412.

Xu, Luyao et al. (Apr. 2017). "Metasurface quantum-cascade laser with electrically switchable polarization". In: *Optica* 4.4, pp. 468–475. DOI: 10.1364/OPTICA.4.000468. URL: http://opg.optica.org/optica/abstract.cfm?URI=optica-4-4-468.

Xu, Ruijia et al. (July 2021). "Actively logical modulation of MEMS-based terahertz metamaterial". In: *Photon. Res.* 9.7, pp. 1409–1415. DOI: 10.1364/PRJ.420876. URL: http://opg.optica.org/prj/abstract.cfm?URI=prj-9-7-1409.

Xu, Wendao, Lijuan Xie, and Yibin Ying (2017). "Mechanisms and applications of terahertz metamaterial sensing: a review". In: *Nanoscale* 9.37, pp. 13864–13878. DOI: 10.1039/C7NR03824K.

Yang, Fengyuan, Prakash Pitchappa, and Nan Wang (2022). "Terahertz Reconfigurable Intelligent Surfaces (RISs) for 6G Communication Links". In: *Micromachines* 13.2. ISSN: 2072-666X. DOI: 10.3390/mi13020285. URL: https://www.mdpi.com/2072-666X/13/2/285.

Yang, Shang-Hua et al. (2014). "7.5% Optical-to-Terahertz Conversion Efficiency Offered by Photoconductive Emitters With Three-Dimensional Plasmonic Contact Electrodes". In: *IEEE Transactions on Terahertz Science and Technology* 4.5, pp. 575–581. DOI: 10.1109/TTHZ.2014.2342505.

Yao, Yu et al. (2014). "Electrically Tunable Metasurface Perfect Absorbers for Ultrathin Mid-Infrared Optical Modulators". In: *Nano Lett* 14.11, pp. 6526–6532. DOI: 10.1021/nl503104n. URL: https://doi.org/10.1021/nl503104n3.

Yariv, Amnon (1989). *Quantum Electronics*. 3rd. New York, New York, US: John Wiley & Sons, Inc.

Yasui, Takeshi et al. (Nov. 2005). "Terahertz paintmeter for noncontact monitoring of thickness and drying progress in paint film". In: *Appl. Opt.* 44.32, pp. 6849–6856. DOI: 10.1364/AO.44.006849. URL: https://opg.optica.org/ao/abstract.cfm?URI=ao-44-32-6849.

Yaxin, Zhang et al. (Sept. 2020). "Terahertz smart dynamic and active functional electromagnetic metasurfaces and their applications". In: *Phil. Trans. R. Soc. A.* 378.2182. doi: 10.1098/rsta.2019.0609, p. 20190609.

Yoo, SeokJae and Q-Han Park (Jan. 2019). "Metamaterials and chiral sensing: a review of fundamentals and applications". In: *Nanophotonics* 8.2. doi: 10.1515/nanoph-2018-0167, pp. 249–261.

Yu, C et al. (Mar. 2012). "The potential of terahertz imaging for cancer diagnosis: A review of investigations to date". In: *Quant Imaging Med Surg* 2, pp. 33–45. DOI: 10.3978/j.issn.2223-4292.2012.01.04.

Zaman, Abdullah M. et al. (2022a). "Terahertz Metamaterial Optoelectronic Modulators with GHz Reconfiguration Speed". In: *IEEE Transactions on Terahertz Science and Technology* 12.5, pp. 520–526. DOI: 10.1109/TTHZ.2022.3178875.

Zaman, Abdullah M. et al. (2022b). "Ultrafast modulation of a THz metamaterial/graphene array integrated device". In: *Appl. Phys. Lett.* 121.9, p. 091102. DOI: https://doi.org/10.1063/5.0104780.

Zaman, Abdullah M. et al. (2023). "Versatile and active THz wave polarization modulators using metamaterial/graphene resonators". In: *Front. in Nanotechnol.*

5. ISSN: 2673-3013. DOI: 10.3389/fnano.2023.1057422. URL: https://www.frontiersin.org/articles/10.3389/fnano.2023.1057422.

Zeng, Hongxin et al. (Aug. 2021). "High-precision digital terahertz phase manipulation within a multichannel field perturbation coding chip". In: *Nat. Photon.* 15.10. doi: https://doi.org/10.1038/s41566-021-00851-6, pp. 751–757.

Zhang, Lu et al. (Nov. 2020a). "Beyond 100 Gb/s Optoelectronic Terahertz Communications: Key Technologies and Directions". In: *IEEE Communications Magazine* 58.11. doi: 10.1109/MCOM.001.2000254, pp. 34–40.

— (2020b). "Beyond 100 Gb/s Optoelectronic Terahertz Communications: Key Technologies and Directions". In: *IEEE Communications Magazine* 58.11, pp. 34–40. DOI: 10.1109/MCOM.001.2000254.

Zhang, Yaxin et al. (May 2014). "Photoinduced active terahertz metamaterials with nanostructured vanadium dioxide film deposited by sol-gel method". In: *Opt. Express* 22.9, pp. 11070–11078. DOI: 10.1364/OE.22.011070.

Zhang, Yaxin et al. (Apr. 2015). "Gbps Terahertz External Modulator Based on a Composite Metamaterial with a Double-Channel Heterostructure". In: *Nano Lett.* 15.5. doi: 10.1021/acs.nanolett.5b00869, pp. 3501–3506.

Zhang, Yaxin et al. (2019). In: *Nanophotonics* 8.1, pp. 153–170. DOI: doi:10.1515/nanoph-2018-0116. URL: https://doi.org/10.1515/nanoph-2018-0116.

Zhang, Yin, Yijun Feng, and Junming Zhao (2020). "Graphene-enabled tunable multifunctional metamaterial for dynamical polarization manipulation of broadband terahertz wave". In: *Carbon* 163, pp. 244–252. ISSN: 0008-6223. DOI: https://doi.org/10.1016/j.carbon.2020.03.001. URL: https://www.sciencedirect.com/science/article/pii/S0008622320302384.

Zhao, Haolan et al. (2020). "Electromagnetic induced transparency in graphene waveguide structure for Terahertz application". In: *Results in Physics* 16, p. 102971. ISSN: 2211-3797. DOI: https://doi.org/10.1016/j.rinp.2020.102971. URL: https://www.sciencedirect.com/science/article/pii/S221137971932460X.

Zhao, Yuncheng et al. (Aug. 2019a). "High-Speed Efficient Terahertz Modulation Based on Tunable Collective-Individual State Conversion within an Active 3 nm Two-Dimensional Electron Gas Metasurface". In: *Nano Lett.* 19.11, pp. 7588–7597. DOI: 10.1021/acs.nanolett.9b01273.

— (Aug. 2019b). "High-Speed Efficient Terahertz Modulation Based on Tunable Collective-Individual State Conversion within an Active 3 nm Two-Dimensional Electron Gas Metasurface". In: *Nano Lett.* 19.11. doi: 10.1021/acs.nanolett.9b01273, pp. 7588–7597.

Zhu, Lei and Liang Dong (Apr. 2022). "Electromagnetically induced transparency metamaterials: theories, designs and applications". In: *J. Phys. D: Appl. Phys.* 55, p. 263003. DOI: 10.1088/1361-6463/ac60cc.